

Computational and Data Driven Approaches for Investigation of Microwave-Plasma Interaction

by

PRATIK GHOSH
201721010

A Thesis Submitted in Partial Fulfilment of the Requirements for the Degree of

DOCTOR OF PHILOSOPHY

to

DHIRUBHAI AMBANI INSTITUTE OF INFORMATION AND COMMUNICATION TECHNOLOGY

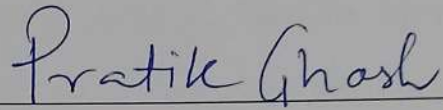


October, 2023

Declaration

I hereby declare that

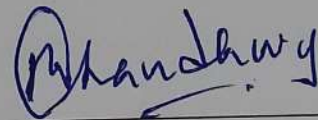
- i) the thesis comprises of my original work towards the degree of Doctor of Philosophy at Dhirubhai Ambani Institute of Information and Communication Technology and has not been submitted elsewhere for a degree,
- ii) due acknowledgment has been made in the text to all the reference material used.



Pratik Ghosh

Certificate

This is to certify that the thesis work entitled COMPUTATIONAL AND DATA DRIVEN APPROACHES FOR INVESTIGATION OF MICROWAVE-PLASMA INTERACTION has been carried out by PRATIK GHOSH for the degree of Doctor of Philosophy at *Dhirubhai Ambani Institute of Information and Communication Technology* under my supervision.



Prof. Bhaskar Chaudhury
Thesis Supervisor

Acknowledgments

I extend my heartfelt gratitude to God, the Almighty, for His abundant blessings that guided me through my research journey to its successful completion.

I want to acknowledge my late father, Late Partha Pratim Ghosh, who was my pillar of strength during the early stages of my PhD, and whose memory continues to inspire me. His unwavering support and guidance have been my driving force, and I believe he watches over me from above, providing the courage to navigate life's challenges. I am forever grateful for the privilege of being his son and hope to honor his legacy in all my endeavors.

I owe a profound debt of thanks to my thesis supervisor, Prof. Bhaskar Chaudhury, for entrusting me with the opportunity to undertake this research and for his invaluable guidance throughout the journey. His vision, dedication, and motivation have been a constant source of inspiration. Prof. Chaudhury's mentorship not only imparted research methodologies but also instilled clarity in presenting my work. Working under his tutelage has been an honor and a privilege, and without his support, none of this would have been possible. His unwavering encouragement and readiness to assist, even on holidays, have been instrumental in my success.

I express my deep appreciation to Distinguished Scientist Dr. Shisir Purohit from the Institute of Plasma Research (IPR) for his consistent guidance and willingness to engage in fruitful discussions and provide valuable suggestions. Dr. Ahlad Kumar also deserves my thanks for his guidance in implementing deep learning-based modeling for microwave-plasma experiments. My sincere gratitude extends to the members of my RPS committee, Prof. Arnab Ray and Prof. Sanjeev Gupta, for their encouragement, insightful

comments, and challenging questions during the defense of my research progress seminars (RPS).

I am indebted to the DST-SERB, Govt. of India, for granting me a research fellowship under the SERB project for three consecutive years from 2019 to 2022.

My appreciation goes to the dedicated staff at the DA-IICT help desk, including Rajendra Shah, Gyanesh Pandya, and Ramesh Prajapati. I would also like to acknowledge the contributions of B-tech CS students for their contributions in the development of the SMR, DMR, DL architecture for the forward and inverse problems. Vishrut Jaitley, Bhargav Jhetwa and Kishan Kavathiya, for contributing in development of the mesh refinement (SMR) code. Prayush Dave, Satyadev Patel, Dhwanil Manish Shah and Krish Shah for helping in development of OpenMP based shared memory implementation of the dynamic mesh refinement code (DMR). Mihir Joshi, for helping me to develop the DL architecture for the forward problem, and, Ashray Kothari and Vishv Ketankumar Joshi in the development of a DL-architecture for the inverse problem. Devdeep Shetranjiwala, for helping in developing the asymmetric profiles and highly sparse masks required for the DL based asymmetric plasma profile estimation using microwave-plasma interactions.

I am thankful to my fellow Ph.D. colleagues, including Dr. Miral J. Shah, Dr. Pankaj Chaudhury, Dr. Rahul Vashist, Dr. Nidhi Desai, Dr. Mayank Patel, Sourav Dev, Alik Banerjee, Pranav Verma, and lab mates Shivam Gandha, Ayushi Sharma, Libin Verghese, Ashok Jayaraman, and Raghav Gorasiya, who made my Ph.D. journey enriching and offered unwavering support. I would also like to thank Dr. Miral J. Shah, Shivam Gandha, Ayushi Sharma, Libin Verghese, for devoting their valuable time in reviewing my thesis.

My gratitude extends to my parents for their love, prayers, sacrifices, and dedication to my education and future. I deeply appreciate my mother, Smt. Paromita Ghosh, for her love, understanding, prayers, and continuous support throughout my research journey. I also want to express my thanks to my uncles, aunts, brothers, sisters, and other relatives for their unwavering support and prayers.

Contents

Abstract	xiv
List of Principal Symbols and Acronyms	xiv
List of Tables	xv
List of Figures	xvi
1 Introduction and Literature survey	1
1.1 Partially ionized unmagnetized cold collisional plasma	4
1.2 EM wave propagation in plasma	10
1.2.1 Complex propagation constant of plasma	10
1.3 High Power Microwave breakdown - a multi-physics and multi-scale problem	13
1.4 Conventional methods to computationally model the HPM breakdown	15
1.5 Data-driven approaches for investigating EM-plasma interactions	17
1.6 Applications of microwave-plasma interaction	18
1.6.1 High frequency microwave breakdown induced discharge	18
1.6.2 HPM switching and protection	19
1.6.3 Microwave assisted plasma diagnostics	20
1.7 Microwave propagation in plasma as a 2-D problem	22
1.8 Contribution of the Thesis	23
1.9 Organization of the thesis	24
2 2-D simulation of plasma dynamics during HPM breakdown - spatio-temporal investigation	26
2.1 Introduction	26

2.2	Physical model of HPM breakdown	27
2.3	Computational modelling of HPM breakdown	31
2.3.1	Numerical implementation of solvers	33
2.4	Simulation of a benchmark problem	34
2.5	Physics of complex plasma dynamics during HPM breakdown: spatio-temporal analysis	36
2.6	Associated challenges with 2-D simulation of HPM breakdown	40
2.7	Conclusions	41
3	Efficient dynamic mesh refinement technique for simulation of HPM breakdown	43
3.1	Introduction	43
3.2	Self aware DMR technique and it's implementation	45
3.2.1	Initiation of fine mesh expansion	46
3.2.2	Amount of fine mesh expansion	50
3.2.3	Quantity Updates on Mesh and Synchronization	51
3.2.4	Implementation of DMR algorithm	54
3.2.4.1	Step-wise implementation of DMR	54
3.2.5	DMR Computational Complexity	57
3.3	DMR Performance Analysis	58
3.3.1	Speedup and Efficiency of DMR	60
3.4	Conclusions	63
4	DMR assisted computational investigation of HPM switching and protection	65
4.1	Introduction	65
4.2	HPM switching and protection	67
4.2.1	Breakdown process initiation and plasma generation	68
4.2.2	EM-plasma interaction assisted HPM switching/ protection	70
4.3	Local gas-heating during HPM breakdown	72
4.3.1	HPM plasma generation with and without gas heating	73
4.3.2	Effect of microwave-induced local gas heating on HPM switching and protection	77

4.4	Conclusions	81
5	Machine learning based approach for 2-D simulation of microwave-plasma interaction	83
5.1	Proposed deep-learning architecture	85
5.1.1	CNN-based UNet deep learning architecture	86
5.1.2	Mathematical representation of encoder-decoder in CNN	88
5.2	Data-set generation methodology	89
5.3	Training details	91
5.4	Performance Comparison Metrics	93
5.5	Computational experiment Results and discussion	94
5.6	Ablation Study	95
5.6.1	Effect of encoder-decoder units	97
5.6.2	Effect of skip connections	97
5.6.3	Effect of up-sampling method	99
5.7	Network visualization using feature maps	99
5.8	Conclusions	100
6	Deep learning assisted microwave-plasma interaction based technique for plasma density estimation	101
6.1	Introduction	101
6.2	Data-set generation methodology	102
6.2.1	Synthetic data-set preparation for training DL-model . .	105
6.3	Deep learning based methodology	108
6.3.1	Deep learning architecture	110
6.3.2	Performance metrics	111
6.4	Results and discussion	112
6.4.1	Training details	112
6.4.2	Experiments with dense data (D_D and $D_{N,D}$)	114
6.4.3	Experiments with sparse data (D_S and $D_{N,S}$)	115
6.5	Conclusions	118
7	Data-driven approaches for investigation of microwave interaction with asymmetric plasma profiles	122
7.1	Introduction	122

7.2	Synthetic data-set generation methodology	123
7.2.1	Phase-1 plasma-profile generation technique	124
7.2.1.1	Mathematical function based density profiles	124
7.2.1.2	Fluid simulation based plasma density profiles	125
7.2.2	Phase-2 plasma profile generation technique	126
7.2.2.1	Data-set preparation	127
7.2.3	FDTD-based synthetic training data-set generation	128
7.3	Data-driven deep learning based approach	129
7.3.1	Deep-learning methodology	129
7.3.2	Deep-learning architecture	130
7.3.3	Training details	130
7.4	Results and discussion	131
7.4.1	Phase-1: Experiments with Non-Gaussian profile and filaments for forward-problem	131
7.4.1.1	DL-model training/testing simulated results	131
7.4.1.2	Model performance evaluation using different metrics	132
7.4.1.3	Model feature-map based learning from asymmetric filamentary plasma	134
7.4.2	Phase-2 : Experiments with asymmetric plasma profiles for inverse-problem	134
7.4.2.1	1D/2D comparison of DL-model simulated results and performance evaluation	135
7.4.2.2	Effect of noisy input data on the DL-model performance	137
7.4.2.3	Feature-map based learning for inverse-problem	139
7.5	Conclusion	140
8	Conclusion and future scope	141
8.1	Introduction	141
8.2	Summary of main results and accomplishments of the thesis	142
8.3	Future scope	144
	List of Publications	147

Abstract

Microwave-plasma interaction and High power microwave (HPM) breakdown involving plasma formation have been studied theoretically as well as experimentally since the 1950s for a wide variety of applications. Microwave plasma interaction can be classified into two broad categories, firstly involving low power non-ionizing waves and secondly high power ionizing waves leading to HPM breakdown. Early studies on HPM breakdown primarily focused on the determination of the breakdown field as a function of pressure, frequency and pulse duration. However, only recently, detailed experimental investigations of the plasma dynamics during breakdown have been possible with the use of sophisticated high-speed ICCD cameras. Particularly, in the past few years, several experiments and numerical simulations using millimeter and sub-millimeter wave irradiation (100 GHz) at high pressures (ten to hundreds of Torr) have been carried out. The renewed interest in this area is primarily because of two reasons. Firstly, the potential applications of such discharges to aerodynamic flow control, combustion ignition, flame stabilization and to propulsion have been investigated very recently. Secondly, the dynamics of high frequency wave breakdown at high pressures leading to formation of complex plasma structures (spatio-temporal propagation of plasma) such as self-organized plasma arrays is a subject of great interest from scientific point of view.

To completely understand the physics and properties of different types of discharges associated with microwave breakdown, it is crucial to further improve our current understanding of the microwave-plasma interaction and plasma formation at high pressures. To fully utilize the potential of this promising area of research, it is crucial to understand microwave-plasma interactions, both in the context of low-power non-ionizing microwaves and

when the power is sufficient to ionize the gaseous species and form plasma. Modeling and simulation of the strong coupling between the high frequency EM waves and the plasma is still a challenging research problem due to the different time and space scales involved in the process. Particularly accurate 2D/3D simulations are computationally very expensive and we require new efficient computational approaches to investigate this problem for real life applications. Most of the computational studies reported in the literature till now (particularly recent 2D simulations) have focused only on the wave scattering by the plasma and ionization-diffusion mechanism for plasma evolution (time scale of 100s of nanoseconds) due to computational constraints. Researchers have primarily studied this problem using a simple model wherein Maxwell's equations have been coupled with plasma continuity equations and these models have been used to investigate the plasma dynamics in nanosecond timescales.

As a first step, we have developed a comprehensive computational model for investigating microwave-plasma interaction and different kinds of millimeter wave breakdown at high pressures. An in-house 2D simulator has been implemented in C language and the validity of the code has been established by directly comparing the simulation results with the experimental observations available in the literature. The computational tool consist of three computational solvers (EM wave solver, Plasma solver and Fluid solver) coupled with each other. The inputs to this computational tool are the field strength of the EM wave, frequency of the wave, pressure and gas details. The important output required for investigating the physics of plasma dynamics are: plasma density, electric field distribution, electron temperature, gas density distribution etc.

As a second step, to address the computational challenges associated with such simulations, a self-aware mesh refinement algorithm has been presented that uses a coarse mesh and a fine mesh that dynamically expands based on the plasma profile topology to resolve the sharp gradients in E-fields and plasma density in the breakdown region. The dynamic mesh refinement (DMR) technique is explained in detail, and its performance has been evaluated using two metrics, the accuracy and efficiency, on a standard benchmark microwave breakdown problem. Different 2-D simulations are performed to

capture the front velocity and the filamentary pattern formation, and, results are compared for DMR (different refinement factors ($r = 2, 4$)) with the results obtained from uniform fine mesh. From the efficiency analysis, we observe a speedup of 8 (of the order of $O(r^3)$, when the refinement factor (r) is 2) compared to a traditional single uniform fine mesh-based simulation. The technique is scalable and performs better when the problem size increases.

Two applications related to HPM breakdown have been explored using our in-house 2D simulator, one associated with the protection of electronic components and the second on HPM switching. Breakdown thresholds, the field strength and the initial plasma density that determines breakdown time for such applications are reported. The dependence of cutoff time on initial plasma as well as strength of microwave E-field are investigated. The transmission and rejection capability of plasma for certain frequencies are investigated. Additionally, effect of gas heating on the HPM breakdown induced plasma and the cutoff time is studied for switching and limiter action. We propose a completely new machine learning based data driven approach for investigation of microwave-plasma interaction. Complete deep learning (DL) based pipeline to train, validate and evaluate the model has been discussed in this thesis. A convolutional neural network (CNN)-based deep learning model, inspired from UNet with series of encoder and decoder units with skip connections, for the simulation of microwave-plasma interaction has been discussed. The microwave propagation characteristics in complex plasma medium pertaining to transmission, absorption and reflection primarily depends on the ratio of electromagnetic (EM) wave frequency and electron plasma frequency, and the plasma density profile. The scattering of a plane EM wave with fixed frequency (1 GHz) and amplitude incident on a plasma medium with different Gaussian density profiles (in the range of $1 \times 10^{17} - 1 \times 10^{22} m^{-3}$) have been considered. The training data associated with microwave-plasma interaction has been generated using 2D-FDTD (Finite Difference Time Domain) based simulations. The trained deep learning model is then used to reproduce the scattered electric field values for the 1GHz incident microwave on different plasma profiles with error margin of less than 2%. We compare the results of the network, using various metrics like SSIM index, average percent error and mean square error, with the

physical data obtained from well-established FDTD based EM solvers. The proposed deep learning technique is significantly fast as compared to the existing computational techniques, and can be used as a new, prospective and alternative computational approach for investigating microwave-plasma interaction in a real time scenario.

Most of the plasma applications and research in the area of low-temperature plasmas (LTPs) is based on accurate estimation of plasma density and plasma temperature. The conventional methods for electron density measurements have major disadvantages of operational range (not very wide), cumbersome instrumentation, and complicated data analysis procedures. To address such practical concerns, the thesis further proposes a novel machine learning (ML) assisted microwave-plasma interaction based strategy which is capable enough to determine the electron density profile within the plasma. The electric field pattern due to microwave scattering is measured to estimate the density profile. The proof of concept is tested for a simulated training data set comprising a low-temperature, unmagnetized, collisional plasma. Different types of Gaussian-shaped density profiles, in the range $10^{16} - 10^{19}m^{-3}$, addressing a range of experimental configurations have been considered in our study. The results obtained show promising performance in estimating the 2D radial profile of the density for the given linear plasma device. The performance of the proposed deep learning based approach has been evaluated using three metrics- SSIM, RMSLE and MAPE. The favourable performance affirms the potential of the proposed ML based approach in plasma diagnostics and in future to replace existing plasma diagnostics.

In conclusion, the thesis presents new approaches for investigation of microwave-plasma interaction and HPM breakdown, which are significantly efficient compared to existing simulation techniques. To the best of our knowledge, this is the first effort towards exploring a data-driven DL based approach for the simulation of complex microwave plasma interaction. The simulations presented in the thesis provide a better understanding of both ionizing and non-ionizing applications of microwave-plasma interaction. They contribute to the study of complex plasma dynamics associated with high-frequency HPM breakdown-induced plasma, with potential applications such as switching/limiters, and plasma diagnostics.

List of Principal Symbols and Acronyms

Principal Symbols

Plasma parameter

m	mass of particle	m_e and m_i	electron and ion mass
n	plasma density	n_e and n_i	electron & ion plasma density
N_g	neutral or gas density	λ_D	Debye Length
k_B	Boltzmann constant	∇n	density gradient
e	electron charge	ρ_l	local net charge
T_e & T_i	electron and ion temperature	T_g	gas temperature
L	Length of plasma	q	charge of particle
ν_m	electron-neutral collision frequency	ω_p	plasma frequency
D_e & D_i	electron and ion diffusion coefficient	D_a	ambipolar diffusion coefficient
μ_e & μ_i	electron and ion mobility	D_{eff}	effective diffusion coefficient
ν_i	ionization frequency	ν_a	attachment frequency
r_{ei}	electron-ion recombination rate	ν_{eff}	effective ionization frequency
γ	ionization coefficient	Γ_e & Γ_i	flux of electron and ion
v_e & v_i	electron and ion velocity	Z	charge number
v_{front}	front velocity	\vec{j}	current density

EM parameter

\vec{E} & \vec{H}	electric and magnetic field	E_0	electric field amplitude
$\frac{E_{eff}}{p}$	reduced effective field	ω or f	EM wave frequency
E_{rms}	rms E-field	k	wave propagation vector
ϵ_r	relative permittivity	c	speed of light

Simulation parameter

$N_{c,x}$ & $N_{c,y}$	coarse grid points in X and Y	$N_{f,x}$ & $N_{f,y}$	fine grid points in X and Y
ΔS_c & ΔS_f	coarse and fine grid size	r	refinement factor
Δ_{EM} & Δ_d	grid size of EM and plasma	Δt_{EM} & Δt_d	time step of EM and plasma
L_x	Length of domain along X	L_y	Length of domain along Y

Acronyms

AI	Artificial Intelligence
CFL	Courant-Friedrichs-Lewy
CNN	Convolutional Neural Network
CPU	Central Processing Unit
DGTD	Discontinuous Galerkin Time Domain
DL	Deep Learning
DMR	Dynamic Mesh Refinement
DNN	Deep Neural Network
EM	Electromagnetic
FDTD	Finite Difference Time Domain
FD	Finite Difference
FETD	Finite Element Time Domain
FVTD	Finite Volume Time Domain
FLOPS	Floating point operations per second
GPU	Graphics Processing Unit
GW	Gigawatt
HF	High Frequency
HPM	High Power Microwave
LEFA	Local Electric Field Approximation
LTP	Low Temperature Plasma
MAPE	Mean Absolute Percentage Error
ML	Machine Learning
MSE	Mean Squared Error
PDE	Partial Differential Equations
PDF	Probability Distribution Function
PIC	Particle In Cell
PINN	Physics Informed Neural Networks
Relu	Rectified Linear Unit
RMSLE	Root Mean Squared Logarithmic Error
SSIM	Structural Similarity Index Measure
TF/SF	Total Field/ Scattered Field
TR	Transmit-Receive

List of Tables

2.1	Approximate simulation time for different problem sizes.	41
5.1	EM-Wave scattering predicted data comparison with the actual data	94
5.2	Impact of varying the number of encoder-decoder units	97
5.3	Impact of varying the skip connections	97
5.4	Impact of using various up-sampling methods	99
6.1	RMSLE and MAPE-based comparison of predicted plasma density with the actual density data for different types of dense data samples	113
6.2	Performance evaluation for computational experiments performed with dense data samples (D_D) in the limited range having $n_0 : 1e18 - 1e19 \text{ m}^{-3}$	114
6.3	RMSLE and MAPE-based comparison of predicted plasma density with the actual density data for different sparse data sets	115
7.1	Performance metrics evaluation for scattered E_{rms} obtained from different computational experiments on asymmetric dense plasma density profile data. The peak plasma density is n_0 . . .	133
7.2	Performance evaluation for computational experiments performed with E_{rms} data both (dense and sparse) corresponds to plasma density profile having partial and full asymmetry. The peak density range having $n_0 : 1e18 - 1e19 \text{ m}^{-3}$	137
7.3	Performance evaluation for computational experiments performed with dense E_{rms} data corresponds to plasma density profile having asymmetry. The peak density range having $n_0 : 1e18 - 1e19 \text{ m}^{-3}$	138

List of Figures

1.1	(a) Time integrated breakdown plasma image in E-plane, Hidaka et al. (2008,2009) [1,2]. (b) Streamer discharges in air at 760 torr, Barashenkov et al. (2000) [3]. (c) Air breakdown induced plasma filamentary structures formed for high pressure (760 torr), Cook et al.(2010) [4] (d) Volumetric discharge, Khodataev et al. (2008) [5]. (e) Side view (combed shaped) of plasma formed by air breakdown under non-focussed HPM beam, Y.Oda et al (2020) [6]. (f) HPM breakdown images for circular and linear polarized Microwave, Cook et al.(2011) [7]. All the experimental results correspond to 100's of GHz of Microwave (in millimeter band)	4
1.2	The 1-D distribution of k_r and k_i in the ω_p/ω for different ν_m/ω ratios.	11
1.3	Plane EM wave propagation into a partially ionized cold collisional unmagnetized plasma. Two axes are presented along x-axis. The time-axis (t) represented in blue. The length-axis ($x_{central}$) represented in brown color. Using both, the time and length axes, the damping of EM wave oscillations with time for various locations inside the plasma is shown.	13
1.4	The complete fluid-based model of the HPM breakdown phenomenon. The different solvers correspond to the coupled physical processes. The time steps (Δt) are different for the three solvers (ranges from 10^{-15} to 10^{-9} s). The solvers requiring frequent updates can be accelerated by implementing dynamic mesh refinement (DMR).	14

1.5	Two different formulations for 2-D simulation of microwave interaction with plasma based on the location of the E-field. Multiple plasma structures formation when (a) E-field parallel to the simulation plane (XY) [8] and (b) E-field perpendicular to the simulation plane [9].	22
1.6	Organization of the thesis chapters.	24
2.1	Computational implementation of multi-physics and multi-scale 2-D plasma fluid model.	32
2.2	(a) Schematic of the Computational domain. $\{(c_{kx}, c_{ky}) \in \mathbb{Q}^+\}$, and, x_0 and y_0 are fractions in $[0, 1]$ of L_x and L_y respectively. The MUR outer radiation boundary condition has been used for scattered field formulation. (b) A partial 2-D Cartesian grid representation of $L_x \times L_y$ domain for FDTD (E and H-field) and plasma fluid model: plasma velocity (v_e) and current density (J) solver. Grid-spacing for EM and plasma solver, Δ_{EM} and Δ_d , respectively.	35
2.3	The choice of initial density (n_{0i} , where $i= 1,2,3$ and 4) in m^{-3} for initiating the HPM breakdown-induced filamentation process.	36
2.4	(i-iv) plasma density (m^{-3}) distribution in the filaments at four-time instances.	36
2.5	(i-iv) The evolution of the plasma density (m^{-3}), rms E-field (V/m), the effective diffusion coefficient (m^2/s), and the rate of ionization (s^{-1}) along the $x_{central}$ of the computational domain. (v-viii) the evolution of the same quantities along the $y_{central}$ passing through the center of the rightmost filament (in a dotted circle). Here, L: Left and R: Right, $L_x = L_y = 1\lambda$	37
3.1	(a) Schematic of the Computational domain. $\{(c_{kx}, c_{ky}) \in \mathbb{Q}^+\}$, and, x_0 and y_0 are fractions in $[0, 1]$ of L_x and L_y respectively. The MUR outer radiation boundary condition has been used for scattered field formulation. (b) Formation of self-organized plasma filaments during HPM breakdown (snapshot at $t = 45$ ns, $E_0 = 5.5$ MV/m, freq = 110 GHz). The maximum density (max) is $6 \times 10^{21} m^{-3}$ and (min) is 0.	45

3.2	The self-aware expansion of fine mesh in DMR to capture the 2D distribution of plasma density as the filamentary pattern evolves.	46
3.3	(a) The spatial variation of ϵ_r and σ for a 1D plasma density (n_e) distribution. (b) Convergence study for different threshold densities (m^{-3}) to arrive at the threshold density criteria for mesh initiation. The EM wave of frequency 110 GHz is considered here.	47
3.4	The 1D distribution of (a) plasma density and (b) rms E-field and their corresponding gradient scale lengths l_{den} and $l_{E_{\text{rms}}}$ respectively, along the upper half of central y-axis (y_{central}) through the initial plasma density. The initial plasma density is located at $\{x_0, y_0\} = \{0.85L_x, 0.5L_y\} = \{1.2\lambda, 0.75\lambda\}$, $L_x = L_y = 1.5\lambda$. The $\lambda \approx 0.0027$ m corresponds to frequency (f) = 110 GHz.	48
3.5	The 1D distribution of (a) plasma density and (b) rms E-field and their corresponding gradient scale lengths l_{den} and $l_{E_{\text{rms}}}$ respectively, along the central x-axis (x_{central}) through the initial plasma density. The initial plasma density is located at $\{x_0, y_0\} = \{0.85L_x, 0.5L_y\} = \{1.2\lambda, 0.75\lambda\}$, $L_x = L_y = 1.5\lambda$. The $\lambda \approx 0.0027$ m corresponds to frequency (f) = 110 GHz. . .	49
3.6	(a) The mesh refined (the dashed region with refinement factor 2) discretized computational grid showing locations for computation of EM fields and density. (b) The expanded view of overlapped coarse and fine mesh. The different data transfer of updated E -field, H -field and the plasma density from coarse mesh to its corresponding fine mesh locations on both coarse-fine boundary (<i>cfb</i>) as well as the fine boundary (<i>fb</i>) are shown. (c) Schematic representation of interpolation techniques for $r=2$. Here, I : E-field (and velocity), II : H-field, and III : plasma density represent different interpolations for the coarse mesh data.	52

- 3.7 (a) Schematic representations of the DMR technique, mesh initiation, and expansion. Initial Gaussian plasma density is located at (x_0, y_0) . b_x and b_y are the dimensions of the fine mesh. X_{Fi} , X_{Bi} , Y_{uj} , and Y_{lj} (or Y_{dj}) denote the forward, backward, upper, and lower thresholds, respectively. The initial fine mesh is labeled a-b-c-d, while the fixed coarse mesh is labeled A-B-C-D. (b) Flowchart representation of computational steps: Subroutines **A**, **B**, **C**, **E**, **F**, and **G** update the EM and plasma solvers for both meshes, with interpolation (**D**) between them. Den represents plasma density. The time updates for coarse (c) and fine (f) meshes are Δt and $\Delta t/r$, respectively, where r is the refinement factor. 55
- 3.8 Schematic representation of the dynamic mesh generation process with an initial fine mesh, a^{11} - b^{11} - c^{11} - d^{11} , centered around the initial plasma density located at x_0 and y_0 , which expands along x and y based on threshold criteria. The coarse mesh is present in the complete computational domain, A-B-C-D. 56
- 3.9 The 2D distribution of (a) plasma density (m^{-3}) at time $t = 140$ ns and (b) corresponding rms E-field, for a problem size of $7.5\lambda \times 1.5\lambda$. The maximum density is $8.7 \times 10^{21} m^{-3}$ and maximum E-field strength is 6.97×10^6 V/m as represented on the color scale. 59
- 3.10 (a) The 2D distribution of plasma density (m^{-3}) at time $t = 90$ ns has been obtained using a single uniform mesh (Uni) and DMR ($r=2$ and $r=4$). (b) The comparison between the plasma front propagation using temporal evolution of the plasma density (m^{-3}) along $x_{central}$ for a uniform mesh (Uni) and dynamic mesh (DMR) with different refinement factors (r), here $r = 2, 4$. The color-bar represents plasma density distribution, $max : 7 \times 10^{21} m^{-3}$ 59

3.11	For different simulation times in seconds using different techniques, Uni and DMR, the plots of (a) the subroutine-wise execution time to simulate P1, and (b) the total execution time taken to simulate P1.	61
3.12	For different simulation times in seconds using different techniques, Uni and DMR, the plots of (a) the overall speedup and (b) the growth of total cells with time for different problem sizes, P1 to P3.	62
4.1	Schematic representation of the HPM breakdown application in protection and switching.	67
4.2	(a) Schematic of computational domain with E_{max} and n_0 . 2D profile (b). n_e and (c) E_{rms} at 60 ns.	69
4.3	Spatial distribution of 1D plasma along x-axis passing through the center of the computation domain for different time instants (40 to 100 ns) with (a) effective diffusion (D_{eff}) coefficient, (b) ambipolar diffusion (D_a) coefficient respectively.	69
4.4	Plot of t_{cutoff} distribution for (a) varying E_0 at fixed n_0 and (b) varying n_0 at fixed E_0	70
4.5	Behaviour of 1D plasma density profile (n_e) obtained from 2D simulations with cut-off density (n_{cutoff}), either blocking or allowing frequency range (1 to 200 GHz).	71
4.6	Plot of the relative permittivity (ϵ_r) and conductivity (σ) correspond to 1D plasma density (n_e) profile at two-time instants 40 ns and 70 ns. σ in (S/m). x-axis: plasma density profile	72
4.7	(a) Computational domain schematic with enhanced MW E-field ($2E_0$, $E_0 = 2.72$ kV/cm) and initial seed electrons. 2D plasma profile (streamer) at 250 ns (b1) without (b2) with gas heating and spatio-temporal density evolution along the streamer axis, indicating time to reach $n_{critical}$ and shape changes at $t = 2.5 \times 10^{-7}$ s, (c1) Without and (c2) with gas heating.	74

4.8	2-D Plots representing the effect of (a) without and (b) with gas-heating on n_e , as well as the effect of gas heating on (c) N_g and (d). T_g , for a given time instant, $t= 250$ ns. For without gas heating, the $max n_e$ values is $5.25 \times 10^{19} \text{ m}^{-3}$, with gas heating, $max n_e$ value is $1.53 \times 10^{20} \text{ m}^{-3}$. For with gas heating, the max value is fixed, $N_0 = 2.25 \times 10^{24}$ at $p = 70$ torr, and min values is $0.53 \times 10^{24} \text{ m}^{-3}$. For with gas heating, $max T_g$ value is 1266.5 K and min is $T_0 = 300$ K. For without gas heating $N_g = N_0$ and $T_g = T_0$	75
4.9	The 1D distribution of n_e, v_{eff}, D_{eff} and E_{eff}/N_g for (a-d) without and (e-h) with gas heating, respectively, for five different time instants along the vertical streamer axis, $y_{central}$ line.	76
4.10	The effect of (a) without and (b) with gas heating, on the growth of the peak plasma density (1D) at the center of streamer core (at (x_c, y_c)).	78
4.11	The effect of (a) without and (b) with gas heating, on the behavior of spatial plasma density profile along $x_{central}$ (passing through the center of streamer core, (x_c, y_c)). To block or allow certain microwave frequency based on the peak plasma density at the streamer core at 200 ns ($\sim 1 \times 10^{20} \text{ m}^{-3}$). For the simulation, discrete frequencies have been chosen from the 1 to 150 GHz range, and a normalized rms E-field ratio ($E_{T,rms}/E_{i,rms}$) is used to observe the blocking/transmitting nature of the profile. $E_{T,rms}$: Total E-field ($E_{T,rms}= E_{i,rms} + E_{scattered,rms}$), $E_{i,rms}$: rms incident E-field ($2E_0/\sqrt{2} = 3.84 \text{ kV/cm}$ or $3.84 \times 10^5 \text{ V/m}$).	79
4.12	The effect of (a) without and (c) with gas heating on the cut-off time (t_{cutoff}) and ($t_{critical}$). The lower breakdown time is indicated by the (d) drop (2.7 times) (b) drop (1.7 times) in the signal transmission ($E_{T,insta}$) through the plasma at the corresponding t_{cutoff} , shifted from 200 ns (without gas heating) to 120 ns (with gas heating). $E_{T,insta}$: instantaneous Total E-field, $max E_{T,insta} = 5.4 \times 10^5 \text{ V/m}$ (before breakdown)	80

5.1	Flowchart for training the proposed data-driven ML model . . .	85
5.2	The proposed architecture having encoder, decoder, and skip connections for EM-wave scattered by plasma density prediction	87
5.3	(a) The schematic representation of the square computational domain, $\{(c_{kx}, c_{ky}) \in \mathbb{Q}^+\}$; length of the domain L_x and L_y are taken in terms of the wavelength of the incident EM wave. The location x_0, y_0 is $0.5L_x$ and $0.5L_y$, respectively, and, $\{c_{kx}, c_{ky}\} = \{1.5, 1.5\}$, where λ corresponds to freq = 1 GHz. The parameter space can be varied by changing two parameters of the 2D Gaussian profile - width and peak density. (b) plasma profile along the central x-axis ($x_{central}$) for different widths of Gaussian (S1:0.05 λ (highest) to S10:0.02 λ (lowest)) for a fixed peak plasma density, $n_0 = 10^{22} \text{ m}^{-3}$ (c) different peak plasma densities for a fixed width of Gaussian. The den1S1: $n_0 = 10^{22} \text{ m}^{-3}$ to den6S1: $n_0 = 10^{21} \text{ m}^{-3}$	90
5.4	(a-f) Generated dataset of Plasma Density and corresponding scattered E_{rms} for varying peak density. The color-bar represents the maxima and minima corresponding to plasma density and the E_{rms} . The maxima for plasma density is indicated by n_0 and the minima is 0. For E_{rms} , maxima are 7.07, 7.15, 7.74, 9.37, 10.36, and 10.47 V/m, respectively, and minima is 0. The skin depth of microwave into plasma profile reduces as n_0 increases indicated by visibility of exact scatterer dimension (2D Gaussian profile) from E_{rms} plot (a) to (f).	92
5.5	Mean squared error loss in training the model	93
5.6	Comparative study and results of example cases; Row 1 (a1-a5): 2D profile of input plasma density (for increasing n_0 , $6e18, 6e19, 4e20, 6e21$ and $8e21 \text{ m}^{-3}$ from left to the right); Row 2 (b1-b5): 2D Scattering (E_{rms}) pattern obtained from FDTD solver; Row 3 (c1-c5): 2D Output E_{rms} image from the proposed deep learning based architecture; Row 4 (d1-d5): Comparison of 1D E_{rms} along the central x-axis ($x_{central}$) of the computational domain predicted from our work and FDTD based solver. . . .	96

- 5.7 Row 1: Feature maps of the output of the six encoder units; Row 2: Feature maps of the output of the six decoder units. (a) is the final output E_{rms} image of the network; The corresponding (a)-(f) pairs of the encoder-decoder pairs give the feature output in the same spatial dimensions. Only four feature maps for a convolution unit are shown for representational purposes. The total number of feature maps for a unit is equal to the number of filters used in the convolution or transposed convolution layer.) 98
- 6.1 Schematic representation of the forward and inverse problem for EM-plasma interaction is shown. The 2-D representation of plasma density and corresponding E_{rms} obtained through the Maxwell-plasma fluid model (solution to forward problem) exists, but no direct inverse mapping exists. 102
- 6.2 (a) A typical linear LTP device schematic. (b) The schematic representation of the square computational domain, $\{(m_x, m_y) \in \mathbb{Q}^+\}$; the length of the domain L_x and L_y is expressed in terms of the wavelength of the incident EM wave. The location coordinates x_0, y_0 is $0.5L_x$ and $0.5L_y$, respectively, and, the coefficients, $\{m_x, m_y\} = \{1.0, 1.0\}$, where λ corresponds to the freq = 500 MHz. The parameter space can be varied by changing two parameters of the 2D Gaussian profile - width ($\sigma_x = \sigma_y$) and peak density (n_0). $\sigma_x = \{0.01\lambda, 0.02\lambda, \dots, 0.05\lambda\}$ for a fixed peak plasma density, $n_0 = \{10^{16}, 10^{17}, \dots, 10^{19}\} \text{ m}^{-3}$ 104
- 6.3 (a1-a5) Generated data-set of reflected E_{rms} from, (b1-b5) different plasma density profile having varying peak density (n_0). The maxima for plasma density is indicated by n_0 , and the minima is 0. For E_{rms} , maxima are 8.29, 9.34, 10.31, 10.36, and 10.37 V/m, respectively, and minima is 0. The skin depth of the microwave into the plasma profile reduces as n_0 increases. . 105

6.4	Dense E_{rms} data generation for ML training: (a) by removing the central part of the data and retaining the remaining, (b) addition of noise to the generated dense data, followed by removing the central part and retaining the remaining. (c1-c3) represents the 2-D as well as 1-D density profile, Furthermore, corresponding, dense E_{rms} data has been collected with and without noise (left to right). The color-bar maxima and minima correspond to E_{rms} . D_I : Initial data, M_D : Mask for dense data, N : Noise data	106
6.5	Sparse E_{rms} data generation for ML training: (a) by removing the central part of the data and retaining the sparse data using a concentric ring-based mask, (b) addition of noise to the generated dense data, followed by removing the central part and retaining the remaining. (c1-c3) represents the 2-D as well as 1-D density profile, and corresponding, dense E_{rms} data collected for both with and without noise (left to right). The color-bar maxima and minima correspond to E_{rms} . D_I : Initial data, M_S : Mask for sparse data, N : Noise data	107
6.6	Complete workflow used in this study for prediction of plasma density via DL	109
6.7	The model architecture uses encoder, decoder, and skip connections to predict the plasma density profile from masked EM-wave scattered pattern data-sets	110
6.8	Comparative study and results for dense data-set (D_D); Row 1 (a1-a5) masked 2-D E_{rms} dense data obtained from simulations for given input density profile; Row 2 (b1-b5) The actual input plasma 2-D density profile; Row 3 (c1-c5) The predicted 2-D profile of plasma density from the proposed deep learning based architecture; Row 4, Comparison of the accuracy between the magnitude of the actual and predicted 1-D plasma density along the central X-axis ($x_{central}$) of the computational domain.	116

- 6.9 Comparative study and results for dense data-set with noise ($D_{N,D}$); Row 1 (a1-a5) 2-D E_{rms} (the increasing maxima in V/m from left to right) dense data with Gaussian noise obtained from plasma density profile using FDTD; Row 2 (b1-b5) The actual plasma 2-D density profile; Row 3 (c1-c5) The predicted 2-D profile of plasma density from the proposed deep learning based architecture; Row 4, Comparison of the accuracy between the magnitude of the actual and predicted 1-D plasma density along the central X-axis ($x_{central}$) of the computational domain in the presence of noise. 117
- 6.10 Comparative study and results for sparse data-set (D_S); Row 1 (a1-a5) 2-D E_{rms} (the increasing maxima in V/m from left to right) sparse data obtained from plasma density profile using FDTD; Row 2 (b1-b5) The actual plasma 2-D density profile; Row 3 (c1-c5) The predicted 2-D profile of plasma density from the proposed deep learning based architecture; Row 4, Comparison of the accuracy between the magnitude of the actual and predicted 1-D plasma density along the central X-axis ($x_{central}$) of the computational domain. 119
- 6.11 Comparative study and results for sparse data-set with noise ($D_{N,S}$); Row 1 (a1-a5) 2-D E_{rms} (the increasing maxima in V/m from left to right) sparse data with Gaussian noise obtained from plasma density profile using FDTD; Row 2 (b1-b5) The actual plasma 2-D density profile; Row 3 (c1-c5) The predicted 2-D profile of plasma density from the proposed deep learning based architecture; Row 4, Comparison of the accuracy between the magnitude of the actual and predicted 1-D plasma density along the central X-axis ($x_{central}$) of the computational domain in the presence of noise. 120

7.1	Mathematical function-based partial/ fully asymmetric plasma density, (a1-a3) 2-D distribution and (b1-b3) 1-D distribution along x-line. Fluid simulation based fully asymmetric plasma density, (c1-c3) 2-D distribution, and (d1-d3) 1-D distribution along x-line.	126
7.2	Schematic representation of the computational domain to simulate the microwave interaction with various asymmetric plasma profiles. Domain length along x and y, L_x and L_y , is expressed in terms of EM wavelength (λ).	127
7.3	Mathematical formulation of Partial/Full asymmetric profile (Gaussian multiple plasmoids, Non-Gaussian (multiple plasmoids and Ellipsoid)) data-set, plasma density (a1-a3) 2-D distribution, and (b1-b3) 1-D distribution along x-line. (c1-c3) The corresponding scattered E_{rms} 2-D pattern.	128
7.4	Fluid simulation based filamentary profile data-set, plasma density (a1-a3) 2-D distribution and (b1-b3) 1-D distribution along x-line. (c1-c3) The corresponding scattered E_{rms} 2-D pattern.	129
7.5	Mean squared error loss in training (learning sample)/testing (unseen data-sample) the model for (a) Non-Gaussian and (b) filament plasma profile.	131
7.6	The 2-D, 1-D qualitative and quantitative comparison of actual and predicted scattered E_{rms} from Non-Gaussian (a1-a5) and (b1-b5) filamentary plasma profile, respectively.	132
7.7	Feature maps correspond to the output of each of the encoder and decoder units of the DL model. A single feature map from each convolutional unit is shown for representation. The model input and the final output of the DL-network are the plasma density profile and its corresponding E_{rms} image.	133
7.8	Comparison of results for dense (D_D) and sparse (D_S) data samples without and with noise (for partially asymmetric), having two Gaussian plasma profiles with peaks not located at the center of the simulation domain (x_0, y_0).	135

7.9	Comparison of results for completely asymmetric density profile for dense E_{rms} data, D_D . (a1-a4) the masked E_{rms} , (b1-b4) the ground truth, (c1-c4) the predicted plasma density profile for D_D , and (d1-d4) the residual (difference between actual and predicted) to indicate the degree of mismatch.	136
7.10	Comparison of results for completely asymmetric density profile for sparse E_{rms} data, D_S . (a1-a4) the masked E_{rms} , (b1-b4) the ground truth, (c1-c4) the predicted plasma density profile for D_S and (d1-d4) the residual to indicate the degree of mismatch between actual and predicted asymmetric profiles.	136
7.11	Comparative study and results for dense data (D_D), considering two Gaussian plasma profiles not symmetric about the computation domain center, with different relative noise amplitudes.	138
7.12	Feature maps correspond to the output of each of the encoder and decoder units of the DL model. The model input and output are the E_{rms} image and the image of the plasma density profile.	139

CHAPTER 1

Introduction and Literature survey

The study of the interaction between electromagnetic (EM) waves and plasma has been an important area of research that has been explored for several decades due to its numerous applications [10, 11]. Various experimental, theoretical, and computational studies have been carried out to understand the EM wave propagation characteristics such as transmission, reflection, scattering, and absorption in the plasma. Initial studies were primarily motivated to understand/ mitigate the communication blackout problems associated with satellite or supersonic re-entry vehicles into earth's ionosphere plasma [12], determination of breakdown voltages for discharges [10], ECR heating of thermal plasmas [13], plasma antennas [14], plasma stealth technology [15, 16] and many more. The advancement of the microwave (frequency- 3 GHz to 30 GHz, wavelength- 10 cm to 1 cm) and millimeter wave (frequency-30 GHz to 300 GHz, wavelength- 10mm to 1mm) technology [17], such as development of various microwave sources ranging from low to high power and their easy availability, opened up many new areas of research involving microwave-plasma interaction [18]. The microwave-plasma interaction studies have been generally categorized under two broad classes, the non-ionizing and the ionizing, based on the strength of the microwave E-field (non-ionizing if $E\text{-field} < \text{breakdown field}$). When a low-power, high-frequency microwave interacts with stray electrons in the gas, the electrons immediately respond to the wave and suffer multiple collisions with the neutrals in every wave cycle due to their lower mass. The electrons acquire drift velocity from the wave E-field and subsequently gain instantaneous momentum. However, the high collisions with neutrals

interrupt the electron motion, and the electron loses the entire momentum at each collision. The energy exchange between the electrons and neutrals is of the order of $((m_e/m_{neutral})KE_0)$, where KE_0 is electron kinetic energy before collision. Since $m_e \ll m_{neutral}$, energy remains conserved before and after the collision. Thus, only momentum transfer through collisions dominates. Since the microwave has low power, it cannot impart sufficient energy to the electrons ($KE < \text{the ionization potential of the neutrals}$) to sustain breakdown. Thus, non-ionizing its effect on plasma discharge dynamics is negligible. However, high-power microwaves have sufficient EM energy to impart high KE to the stray electrons in gases (such as air).

The non-ionizing microwave-plasma interaction, where the wave cannot ionize the existing plasma, has different applications such as reflectors and absorbers [15], plasma antennas [14], plasma stealth technology [16], plasma meta-materials [19], plasma diagnostics [12, 20]. Microwave-plasma interaction in the context of gas breakdown in a High Power Microwave (HPM) field (ionizing case) has also been extensively studied due to its numerous applications in areas such as aerospace applications, plasma propulsion, flow control, combustion initiation, plasma-based limiters, HPM switching, electromagnetic warfare etc. [5, 21–30]. Additionally, recent technological advancements in high-speed cameras [1, 6, 7, 31, 32] have allowed for more detailed experimental investigations of plasma dynamics during HPM breakdown at high pressures. Several experiments have been conducted using millimeter and sub-millimeter wave irradiation at high pressures, which have resulted in the observation of various types of gas discharges such as streamer, overcritical, subcritical, volumetric, and attached to an initiator [5, 33, 34]. To completely understand the properties of each type of discharge and the associated plasma dynamics, it is crucial to improve our understanding of the electromagnetic wave-plasma interaction, plasma formation, and subsequent energy exchange between wave and plasma, as well as between gas and plasma. Recent experiments with high-frequency waves (100's of GHz) [1, 2, 5–7, 31, 32, 34] have revealed the formation of self-organized plasma structures, such as fish-bone-like filaments and comb-shaped branching, during air breakdown from high-frequency microwave under atmospheric pressure. Some of those experimental results are shown in Fig.1.1. These plasma

structures propagate toward the microwave source, and the high-density plasma filaments enhance the scattered EM field at the anti-node of standing waves, resulting in sustained self-organized plasma pattern formation [35,36]. Several researchers have used this problem as a benchmark to investigate or validate computational techniques [8]. In this thesis, we have also considered this our benchmark problem and mainly focus on partially ionized, unmagnetized, collisional plasmas. The HPM breakdown phenomenon is a multi-physics, multi-scale problem and involves non-linear dependencies on various parameters (pressure, E-field strength, and more) that control the various physical processes (such as diffusion, ionization, attachment, and recombination), resulting in a breakdown. Consequently, such a complex problem is experimentally, analytically, and computationally challenging. The requirement of high-power microwave sources operating at high frequency over a wide range of pressures (low, intermediate, and high) makes it difficult as an experimental problem. The analytical modeling becomes too simplistic compared to the real phenomenon. However, the advanced numerical techniques, which are powerful (realistic compared to analytical model) to replicate actual HPM breakdown experimental observations, still face a challenge for simulating such a problem in a computational resource constraint environment.

This chapter provides a brief overview of the type of plasma we have considered in our study, along with the various mathematical equations describing the charge transport in the plasma. Then, we discuss the electromagnetic wave propagation in such types of plasmas. Subsequently, we highlight the multi-scale and multi-physics nature of the HPM breakdown problem. Next, we discuss the conventional methods available to computationally model the HPM breakdown problem along with the associated challenges. Further, we discuss the necessity of exploring data-driven approaches in the context of microwave-plasma interaction. We also briefly introduce the three important applications based on microwave-plasma interaction physics investigated in this thesis: plasma dynamics associated with HPM breakdown, HPM-based switching and protection, and microwave-assisted plasma diagnostics.

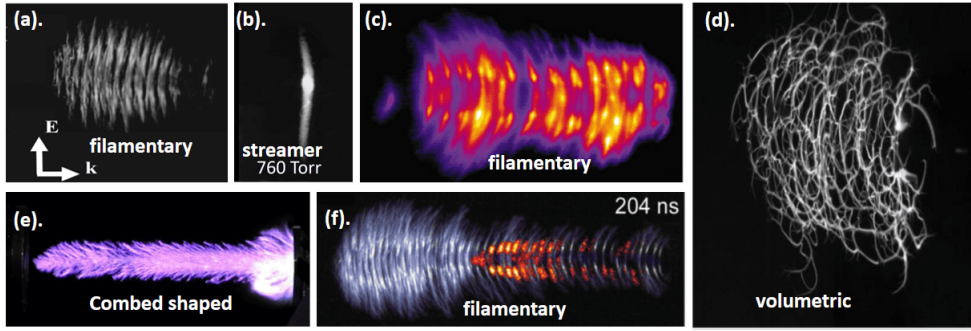


Figure 1.1: (a) Time integrated breakdown plasma image in E-plane, Hidaka et al. (2008,2009) [1,2]. (b) Streamer discharges in air at 760 torr, Barashenkov et al. (2000) [3]. (c) Air breakdown induced plasma filamentary structures formed for high pressure (760 torr), Cook et al.(2010) [4] (d) Volumetric discharge, Khodataev et al. (2008) [5]. (e) Side view (combed shaped) of plasma formed by air breakdown under non-focussed HPM beam, Y.Oda et al (2020) [6]. (f) HPM breakdown images for circular and linear polarized Microwave, Cook et al.(2011) [7]. All the experimental results correspond to 100's of GHz of Microwave (in millimeter band)

1.1 Partially ionized unmagnetized cold collisional plasma

Plasma is considered the fourth state of matter alongside the solids, liquids, and gases [37]. When sufficient energy is delivered to a molecular gas that dissociates into atomic gas (through a collisional process between high KE particles), then a fraction of atoms possess KE to overcome the binding energy of outermost electrons, resulting in an ionized gas. The ionized gas consists of different charged and neutral species, which follow quasi-neutrality and collective behavior.

Quasi-Neutrality: In gaseous plasma, within a volume, the number of positively charged ions is roughly equal to the number of free electrons, resulting in the overall charge densities canceling each other maintaining the electrical neutrality on macroscopic scales. If the number densities of electron and ion (with charge number Z) are, n_e and n_i . Then, under quasi-neutral conditions, they are locally balanced, $n_e = Z n_i$. The quasi-neutrality is not just an ideal equilibrium but the plasma always tries to achieve the most desirable state by re-adjusting the local charge distribution as a response to any perturbation. The potential (Φ_l) as a result of such disturbance (results charge accumulation Q within a local volume), after solving Poisson's equation can

be expressed by,

$$\Phi_l = \frac{Q}{r} \exp(-r/\lambda_D) \quad (1.1)$$

where, Φ_l , screens as $r > \lambda_D$, also called Debye screening. The characteristic length λ_D is known as Debye length, within which the quasi-neutrality exists. The Debye length can be expressed as ,

$$\lambda_D = \sqrt{\frac{\epsilon_0 k_B T_e}{e^2 n_e}} \quad (1.2)$$

where k_B is Boltzmann constant, and T_e is electron temperature (based on the thermal KE of electrons). For an ideal plasma, more charge particles must exist within a Debye sphere, given by, $\left(n_e \frac{4\pi}{3} \lambda_D^3 \gg 1 \right)$. This quasi-neutrality allows plasmas to exhibit collective behaviors and respond to electric and magnetic fields as a whole, unlike ionized gases, which do not exhibit such behavior.

Collective Behavior: Gaseous plasmas can collectively respond to external forces, propagating waves, and self-organize into structures such as filaments and sheaths due to the interactions between charged particles. The collective behavior arises due to the long-range nature of the $1/r$ Coulomb potential, which indicates that the effect of local disturbances can be experienced at remote locations within the plasma. As a consequence, the local perturbations are short-lived compared to the dominating macroscopic fields. Assuming, local net charge imbalance, $\rho_l = e (Z n_i - n_e)$, resulting an electrostatic field according to Gauss's law,

$$\nabla \cdot \vec{E} = \rho_l / \epsilon_0 \quad (1.3)$$

The same charge cloud, consisting of electrons and ions, moving with velocity v_e and v_i , will give rise to a current density $\vec{J}_l = e (Z n_i \vec{v}_i - n_e \vec{v}_e)$. From Ampere's Law, we can express the resulting magnetic field,

$$\nabla \times \vec{H} = \vec{J} \quad (1.4)$$

Such internally driven \vec{E} and \vec{H} fields determine plasma dynamics. Plasma also responds to externally applied fields, such as microwave interaction with plasma.

For plasma to exist, the following criteria must satisfy $\lambda_D \ll L$, where L is the length of the plasma. The other criteria is based on the plasma relaxation time, such that the rate of collisions (mainly between charge particles and neutrals in a partially ionized plasma) must be less compared to the plasma frequency (the rate at which plasma re-adjusts charge imbalance due to any local perturbation).

Plasma can be classified based on the degree of ionization, the temperature of the charge species, and whether magnetized or unmagnetized. Based on the degree of ionization, the following types of plasma can exist:

Fully Ionized Plasma: In these plasmas, almost all of the gas particles ($N_g \sim 10^{25}$) are ionized, resulting in a high density of free electrons and ions (if $n_i = n_e = n \sim 10^{22}$, then the degree of ionization = $n/N_g \geq 10^{-3}$). The collisions with neutral molecules become negligible, hence the smooth trajectory of charges (high KE particles). Such plasma experiences long-range coulombic interaction with surrounding electrons and ions. Due to larger λ_D , bigger debye spheres (sparsely populated charges), the resulting plasma can be considered weakly coupled plasmas.

Partially Ionized Plasma: In this type of plasma, only a fraction of the gas particles are ionized, and the rest remain in neutral form. For such plasmas, $n/N_g < 10^{-3}$. More collisions with neutral molecules result in randomized motion. In the absence of an external field, the KE of particles is lower. Due to smaller λ_D , a smaller debye sphere (less dense) results in strongly coupled plasma (more local interaction) and less long-range interaction. The work presented in this thesis primarily focused on partially ionized or weakly ionized plasmas.

Based on their temperature, plasmas can also be classified into two primary categories:

- **High-Temperature (or thermal) Plasma:** These plasmas have extremely high temperatures (due to high KE, fully ionized, $n_e = n_i = n$, the ion and electron temperatures are comparable, $T_i \sim T_e$ and heats the background gas species ($T_g \sim T_i$)), often in the millions or billions of degrees Kelvin. Mostly, such plasmas have thermal equilibrium between the charge species and neutral gas molecules. The typical temperatures,

10 – 100 eV ($\geq 10^5$ K).

- **Low-Temperature (non-thermal) Plasma:** Low-temperature plasmas have temperatures ranging from a few hundred to tens of thousands of degrees Kelvin. The typical temperature range for such plasmas is 1 – 10 eV. Mostly, such plasmas have a non-thermal equilibrium that exists between the lighter charge species (electrons) and heavier charge (ions) and neutral gas molecules (the electrons have high KE having high temperatures compared to less KE ions and neutrals). Here, T_e can reach 10,000 K whereas $T_i \sim T_g = 300$ K.

For a collisional plasma (partially ionized), the plasma can be treated as unmagnetized, provided the mean free path of the charged species (mainly the lighter high KE electrons) is less than its gyroradius in the presence of an induced magnetic field. Thus, the influence of the magnetic field on the charged species transport in the plasma bulk depends on the length and time-scale we consider in the study.

Based on the above discussions comprising a brief overview of plasma and its various classifications, we finally discuss the cold collisional unmagnetized plasmas, which has been considered in this thesis's due to potential research significance. These plasmas are a subset of LTPs characterized by low temperatures, typically within a few thousand degrees Kelvin. The collisions between charged and neutral particles dominate in deciding unique properties, such as EM-plasma interactions. They have low KE and are densely populated (within a small debye sphere), and are strongly coupled and non-thermal ($T_e \gg T_i \sim T_g$). Research on LTP focuses on understanding the dynamics of particle collisions, energy transport, and the development of novel technologies that harness the properties of cold collisional unmagnetized plasmas for various purposes, including fusion energy research and astrophysical simulations.

When an external EM wave having E-field (\vec{E}) is applied on a collisional plasma, based on the fluid model the two equations that generally describe the plasma transport, the drift velocity(v) and evolution of the density of the particles(n) are: the Equation of Motion and the Equation of Continuity [38].

The Equation of Motion: Applying Newton's 2nd Law of Motion, "The rate

of change of momentum equals the applied force or the force experienced by particles (such as charged species electrons or ions), where

$$m \frac{d\vec{v}}{dt} = \vec{F} \quad (1.5)$$

where $d\vec{v}/dt = (\partial\vec{v}/\partial t + \vec{v} \cdot \nabla\vec{v})$, for a flow under uniform field with no convective acceleration ($\vec{v} \cdot \nabla\vec{v} = 0$). \vec{F} has a contribution from the electric field, magnetic field, collisional drag (or momentum loss), and due to pressure gradient ($\nabla(nT)/n$), T can be T_e or T_i , which can be mathematically expressed as,

$$\vec{F} = q\vec{E} + q(\vec{v} \times \vec{B}) - m\nu_m\vec{v} - \frac{1}{n}\nabla(nT) \quad (1.6)$$

where ν_m is collision frequency, m is the particle's mass, \vec{v} is the velocity field corresponding to the average velocity of the plasma element (assuming the whole plasma is divided into a large number of volume elements). The modified equation of motion for an unmagnetized ($\vec{B}_0 = 0$) collisional plasma,

$$m \frac{\partial\vec{v}}{\partial t} = q\vec{E} - m\nu_m\vec{v} - \frac{1}{n}\nabla(nT) \quad (1.7)$$

For high-frequency EM waves, the average velocity equation of the particle can be obtained using a valid assumption. We assume that the distance traveled over one E-field period is small (drift) compared to the length scale of the E-field and pressure variation (due to density gradient), neglecting diffusion. The equation is given by,

$$\frac{\partial\vec{v}}{\partial t} = \frac{q}{m}\vec{E} - \nu_m\vec{v} \quad (1.8)$$

For a longer time scale (under steady state, $\frac{\partial\vec{v}}{\partial t} \approx 0$), to describe charge transport averaged over one cycle of the EM wave considering the effect of diffusion. On rearranging the equation (1.7), we obtain the velocity equation,

$$\vec{v} = \frac{q\vec{E}}{m\nu_m} - \frac{T}{m\nu_m} \frac{\nabla n}{n} \quad (1.9)$$

Where, for electron, T_e , can be replaced by $k_B T_e$ in (eV), similarly for ions $T_i = k_B T_i$. The mobility of charge carrier, ($\mu \equiv \frac{|q|}{m\nu_m}$). Diffusion coefficient ($D = \frac{k_B T}{m\nu}$), for electrons, $D_e = \left(\frac{\mu_e k_B T_e}{e}\right)$, and, for ions, $D_i = \left(\frac{\mu_i k_B T_i}{e}\right)$.

For a collisional plasma, the charge transport is governed by the drift-diffusion

equation. The flux (Γ) of particles (both electrons and ions) across a boundary can be expressed by multiplying n to equation (1.10),

$$|\Gamma| = nv = |\mu|n\vec{E} - D\nabla n \quad (1.10)$$

where, $|\Gamma_i| = \mu_i n_i \vec{E} - D_i \nabla n_i$ and $|\Gamma_e| = \mu_e n_e \vec{E} - D_e \nabla n_e$, are electron and ion fluxes, respectively.

The Equation of continuity

The continuity equation describes the partial rate of change of density with time. Under source-free condition, it is expressed as,

$$\frac{\partial n}{\partial t} + \nabla \cdot (n\vec{v}) = 0 \quad (1.11)$$

where $n\vec{v}$ is the flux of particles reduced per volume. The continuity equation balances the creation and loss mechanisms that sustain the charge particle flow within a plasma medium, where charged particles like electrons and ions move through a given volume.

For the plasma evolution under the influence of a microwave and a slowly varying DC space charge field (due to perturbation from external microwave field), the continuity equation can be re-written in a drift-diffusion form combining equation (1.10 and 1.11) described by,

$$\frac{\partial n}{\partial t} + \nabla \cdot (|\mu|n\vec{E} - D\nabla n) = S \quad (1.12)$$

The S is the net particle number density created per unit time per unit volume, which consists of contribution from collision-assisted processes such as ionization, attachment, and recombination. Under quasi-neutrality, assuming $\Gamma_i = \Gamma_e = \Gamma$, the plasma bulk ambipolar transport in a space charge field (E_{sp}) given by,

$$E_{sp} = \left(\frac{D_i - D_e}{\mu_i + \mu_e} \right) \frac{\nabla n}{n} \quad (1.13)$$

We obtain the ambipolar flux $\Gamma = -D_a \nabla n$, where $D_a = \left(\frac{\mu_i D_e + \mu_e D_i}{\mu_e + \mu_i} \right)$ is the ambipolar diffusion coefficient, we obtain the modified equation (1.12),

$$\frac{\partial n}{\partial t} - \nabla \cdot (D_a \nabla n) = S \quad (1.14)$$

The diffusion occurs over the characteristic length of plasma, $L = \|\nabla n/n\|^{-1}$, the debye length ($\lambda_D < L$) for quasi-neutral behaviour.

1.2 EM wave propagation in plasma

The EM wave propagation characteristics in a collisional unmagnetized plasma are described through different physical phenomena, transmission, scattering, reflection, and absorption. The processes depend on both EM wave properties, decided by the frequency (ω) and the wave strength (E_0), and the plasma properties, decided by density (n_e) or plasma frequency (ω_p), collision frequency ($\nu \equiv \nu_m$). The ν_m or ν interchangeably used in the text determines the damping of the waves due to collisions between charged and neutral particles, which affects wave attenuation and absorption. The ω_p plays a significant role in determining the dispersion properties of the plasma. Various methods exist to study the EM wave propagation in a plasma. These methods include the coupling of Maxwell's equations to the Boltzmann equation to obtain the electron-velocity distribution function [39], fully kinetic particle simulations [40], magnetohydrodynamics, and hybrid particle-fluid methods [41] and magnetoionic theory based dispersion relation [42,43]. For a cold, collisional, unmagnetized plasma, the response to EM waves can be fully specified by a dispersion relation based on magnetoionic theory [43]. The dispersion relation provides a frequency-dependent propagation in plasma [12, 43]. This relation (Eq.1.15) interconnects the wave properties with the plasma properties using the complex propagation constant, where, $\omega_p = (n_e e^2 / m_e \epsilon_0)^{1/2}$ is the plasma frequency, ω is the wave angular frequency and n_e is the spatial local electron density. Moreover, the dispersion relation can be used to obtain the medium's refractive index and permittivity.

$$\omega_p^2 = (\omega^2 - k^2 c^2) \left(1 + i \frac{\nu_m}{\omega} \right) \quad (1.15)$$

1.2.1 Complex propagation constant of plasma

The dispersive nature of plasma can be explained through the propagation constant (k). The propagation constant in the plasma can be expressed by,

$k = k_r + ik_i$. Where the $Re\{k\} = k_r$ decides the wave propagation through the medium, also termed as phase shift constant, and $Im\{k\} = k_i$ decides the attenuation of the wave as it propagates through the plasma medium also termed as the attenuation coefficient. The k_r and k_i can be expressed in terms of the real and imaginary parts as,

$$k_r = \left(\frac{\omega}{c}\right) \sqrt{\frac{1}{2} \left(1 - \frac{\omega_p^2}{\omega^2 + \nu_m^2}\right) + \frac{1}{2} \sqrt{\left(1 - \frac{\omega_p^2}{\omega^2 + \nu_m^2}\right)^2 + \left(\left(\frac{\omega_p^2}{\omega^2 + \nu_m^2}\right) \left(\frac{\nu_m}{\omega}\right)\right)^2}} \quad (1.16)$$

$$k_i = \left(\frac{\omega}{c}\right) \sqrt{-\frac{1}{2} \left(1 - \frac{\omega_p^2}{\omega^2 + \nu_m^2}\right) + \frac{1}{2} \sqrt{\left(1 - \frac{\omega_p^2}{\omega^2 + \nu_m^2}\right)^2 + \left(\left(\frac{\omega_p^2}{\omega^2 + \nu_m^2}\right) \left(\frac{\nu_m}{\omega}\right)\right)^2}} \quad (1.17)$$

The complex dispersion relation for EM propagation in the plasma has been

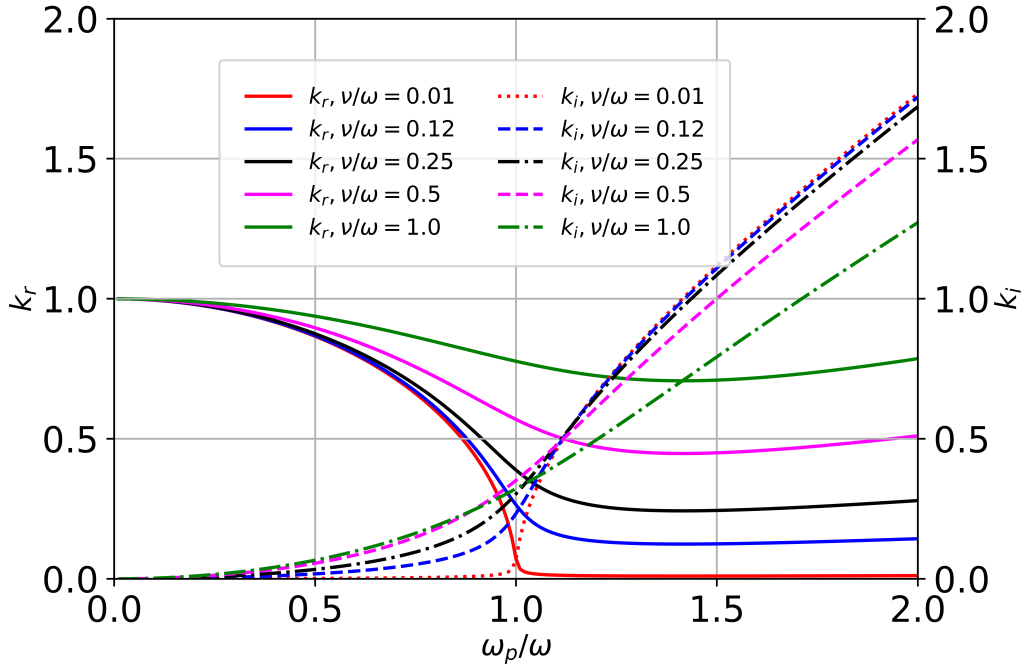


Figure 1.2: The 1-D distribution of k_r and k_i in the ω_p/ω for different ν_m/ω ratios.

shown in Fig. 1.2. We can classify our observation under three regions based on the ratio of ν_m/ω ,

- $\nu_m/\omega \ll 0.1$: full wave propagation ($k_r \sim 1.0$) for $\omega_p/\omega < 1.0$ and no propagation ($k_r \sim 0$) otherwise (sharp cutoff at $\omega_p/\omega = 1.0$). Similarly, minimum absorption $\omega_p/\omega < 1.0$ ($k_i \ll 0.25$) and high absorption otherwise.

- $\nu_m/\omega \sim [0.1 - 0.5]$: sharp cutoff condition fails ($k_r > 0.5$) $\omega_p/\omega = 1.0$ and wave can propagate $\omega_p/\omega > 1.0$ as well as there is associated absorption $\omega_p/\omega < 1.0$ ($k_i \sim 0.25$).
- $\nu_m/\omega \geq 1.0$: No sharp cutoff condition exists for $\omega_p/\omega = 1.0$ and wave propagates through a lossy medium ($k_i \gg 1$).

The complex relative permittivity ($\epsilon(\omega)$) can be obtained from the dispersion relation using the following relation ($k = (\omega/c)\sqrt{\epsilon(\omega)}$), where c is the speed of light in free-space. For a collisional plasma $\epsilon(\omega)$ is defined as [28,35],

$$\epsilon(\omega) = \left(1 - \frac{\omega_p^2}{\omega^2 + \nu_m^2}\right) - i \left(\frac{\omega_p^2}{\omega^2 + \nu_m^2}\right) \left(\frac{\nu_m}{\omega}\right) \quad (1.18)$$

where $Re\{\epsilon(\omega)\}$ is the propagation constant, whereas the conductivity of the plasma depends on $Im\{\epsilon(\omega)\}$. The cutoff density (n_{cutoff}), in the context of EM propagation in plasma, is given by $n_{\text{cutoff}} = n_{\text{critical}}(\nu_m/\omega)$, where $n_{\text{critical}} = (m\epsilon_0/e^2)\omega^2$. At critical density ($n_{\text{critical}} = (m\epsilon_0\omega_p^2)/e^2$), when the $\omega_p \approx \omega$, the microwave wave starts getting reflected. When plasma density crosses the cutoff density, plasma almost reflects a large percentage of the EM wave power with minimal transmission. Thus, at cutoff, the plasma almost shields the incoming microwave [44].

The complex wave propagation vector describes the microwave propagation in the plasma. By assuming a Y-directed and X-propagating wave, the wave propagation in the plasma can be written as,

$$\mathbf{E}(\mathbf{x}, t) = Re \left\{ E_{0,y} \exp \left(j(\omega t - \mathbf{k} \cdot \mathbf{x}) \right) \right\} \quad (1.19a)$$

$$\mathbf{E}(\mathbf{x}, t) = Re \left\{ E_{0,y} \exp \left(- \int k_i(x) dx \right) \exp \left(j(\omega t - \mathbf{k}_r \cdot \mathbf{x}) \right) \right\} \quad (1.19b)$$

k stores the information of the plasma medium in the amplitude and the phase of the wave, based on the $\epsilon(\omega)$ value. EM-wave propagation is shown in Fig.1.3, by assuming the plasma density to have an Epstein profile, which is given by,

$$n_e(x) = \frac{n_0}{1 + \exp(-x/S)} \quad (1.20)$$

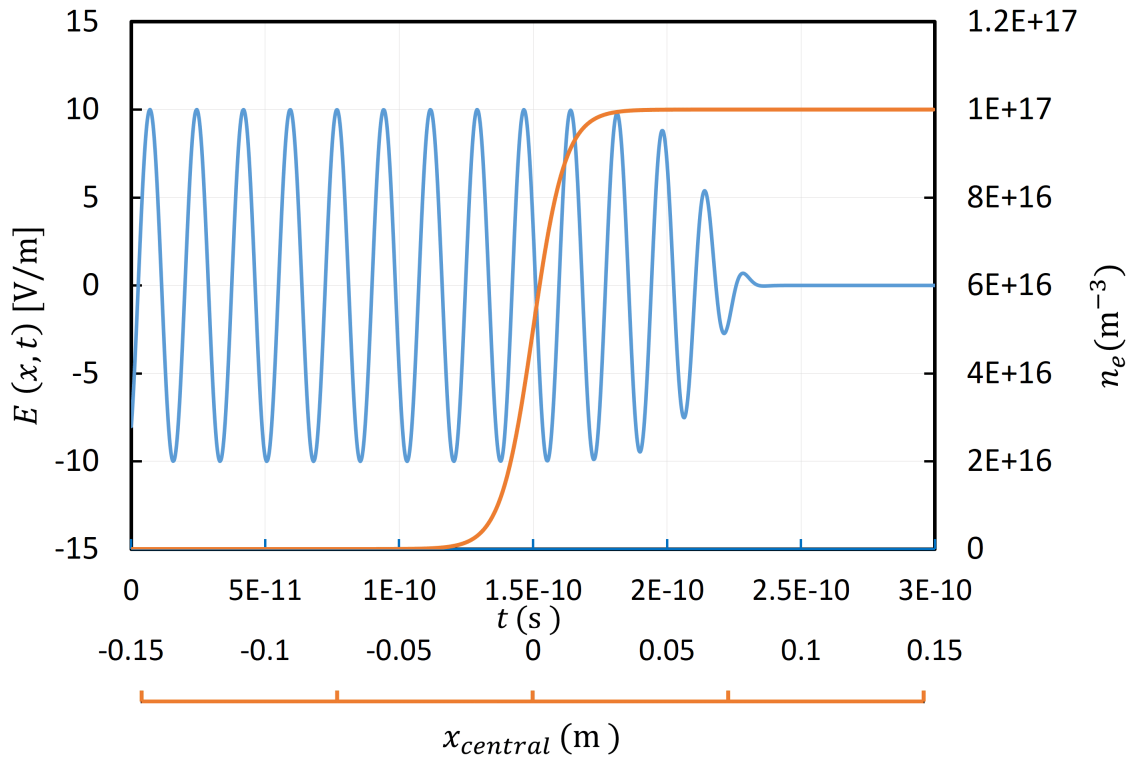


Figure 1.3: Plane EM wave propagation into a partially ionized cold collisional unmagnetized plasma. Two axes are presented along x-axis. The time-axis (t) represented in blue. The length-axis ($x_{central}$) represented in brown color. Using both, the time and length axes, the damping of EM wave oscillations with time for various locations inside the plasma is shown.

where $S = 10L$, L is the gradient length for the given plasma density profile, $x \in [-0.15, 0.15]$.

1.3 High Power Microwave breakdown - a multi-physics and multi-scale problem

Since HPM breakdown at high pressure and high frequency is a multi-scale and multi-physics phenomenon, it must provide accurate results within the desired run-time for a given simulation technique to be useful and acceptable for parametric investigations. For desired accuracy, the various physical processes at different time-scales, such as EM wave-plasma interaction, plasma formation, the subsequent energy exchange between wave and plasma, and afterward between the gas and the plasma, must be captured properly. This can be achieved using three different solvers as shown in Fig.1.4 - the Electromagnetic (EM) solver, Plasma solver, and Fluid solver. However, different time-scales are associated with these three solvers and the overall

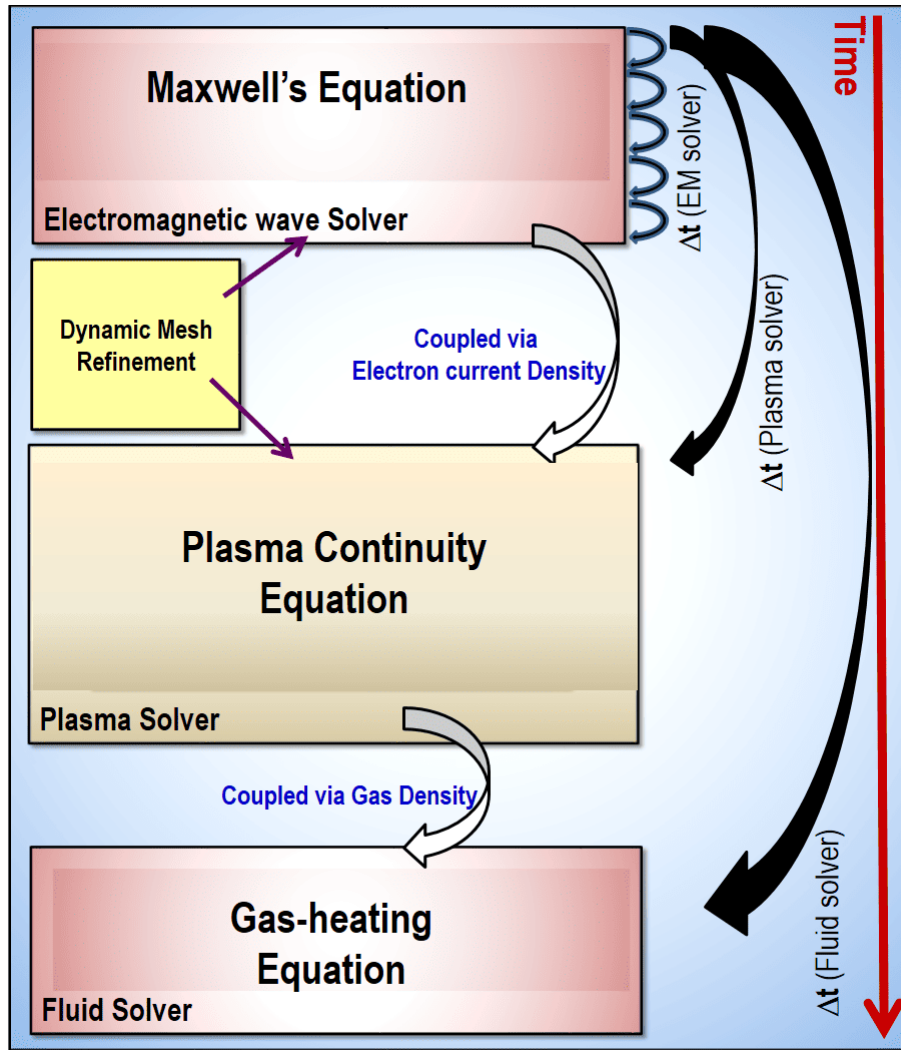


Figure 1.4: The complete fluid-based model of the HPM breakdown phenomenon. The different solvers correspond to the coupled physical processes. The time steps (Δt) are different for the three solvers (ranges from 10^{-15} to 10^{-9} s). The solvers requiring frequent updates can be accelerated by implementing dynamic mesh refinement (DMR).

run-time (efficiency) is determined by the time-steps associated with the EM-Plasma solvers. For example, in applications discussed in Fig.1.1 involving 100s of GHz, the time scale associated with EM solver is of the order of 10^{-12} s. The time-scale associated with the Plasma solver is 10^{-9} s. The Fluid solver that solves the gas dynamic equations is associated with 100's of nanoseconds time scale. The presence of sharp gradients both in the plasma density and E-field during the HPM breakdown needs to be accurately resolved using a very fine mesh during simulation. Due to this, most of the existing techniques require significant computational time to simulate the high-frequency breakdown problem.

As shown in Fig.1.4, since the solvers are coupled with each other, unless the Electromagnetic and Plasma solvers get accelerated, the higher time scale phenomenon, such as gas heating that is simulated through the Fluid solver will be difficult to realize. Also, based on the time scale of events, the Fluid solver is less frequently updated than the other two solvers. Computational modeling and simulation of microwave-plasma interaction is still a challenging task and remains one of the researched domains. Developing efficient computational techniques can help researchers accelerate the most frequent solvers (EM and plasma) while investigating the physics of EM-plasma interaction.

1.4 Conventional methods to computationally model the HPM breakdown

FDTD-based Maxwell-plasma fluid model is the most widely used approach for the simulation of HPM breakdown physics [35]. FDTD technique uses a domain discretization and evaluation of the quantities (fields) at every point on the Cartesian grids in a time-marching fashion. Similarly, the finite difference technique solves the plasma continuity equation to capture the plasma evolution phenomenon. The limitations associated with the finite difference time domain (FDTD) based fluid model [9, 35, 45] arise from restrictions on stringent grid spacing for accuracy and time spacing for stability of evaluated fields and density. To overcome these issues, the works

of Yan et. al. [46, 47] discuss the application of the discontinuous Galerkin time-domain (DGTD) method to realize the plasma filamentation under HPM breakdown in air. The DGTD algorithm is an interplay between the finite element time domain (FETD) technique, whereby the local unstructured tetrahedral basis is used to realize the fields and the plasma evolution, and the finite volume time domain (FVTD) technique, where the continuity is weakly associated with each nodal volumes that are related using the fluxes. The DGTD technique inherently supports the trade-off balance between accuracy and computation cost. However, the advantages associated with the DGTD technique come at the cost of the complex mathematical formulation, requirement of the proper choice of higher order basis function, and modification in the existing computational setup for the HPM breakdown model. In terms of mathematical formulation, the FDTD technique is much simpler, and using structured grids to evaluate field quantities conserves the quantities across the grid interfaces. Besides the Maxwell equations solved by the FDTD method and the electron fluid equation solved by using the finite difference scheme, the Maxwell equations and Newton-Lorentz equation have also been used to simulate the HPM breakdown problems such as in the study of vacuum-insulator interface discharge that limits the power handling capacity of pulsed power system [48] [49]. The FDTD method is used to solve the Maxwell equations, and the particle-in-cell (PIC) method [50] is applied to solve the Newton-Lorentz equation.

PIC is particularly good at capturing different non-local particle kinetics and is generally used for investigating weakly collisional or collisionless plasmas. For high-pressure plasmas (highly collisional process), as considered in our study, the non-local effects are less important than the total effect, considering the particles as a continuum (fluids) with the particles following a specific velocity distribution based on the local electric field approximation. In such cases, the fluid models are better suited due to their simplicity in describing the plasma via macroscopic quantities. In highly collisional plasmas, the mean free path is much smaller than the plasma size.

1.5 Data-driven approaches for investigating EM-plasma interactions

In the last decade, there have been vast improvements in the development of large and powerful deep neural networks (DNNs), which have been applied to solve complex problems in computer vision and image processing. Physics-informed neural networks, a DNN framework, can also be used as a black box to approximate a physical system [51], and recent results have shown that DNNs with many layers perform a surprisingly good job in modeling partial differential equation-based complicated physics problems in terms of both speed and accuracy [52]. Of late, machine learning (ML)/deep learning (DL) has also been used to successfully address different complex problems in plasma physics and computational electromagnetics. Deep reinforcement learning has been applied for tokamak magnetic controller design to produce new plasma configurations [53], the potential of AI/ML in predicting disruptive instabilities in controlled fusion plasmas has been established in several studies [54, 55], the feasibility of applying ML models for modeling, diagnostics, and control of non-equilibrium plasmas has been discussed in [56] and deep learning has also been used for extracting electron scattering cross sections from plasma swarm Data [57].

A Convolutional Neural Net (CNN) based architecture is learned to solve full-wave inverse scattering problems [58]. The visualizations generated from the problems can be used to train and get the results from the neural network, which can potentially help solve and accelerate the traditional equation-based solvers [59]. Deep Learning (DL) applied to electromagnetics, antenna, and EM wave propagation has been well reviewed in [60]. EM-Net [61] is a modified end-to-end CNN architecture with residual blocks and skip-connections inspired by the UNet [62], a robust network with encoder-decoder like structure which generates an image as an output, is widely used in image segmentation problems. The authors of EM-Net predict the electromagnetic field scattered by the complex geometries [61]. An unsupervised deep learning model is used for solving time-domain electromagnetic simulations, encoding the initial and boundary conditions and

Maxwell's equations when training the network [63]. CNNs have also been explored for plasma tomography and disruption prediction from Bolometer data [64]. Cheng et al. [65] compares various CNN-based architectures like UNet and MSNet to solve the 2D Poisson equation for electric field computation in Plasma simulations.

The UNet architecture provides good, acceptable results, and its capabilities are discussed in the existing literature [62, 66]. UNet has several advantages over similar networks, such as FCN [67] and SegNet [68], as it is relatively simple, fast, and works with smaller training data than other networks. Hence, UNet is suitable to analyze the given problem. To this end, we explored the feasibility of using UNet to accelerate the accurate simulation of microwave-plasma interaction, as will be discussed in detail in the later chapters.

1.6 Applications of microwave-plasma interaction

In this thesis, various numerical investigations of microwave interaction with collisional, unmagnetized, and low-temperature plasma have been performed, considering the following three applications as discussed in this section.

1.6.1 High frequency microwave breakdown induced discharge

Microwave discharges occur when a high power EM field ($> E_{breakdown}$, 10's to 100's kV/cm) of a microwave accelerates free electrons, creating a plasma by colliding with neutral gas molecules. The breakdown phenomenon is governed by several factors, including drift-diffusion, ionization rate constant, multiplication of electrons, self-sustained secondary emission, and Paschen's law. These discharges can exist in diffuse or streamer forms based on their electric field strength and pressure in the (E, p) plane.

The most widely studied discharges are streamer generation, which occurs when intense microwaves (in 100's of GHz) interact with air/gas (pressure of 100's torr), leading to breakdown. The numerical modeling of the HPM breakdown problem uses a well-established fluid model (highly collisional

system), which involves the coupling of Maxwell's equations and the plasma continuity equation [8], generally used to perform accurate 2D simulations of HPM breakdown experiments. However, the complex multi-physics multi-scale model(as discussed in section1.3,) requires accurate resolution of different space and time scales [9]. The finite difference time domain (FDTD) technique is one of the most preferred numerical methods that have been used to investigate the Maxwell-plasma fluid model. The method helps to reproduce experimental observations well but is computationally expensive. Due to the strict constraints on grid spacing and time steps [35,36,45,69], most past 2D numerical investigations using the fluid model have been carried out only for hundreds of nanoseconds. The high computational cost makes it challenging to simulate large problem sizes over longer time-scales (tens of microseconds). Hence, it is difficult to efficiently realize higher time-scale phenomena such as gas heating [36]. The simulation of this complex phenomenon at longer time-scales can help to understand underlying physics for various applications in microwave rockets, aerospace research, high-speed combustion, and safe operation of HPM devices [8] and HPM switching.

1.6.2 HPM switching and protection

The microwave breakdown causes problems in HPM transmission in microwave radar waveguides, antenna systems, and in space communication through the ionosphere [70]. Initially, the studies focused on understanding the challenges associated with high-power microwave (HPM) transmission and mitigating the breakdown phenomenon. However, recent studies show the breakdown proves to be beneficial for HPM protection to electronic components behind slots [71] as well as designing the microwave transmit-receive (TR) switches that act as receiver protection devices [70]. The protection mechanism lies in the high power breakdown induced plasma (center of slot) that reflects the incident pulse in the on state and transmits when in the off state. The induced breakdown is important in protecting sensitive receivers from jamming in electronic warfare [71]. Another application of intentional microwave breakdown includes the design of a

tunable miniaturized high power high frequency (HF) switch for the GHz band [72]. The breakdown results from avalanche ionization under a powerful microwave electric field in all the above applications. The resulting plasma density must be sufficient to perturb the EM propagation [7], and plasma must be formed within a desired time-scale. The breakdown experiments for HPM protection experiments, using air, around 10 torr pressure at 10 GHz, for a typical pulse length of 1 to 3 μs , the rms breakdown field is required to be greater than 1 kV/cm [4]. The cutoff time typically ranges in nanoseconds (ns) for incident power density in kW/cm^2 [70,71]. The plasma formation/sustainment time is comparable to pulse length in μs [7]. The use of keep-alive contact currents in TR switches [11] for seeding electrons to initiate and sustain the plasma after breakdown has been studied analytically and experimentally with numerical validation.

1.6.3 Microwave assisted plasma diagnostics

The accurate diagnostics of low-temperature plasmas [73] is of eminent significance due to its wide array of applications, especially in microelectronics, medicine, surface engineering, packaging, biomedical research, material synthesis, pollutant degradation, chemical conversion, propulsions systems, electronic switching devices, automotive, luminous systems, and many more [74–81]. Low-temperature plasmas can be created at various pressures, with typical ionization degrees of 10^{-6} – 10^{-4} , characteristic electron energies of a few eV to 10 eV and electron density typically from 10^{14} – 10^{23} m^{-3} [77–79]. Several physical parameters characterize any plasma; however, the electron density (n_e) and electron temperature (T_e) are the two fundamental parameters often employed, as the plasma properties are majorly influenced by the electron dynamics [82–84]. These two parameters are important as they directly impact the plasma stability and physical or chemical properties. Plasma temperature gives a realization of the average energy carried by the plasma. In contrast, the electron density gives information about the number of particles with such average energy within the given plasma volume [82,83,85]. Accurate diagnosis and precise understanding of the spatial distribution of (n_e) and (T_e) is a prerequisite for

any experimental investigation or application development [86]. The spatial distribution or profile can change temporally. Some of the well-established approaches carry out plasma electron density determination. Comprehensive reviews on different plasma diagnostics techniques can be found in the existing literature [73,87,88].

Langmuir probe, an invasive technique, is widely used to investigate electron characteristics in plasma; however, the mathematical theory of the density obtained from the Langmuir probe data (current density vs. applied potential) is quite cumbersome. The lack of a general analytic theory for any arbitrary values of density, difficulty in interpretation due to the presence of RF fields, and other issues limit the application of the Langmuir probe in plasma diagnostics. Microwave interferometry and the CO₂-laser heterodyne interferometry are extensively employed in diagnostics for n_e estimation [89,90]. This method has an advantage over the line-broadening method, which applies to densities lower than 10^{13} cm^{-3} . Notably, the thermal effect influences the phase shift detection, and the measurements are line integrated; therefore, it constrains the n_e profile measurement. Microwave reflectometry is also an interesting method for estimating n_e [12], where the experimental data are fitted to the results of a numerical calculation code derived from a refined electromagnetic model. Microwave reflectometry uses the principle of reflection of electromagnetic waves from the target, such as gaseous plasma. Previously used in ionospheric plasma study [91], it uses group delay of the reflected microwave to correlate it with the plasma density determination. Later, the technique has been used extensively in the diagnosis of Tokamak plasmas [91]. The method requires sophisticated data processing and fitting. The requirement of real-time measurements of the plasma electron density and the profile information is critical to high-pressure plasma applications.

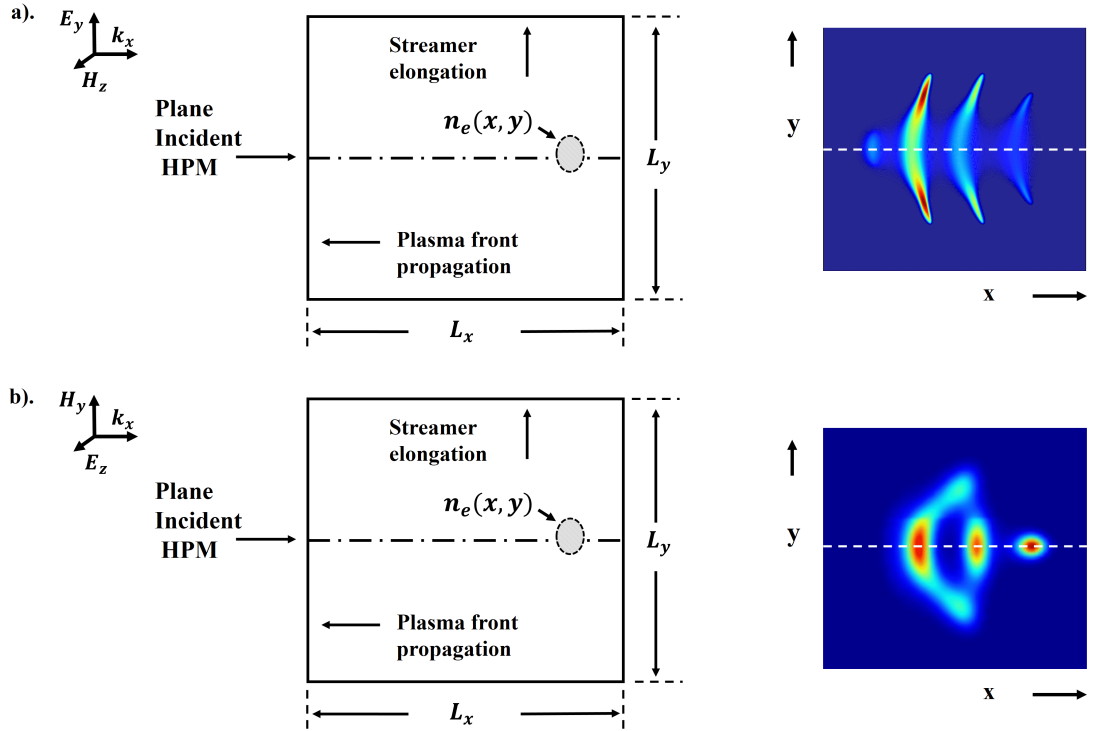


Figure 1.5: Two different formulations for 2-D simulation of microwave interaction with plasma based on the location of the E-field. Multiple plasma structures formation when (a) E-field parallel to the simulation plane (XY) [8] and (b) E-field perpendicular to the simulation plane [9].

1.7 Microwave propagation in plasma as a 2-D problem

Most of the research work in the current literature [9, 35, 92, 93] suggests that the majority of the physics and 3-D effects of such a multi-scale and multi-physics nature of the problem can be realized in 1-D or 2-D, either using transverse electric (TE) or transverse magnetic (TM) based formulation. In the TE formulation, microwave E-field in the plane of simulation, with non-zero components of E_y, E_x , and H_z (refer Fig.1.5 (a)). For TM formulation, microwave E-field is perpendicular to the plane of simulation, with non-zero components of H_x, H_y , and E_z (refer Fig.1.5 (b)). Our problem uses TE mode formulation in 2D.

1.8 Contribution of the Thesis

Microwave-plasma interaction is a complex phenomenon, and particularly, simulation of plasma dynamics during HPM breakdown is a computationally challenging problem due to its multi-scale and multi-physics nature. A better understanding of this complex phenomenon and the development of new computational approaches will help evaluate and establish the potential applications associated with microwave-plasma interaction. A primary requirement to address this issue is to develop novel approaches and algorithms for investigating high-frequency EM wave-plasma interaction, which forms the primary motivation of this research work. The thesis is focused on the following main lines:

- Investigation of microwave-plasma interaction and understanding the multi-scale/multi-physics nature of the HPM breakdown.
- Plasma Fluid model-based code development for 2D simulation of HPM breakdown starting from wave-plasma interaction (nanoseconds) to the gas heating stage (microseconds) and comparison with experimental results.
- Development of self-aware mesh refinement algorithm to efficiently simulate and accurately capture the plasma dynamics during HPM breakdown.
- To investigate the effect of gas heating on HPM switching and protection application using the DMR-based plasma simulation technique.
- Explore and evaluate the possibility of data-driven machine learning-based approaches for studying microwave-plasma interaction.
- Feasibility of plasma density estimation using the physics of microwave-plasma interaction and deep learning. Perform different case studies with experimental viewpoints to provide useful feedback for realizing the proposed ML-based plasma diagnostics.
- We examined the viability of a data-driven approach for studying microwave-plasma interactions in real experiments, particularly in

scenarios involving asymmetric plasma profiles and challenging noisy, sparse data. We emphasized building a diverse data set with various asymmetric profiles and conducted multiple case studies to evaluate the predictive power of the deep learning technique on this enriched data.

1.9 Organization of the thesis

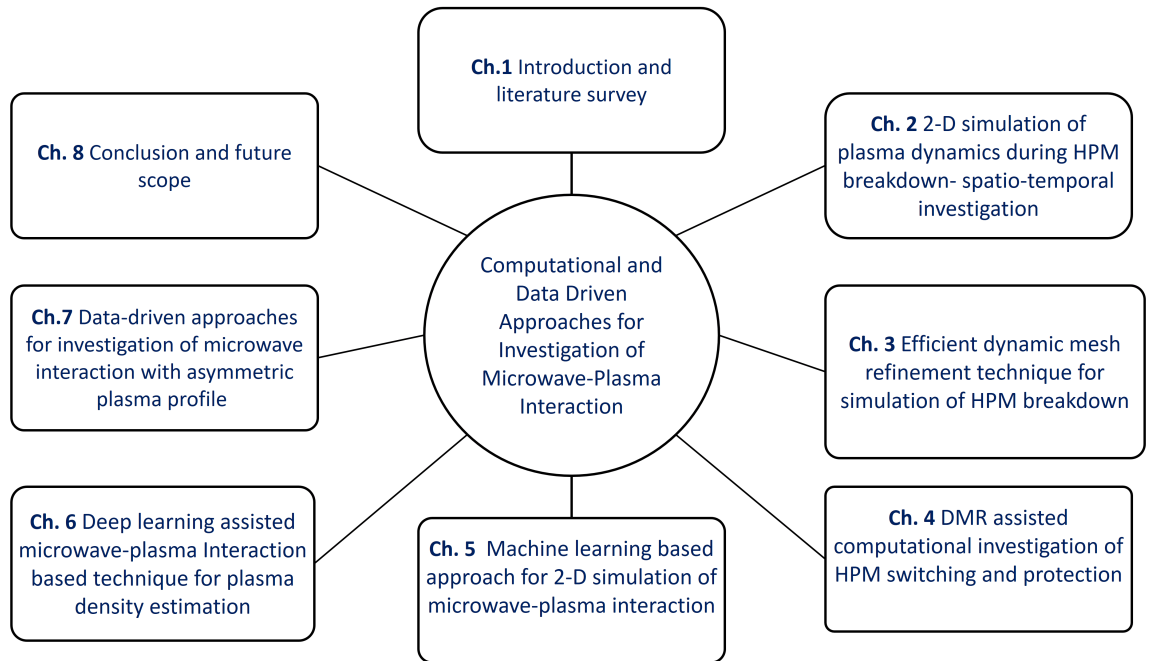


Figure 1.6: Organization of the thesis chapters.

The thesis is planned to be structured in seven chapters, as shown in Fig. (1.6). Chapter 1 contains the introduction of the thesis along with a detailed literature survey on EM wave propagation in a collisional unmagnetized plasma, computational modeling of high-frequency HPM breakdown at high pressures, and the requirement of new computational tools for efficient investigations of such phenomena and their applications. Chapter 2 discusses the plasma fluid model for HPM breakdown and the associated computational challenges. Using a spatio-temporal investigation, we have included the results from 2D benchmark simulations replicating an actual experiment. Chapter 3 focuses on developing an efficient dynamic mesh refinement technique for computationally expensive 2D simulations and its performance evaluation. Chapter 4 investigates the HPM switching application based on microwave breakdown physics using the DMR-based plasma fluid model. In Chapter 5, a new data-driven machine learning-based approach for

investigating EM-plasma interaction has been proposed, and its comparison with the traditional FDTD-based approach has been provided. In Chapter 6, a Deep Learning microwave-plasma interaction-based technique for plasma density estimation, along with several case studies, have been included. Chapter 7 discusses the performance evaluation of the Deep Learning model to simulate the microwave interaction with various asymmetric plasma density profiles. The model developed in the previous two chapters has been used to efficiently reconstruct scattered E-field patterns and for the asymmetric plasma density profile estimation. Conclusion, general remarks, and future scope are included in the final chapter.

CHAPTER 2

2-D simulation of plasma dynamics during HPM breakdown - spatio-temporal investigation

2.1 Introduction

The microwave breakdown in air/ gases at high pressure (> 100 's torr) leading to complex plasma dynamics is a highly collisional and nonlinear process [27,28,32,35,36,45,92–95]. To completely understand the properties of such a type of discharge, improving our current understanding of the electromagnetic (EM) wave-plasma interaction, plasma formation, the subsequent energy exchange between wave and plasma, and afterward between the gas and the plasma is crucial. Different semi-analytical models and computational techniques have been used to study this problem. [9,27,35,36,45,47–49,69,94–101]. Fluid [35,36,45,69,99,100] and kinetic [48,49] models are generally used for investigating such problems. However, computationally expensive kinetic simulations are required for weakly collisional and collisionless plasmas, whereas fluid models are generally used to capture the physics of collisional plasmas accurately. In the case of high-pressure plasmas, which are highly collisional, the mean free path is much smaller than the size of the plasma, and the plasma can be treated as a continuum (fluid). To reproduce the experimental observations [1, 2, 7], several researchers [27, 28, 35, 36, 47, 69, 94, 95, 97, 100] have used the well-established EM-plasma fluid model. The nonlinear dependence of the plasma species transport in the presence of the intense microwave and various complex physio-chemical interactions

necessitates a comprehensive exploration of the given problem. Previous studies have focussed on understanding parametric dependence on EM wave power, pressure, ionization-attachment rate coefficients, and diffusion rate on high-power microwave (HPM) induced plasma dynamics. Very few attempts have been made to understand the detailed spatio-temporal evolution of such quantities during HPM breakdown. Also, more explanation is needed regarding the computational complexity associated with the numerical simulation of such a multi-scale and multi-physics discharge problem. The modeling requires stringent mesh discretization (grid size and time-step selection) to capture sharp gradients in the scattered field resulting from the asymmetric and non-homogeneous plasma structures. In this chapter, we discuss the fluid-based approach for the simulation of HPM breakdown along with its algorithmic implementation and associated computational challenges to address the multi-physics and multi-scale nature of the problem. Simulation results using real physical parameters from a benchmark problem involving filamentary plasma pattern formation in high-frequency HPM breakdown in the air have been explained by performing a detailed spatio-temporal investigation.

Organization of chapter

In section 2.2, we introduce the physical model of HPM breakdown, which includes a brief discussion on the governing physics, a self-consistent 2-D EM-plasma fluid-based model describing the constituent equations to describe the plasma dynamics. Section 2.3, discusses the computational model and its numerical implementation. In section 2.4, we introduce the simulation setup of the benchmark problem. This problem has been used to discuss the physics of complex plasma dynamics using a novel Spatio-temporal analysis, as provided in section 2.5. The computational challenges associated with the 2-D simulation have been provided in section 2.6, followed by conclusions in section 2.7.

2.2 Physical model of HPM breakdown

HPM breakdown is an example of electrodeless free-space discharge [102], which results when a very intense microwave (with electric field strength

higher than the breakdown field of the background air/gas) is focussed on air/gas. To describe the coupling of the EM-energy to the induced gaseous plasma and the associated plasma dynamics such as the filamentation process, a well-established EM-plasma fluid model is generally used [35,36,46,97]. The plasma fluid model follows a Maxwell-Boltzmann Probability Distribution Function (PDF) to define the plasma species, and various macroscopic quantities such as particle number density, mean velocity, and mean energy are obtained by integrating the PDF over the momentum space of the Boltzmann equation [46]. The model primarily comprises Maxwell's equations and plasma continuity equation [27, 35, 36, 46]. Maxwell's equation describes the microwave interaction with the plasma through the electron current density, while the ion contribution to the current density is neglected. The coupled sets of the equation consists of the two Maxwell's equation as given by,

$$\frac{\partial \vec{E}}{\partial t} = \frac{1}{\epsilon_0} (\nabla \times \vec{H}) - \frac{1}{\epsilon_0} (\vec{J}) \quad (2.1)$$

$$\frac{\partial \vec{H}}{\partial t} = -\frac{1}{\mu_0} (\nabla \times \vec{E}) \quad (2.2)$$

where the transverse EM wave vectors, electric field (\vec{E}) and magnetic field (\vec{H}) intensity, μ_0 and ϵ_0 stands for magnetic permeability and electrical permittivity of vacuum, respectively, \vec{J} is the plasma current density ($\vec{J} = -e n_e \vec{v}_e$) in (A m^{-2}), n_e is the plasma density (here electron density) in (m^{-3}). The simplified momentum conservation equation (assuming that there is no external magnetic field and the collisions take place on much shorter time and length scales than the macroscopic pressure and cyclotron motions [103]) is used to obtain the velocity of electrons in a collisional air plasma (at high pressure),

$$\frac{\partial \vec{v}_e}{\partial t} = -\frac{e \vec{E}}{m_e} - \nu_m \vec{v}_e \quad (2.3)$$

v_e is the electron velocity in (m/s), m_e is the mass of electron in (kg) and e is electron charge in Coulomb (C), ν_m (or ν) is the electron-neutral collision frequency in (s^{-1}) (for air, $\nu_m = 5.3 \times 10^9 p$, where p is the ambient pressure in (torr) [35]). The electron current density (\vec{J}) couples both sets of equations (Maxwell's and Plasma) [35]. The rate coefficients, such as

the rate of ionization (ν_i), attachment (ν_a), and recombination (r_{ei}) and the effective diffusion rate (D_{eff}) decide the plasma charge transport under external microwave E-field. Under the quasi-neutral assumption of plasma, and taking into account the above processes such as ionization, attachment, and recombination effects, the diffusion-assisted plasma continuity equation can be expressed as,

$$\frac{\partial n_e}{\partial t} - \nabla \cdot (D_{eff} \nabla n_e) = n_e(\nu_i - \nu_a) - r_{ei}n_e^2 \quad (2.4)$$

The fluid continuity equation governs the temporal evolution of the plasma density averaged over one period of the EM wave. The time scale for the plasma density to evolve is much longer than the EM wave period, which validates the approximation [45]. Under the local electric field, or effective E-field (E_{eff}) approximation (LEFA), the losses due to collisions balance the gain of energy and momentum from the electric field. The equilibrium results in the local electric field to govern the ionization and attachment processes. Also, the diffusion mechanism dominates over drift for the plasma propagation in the high-frequency regime. Therefore, only the diffusive term appears in the flux divergence term in the continuity equation [45]. The effective diffusion coefficient transitions between the bulk ambipolar diffusion to free-electron diffusion in the plasma front [27,35,46]. The effective diffusion coefficient (D_{eff}) in (m^2/s) is given by,

$$\left(D_{eff} = \left(\frac{\alpha D_e + D_a}{1 + \alpha} \right) \right) \quad (2.5)$$

where, $D_e = \mu_e (k_B T_e / e)$ and $D_a \approx (\mu_i / \mu_e) D_e = \mu_i (k_B T_e / e)$, $\mu_e = e / (m_e \nu_m)$ and $\mu_i = \mu_e / 200$ in ($\text{m}^2/\text{V s}$) where, μ_e and μ_i are electron and ion mobilities respectively, D_e and D_a are free and ambipolar diffusion coefficient. D_e and D_a require the calculation of the electron temperature in terms of the reduced field E_{eff} / p , in ($\text{V}/\text{cm.torr}$) is given by,

$$E_{eff} = \sqrt{\frac{E_{rms}^2}{1 + (\omega / \nu_m)^2}} \quad (2.6)$$

where E_{rms}^2 , is the time-averaged high-frequency E-field over one EM wave period, ω is the angular frequency of the wave [27, 28, 35]. The electron temperature (T_e) in eV can be obtained using the following relation,

$$\left(\frac{k_B T_e}{e}\right) = \left[2.1 \times 10^{-3} (E_{eff}/p) \left(91.0 + (E_{eff}/p)\right)\right]^{1/3} \quad (2.7)$$

The remaining quantities that are part of the effective diffusion coefficient expression are discussed below. $\alpha = \nu_i \tau_m = \lambda_D^2 / L^2$ is a unitless factor that controls the transition between the free and ambipolar diffusion. τ_m in (s) stands for dielectric (or Maxwell's) relaxation time $\tau_m = \epsilon_0 / [en_e(\mu_e + \mu_i)]$ [27]. $\lambda_D = (\epsilon_0 k_B T_e / e^2 n_e)^{1/2}$ in (m), is local Debye length, $k_B / e = 8.61733 \times 10^{-5}$ in (eV/K), $L = \left\| \frac{\nabla n}{n} \right\|^{-1} = (D_e / \nu_i)^{1/2}$ in (m), is the characteristic diffusion length of the propagating plasma filament front.

The effective ionization, $\nu_i - \nu_a = \gamma v_d$, in (s^{-1}), the electron drift velocity $v_d = \mu_e E$ in (m/s). The ionization coefficient (γ) in (m^{-1}) defines the number of ionization events an electron undergoes per unit length along the E-field. In the HPM breakdown problem, the ionization corresponds to air whose all rate coefficients (A, B) values have been referred from [35, 46]. The ionization coefficient can be expressed using two equations based on the E_{eff}/p terms. For $E_{eff}/p < 50$ (V/cm.torr),

$$\gamma = A_0 p \left[\exp \left(-B_0 \left(-p/E_{eff} - p/E_{critical} \right) \right) - 1 \right] \quad (2.8)$$

where $A_0 = 0.005$ ($cm^{-1} torr^{-1}$), $B_0 = 200$ (V/cm.torr), $E_{critical}/p = 31.25$ (V/cm.torr), the critical field intensity that decides the breakdown criteria in air, beyond which the ionization dominates over the attachment process. If $E_{eff}/p \geq 50$ (V/cm.torr),

$$\gamma = A p \left[\exp \left(-B p / E_{eff} \right) \right] \quad (2.9)$$

Where, if $50 \leq E_{eff}/p \leq 200$ (V/cm.torr) $A = 8.805$ ($cm^{-1} torr^{-1}$), $B = 258.45$ (V/cm.torr), and if $100 \leq E_{eff}/p \leq 800$ (V/cm.torr) $A = 15$ ($cm^{-1} torr^{-1}$), $B = 265$ (V/cm.torr). The recombination coefficient (r_{ei}) in ($m^{-3}s^{-1}$) is given by, $r_{ei} = \beta \times 10^{-13} (300/T_e)^{1/2}$, β varies between 0 and 2.

For proper modeling of the HPM breakdown process, it is important to determine the parameter space (microwave E-field, frequency, and gas pressure) within which the local E-field approximation (LEFA) holds. The LEFA holds when the variation in the electron energy lies within 10% of the mean electron energy but breaks if it is greater than 50% or more. The LEFA to be valid at different pressures, the following frequency and reduced field conditions must be satisfied. For high pressure, the incident EM wave frequency (f) must satisfy $f > 100$ GHz; for lower pressure, $f > 2$ GHz. The reduced field, (E_{eff}/p) measured in Townsend (Td), should be within 200 Td [104].

2.3 Computational modelling of HPM breakdown

The complete 2-D fluid-based computational modeling of the HPM breakdown requires three different types of solvers. Electromagnetic (EM), Plasma, and Fluid solver (or gas solver) are the three solvers. Each of these solvers represents the different time-scales of events, including EM wave-plasma interaction, plasma formation, the subsequent energy exchange between wave and plasma, and afterward between the gas and the plasma. The useful physics can be safely captured for the time scale below 100's of ns, considering only the EM and the plasma solvers. Figure 2.1 gives an overview of the computational tool to implement a 2-D plasma fluid-model to simulate HPM breakdown. The flow diagram indicates the inputs to the tool, such as microwave E-field strength (E_0), frequency (f) of the wave, the gas species (in this case, air) to decide reaction rate coefficients, gas pressure (p), and the initial plasma density (n_0). The important outputs collected during the simulation are E_{rms} , n_e , diffusion and ionization rate coefficients. Block-I represents- the 2-D Cartesian grid initialization and simulation setup, Block-II represents- the complete EM solver, and Block-III represents- the Plasma solver. The important mathematical equations (partial differential equations (PDEs)) in different solvers and their coupling are also shown in the block diagram. Moreover, the different time steps indicate the iterative solution of the overall simulation. The EM-solver uses the finite difference time domain (FDTD) technique to solve the two Maxwell's equations ((2.1) and (2.2)) along

with the plasma momentum transfer equation (2.3) which are coupled using the current density term \vec{J} . The plasma solver uses a finite difference (FD) scheme to solve the plasma continuity equation (2.4). The plasma solver requires the diffusion (D_{eff}) and growth (ν_i) or decay-associated (ν_a) terms that use the E_{eff} provided by the EM-solver. FDTD is an explicit second-order accurate time-domain method using centered finite differences on a uniform Cartesian grid, yielding the spatio-temporal variation of the E and H fields has been applied to various EM scattering problems [105]. The direct integration scheme discretizes the velocity equation. The plasma continuity equation uses a simple explicit scheme for continuity equation. The plasma density and EM fields are evaluated at specific locations on the overlapped Cartesian grids, as shown in Fig. 2.2 (b).

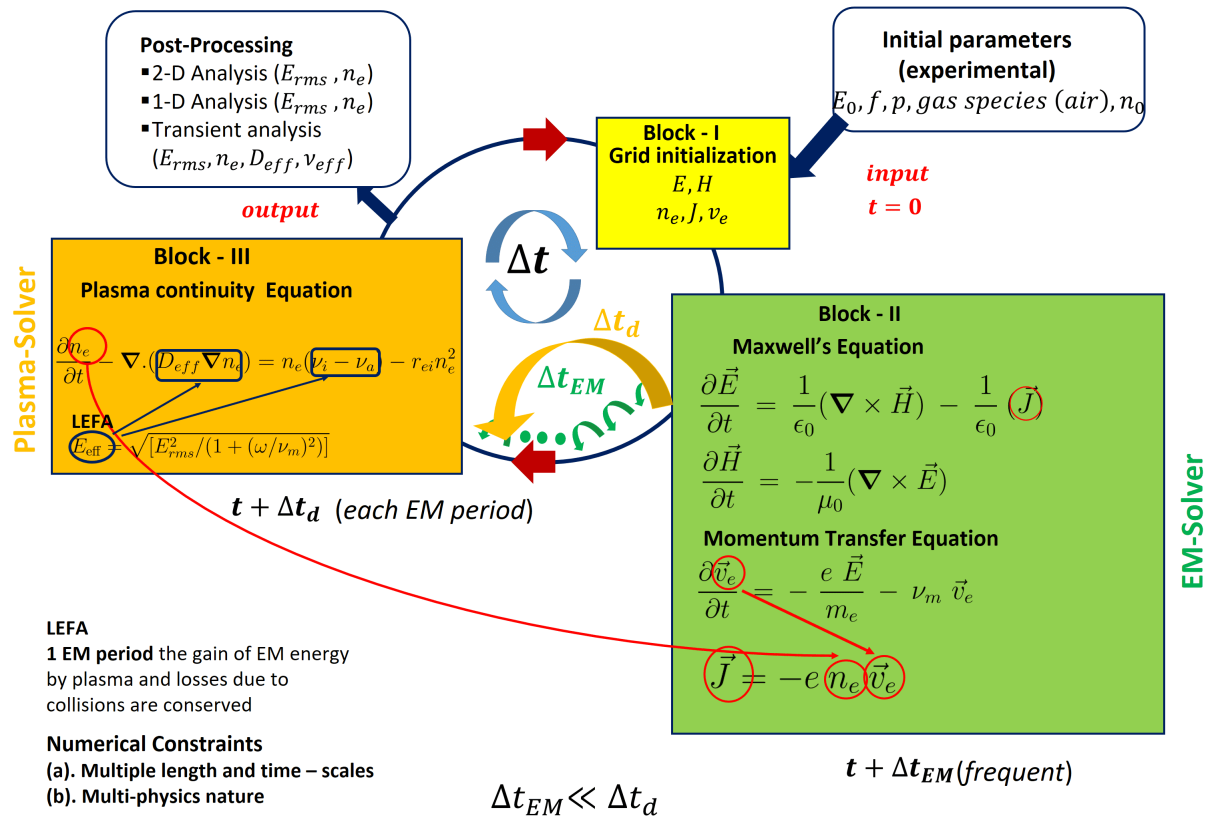


Figure 2.1: Computational implementation of multi-physics and multi-scale 2-D plasma fluid model.

2.3.1 Numerical implementation of solvers

The 2-D fluid simulation considered in our study consists of a parallel E-field and perpendicular H-field within the simulation domain, as shown in Fig. 2.2 (a). The 2D Cartesian grid on which the discretized form of the system of Maxwell's-plasma equations needs to be updated is shown in Fig. 2.2 (b). The non-zero components of the E and H fields (E_x , E_y , H_z) are considered. The Yee's approximation is used on the square 2-D Cartesian grid, with E-fields located on the edges and H-fields on the faces of the grid. \vec{v}_e is calculated on the edges in the direction of the E-field, and n_e and \vec{J}_e are calculated on the grid corners as shown in Fig. 2.2 (b). The discretized equations corresponding to the two Maxwell's equation, the electron velocity equation (from momentum conservation equation) and the plasma continuity equation are as follows:

$$\frac{E_{x,i,j}^{n+1} - E_{x,i,j}^n}{\Delta t_{EM}} = \frac{1}{\epsilon_0} \left\{ \left(\frac{H_{z,i,j}^{n-1/2} - H_{z,i,j-1}^{n-1/2}}{\Delta_{EM}} \right) - \left(\frac{J_{x,i,j}^{n+1} + J_{x,i,j}^n}{2} \right) \right\} \quad (2.10a)$$

$$\frac{E_{y,i,j}^{n+1} - E_{y,i,j}^n}{\Delta t_{EM}} = \frac{1}{\epsilon_0} \left\{ \left(\frac{H_{z,i-1,j}^{n-1/2} - H_{z,i,j}^{n-1/2}}{\Delta_{EM}} \right) - \left(\frac{J_{y,i,j}^{n+1} + J_{y,i,j}^n}{2} \right) \right\} \quad (2.10b)$$

$$\frac{H_{z,i,j}^{n+1/2} - H_{z,i,j}^{n-1/2}}{\Delta t_{EM}} = \frac{1}{\mu_0} \left\{ \left(\frac{E_{x,i,j}^n - E_{x,i,j+1}^n}{\Delta_{EM}} \right) - \left(\frac{E_{y,i+1,j}^n - E_{y,i,j}^n}{\Delta_{EM}} \right) \right\} \quad (2.10c)$$

$$\frac{v_{e_{x,i,j}}^{n+1} - v_{e_{x,i,j}}^n}{\Delta t_{EM}} = \left\{ \frac{e}{m_e} \left(\frac{E_{total\ x,i,j}^{n+1} + E_{total\ x,i,j}^n}{2} \right) - v_m \left(\frac{v_{e_{x,i,j}}^{n+1} + v_{e_{x,i,j}}^n}{2} \right) \right\} \quad (2.10d)$$

$$\frac{v_{e_{y,i,j}}^{n+1} - v_{e_{y,i,j}}^n}{\Delta t_{EM}} = \left\{ \frac{e}{m_e} \left(\frac{E_{total\ y,i,j}^{n+1} + E_{total\ y,i,j}^n}{2} \right) - v_m \left(\frac{v_{e_{y,i,j}}^{n+1} + v_{e_{y,i,j}}^n}{2} \right) \right\} \quad (2.10e)$$

$$\begin{aligned} n_{e(k,l)}^{n+1} = & \left(\frac{1}{1 + \Delta t_d (v_a + r_{ei} n_{e(k,l)}^n)} \right) \times \left\{ n_{e(k,l)}^n [1 + \Delta t_d v_i] \right. \\ & + \left(\frac{D_{eff} \Delta t_d}{\Delta_d^2} \right) \times \left[n_{e(k+1,l)}^n \right. \\ & \left. \left. + n_{e(k-1,l)}^n + n_{e(k,l+1)}^n + n_{e(k,l-1)}^n - 4n_{e(k,l)}^n \right] \right\} \quad (2.10f) \end{aligned}$$

The total-field/scattered-field (TF/SF) formulation has been used, where it is assumed total E-field, $E_{total} = E_{scattered} + E_{incident}$ [105, 106]. The TF/SF formulation applies to plane-wave sources (such as the HPM considered here). The formulation assumes the $E_{incident}$ is present throughout the computational domain at each time step and similar to fields in vacuum (absence of plasma), whereas the $E_{scattered}$ (interaction of incident microwave with plasma medium) are initially unknown and iteratively calculated as the simulation proceeds. We have used MUR outer radiation boundary condition for FDTD-based scattered field formulation to prevent discontinuity in E-field updates at the grid boundaries [35, 107].

The grid spacing (Δ_{EM} or Δ_d) and time stepping (Δt_{EM} or Δt_d) for the EM and plasma solvers are determined based on specific criteria. For the EM solver using FDTD, the grid spacing (Δ_{EM}) captures a minimum of either 1/10 or 1/20 of the incident wavelength or the smallest EM feature (e.g., wave skin-depth) or the gradients in the E-field. Existing literature suggests that a grid spacing of 1/500 of the incident EM wavelength is required to resolve the sharp gradients observed in such HPM breakdown [45]. The time step for EM solver (Δt_{EM}) is set to $0.5\Delta_{EM}/c$, under the CFL condition [105]. For the plasma solver, the grid spacing (Δ_d) is determined by the gradient scale length of the plasma, and the fluid time step (Δt_d) must satisfy the CFL condition $\Delta t_d < (\Delta_d)^2 / (2D_{max})$, where D_{max} corresponds to the maximum D_{eff} . The numerical simulation process involves two events of different time-scales: the fast-evolving EM wave that requires frequent E and H-field updates with smaller time steps (Δt_{EM}) and the slow-evolving plasma density that requires less frequent updates with bigger time steps (Δt_d) [108].

2.4 Simulation of a benchmark problem

We consider the HPM breakdown-induced filamentary plasma propagation problem as reported in [27, 35, 45]. Figure 2.2 (a) shows a schematic of our computational domain where, $\{c_{kx}, c_{ky}\} = \{1.0, 1.0\}$. A linearly polarized plane EM wave with the electric field, $E_0 = 5.0$ MV/m ($>$ the breakdown field ≈ 3.53 MV/m) having frequency, 110 GHz, is incident on the domain from the left side. The E-field is Y-directed and the wave propagation vector is along

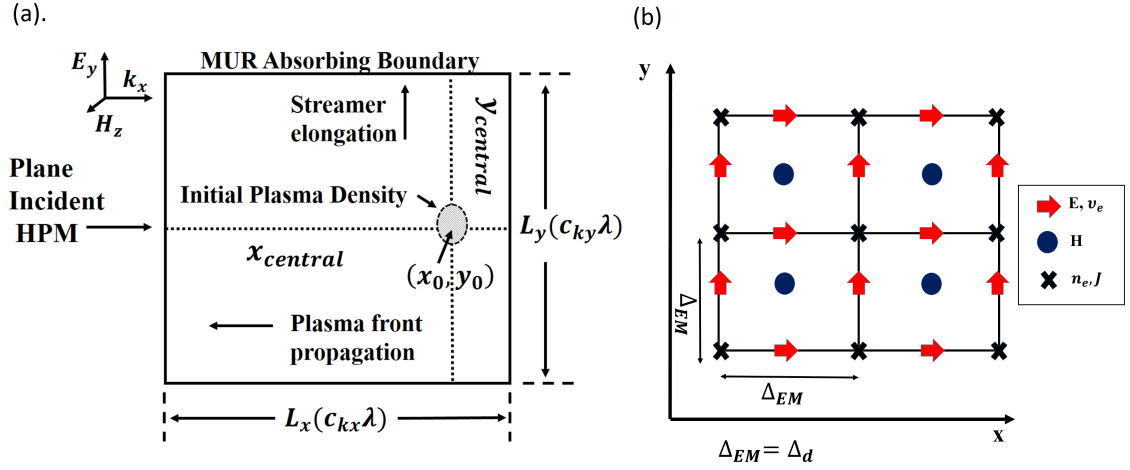


Figure 2.2: (a) Schematic of the Computational domain. $\{(c_{kx}, c_{ky}) \in \mathbb{Q}^+\}$, and, x_0 and y_0 are fractions in $[0, 1]$ of L_x and L_y respectively. The MUR outer radiation boundary condition has been used for scattered field formulation. (b) A partial 2-D Cartesian grid representation of $L_x \times L_y$ domain for FDTD (E and H-field) and plasma fluid model: plasma velocity (v_e) and current density (J) solver. Grid-spacing for EM and plasma solver, Δ_{EM} and Δ_d , respectively.

X. For the given problem, both the grid spacing for the solution of Maxwell's and the plasma continuity equation are chosen to be the same (mesh size $\Delta_{EM} = \Delta_d = 0.5 \times 10^{-6}$ m) due to the comparable scale lengths of the electric field and density [8,9]. The corresponding time steps for both the solvers are $\Delta t_{EM} = 8.85 \times 10^{-15}$ s and $\Delta t_d = 1.56 \times 10^{-12}$ s. The initial plasma density (with $n_0 = 1.6 \times 10^{16}$ m $^{-3}$ located at $0.75 L_x$ and $0.5 L_y$) is modeled as a Gaussian profile at a small region centered at (x_0, y_0) , which evolves into a self-organized plasma filamentary structure and propagates towards the HPM source as the simulation progresses [2, 27, 35, 45]. Notably, the filamentary process depends on the high-power microwave interaction with the plasma through microwave transmission, absorption, and reflection phenomenon. However, reflection starts only after the plasma density in the filament reaches $n_{critical}$ as the simulation proceeds. Further, the incoming microwave gets shielded as $n_e = n_{cutoff}$. Most simulation time is consumed as the initial plasma density grows from n_0 to $n_{critical}$. Based on a simulation-based convergence study as shown in Fig. 2.3, we can observe that the typical time to reach $n_{critical}$ and n_{cutoff} depends on the choice of n_0 . Therefore, the choice of initial plasma density (n_0) enables the acceleration of the HPM breakdown phenomenon leading to the filamentation process.

The powerful millimeter-wave with a strong E-field ($E_0 = 5.0$ MV/m)

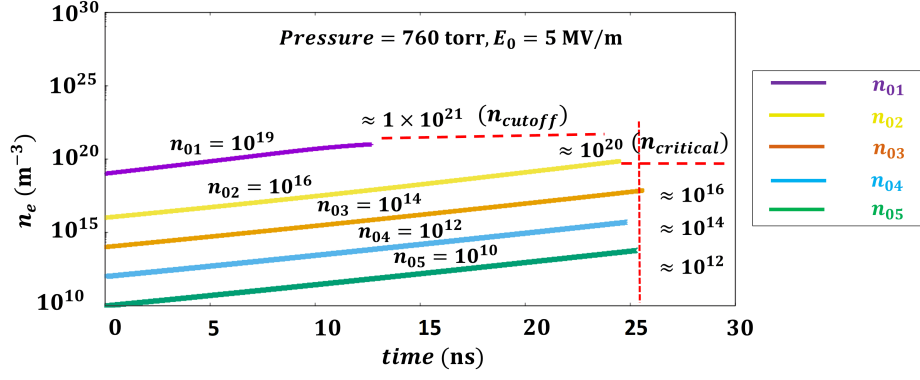


Figure 2.3: The choice of initial density (n_{0i} , where $i=1,2,3$ and 4) in m^{-3} for initiating the HPM breakdown-induced filamentation process.

interacts with the air (or gas) at high pressure (760 torr), delivers sufficient energy to the free electrons that accelerate and causes continuous ionization of the air/gas and leads to an avalanche breakdown (when ionization overcomes the attachment, diffusion, and recombination). The process results in the plasmoid formation. We can observe the plasmoid formation in Fig. 2.4(i), its growth into consecutive first, second, and third filaments, and the propagation of the plasma filamentary structure from right to left with time in Fig. 2.4 (ii-iv) respectively. This complex and nonlinear plasma filamentary structure evolution occurs over hundreds of nanoseconds. A detailed analysis of this complex plasma dynamics is provided in the next section.

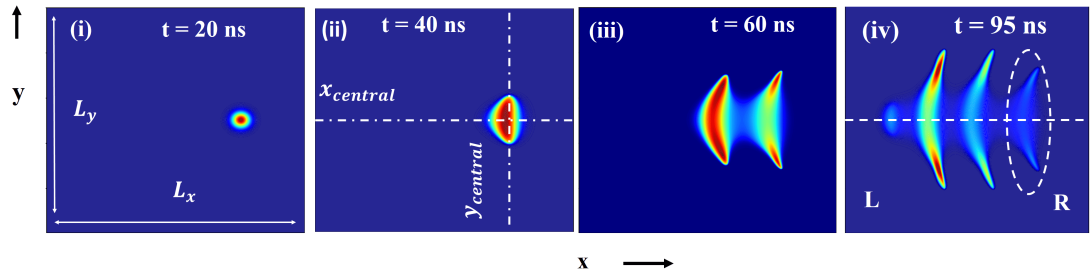


Figure 2.4: (i-iv) plasma density (m^{-3}) distribution in the filaments at four-time instances.

2.5 Physics of complex plasma dynamics during HPM breakdown: spatio-temporal analysis

The simulation results in Fig. 2.5 (i-iv) show the temporal evolution of plasma density, rms E-field, diffusion coefficient, and rate of ionization along the central x-axis of the computational domain, whereas Fig. 2.5 (v-viii) represents

the same quantities along the y direction (y -axis passing through the center of the rightmost filament). Figure 2.5 helps us to capture the plasmoid's complete spatio-temporal evolution into filaments and its propagation during the first 100 ns. This detailed scientific visualization further aids in understanding the complex plasma dynamics.

The initial plasmoid is located at 0.75λ from the leftmost boundary, as shown

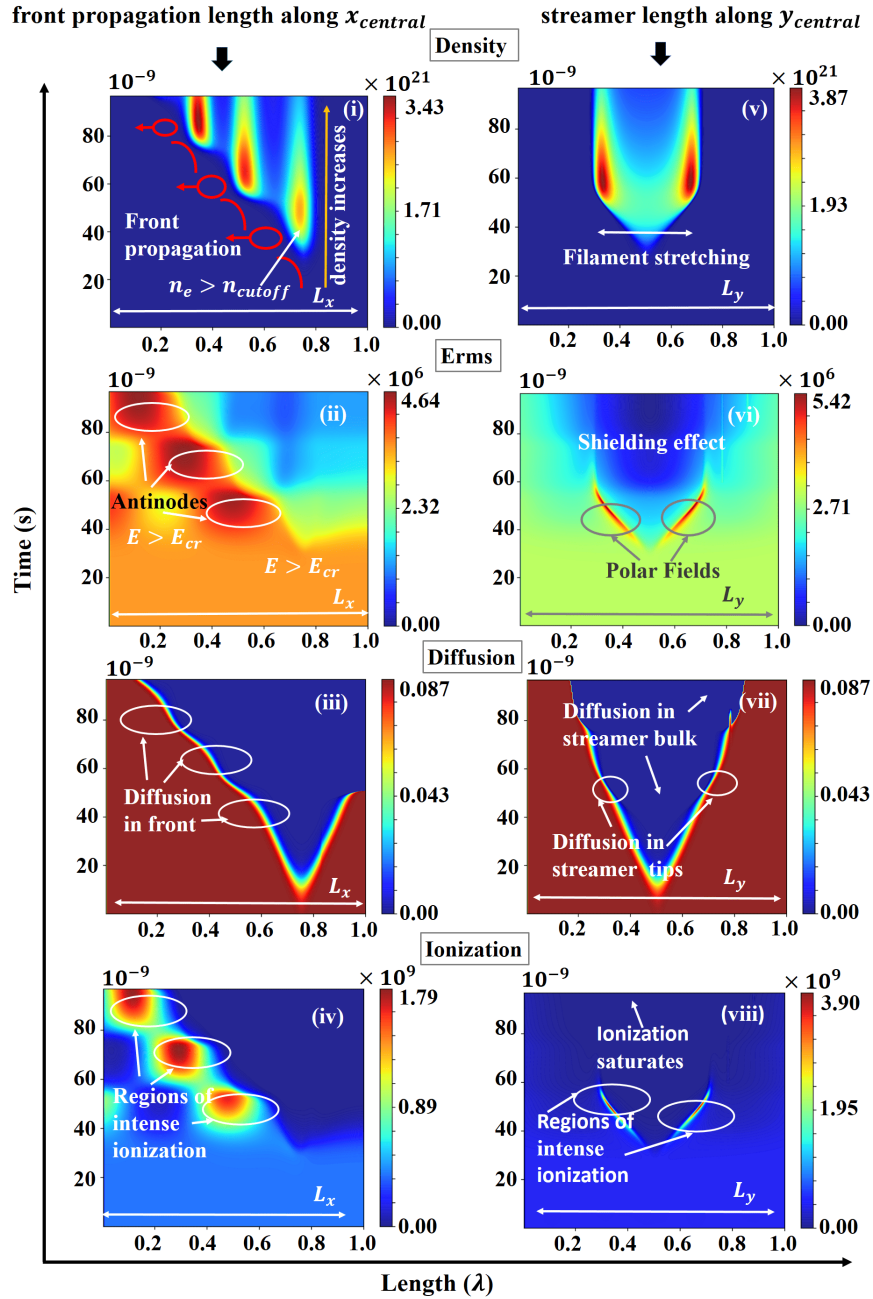


Figure 2.5: (i-iv) The evolution of the plasma density (m^{-3}), rms E-field (V/m), the effective diffusion coefficient (m^2/s), and the rate of ionization (s^{-1}) along the x_{central} of the computational domain. (v-viii) the evolution of the same quantities along the y_{central} passing through the center of the rightmost filament (in a dotted circle). Here, L: Left and R: Right, $L_x = L_y = 1\lambda$.

in Fig. 2.4(i), which is captured at 20 ns. It remains Gaussian until the

plasma density is small and cannot perturb the incoming microwave E-field as observed in Fig. 2.5 (ii) [28]. The plasma density growth over time (Fig. 2.5(i)) can be attributed to the high incident rms E-field ($E_{\text{rms}} = 3.5 \text{ MV/m}$) $> E_{\text{cr}}$, where critical (or breakdown) field $E_{\text{cr}} \approx 2.5 \text{ MV/m rms}$ [35]. From Fig. 2.5 (ii), the changes in the E-field distribution along the central x-axis during the time duration of 20 to 50 ns can be observed, and during the same time interval, from Fig. 2.5 (iv), we can observe the increase in the rate of ionization from $0.18 \times 10^9 \text{ s}^{-1}$ to $1.3 \times 10^9 \text{ s}^{-1}$ along the X-direction. From Fig. 2.5 (ii) and (iv), we can see the strong correlation between the E-field peaks and the increased rate of ionization in space and time. The high ambient pressure results in multiple collisions between the electrons and neutral gas species. The ionization is a collision-assisted process governed by the local E-field or E_{eff} . In our study at $f = 110 \text{ GHz}$, the wave angular frequency (ω) is $2\pi f \approx 6 \times 10^{11} \text{ s}^{-1}$, $v_m \approx 4 \times 10^{12} \text{ s}^{-1}$, when $E_{\text{rms}} \geq 3.5 \text{ MV/m}$, then the $E_{\text{eff}} \approx 3.46 \text{ MV/m} \geq E_{\text{cr}}$, also satisfies the breakdown criteria. Thus, high collisions result in much more ionization, increasing the plasma density. The increase in ionization rate causes an increase in the density of the plasma bulk, and the plasma starts modifying the total field like a dielectric. It is also important to consider the growth of the filament along the vertical (y) axis (as shown in Fig. 2.5 (v-viii)). From Fig. 2.5 (i and v) between $t = 20$ to 50 ns duration, we can see that the plasma density starts growing, and the filament stretches along the vertical cross-section. The filament growth along the vertical direction can be attributed to the very large polar field that increases from 2.7 MV/m to a maximum $\approx 5.42 \text{ MV/m}$ (Fig. 2.5 (vi)), that results from Electrostatic polarization [28]. The E-field in the center and at the tip of the filaments starts oscillating as the filament length approaches half wavelength. As discussed in [28], a resonance-like behavior may result in the streamer acting as a half-wave dipole and reflecting the incoming microwave E-field. The polar fields can be observed in Fig. 2.5(vi). The field enhancement results in intense ionization (≈ 2 times the ionization along the x-direction), as can be seen in Fig. 2.5 (iv and viii). The high polar fields stretch the plasma filaments along the vertical direction (vertical polarization of incident microwave E-field) due to higher ionization, and the free electrons in the filament tips start diffusing with diffusion coefficient (D_e). The filament growth is related to the plasma

tip elongation rate given by $v_{\text{streamer}} = 2\sqrt{D_e v_i}$. The ionization frequency, ν_i , strongly depends on the polar rms E-fields. Therefore, the streamer tip velocity is also enhanced due to the high E-field. In our study, we obtain the streamer (or filament) elongation velocity- $v_{\text{streamer}} \approx 30$ km/s, which is ≈ 15 km/s along each tip of the filament. The filaments achieve high $v_{\text{streamer}} \approx 30$ km/s, in the time duration of 20 to 60 ns.

At $t > 40$ ns, the plasma density, $n_e \approx 2 \times 10^{21}$ reaches well above the cutoff density. When plasma density crosses the cutoff density, (here $n_{\text{cutoff}} \approx 9 \times 10^{20} \text{ m}^{-3}$), plasma starts reflecting the EM wave [35]. We can observe from Fig. 2.5 (i) and also in the Fig. (v), at $t > 40$ ns, the $n_e > n_{\text{cutoff}}$, thus the plasma filament/streamer transits from a dielectric behavior to a conductor. The scattered and incident E-field of the EM wave interferes and forms nodes and antinodes of the standing wave ahead of the first filament. The E-field has its node (minima) at the streamer center and the antinode (maxima) at $\approx 0.25\lambda$ from the initial plasmoid center (0.75λ from the left boundary), and it corresponds to the location where the new plasmoid starts to form. We can validate from Fig. 2.5 (ii) that the E-field strength is of the order of ≥ 4 MV/m at the antinodes. The high field results in very intense ionization at the edge of the plasma filament. Therefore, the electrons at the filament edges start to diffuse out with an effective diffusion coefficient- $D_{\text{eff}} \approx 0.087 \text{ m}^2/\text{s}$ as can be seen in Fig. 2.5 (ii-iv). Interestingly, the filament edge with low plasma density always diffuses quickly and forms a narrow diffusion channel called the plasma front. The plasma front propagates along the X-direction (right to left of computation domain) with a theoretical front velocity, $v_{\text{front}} = 2\sqrt{D_e v_i}$, here, $v_{\text{front}} \approx 20$ km/s. We can observe that the streamer elongation is faster than the front propagation due to a higher E-field in the tip of plasma filaments compared to the E-field at the antinode of the standing wave ahead of the filament. Both the plasma front and the streamer diffuse with similar diffusion coefficients- $D_{\text{eff}} \approx D_e$, but the filament tip has a higher density in comparison to the front, and the growth of the streamer tip gets modulated with the polar fields of the streamer.

For $t > 50$ ns, the second plasmoid follows a similar physics to elongate into a streamer. It starts perturbing the incoming E-field by obstructing it from reaching the initial (first) filament. The less penetration of the incoming

microwave can be attributed to the high density in the second filament, which results in high plasma conductivity. Also, the width of the streamer almost nears the skin depth in plasma [28,35]. Therefore, microwave shielding occurs by the second filament on the first filament towards the right of the simulation domain. The shielding can be observed in Fig. 2.5 (v, vi, and viii). The shielding effect obstructs the filament from stretching in the vertical direction. Subsequently, the ionization along the filament tips gets saturated and stops the streamer elongation. The newly formed filament acts as the reflector of the incoming microwave. The standing wave formation and enhancement of the front E-field follow, resulting in continuous ionization and diffusion-assisted front propagation. Further, it continues till the end of the simulation (around 95 ns), and we observe a self-organized fish-bone-like plasma filamentary structure exactly similar to experimental observations [2,32].

2.6 Associated challenges with 2-D simulation of HPM breakdown

The HPM breakdown in air/gas leads to sharp gradients in plasma density and the corresponding scattered electric field (E-field) along both the X and Y-directions throughout the evolution of the self-sustained plasma structures. For accurate simulations, n_e and EM fields need to be calculated on a very fine mesh, which can resolve such sharp gradients in n_e and E [28,45]. The recommended minimum number of grid points per wavelength (N_λ) of the electromagnetic (EM) wave is around 500, i.e., $N_\lambda = \lambda/\Delta > 500$, for E-field in simulation plane as considered in our study. Here, Δ is the grid size. The requirement of very fine grids significantly increases the computational cost (in terms of the number of grid points in the simulation domain and a very small time step) for high-frequency problems such as 100's of GHz ($\lambda \approx 2$ mm). The simulation follows an iterative algorithm. The Total_Computations (FLOPs) required during the simulation = Total Number of grid points \times Number of FLOP per iteration \times Number of iterations = $(c_k N_\lambda)^2 \times F_L \times M$, where, problem size: $c_k \lambda \times c_k \lambda$, $c_k \in \mathbb{Q}^+$, F_L - FLOPs per iteration, M- Total iterations (physical time/ Δt). Typical values of $F_L \approx 100$, $\Delta t = 10^{-15}$ s, typical

Table 2.1: Approximate simulation time for different problem sizes.

Problem Size	Grid Size($N_\lambda \times N_\lambda$)	Total_Computations(FLOP)	approximate Run_Time
$1\lambda \times 1\lambda$ $\approx 2 \text{ mm} \times 2 \text{ mm}$	512×512	$\approx N_\lambda^2 F_L M$	5 days (from simulation)
$2\lambda \times 2\lambda$ $\approx 4 \text{ mm} \times 4 \text{ mm}$	1024×1024	$\approx c_k^2 N_\lambda^2 F_L M (c_k = 2)$	$\approx 2^2 \times 5 \text{ days}$
$10\lambda \times 10\lambda$ $\approx 20 \text{ mm} \times 20 \text{ mm}$	5120×5120	$\approx k^2 N_\lambda^2 F_L M (c_k = 10)$	$\approx c_k^2 \times 5 \text{ days} \approx 500 \text{ days}$

physical simulation time: 100 ns. Table 2.1 shows a generalized expression that scales the Total_Computation as well as the approximate simulation time for different problem sizes based on a factor (c_k) that indicates the amount of increment of the problem size (w.r.t to a $1\lambda \times 1\lambda$ problem). We can observe that the total simulation time increases with the increase in problem size and decrease in time step. The major challenge lies in simulating a bigger problem such as $10\lambda \times 10\lambda \approx 20 \text{ mm} \times 20 \text{ mm}$, that will take around 500 days, i.e., almost two years using a serial code on a standard desktop. Researchers can adopt either of the two approaches to tackle such computational challenges :

- Use massive parallelization on the uniform fine grids throughout the computational domain by utilizing supercomputing facilities [45].
- Use Mesh refinement-based technique to capture the steep gradients in evaluated quantities in the regions of interest.

2.7 Conclusions

In this chapter, we revisit the interaction of the HPM with air/gas while providing a general overview of the multi-scale multi-physics problem and the mathematical model describing all the physical phenomena (EM and evolving plasma physics) associated with this problem. A proper 2-D computational flow diagram representing all the solvers and their numerical implementation has been discussed. Using a benchmark problem representing the HPM breakdown in a $1\lambda \times 1\lambda$, 2-D computational space, we have performed a detailed 2-D spatio-temporal analysis to provide a visual representation of the microwave breakdown induced plasma generation and its evolution

in both space and time as the simulation proceeds. For the first time, using the 2-D spatio-temporal plots, we have visually explained the results indicating the interplay of various plasma transport processes, such as ionization, attachment, recombination, and diffusion as a function of reduced effective field (E_{eff}/p), during the plasma filamentation growth. This novel spatio-temporal visual analysis comprehensively explains the intricate physics governing high-power, high-frequency microwave breakdown and the self-organized filamentation process. Our computational complexity analysis reveals the necessity to develop efficient computational techniques to perform accelerated simulations of HPM breakdown in a resource-constrained environment. This knowledge is a valuable foundation for future advanced research and applications in this field.

CHAPTER 3

Efficient dynamic mesh refinement technique for simulation of HPM breakdown

3.1 Introduction

Accurate 2D simulations of HPM breakdown experiments mentioned in the previous chapter have been performed using a well-established fluid model involving the coupling of Maxwell's equations and plasma continuity equation [35, 36, 45, 94, 109]. It is a complex multi-physics multi-scale model due to different space and time-scales [45, 47], which needs to be resolved accurately. Most of the previous works [9, 26, 28, 35, 36, 45, 69, 93, 95, 98, 100, 108, 109] used finite difference time domain (FDTD) method in the Maxwell-plasma fluid model based simulations. The simulations reproduce the experimental observations quite well but at a high computation cost (which grows exponentially with problem size). Therefore, most past 2D numerical investigations using the fluid model have been carried out to hundreds of nanoseconds. The high computational cost is due to stringent restrictions on the grid spacing and time steps [35, 36, 45, 69]. Therefore, it is challenging to simulate large problem sizes over longer time scales (tens of microseconds) using a homogeneous mesh with the finest grid size resolution to capture the gradients in plasma density and the secondary E-field that originates from it. Different time steps (femto to nanoseconds) are required by the solvers [108] that are coupled with each other to simulate the Maxwell-plasma fluid model. Unless the solver that requires frequent updates gets speedup, the

higher time scale phenomenon such as gas heating [36] cannot be realized efficiently. Simulation of this complex phenomenon at longer time-scales will further help to understand the underlying physics for various applications in microwave rockets [23, 93, 110], aerospace research [5, 34, 45, 111], high-speed combustion [112], safe operation of HPM devices [94] and more.

Recently, advanced parallelization strategies for emerging many-core architectures have been proposed, significantly reducing the simulation time, but this requires sophisticated computing facilities [45]. To address the computational challenges associated with the 2D FDTD-based EM-plasma fluid model, alternative numerical techniques have been developed for structured meshes [36] and unstructured meshes [47]. However, the techniques can balance the trade-off between accuracy and computational cost but require complex mathematical formulation, proper choice of higher-order basis functions, and modification of the existing model. Recently, a static mesh refinement (MR) technique for the well-established FDTD-based fluid model has been presented for studying evolving plasma dynamics [108]. Although the static MR-based technique is accurate and relatively fast compared to single uniform fine mesh, overall performance is restricted by the size of the fixed preset refined mesh that restricts bigger and longer simulations. Therefore, a self-aware dynamic mesh refinement (DMR) technique that generates fine mesh on demand, based on the plasma evolution, is proposed in this chapter. The DMR technique will particularly aid in carrying out comprehensive parametric studies to investigate the influence of different parameters such as the microwave E-field strength, the frequency of the microwave, the pressure, and different gas species on HPM-induced plasma evolution at a significantly lower computational cost. This chapter presents the Development and implementation of the DMR technique for the Maxwell-Plasma fluid model for investigating complex plasma dynamics during HPM breakdown on regular 2D-cartesian grids using the fluid model as discussed in chapter 2. Validation and performance analysis of the proposed DMR technique have been performed against published results.

Organization of the chapter

In section 3.2, we discuss the theory and implementation of the DMR technique, which covers the criteria for initiating and expanding the fine

mesh, quantity (E, H-fields, and plasma density) updates on both meshes, the algorithm and flowchart representation of DMR technique, and, the calculation of computational complexity associated with DMR. In Section 3.3, we report the accuracy and efficiency of the proposed technique, followed by conclusions in section 3.4.

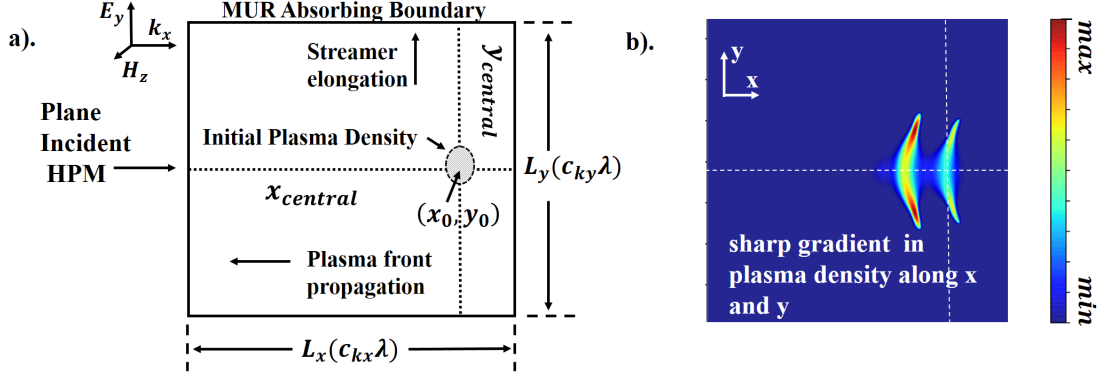


Figure 3.1: (a) Schematic of the Computational domain. $\{(c_{kx}, c_{ky}) \in \mathbb{Q}^+\}$, and, x_0 and y_0 are fractions in $[0, 1]$ of L_x and L_y respectively. The MUR outer radiation boundary condition has been used for scattered field formulation. (b) Formation of self-organized plasma filaments during HPM breakdown (snapshot at $t = 45$ ns, $E_0 = 5.5$ MV/m, freq = 110 GHz). The maximum density (*max*) is $6 \times 10^{21} \text{ m}^{-3}$ and (*min*) is 0.

3.2 Self aware DMR technique and its implementation

The proposed DMR technique is a self-aware mesh refinement technique developed from the static Mesh Refinement (MR) framework, which hierarchically decomposes the computational domain into coarse and fine meshes. The mesh grids are overlapped and logically connected to maintain the continuity between the evaluated quantities, [108, 113–115]. Unlike static MR, the DMR technique considers a fixed coarse mesh and an expanding fine mesh based on the evolving plasma profile during HPM breakdown. This approach avoids unnecessarily large computations due to a large preset refinement region. To explain the proposed DMR technique, we consider a similar simulation setup as shown in Fig. 3.1 (a). Figure 3.2 illustrates the initial fine mesh expansion over time, denoted by $R(t)$.

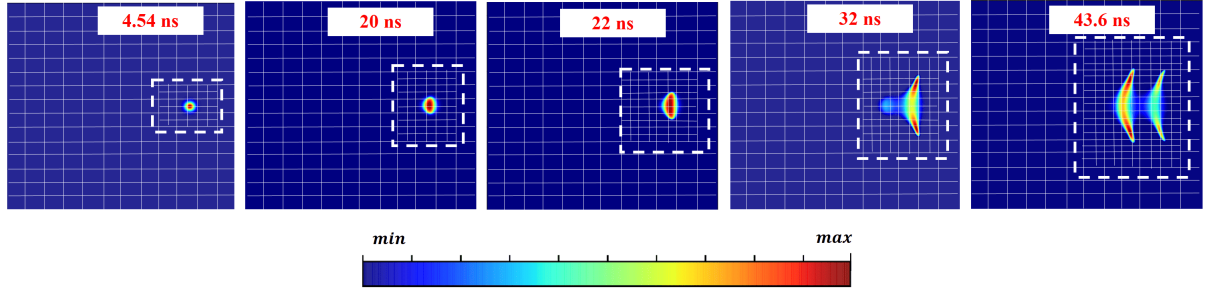


Figure 3.2: The self-aware expansion of fine mesh in DMR to capture the 2D distribution of plasma density as the filamentary pattern evolves.

3.2.1 Initiation of fine mesh expansion

Fine mesh expansion initiation requires detecting sharp variations in evaluated quantities (E and H-fields, plasma density, and velocity) on discretized grids and using a suitable mesh to capture them. Threshold criteria based on overall and instantaneous energy gradients [115] are commonly used to determine the grid size for EM-scattering problems. However, for HPM breakdown, with continuously evolving medium properties, alternative criteria are used to decide on mesh expansion initiation and grid size. The decision to initiate fine mesh expansion depends on a fixed plasma density (threshold density) that is well-validated based on EM propagation characteristics in plasma [43].

The optimal threshold density is determined through a convergence study, where the occurrence of minimum variation in permittivity (ϵ) and conductivity (σ) for a given plasma density profile and incident EM wave frequency as observed in Fig. 3.3 (a) and absence of spikes as shown in Fig. 3.3 (b). The chosen density, $n_e < 10^{18} \text{ m}^{-3} \approx 10^{16} - 10^{17} \text{ m}^{-3}$, satisfies lower scattered E-field, avoids sharp gradients in E-field or energy due to minimum variation in ϵ and σ , and ensures that the fine mesh resolves the minimum gradient scale lengths along the y and x-axis. Finally, arriving at the amount of mesh expansion, refer to Fig. 3.4 (a-b) and 3.5 (a-b). For coarse and fine mesh grid sizing, an inverse approach is taken where the finest grid size is pre-decided based on valid assumptions, and the coarse grid size is decided based on the mesh refinement factor. The cell size remains fixed for both meshes during simulation.

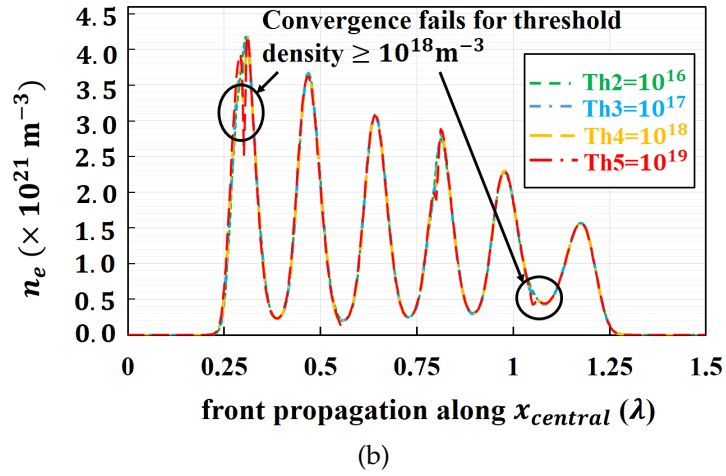
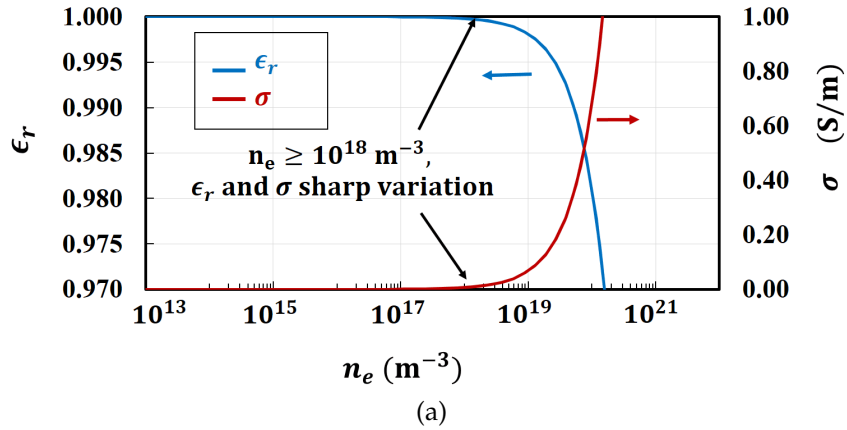


Figure 3.3: (a) The spatial variation of ϵ_r and σ for a 1D plasma density (n_e) distribution. (b) Convergence study for different threshold densities (m^{-3}) to arrive at the threshold density criteria for mesh initiation. The EM wave of frequency 110 GHz is considered here.

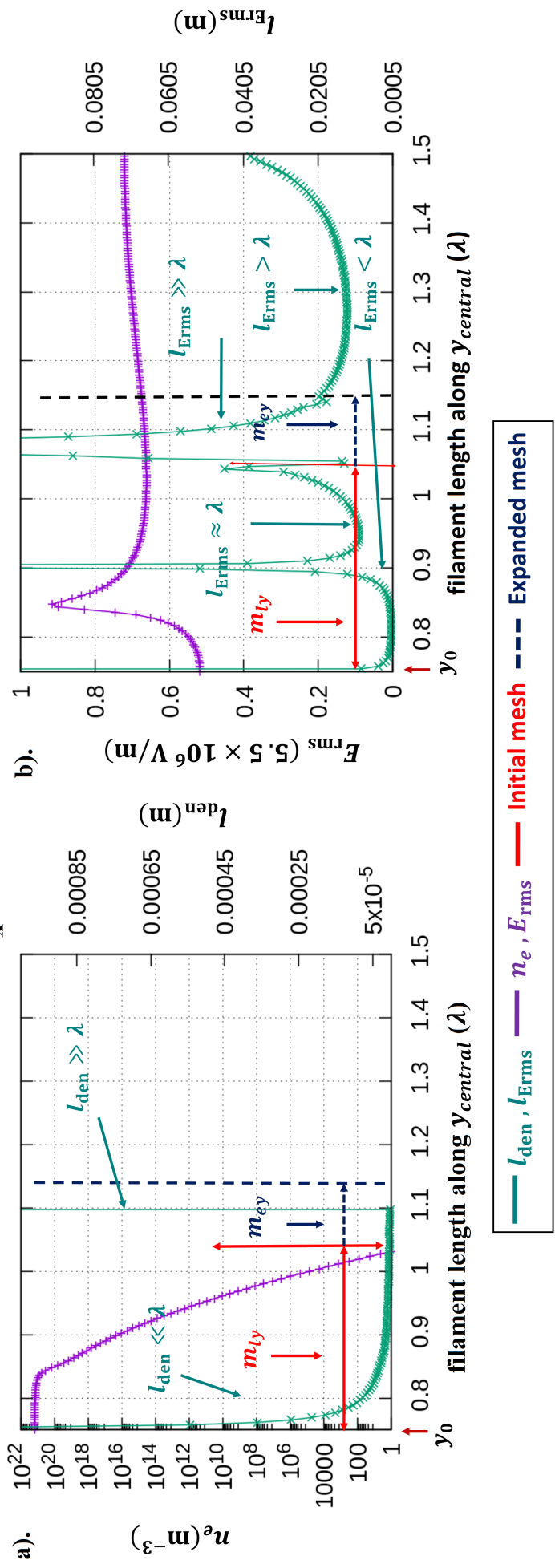
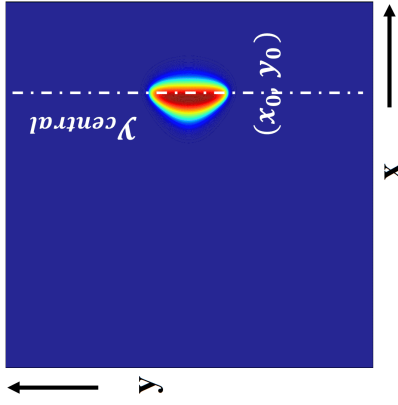


Figure 3.4: The 1D distribution of (a) plasma density and (b) rms E-field and their corresponding gradient scale lengths l_{den} and $l_{E_{\text{rms}}}$ respectively, along the upper half of central y -axis (y_{central}) through the initial plasma density. The initial plasma density is located at $\{x_0, y_0\} = \{0.85L_x, 0.5L_y\} = \{1.2\lambda, 0.75\lambda\}$, $L_x = L_y = 1.5\lambda$. The $\lambda \approx 0.0027 \text{ m}$ corresponds to frequency (f) = 110 GHz.

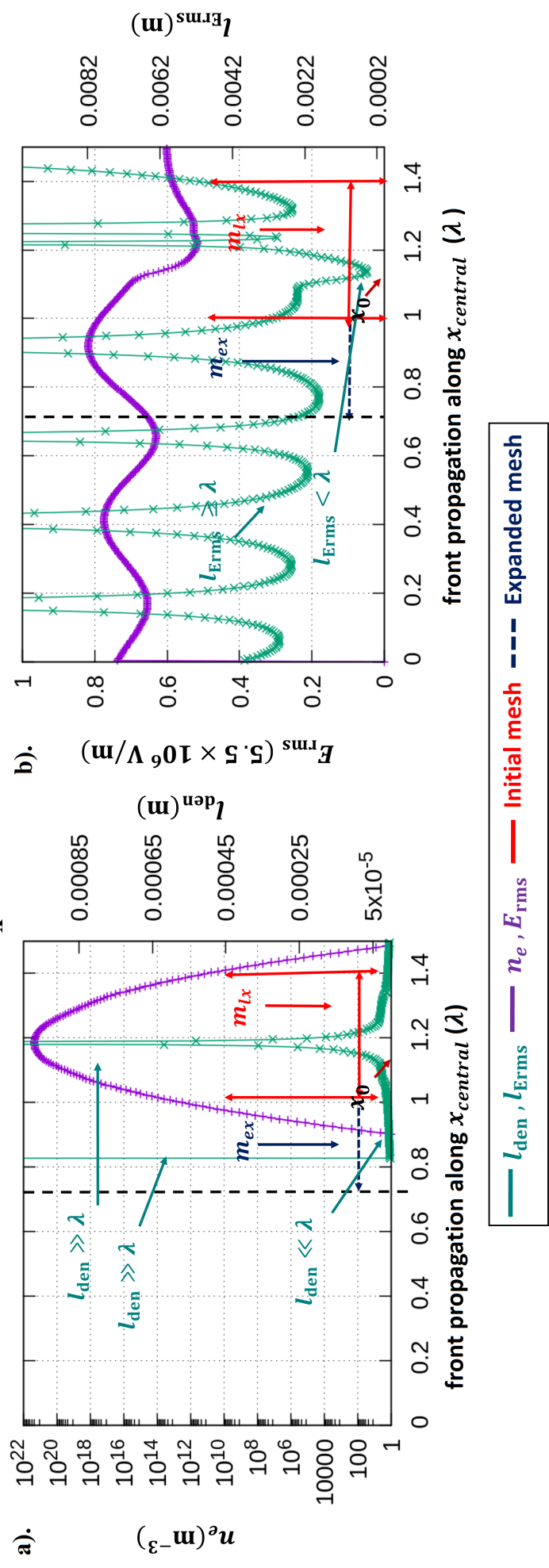
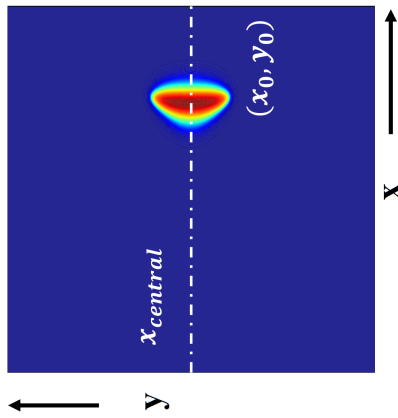


Figure 3.5: The 1D distribution of (a) plasma density and (b) rms E-field and their corresponding gradient scale lengths l_{den} and $l_{E_{\text{rms}}}$ respectively, along the central x-axis (x_{central}) through the initial plasma density. The initial plasma density is located at $\{x_0, y_0\} = \{0.85L_x, 0.5L_y\} = \{1.2\lambda, 0.75\lambda\}$, $L_x = L_y = 1.5\lambda$. The $\lambda \approx 0.0027$ m corresponds to frequency (f) = 110 GHz.

3.2.2 Amount of fine mesh expansion

The presence of sharp gradients in the plasma density during HPM breakdown is an important parameter in deciding the amount of fine mesh expansion [8]. We have considered two gradient length scales corresponding to plasma density and rms E-field (scattered field from plasma), l_{den} and $l_{E_{\text{rms}}}$, respectively. Mathematically, the gradient lengths can be expressed as,

$$l_{\text{den}} = n_e / |\nabla n_e| \quad (3.1)$$

and

$$l_{E_{\text{rms}}} = E_{\text{rms}} / |\nabla E_{\text{rms}}| \quad (3.2)$$

where $|\nabla n_e|$ and $|\nabla E_{\text{rms}}|$ are magnitudes of the gradient in density and rms E-field, respectively. For the expansion of the fine mesh, the growth of filaments and the associated density gradients along y_{central} and x_{central} as shown in Fig. 3.1 (a-b) have been considered. Due to the symmetric nature of the plasma propagation, the region above x_{central} starting at y_0 is only considered for analysis. In Fig. 3.4 (a-b) and 3.5 (a-b), the length of initial fine mesh and the amount of fine mesh expansion along y and x are represented by, m_{ly} and m_{lx} , and, m_{ey} and m_{ex} , respectively. Figure 3.4 (a-b) shows the distribution of plasma density, rms E-field, and the corresponding gradient length scales along the y-direction. The l_{den} has a sharp transition from a high value, $l_{\text{den}} \gg \lambda$ ($\nabla n_e \rightarrow 0$), to a low value, $l_{\text{den}} < (1/100)\lambda$. There is a high gradient in rms E-field that exists from 0.75λ to 0.85λ as shown in Fig. 3.4 (b), and as a result the gradient length scale ($l_{E_{\text{rms}}}$) transits from low ($l_{E_{\text{rms}}} < \lambda \sim (1/5)\lambda$) to high ($l_{E_{\text{rms}}} \gg \lambda$, when ($\nabla E_{\text{rms}} \rightarrow 0$)). The initial fine mesh centered around initial density can capture the sharp gradients in both density and rms E-field along y_{central} provided, m_{ly} is large enough to cover the occurrence of smallest, l_{den} as well as $l_{E_{\text{rms}}}$, and the fine mesh grid size satisfy, $\Delta S \sim \min \{l_{\text{den}}, l_{E_{\text{rms}}}\}$. Next, for the fine mesh expansion along y_{central} , the amount of expansion, m_{ey} , must be able to capture the occurrence of smallest, l_{den} as well as $l_{E_{\text{rms}}}$, as specified above.

Similarly, Fig. 3.5 (a-b) presents the distribution of plasma density and rms E-field and their corresponding gradient length scales in the x-direction (along

$x_{central}$; the plasma front propagation direction). The presence of gradient length scales determines the amount of mesh expansion. By referring Fig. 3.4 (a-b) and 3.5 (a-b), it can be observed that $\min\{l_{den}\} < \min\{l_{E_{rms}}\}$. Thus, l_{den} , instead of $l_{E_{rms}}$, decides fine mesh grid size. Based on the gradients shown in Fig.3.4 (a-b) and 3.5 (a-b), we found that $m_{ex} > m_{ey}$. Therefore, a different amount of mesh expansion is required in the X and Y-directions.

3.2.3 Quantity Updates on Mesh and Synchronization

The schematic in Fig. 3.6 (a) represents the mesh refinement region (in dashed). Here, we have used a single level of refinement as shown Fig. 3.6 (a). Both the coarse and fine meshes overlap with each other, having a grid refinement factor (r) of two, such that the coarse-to-fine grid size ratio is 2 : 1. As depicted in Fig. 3.6 (b), two meshes are overlapped, the coarse and embedded fine. E, H, density, and velocity (synchronized with E), as shown in Fig. 3.6, are updated as discussed in [45]. The fields and density are updated simultaneously on the coarse and fine mesh, maintaining the proper sequence of frequent FDTD and less frequent (on each period of EM wave) update of plasma continuity equation [45]. The different time steps are based on respective CFL conditions. The time step associated with EM wave solver is much smaller compared to plasma solver [35,45].

The updated quantities on both meshes must be synchronized in space and time to maintain continuity. Let the grid size, time step, total cells, and total iterations for the benchmark case (uniform fine mesh) be represented by ΔS_f , Δt_f , N_f and I_f , respectively. In the case of DMR, the coarse mesh cell size and time-step are represented by ΔS_c and Δt_c , and for fine mesh, it is represented by ΔS_f and Δt_f . Δt_c and Δt_f are associated with Maxwell's updates (which primarily determines the total execution time). The subscripts c and f correspond to coarse and fine meshes. Here, $\Delta S_f = \lambda/N_\lambda$ and $\Delta S_c = r\Delta S_f$. Similarly, $\Delta t_c = r\Delta t_f$. In one coarse mesh update, Δt_c , the fine mesh performs r updates with Δt_f . Similar steps follow for all the quantities. The total fine mesh cells depend on the amount of refinement region ($R(t)$). $R(t)$ is a fraction of the total computation domain, and $R(t) \in [0, 1]$.

The MR algorithm transfers the evaluated quantities (fields, velocity, and

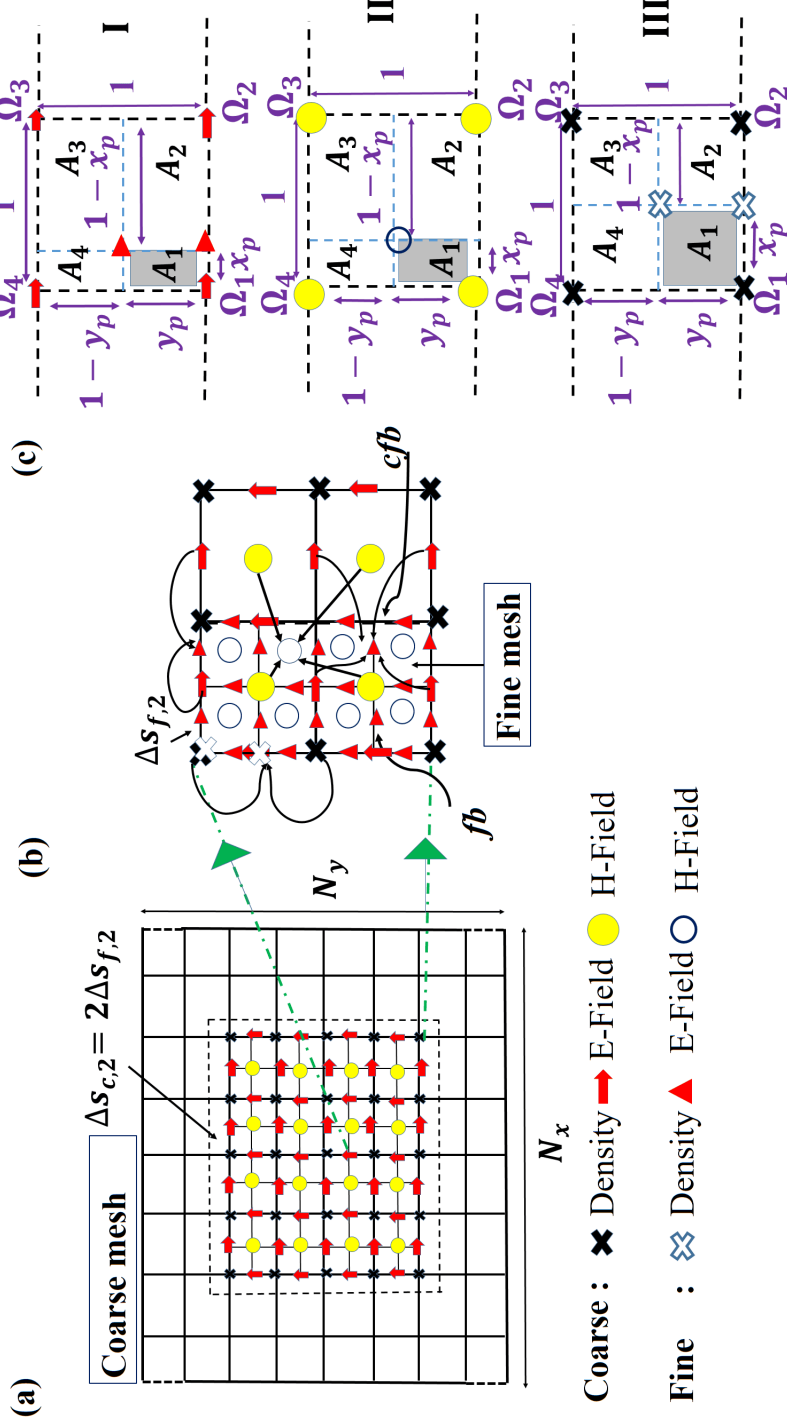


Figure 3.6: (a) The mesh refined (the dashed region with refinement factor 2) discretized computational grid showing locations for computation of EM fields and density. (b) The expanded view of overlapped coarse and fine mesh. The different data transfer of updated E-field, H-field and the plasma density from coarse mesh to its corresponding fine mesh locations on both coarse-fine boundary (cfb) as well as the fine boundary (fb) are shown. (c) Schematic representation of interpolation techniques for $r=2$. Here, I : E-field (and velocity), II : H-field, and III : plasma density represent different interpolations for the coarse mesh data.

plasma density) from the coarse mesh to both the coarse-fine boundary (*cfb*) and the fine boundary (*fb*) for subsequent fine mesh updates. This transfer of evaluated quantities supports the nearest neighborhood dependence of FDTD and FD-based fields and density updates, respectively [35]. Finally, the fine mesh updated quantities are transferred back to the coarse mesh. Both the data transfer process must occur within the coarse mesh update interval. The process avoids discontinuity in the obtained results due to a mismatch between coarse and fine mesh values. The two boundaries (*fb* and *cfb*) and the sub-grids are shown in Fig. 3.6 (b).

The data transfer uses a direct copy or interpolation process, depending on the location (coinciding or non-coinciding) of the quantities on the overlapped grids. The interpolation is either a linear interpolation on *cfb* or a bi-linear interpolation on *fb* as indicated by the direction of arrows in Fig. 3.6 (b). Quantities, Ω_i , $i=1$ to 4, shown in Fig. 3.6 (c), represent either E-field (and velocity), H-field, or plasma density on the coarse mesh. The dotted square represents the interpolation domain. The vertices represent the coarse data, and the desired fine data, either on edge (1D) or inside the bounded area (2D plane), can be obtained using the equation as follows:

$$\begin{aligned}
BL_{f_{new}} = & (1 - frac)(\Omega_{1_{old}}A_3 + \Omega_{2_{old}}A_4 \\
& + \Omega_{3_{old}}A_1 + \Omega_{4_{old}}A_2) \\
& + (frac)(\Omega_{1_{new}}A_3 + \Omega_{2_{new}}A_4 \\
& + \Omega_{3_{new}}A_1 + \Omega_{4_{new}}A_2)
\end{aligned} \tag{3.3a}$$

$$\begin{aligned}
L_{f_{new}} = & (1 - frac)(\Omega_{1_{old}}(1 - x_p) + \Omega_{2_{old}}(x_p)) \\
& + (frac)(\Omega_{1_{new}}(1 - x_p) + \Omega_{2_{new}}(x_p))
\end{aligned} \tag{3.3b}$$

Where suffixes *old* and *new* denote the previous and updated quantities on coarse (*c*) mesh that requires interpolation on fine (*f*) mesh. A_i , $i=1,2,3$ and 4, represents the area inside the interpolation domain (dotted square) calculated in terms of x_p and y_p represented in terms of r . From Fig. 3.6 (c), the locations, $\{x_p, y_p\}$ are as follows: for, I : $\{1/2r, 1/r\}$, II : $\{1/2r, 1/r\}$ and III : $\{1/r, 1/r\}$, where $r=2$ or 4 based on the type of refinement. The *frac* and $(1 - frac)$ are the ratios in which the old and the updated coarse mesh data values must be taken

to obtain a smoothed interpolated quantity on the fine mesh. $BL_{f_{new}}$ and $L_{f_{new}}$ represent the bi-linear and linear interpolated fine mesh data, respectively, from coarse mesh data (E or H-field or velocity or plasma density).

3.2.4 Implementation of DMR algorithm

Figure 3.7 (a) shows a coarse mesh: A-B-C-D and an initial fine mesh: a-b-c-d. The flowchart of the DMR technique is shown in Fig. 3.7 (b). For each iteration, the threshold condition on the plasma density (n_{th}) is checked on both the X and Y threshold lines, (X_{Fi}/X_{Bi} and Y_{uj}/Y_{lj}), refer Fig. 3.7 (a) .

Based on the satisfied criteria, the fine mesh expands. The extent to which the fine mesh expands depends on the plasma topology (gradient length scales for density and its scattered E-field) [8]. The algorithm uses 2D arrays since it stores the data in a specific memory pattern, making it easier to manipulate than other data structures. The updates for electric field, magnetic field, and electron density on both the coarse and fine mesh remain the same but based on the refinement factor (r) the subroutines **E**, **F** and **G** will be updated r times for a single update on the coarse mesh for **A**, **B** and **C**. The interpolation is also done r times to provide the coarse data to the coarse-fine boundary (cfb) and fine boundary (fb). The spatio-temporal evolution of the plasma in the computational domain determines the fine mesh boundary. The iterative algorithm will stop when the plasma filaments reach the fine mesh boundary. The details can be found in [8].

3.2.4.1 Step-wise implementation of DMR

- First, an initial fine mesh region, a^{11} - b^{11} - c^{11} - d^{11} , shown in Fig. 3.8, is considered as indicated by the black solid lines. It is located inside a coarse mesh region that covers the overall computational domain, A-B-C-D. The initial fine mesh contains the initial plasma density profile at x_0 and y_0 . As discussed in the previous section, the E-field, H-field, v_e , and n_e are updated in both the coarse and the initial fine mesh.
- Next, the fine mesh generation proceeds with two steps: the self-aware initiation and the initial fine mesh expansion. Different threshold lines parallel to $x_{central}$ and $y_{central}$, indicated by forward threshold (X_{Fi}),

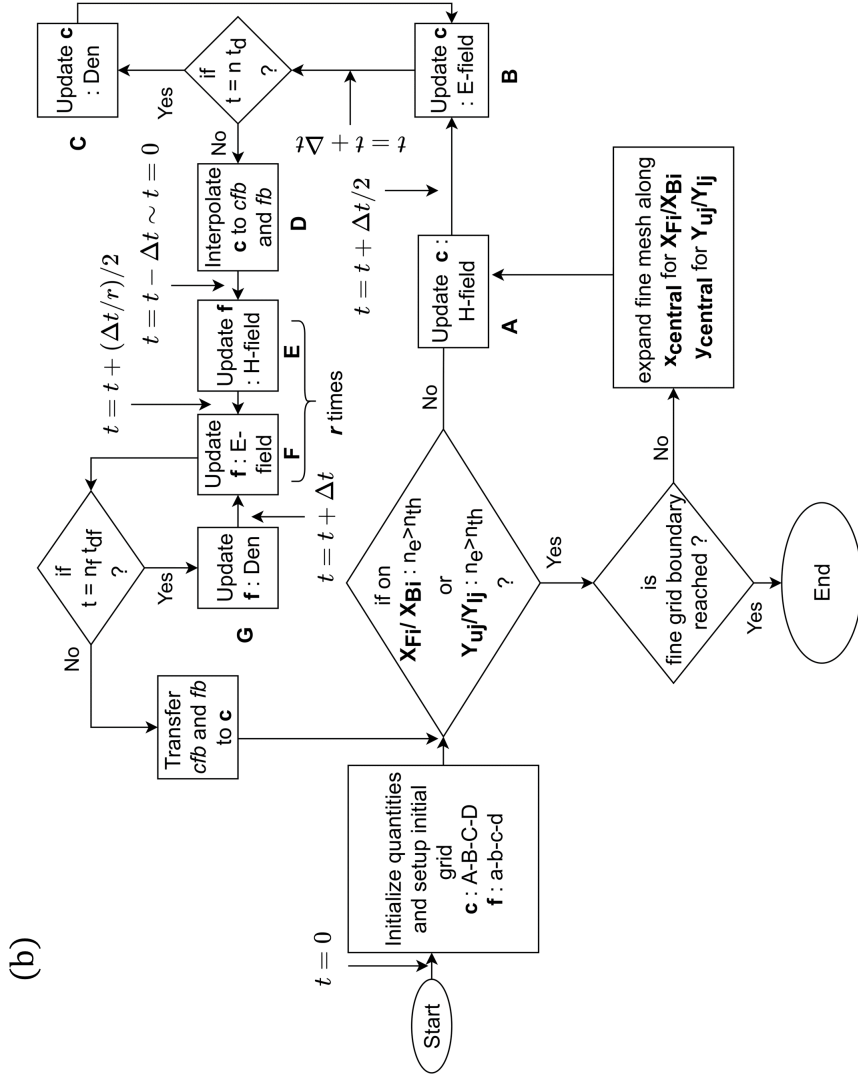
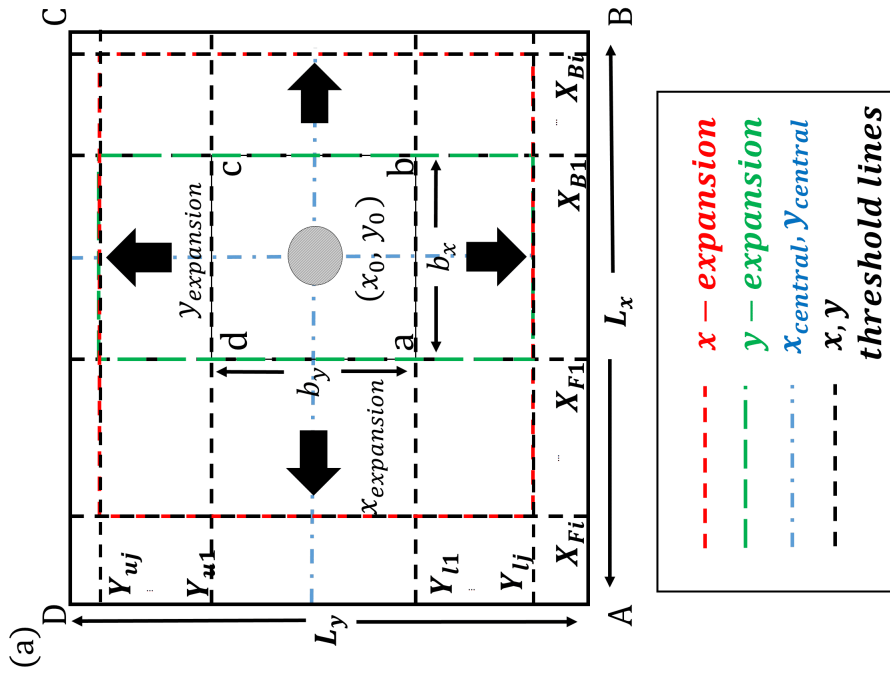


Figure 3.7: (a) Schematic representations of the DMR technique, mesh initiation, and expansion. Initial Gaussian plasma density is located at (x_0, y_0) . b_x and b_y are the dimensions of the fine mesh. X_{Fi} , X_{Bi} , Y_{uj} , and Y_{ij} (or Y_{dj}) denote the forward, backward, upper, and lower thresholds, respectively. The initial fine mesh is labeled a-b-c-d, while the fixed coarse mesh is labeled A-B-C-D. (b) Flowchart representation of computational steps: Subroutines A, B, C, E, F, and G update the EM and plasma solvers for both meshes, with interpolation (D) between them. Den represents plasma density. The time updates for coarse (c) and fine (f) meshes are Δt and $\Delta t/r$, respectively, where r is the refinement factor.

backward threshold (X_{Bi}), upper threshold (Y_{uj}) and lower threshold (Y_{dj}), where $i=1,2,\dots,n$ and $j=1,2,\dots,m$, $\{(n,m) \in \mathbb{N}\}$, are considered as shown by dotted lines. The threshold lines coincide with the fine mesh's respective x and y boundaries (the *cfb*). Before the fine mesh expansion initiates, it is checked whether n_e is greater than the threshold density on either X_{Fi} and X_{Bi} , or Y_{uj} and Y_{dj} . Based on whichever threshold line meets the threshold density criteria, the fine mesh is expanded along $x_{central}$ or $y_{central}$ resulting in a y-expanded: $a^{1j}-b^{1j}-c^{1j}-d^{1j}$ or x-expanded: $a^{ij}-b^{ij}-c^{ij}-d^{ij}$ fine mesh region, as shown in Fig. 3.8. During fine mesh expansion, first, the E-, H-field v_e and n_e data on the entire initial fine mesh are transferred to similar locations on the expanded fine mesh to maintain the continuity from the initial mesh.

- Finally, for the remaining regions in the expanded fine mesh, the overlapped coarse data are interpolated on the fine mesh.

The mesh expansion continues as and when required in a self-aware manner based on the spatio-temporal evolution of plasma.

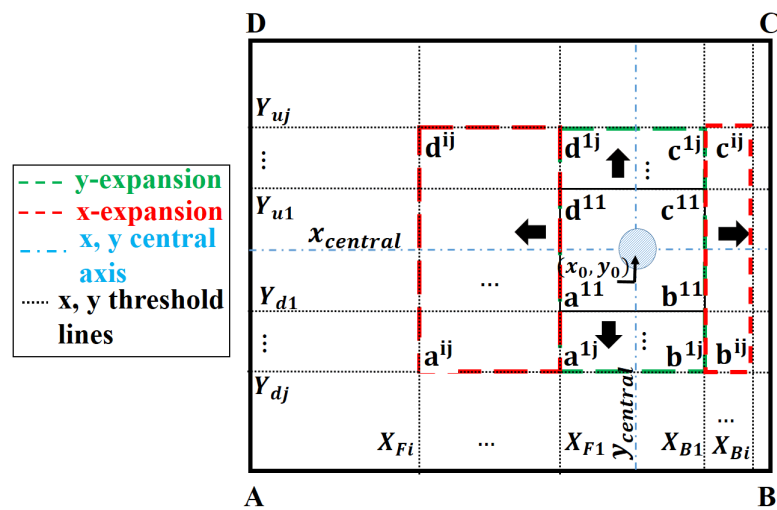


Figure 3.8: Schematic representation of the dynamic mesh generation process with an initial fine mesh, $a^{11}-b^{11}-c^{11}-d^{11}$, centered around the initial plasma density located at x_0 and y_0 , which expands along x and y based on threshold criteria. The coarse mesh is present in the complete computational domain, A-B-C-D.

3.2.5 DMR Computational Complexity

For the DMR, the following quantities remain fixed throughout the simulation: Number of cells per λ on coarse mesh ($N_{\lambda,c}$), refinement factor (r), and physical length of coarse mesh (L_x and L_y). The number of cells in coarse mesh along x ($N_{c,x}$) and y ($N_{c,y}$) direction can be written as $L_x N_{\lambda,c}$ and $L_y N_{\lambda,c}$ respectively. The total cells at $t = 0$ can be expressed as,

$$Total = N_{c,x}N_{c,y} + b_x b_y N_{c,x}N_{c,y}r^2 \quad (3.4)$$

The parameters b_x and b_y represent the initial fraction of fine mesh in the X and Y-direction, respectively. Values of b_x and b_y lie in range $\{0, 1\}$.

Let the computational domain be of size $1\lambda \times 1\lambda$, with $r = 2$ and $N_{\lambda,c} = 256$. Since there are M computations per iteration required for one grid cell in the coarse mesh, then the total computations per iteration for a coarse mesh will be,

$$T_{coarse} = N_{c,x}N_{c,y}M \quad (3.5)$$

By considering the fine mesh as a fraction, b_x and b_y , of the coarse mesh dimension, the total grid cells in the fine mesh is $b_x b_y N_{c,x}N_{c,y}r^2$. Hence, the total computations (T) performed during a single iteration can be expressed as,

$$\begin{aligned} T &= T_{coarse} + T_{fine} \times r \\ &= N_{c,x}N_{c,y}M + Mb_x b_y N_{c,x}N_{c,y}r^3 \\ &= N_{c,x}N_{c,y}M(1 + b_x b_y r^3) \end{aligned} \quad (3.6a)$$

Note : b_x and b_y have been considered constant in (3.4). For a Dynamic mesh, b_x and b_y will vary with time.

Suppose the fraction of fine mesh along the X and Y-direction at any given time t is given by b_x^t and b_y^t respectively. Therefore the area covered by the fine mesh at time t is given by,

$$R(t) = b_x^t b_y^t \quad (3.7)$$

Here, the number of computations will depend on the size of the fine mesh at

time t , and hence the new equation is modeled as,

$$\begin{aligned} T_{dynamic} &= N_{c,x}N_{c,y}M + N_{c,x}N_{c,y}MR(t)r^3 \\ &= N_{c,x}N_{c,y}M(1 + R(t)r^3) \end{aligned} \quad (3.8a)$$

Therefore, as the simulation proceeds in time, the computational cost of fine mesh increases. Thus, for a bigger computational domain, the extent to which the fine mesh can expand increases, and consequently, the performance of DMR saturates to the maximum achievable limit. However, the overall performance of a DMR is much higher than that of an MR with a fixed fine-mesh area.

3.3 DMR Performance Analysis

We have considered two metrics for the performance analysis of the DMR algorithm: the accuracy and the speedup. For performance analysis, we consider the same computational setup as described in Fig. 2.2 (a), where the size of the computational domain is represented by $L_x = c_{kx}\lambda$ and $L_y = c_{ky}\lambda$. We have taken different c_{kx} and c_{ky} for different computational experiments. Initial 2D Gaussian plasma density is $n_e(x, y) = n_0 \exp(-(\{x - x_0\}^2/\sigma_x^2 + \{y - y_0\}^2/\sigma_y^2))$, where x_0 and y_0 is the location of n_0 and, σ_x and σ_y , controls plasma width along x and y , respectively. We consider, $n_0 = 10^{16} \text{ m}^{-3}$, the Incident E-field, $E_0 = 5.5 \text{ MV/m}$ and frequency (f) = 110 GHz. All the computations are carried out on a computer with an Intel Xeon CPU E5-2640 processor with 32 GB RAM.

DMR Accuracy

To evaluate the accuracy of the DMR method, the consistency of shape and size of plasma filaments and plasma front velocity are compared with the uniform fine-mesh implementation. We consider, $\{c_{kx}, c_{ky}\} = \{7.5, 1.5\}$ to investigate the size and shape of filaments. Initial Gaussian peak plasma density (n_0) is located at x_0 and y_0 , which is given by $0.85 L_x$ and $0.5 L_y$ respectively. Figure 3.9 (a,b), represents the distribution of plasma density and the corresponding scattered rms E-field at time $t = 140 \text{ ns}$, obtained using the DMR technique

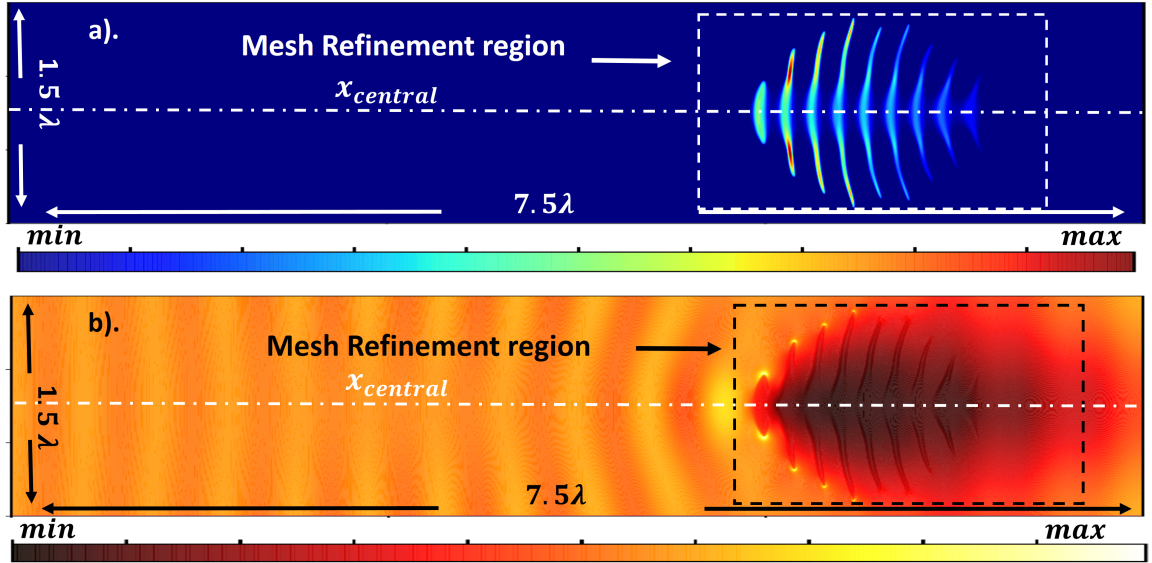


Figure 3.9: The 2D distribution of (a) plasma density (m^{-3}) at time $t = 140$ ns and (b) corresponding rms E-field, for a problem size of $7.5\lambda \times 1.5\lambda$. The maximum density is $8.7 \times 10^{21} \text{ m}^{-3}$ and maximum E-field strength is $6.97 \times 10^6 \text{ V/m}$ as represented on the color scale.

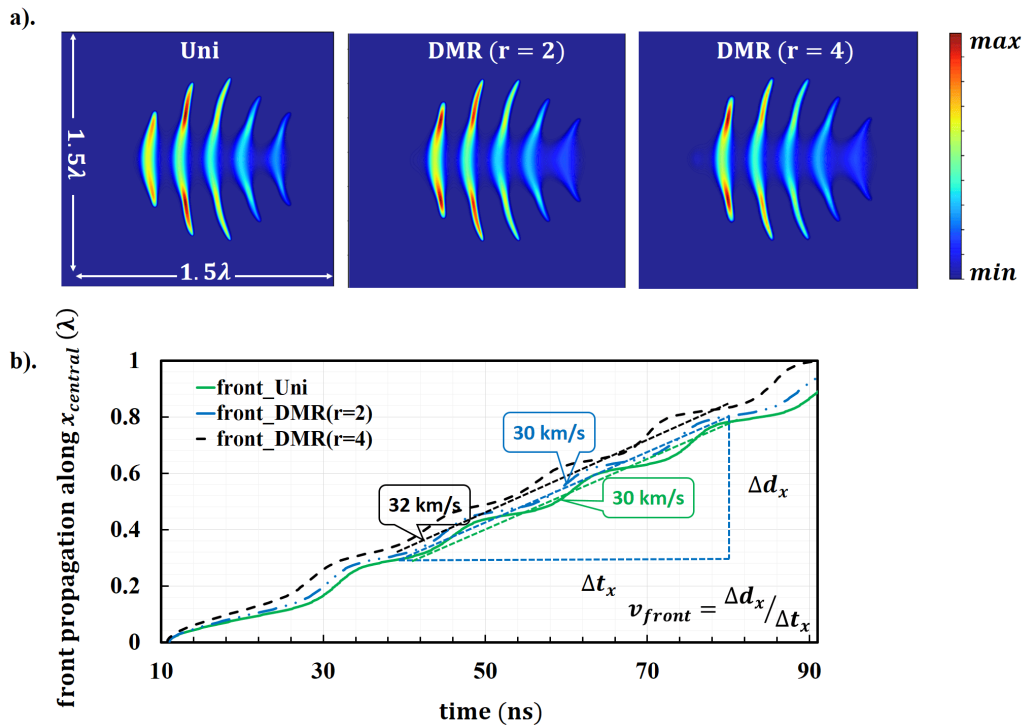


Figure 3.10: (a) The 2D distribution of plasma density (m^{-3}) at time $t = 90$ ns has been obtained using a single uniform mesh (Uni) and DMR ($r=2$ and $r=4$). (b) The comparison between the plasma front propagation using temporal evolution of the plasma density (m^{-3}) along $x_{central}$ for a uniform mesh (Uni) and dynamic mesh (DMR) with different refinement factors (r), here $r = 2, 4$. The color-bar represents plasma density distribution, $max : 7 \times 10^{21} \text{ m}^{-3}$.

with refinement factor ($r = 2$). The observed results are in good agreement with the published results from [2,35,45]. The dynamic mesh could capture the non-uniform gradients in density and scattered E-field by utilizing an optimal fine mesh region shown by dotted lines in Fig. 3.9 (a-b). To validate the plasma front velocity, $\{c_{kx}, c_{ky}\} = \{1.5, 1.5\}$ is considered for the simulation setup. Fig. 3.10, represents the temporal evolution of the plasma density along the central x-axis ($x_{central}$) in the computational domain for a uniform mesh (Uni) and DMR ($r = 2, 4$). The front velocity along $x_{central}$ can be calculated by tracking the propagation of a specific plasma density level at the front (we have used $\approx 1 \times 10^{19} \text{ m}^{-3}$) with time. The calculated plasma front velocity (v_{front}) is $\approx 30 \text{ km/s}$ for both uniform mesh and DMR with $r = 2$. We found that the variation in front velocity and filament length lies within 1 – 2% of the uniform fine mesh case (Uni). We observe that the velocities and lengths are consistent with previously published experimental and simulated results [1,2,9,28,35,45].

3.3.1 Speedup and Efficiency of DMR

For efficiency, subroutine-wise and overall execution time are compared between DMR and uniform fine mesh case (Uni) for a fixed problem size. Further, performance is evaluated for different problem sizes (P1, P2, and P3) to check the scalability of the proposed approach. From Fig. 3.11 (a), it can be observed that the time required to execute the three constituent subroutines the E-field (E), H-field (H), and plasma density (Den) is higher for the uniform fine mesh (Uni) in comparison to dynamic mesh refinement (DMR) for a fixed problem size (P1), P1: $1.5\lambda \times 1.5\lambda$. The highest execution time is taken by E, followed by H and Den. DMR significantly reduces the overall execution time as compared to Uni, as observed in Fig. 3.11 (b).

Figure 3.11 (a-b) shows that the DMR reduces the execution time compared to the standard uniform mesh technique by a dynamic factor. This factor decreases as the simulation proceeds, and the fine mesh expands. Figure 3.12 (a) provides a better understanding of the contribution of DMR to the overall speedup and scalability for different problem sizes. For a fixed problem size, let P1: $1.5\lambda \times 1.5\lambda$, the initial speedup is of the order of 8 and drops to around 2 as the simulation proceeds. The result agrees with Fig. 3.11(b).

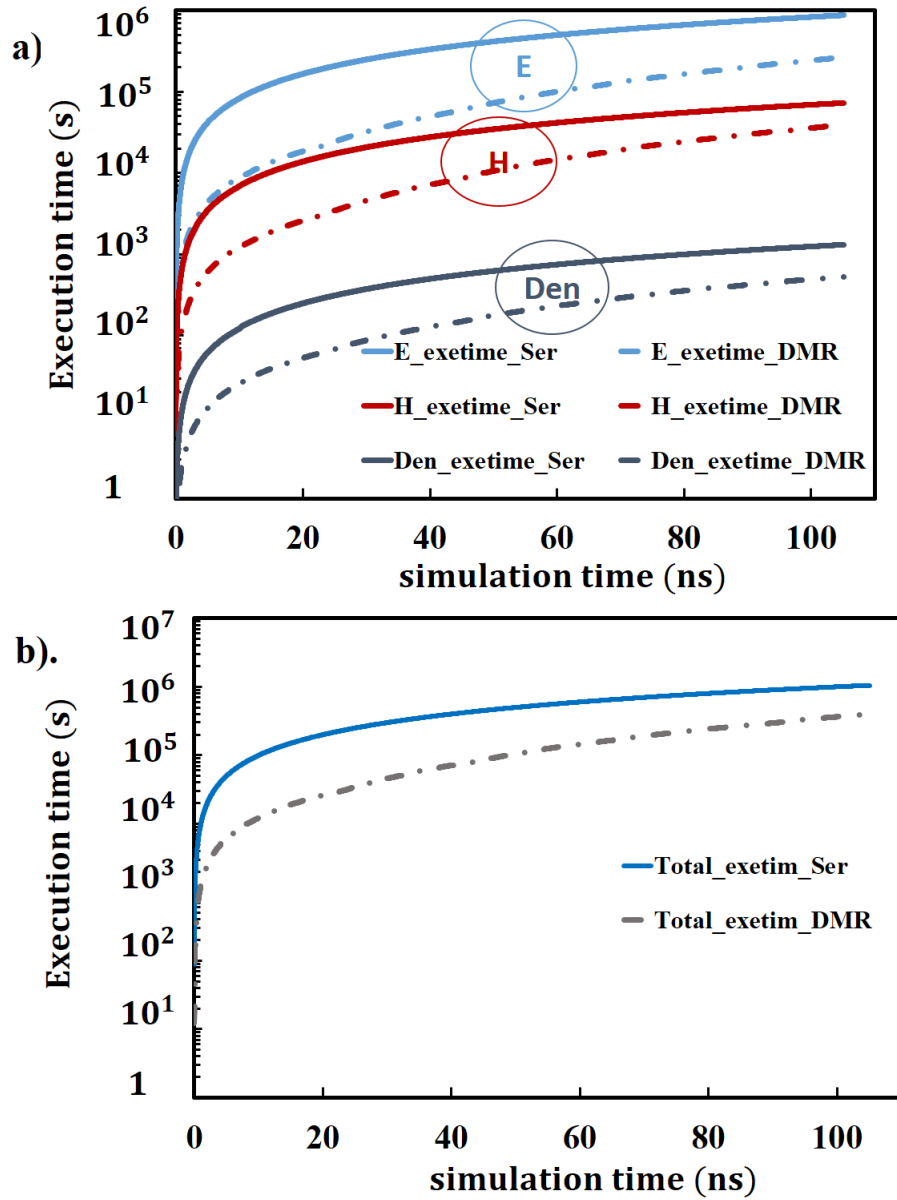


Figure 3.11: For different simulation times in seconds using different techniques, Uni and DMR, the plots of (a) the subroutine-wise execution time to simulate P1, and (b) the total execution time taken to simulate P1.

For different problem sizes P2: $3.5\lambda \times 1.5\lambda$ and P3: $7.5\lambda \times 1.5\lambda$, the speedup transits from high to low and performs better as the problem size increases. For different problem sizes P1 to P3, the overall speedup $\approx 5, 7$ and 8 , respectively. The higher performance for bigger problem sizes is due to the small value of $R(t)$ initially, which grows gradually as the plasma pattern spreads. For uniform fine mesh (Uni) implementation, the total cells $\approx 10^5 - 10^6$ and total computations per iteration are always fixed (Fig. 3.12 (b)). For DMR, the total number of cells and computations grows as the refinement region grows with simulation time, $R(t)$. For uniform mesh, the total computational cost

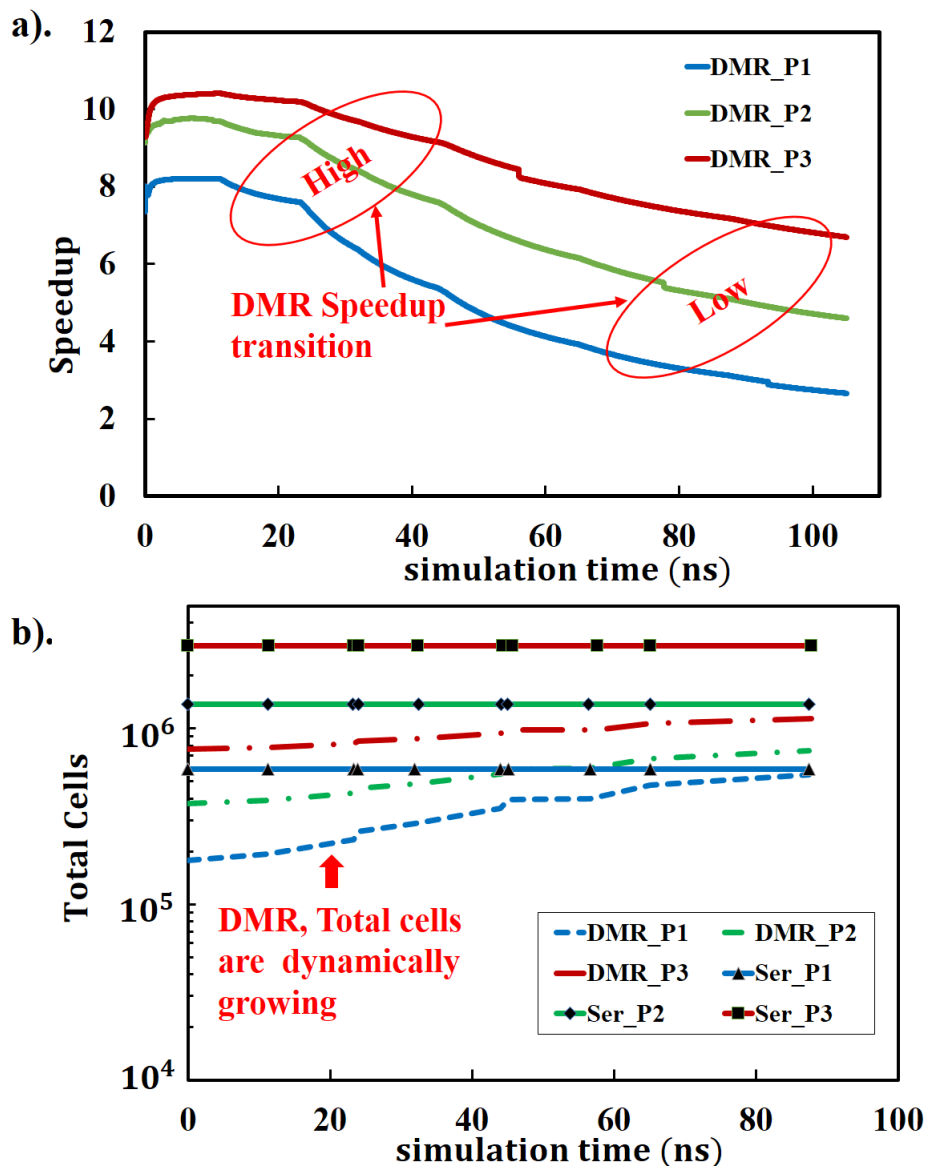


Figure 3.12: For different simulation times in seconds using different techniques, Uni and DMR, the plots of (a) the overall speedup and (b) the growth of total cells with time for different problem sizes, P1 to P3.

is proportional to $N_f I_f$ (total cells x total iterations). Whereas for DMR, the

total computational cost is proportional to the sum of coarse and fine mesh contributions. Coarse mesh has a fixed number of cells (N_f/r^2), and updates are less frequent (by a factor of r) compared to fine mesh. Therefore total cost for coarse mesh is $(1/r^3)N_f I_f$ (Total coarse cells \times Coarse Iterations). For fine mesh, the computational cost is dynamic and is proportional to $R(t) N_f I_f$ (Total fine cells \times Fine Iterations). Therefore, for DMR, we obtain that computational cost is proportional to $N_f I_f \left(1/r^3 + R(t)\right)$, and primarily depends on refinement factor and refinement region. The higher the refinement factor and the smaller the refinement region, the better the speedup. Due to the smaller number of cells in the case of DMR (Fig. 3.12 (b)), the size of the data structure is initially small, and the memory access performance is better compared to uniform fine mesh. Initially, the refinement region is very small, and the fine mesh data structure easily fits into cache memory, leading to higher cache hits. We observe a speedup better than the theoretical speedup of r^3 (Fig. 3.12 (a)).

3.4 Conclusions

This chapter proposes a dynamic mesh refinement (DMR) technique to solve the computationally challenging Maxwell-plasma fluid model for simulating HPM breakdown-induced plasma pattern formation and associated dynamics. The DMR technique leads to generating two meshes: a coarse mesh, which is present throughout the computational domain, and a fine mesh, which evolves with time in a self-aware fashion depending on plasma and electric field gradients. The implementation of the DMR technique has been described in detail. Further, the technique has been evaluated regarding accuracy and speedup by applying it to simulate and reproduce the experimental observations under similar conditions. The technique could accurately reproduce the complex plasma dynamics and structures for different problem sizes and refinement factors. For a refinement factor of 2, we obtain an overall speedup of 5 to 8 times for different case studies. The bigger problem sizes, involving the physical duration of $t > 100$ ns, which typically take months using a uniform fine mesh, can be handled in a few days using the proposed DMR technique. The proposed DMR-based technique will be beneficial for

investigating longer time-scale phenomena in HPM breakdown (in the order of micro to milliseconds), such as gas heating, which is sparsely reported in the existing literature. The DMR technique for self-aware mesh generation can be applied for any fluid-based plasma simulation (primarily involving spatio-temporal evolution of plasma topology) where fine resolution (using fine mesh) is required for accurate results. DMR-aided simulations, at a much lower computational cost, will also help to efficiently investigate and better understand the formation of different plasma structures (involving sharp gradients) observed in experiments.

CHAPTER 4

DMR assisted computational investigation of HPM switching and protection

4.1 Introduction

The progress in high-power microwave (HPM) technology has enabled the building of HPM sources that can handle gigawatt (GW) power over high frequency. Accordingly, innovative applications ranging from aerospace, combustion, HPM propagation experiments, and propulsions [5, 70, 93, 116] are feasible. With the availability of better sources, high-strength HPM pulses are realizable and pose threats to damaging communication devices such as low-noise amplifiers (LNAs), sensors, radars, power supplies, and communication receivers [117]. For wireless communication systems having the same transmitter and receiver antenna, it is important to isolate transmitter leakage into the receiver [118]. Power limiters are required to protect vulnerable electronic components from powerful microwaves. The proposed technology uses intentional HPM breakdown-inducing plasma, which proves to be beneficial for protecting electronic components behind slots [71] and designing microwave transmit-receive (TR) switches for receiver protection in wireless communication. Other application includes the design of a tunable miniaturized high power high frequency (HF) switch for the GHz band [44, 72]. The induced plasma in such applications must form within the desired time scale with sufficient density to perturb the microwave propagation [44]. The plasma generation time delays if the seeding electrons are unavailable and the exponentiation time (growth of initial plasma into

cut-off density) is longer [44]. The local enhancement of the breakdown field and keep-alive contact currents controls the plasma generation time [44]. The keep-alive contacts are prone to wearing and limit the microwave (MW) breakdown. Alternatively, creating an intentional or unintentional local region of intense ionization can modify the HPM breakdown threshold. The modified HPM breakdown threshold can overcome the requirement of a very high MW E-field and availability of initial seed electrons to initiate a faster HPM breakdown.

As discussed in [119], microwave E-field below the breakdown threshold at room temperature can initiate a local breakdown through local gas heating. Gas heating can be intentional or unintentional under the presence of different materials, like materials of low conductivity inside the microwave system. The presence of dirt on the device surface, a thin film of oil, and even debris of different forms such as plastic, rubber, and dust [119] can locally enhance the MW electric field, resulting in a lower breakdown threshold. In the presence of low-conductivity materials inside the MW system, the surrounding gas heating occurs due to low thermal losses from the material surface. The localized HPM discharges are fast MW energy deposition [116], involving microwave-plasma interaction, plasma formation, and energy exchanges between the plasma and the microwave and later between the plasma and the background gas.

We incorporate an ideal gas-heating solver with the widely used fluid-based model to numerically investigate the effect of local gas heating on the HPM breakdown-induced plasma formation in air and its application in the context of switching and power limiter [36,45]. As discussed in previous chapters, the fluid model uses two solvers, EM, and plasma solver, which supports local electric field approximation (LEFA) over a wide range of pressure (from low to high) [44] through a proper scaling in the effective field and the pressure. The gas (air) heating model refers to the work of [22,116]. The multi-scale and multi-physics nature of the HPM breakdown problem makes it challenging to incorporate the gas-heat solver with the EM and Plasma solvers. Proper care must be taken to couple the various physics associated with the breakdown process in the presence of gas-heating through proper synchronization in space and time stepping to obtain a stable numerical solution.

Organization of this chapter

This chapter discusses HPM-induced breakdown applications for switching and protection, which is divided into two parts. The first part which begins in section 4.2, we discuss two objectives: exploring breakdown conditions to reduce plasma formation time and studying EM plasma interactions using a realistic plasma profile. The plasma profile considers the effective diffusion coefficient (D_{eff}) to model the charge transport leading to the streamer formation. The first part does not consider the effect of gas-heating in the HPM breakdown model. The second part begins in Section 4.3; we propose a simplistic gas-heating model and compare the effect of gas heating on HPM breakdown initiation and plasma generation time for HPM switching/protection applications.

4.2 HPM switching and protection

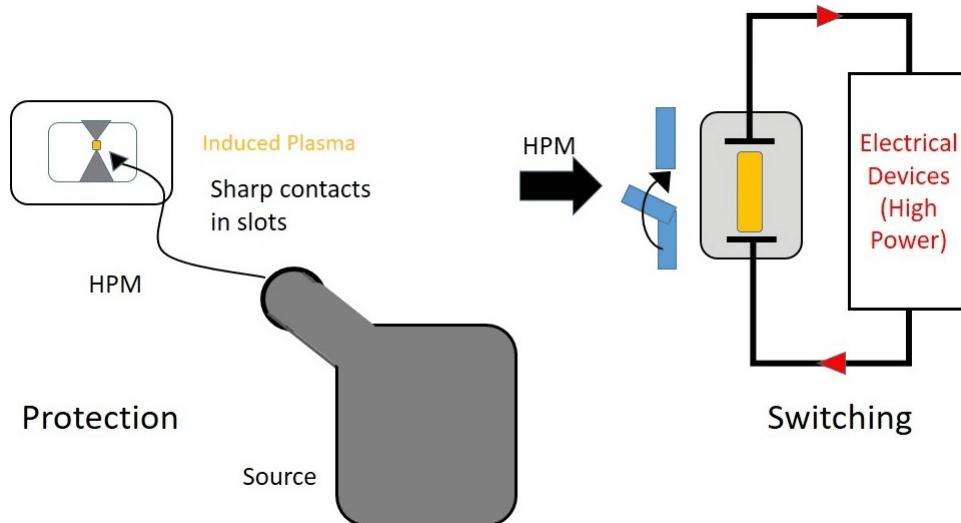


Figure 4.1: Schematic representation of the HPM breakdown application in protection and switching.

High-power microwave (HPM) breakdown benefits HPM shielding and designing miniaturized tunable high-power electrical switches. Previous studies show that HPM breakdown occurs between sharp contacts in a slot-gap, enhancing the microwave E-field and leading to plasma formation [11, 70, 71]. Keep-alive contact currents can expedite breakdown initiation, which is important for RADAR applications [11, 70]. In Figure 4.1, we

illustrate HPM limiter action and switching. Sharp contacts induce plasma in the limiter, isolating HPM from low-power electronics. Whereas, in switching, the high conductivity of plasma acts as a switch for wide-band high-power transmission. We have designed a 2-D computational setup based on Anderson et al.'s [11] experiments to investigate the effect of seed electrons (initial electrons to initiate breakdown) and E-field strength on breakdown time and plasma generation. Numerical investigations will help determine the parameters for required plasma generation within desirable time-scales. Our first objective is to understand the effect of important parameters on plasma formation time without considering gas heating. We simulate HPM breakdown with Gaussian-distributed plasma exposed to a continuous plane wave for $1 \mu\text{s}$. The initial Gaussian plasmoid elongates into a streamer during the breakdown and plasma formation process. Streamer formation and interaction with microwaves will help to optimize the design of HPM switches and limiters. We compare limiter action based on analytically calculated cut-off density for frequencies 1 to 200 GHz frequencies. For switching, we analyze plasma permittivity and conductivity variations. Our results and discussions are divided into two sections. The first section discusses breakdown initiation and plasma generation. The second section discusses EM-plasma interaction in HPM switching and protection applications. This study uses air at a pressure of 10 torr and EM wave with frequency 10 GHz, similar to Anderson et al.'s work [11].

4.2.1 Breakdown process initiation and plasma generation

A localized breakdown in the center of a rectangular domain is modeled using two EM waves ($E_0 = 1 \times 10^5 \text{ V/m}$) of opposite propagation vectors, which interfere at the center of the domain to generate a standing wave. The simulation setup is shown in Fig. 4.2 (a). The breakdown is initiated with an initial density of $n_0 = 10^{16} \text{ m}^{-3}$. We use the DMR technique, as discussed in the previous chapter, to accelerate the simulation of the HPM breakdown. A single level of mesh refinement with a grid refinement factor ($r = 2$) of two and overlapped coarse (c) and fine (f) mesh has been used here [8]. The grid sizes for coarse and fine mesh and associated time steps follow a similar

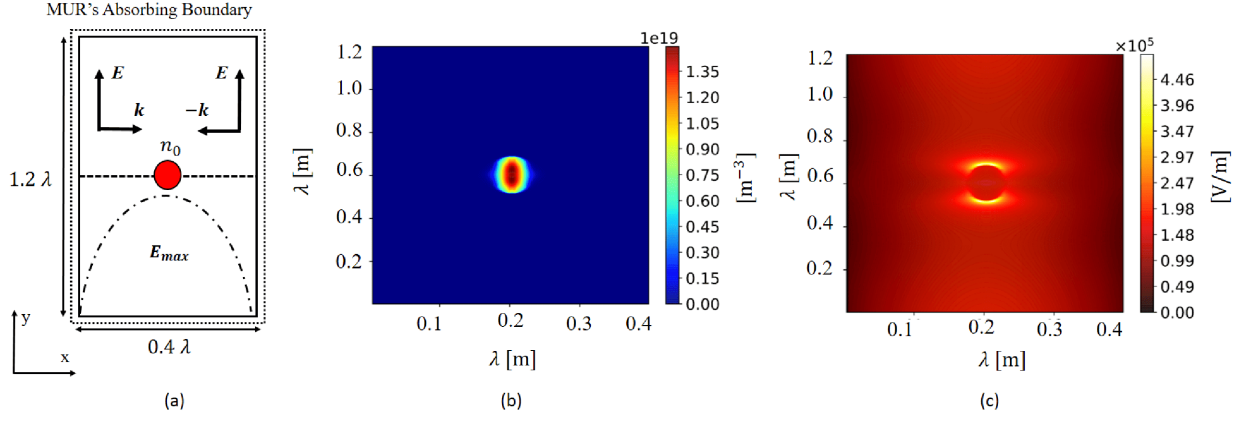


Figure 4.2: (a) Schematic of computational domain with E_{max} and n_0 . 2D profile (b). n_e and (c) E_{rms} at 60 ns.

relation as discussed in the previous chapter. The breakdown region has a fine grid size of $\Delta s_f = \Delta s_c / r$ and a time step of $\Delta t_f = \Delta t_c / r$, where $r = 2$. While, the coarse grid has a grid size of $\Delta s_c = 1.17 \times 10^{-4}$ m and a time step of $\Delta t_c = 1.95 \times 10^{-13}$ s [8].

The 2D plasma density and rms E-field distribution at 60 ns are shown in

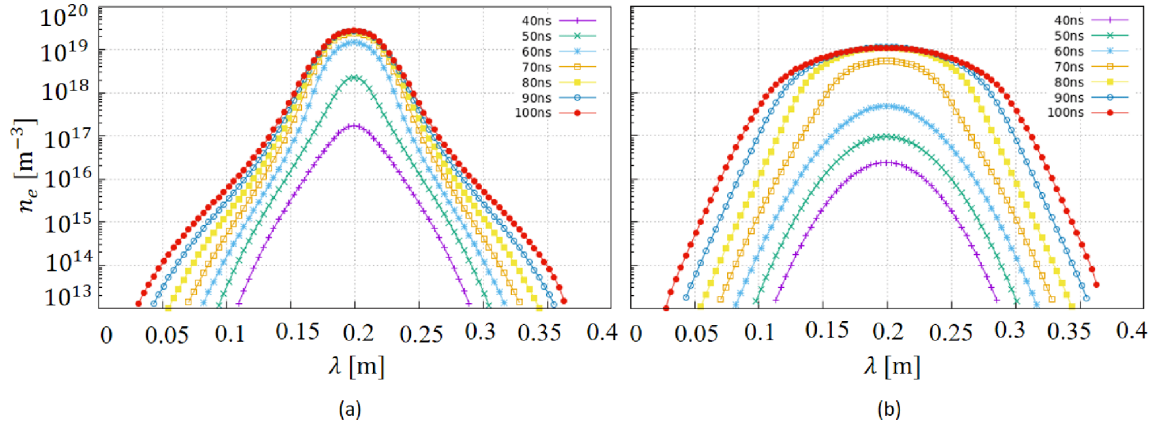


Figure 4.3: Spatial distribution of 1D plasma along x-axis passing through the center of the computation domain for different time instants (40 to 100 ns) with (a) effective diffusion (D_{eff}) coefficient, (b) ambipolar diffusion (D_a) coefficient respectively.

Fig. 4.2 (b-c). Plasma has a significantly high density in the center where the initial seed electrons have been considered in the simulation. Figure 4.3 shows the growth of the plasma density along the x-axis passing through the center of the computation domain (dashed line in Fig. 4.2 (a)) at different times. We have performed two different simulations with the same initial conditions.

However, two different diffusion coefficients (ambipolar and effective) have been used to study the importance of the right choice of diffusion coefficient in the fluid model. Fig. 4.3 (a) shows the results with D_{eff} and Fig. 4.3 (b) with D_a . It is important to note that the plasma width (spread) is different at different times, with center density (highest density) growing to critical density ($n_{critical}$ order of 10^{18} m^{-3}) at around 50 ns. Further, it grows and saturates for $t \geq 70$ ns. The choice of the correct diffusion coefficient is important as it controls the transition from bulk to the plasma edges (tail of profile) where the density drops (plasma quasi-neutrality breaks), for both Fig. 4.3 (a), Fig. 4.3 (b).

Figure 4.4, illustrates the cut-off time dependence on E-field and n_0 . Lower

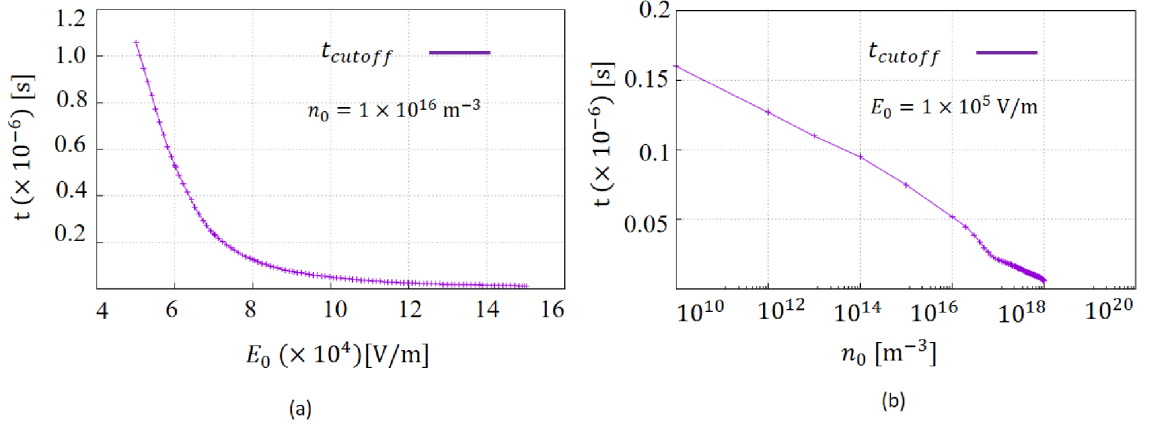


Figure 4.4: Plot of t_{cutoff} distribution for (a) varying E_0 at fixed n_0 and (b) varying n_0 at fixed E_0 .

E-field results in significantly higher cut-off time due to nonlinear ionization, and the choice of n_0 also affects this time. Our study shows that proper selection of n_0 and E_0 in real-life applications can ensure the required plasma formation time (t_b) is within 0.01 to 0.04 μs . Once the desired plasma is formed within the required time limit, it is important to analyze how effectively this plasma can be used for switching and protection applications.

4.2.2 EM-plasma interaction assisted HPM switching/protection

Figure 4.5 displays the evolving plasma density response for frequencies ranging from 1 to 200 GHz. The obtained plasma selectively permits certain frequencies to propagate based on the cut-off density (n_{cutoff}) or blocks the

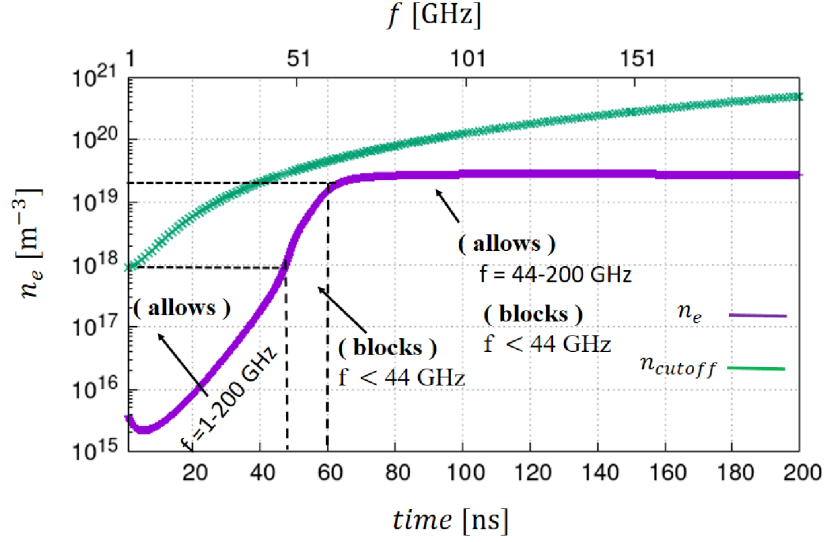


Figure 4.5: Behaviour of 1D plasma density profile (n_e) obtained from 2D simulations with cut-off density (n_{cutoff}), either blocking or allowing frequency range (1 to 200 GHz).

entire frequency range. Figure 4.5 shows that frequencies are allowed or blocked based on whether the plasma density profile (n_e) is below or above the cutoff density (n_{cutoff}), respectively. Below n_{cutoff} , all frequencies are allowed. At 45 ns, $n_e = 10^{18} \text{ m}^{-3}$, corresponding to n_{cutoff} of 1 GHz, which blocks frequencies from 1 to below 44 GHz. Above 60 ns, the density saturates to $\approx 2.8 \times 10^{19} \text{ m}^{-3}$, and blocks all frequencies below 44 GHz but allows those above it. The reduction in transmitted E-field can be attributed to complex permittivity and conductivity changes, affecting the refractive index, which shields the incoming microwave E-field into the plasma. The E-field reduction is significant at lower frequencies based on the dispersion relation discussed in Chapter 1.

Next, we numerically investigate the variation in plasma electrical parameters, ϵ_r and σ , with changes in plasma density (n_e). In Fig. 4.6 (a) and (b), we compared these parameters at two time instants, 40 and 70 ns. At 70 ns, the value of ϵ_r drops 12-fold from its value at 40 ns, while σ increases by 15 times. By manipulating ϵ_r and σ via n_e , we can design a wide-band re-configurable HPM switch. Furthermore, investigating the effects of gas-heating, relevant at time-scales > 100 ns, on breakdown initiation and plasma profile generation is crucial.

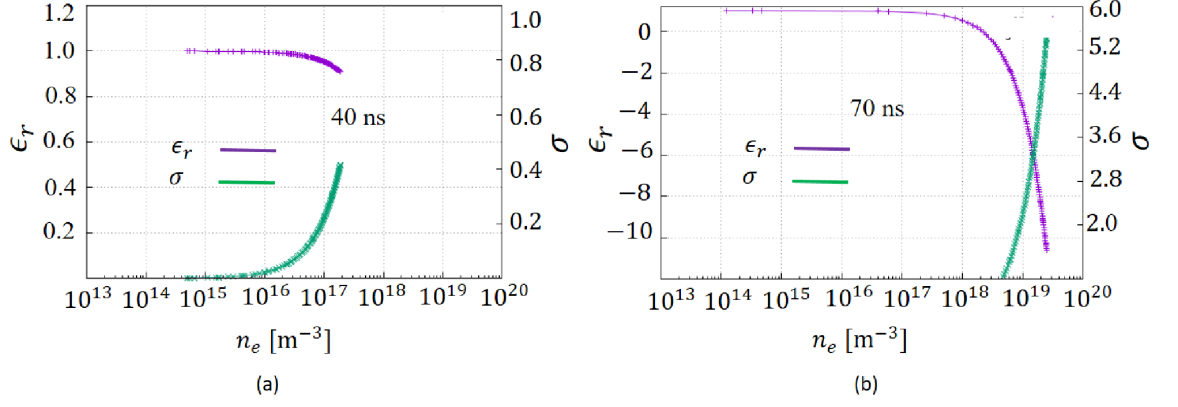


Figure 4.6: Plot of the relative permittivity (ϵ_r) and conductivity (σ) correspond to 1D plasma density (n_e) profile at two-time instants 40 ns and 70 ns. σ in (S/m). x-axis: plasma density profile

4.3 Local gas-heating during HPM breakdown

During HPM breakdown initiation, high-energy electrons can transfer their energy to background gas molecules (neutrals) through different modes. Those modes include the collisional effect ($S_{coll} = 3/2k_B T_e \delta v_m n_e$), where (δ) is the electron-to-heavy species (ions and neutrals) ratio mass ratio, or Joule's heating ($S_{joule} = \eta e n_e \mu_e E_{eff}^2$), which involves transferring a fraction ($\eta = 0.3$) of absorbed electrical energy to excite the gas species and quickly release it into the gas. Additionally, there is associated heat loss due to thermal diffusion ($S_{thermal} = \nabla \cdot (\kappa \nabla T_g)$) in air, where κ is the thermal conductivity of air in $W m^{-1} K^{-1}$. To accurately model gas heating, it is important to consider the coupling between the electrons and neutral transport using 2D inviscid Euler equations. However, in our gas heating model for air, we concentrate on mechanisms that increase only the gas temperature (T_g), and, calculate gas density (N_g) analytically using obtained T_g at each grid point. Mathematically, the gas heating at constant pressure (p_0) in $J m^{-3} s^{-1}$ [22,116] can be expressed,

$$N_g k_B c_{p,m} \frac{\partial T_g}{\partial t} = S_{coll} + S_{joule} + S_{thermal} \quad (4.1a)$$

$$p = N_g k_B T_g \quad (4.1b)$$

$$N_g = N_0 \left(\frac{T_0}{T_g} \right) \quad (4.1c)$$

where, $c_{p,m} = C_p / \text{moles}$ is molar specific heat in $\text{J mol}^{-1} \text{K}^{-1}$. The molar mass of air used $28.966 \text{ g mol}^{-1}$, $C_p = 1.005 \text{ J kg}^{-1} \text{K}^{-1}$ at 300 K. $1 \text{ mole} = N_g / N_A$, N_A is $6.02214076 \times 10^{23} \text{ mol}^{-1}$. For air $c_{p,m} \sim 29.11 \text{ J mol}^{-1} \text{K}^{-1}$, $c_{p,m} \sim 3.5 R$, where R is the universal gas constant, $8.314 \text{ J mol}^{-1} \text{K}^{-1}$. k_B is $1.380649 \times 10^{-23} \text{ J K}^{-1}$, $k_B = R / N_A$. The Gas-heating solver uses a finite difference scheme to iteratively solve for T_g and use it to obtain N_g as given by Eq. 4.2, which couples with the plasma solver through ν_{eff} and D_{eff} terms. These terms depend on the updated values of E_{eff}/p , due to changes in local gas density ($p = (N_g / N_0) p_0$, $p_0 = 70 \text{ torr}$ is fixed), and ν_m , which gets updated and depends on N_g .

$$\begin{aligned}
T_{g(k,l)}^{n+1} = T_{g(k,l)}^n + \left(\frac{\Delta t_g}{N_{g(k,l)} k_B c_{p,m}} \right) \times \left\{ \frac{3}{2} k_B T_e \delta \nu_{m(k,l)} n_{e(k,l)} \right. \\
+ \left(\frac{\kappa}{\Delta_g^2} \right) \times [T_{g(k+1,l)}^n + T_{g(k-1,l)}^n + T_{g(k,l+1)}^n] \\
\left. + T_{g(k,l-1)}^n - 4T_{g(k,l)}^n \right] + [\eta e n_{e(k,l)} \mu_e E_{\text{eff}}^2] \} \quad (4.2)
\end{aligned}$$

2-D simulations are carried out to provide a one-to-one map between variation in plasma density (n_e) distribution with corresponding variation in gas (neutral atoms and molecules) density (N_g) and gas temperature (T_g). Further, 1D analysis validates the effect of a reduced breakdown threshold on the rate of ionization and diffusion, which is a function of E_{eff}/N_g , with gas heating. The detailed analyses help to determine the role of gas heating on the plasma generation time for applications in HPM limiters and switching. The simulation results and discussions are broadly divided into two sub-sections, as discussed below.

4.3.1 HPM plasma generation with and without gas heating

The simulation considers local breakdown-induced plasma generation under over-critical microwave E-field ($E > \text{breakdown field}$) [8, 36, 45] to replicate plasma generation in HPM limiters and switches. Plasma structures elongate parallel to the direction of the microwave E-field, called streamers. Two linear polarized EM waves with opposite propagation vectors (k) interfere to

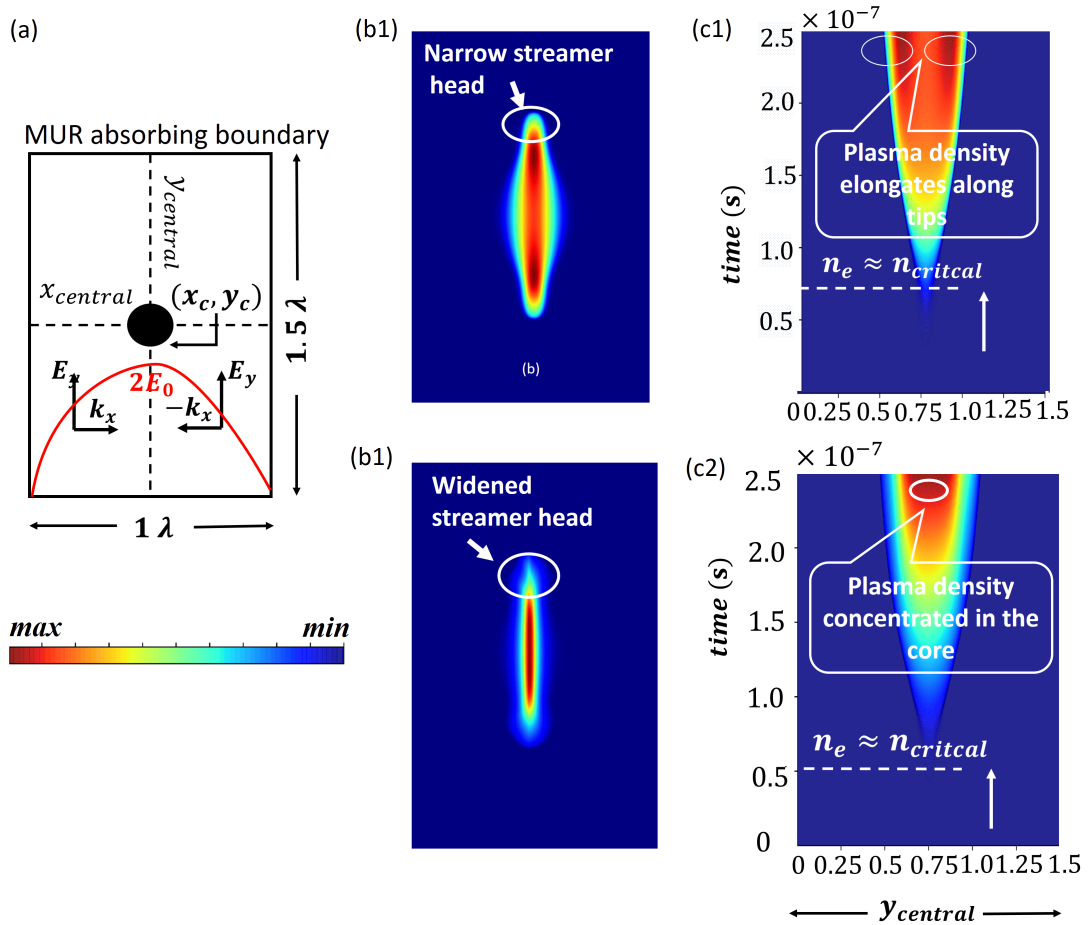


Figure 4.7: (a) Computational domain schematic with enhanced MW E-field ($2E_0$, $E_0 = 2.72$ kV/cm) and initial seed electrons. 2D plasma profile (streamer) at 250 ns (b1) without (b2) with gas heating and spatio-temporal density evolution along the streamer axis, indicating time to reach $n_{critical}$ and shape changes at $t = 2.5 \times 10^{-7}$ s, (c1) Without and (c2) with gas heating.

generate a standing wave with amplitude $2E_0$ and rms intensity greater than 2 kV/cm [4]. The breakdown initiates in a 1.0λ by 1.5λ rectangular domain as shown in Fig. 4.7 (a), where plasma remains confined within a narrow spatial location. The simulation uses air at a pressure of 70 torr and a 10 GHz EM wave with an initial density, $n_0 = 10^{16} \text{ m}^{-3}$. The model uses different time scales for the EM and Plasma solvers, with $\Delta t_{EM} = 1.95 \times 10^{-13}$ s and $\Delta t_d = 0.1$ ns. Gas heating couples every ten periods of the MW E-field, with a gas solver update time of $\Delta t_g = 1$ ns. To observe the same phenomenon at a lower time scale of 150 – 250 ns, an acceleration factor (Accel_fac) of 20 is chosen [120].

The 2D plasma density distribution inside the streamer at 250 ns for without and with gas heating is shown in Fig. 4.7 (b1) and 4.7 (b2), respectively, while Fig. 4.7 (c1) and Fig. 4.7 (c2) show the spatio-temporal evolution of n_e along the streamer axis ($y_{central}$) without and with gas heating, respectively.

As $t \geq 2.0 \times 10^{-7}$ s, the shift in n_e from the core towards the streamer tips is significant without gas heating, while with gas heating, the shift is minor and mainly concentrated surrounding the core. The high plasma density exists in the bulk of the plasma, and the next set of simulations discusses the impact of gas heating on the overall streamer formation process.

Figure 4.8(a-d) shows 2-D plots of n_e , T_g , and N_g for a streamer at $t = 250$ ns,

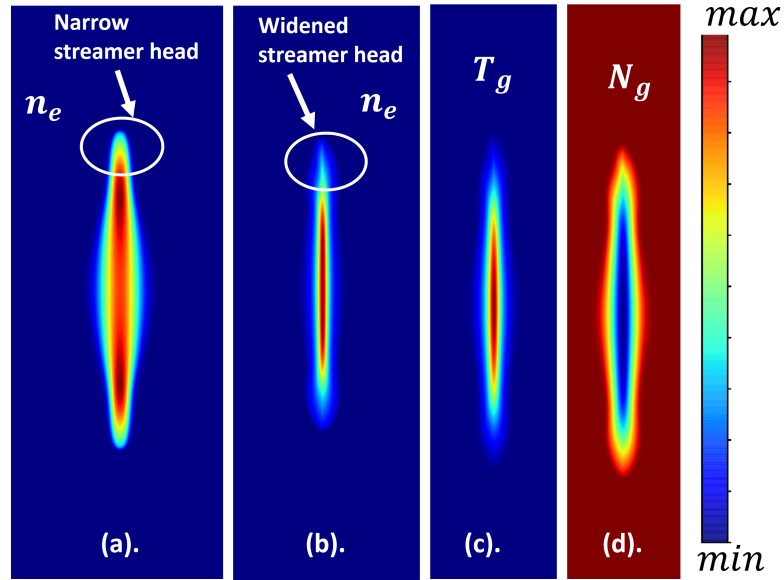


Figure 4.8: 2-D Plots representing the effect of (a) without and (b) with gas-heating on n_e , as well as the effect of gas heating on (c) N_g and (d) T_g , for a given time instant, $t = 250$ ns. For without gas heating, the max n_e values is $5.25 \times 10^{19} \text{ m}^{-3}$, with gas heating, max n_e value is $1.53 \times 10^{20} \text{ m}^{-3}$. For with gas heating, the max value is fixed, $N_0 = 2.25 \times 10^{24}$ at $p = 70$ torr, and min values is $0.53 \times 10^{24} \text{ m}^{-3}$. For with gas heating, max T_g value is 1266.5 K and min is $T_0 = 300$ K. For without gas heating $N_g = N_0$ and $T_g = T_0$.

with and without gas heating. With gas heating, the local temperature T_g at the core is higher than at the edges, and N_g has a lower value in the core. The reduction in N_g causes stronger ionization of the plasma bulk and changes the shape of the streamer pattern. The streamer head becomes wider than without gas-heating, and the plasma concentration at the tips decreases, lowering the scattered MW E-field and subsequent streamer growth. Gas heating can play an important role in deciding the streamer geometry compared to the polarization effect when there is no gas heating [36].

A 1D analysis for distribution of n_e , v_{eff} , D_{eff} and reduced E-field (E_{eff}/N_g) for different times along the streamer axis, y_{central} has been performed. To better understand the effect of gas heating on the ionization and diffusion mechanism compared to without gas heating. From Fig. 4.9 (a,e), under no gas heating,

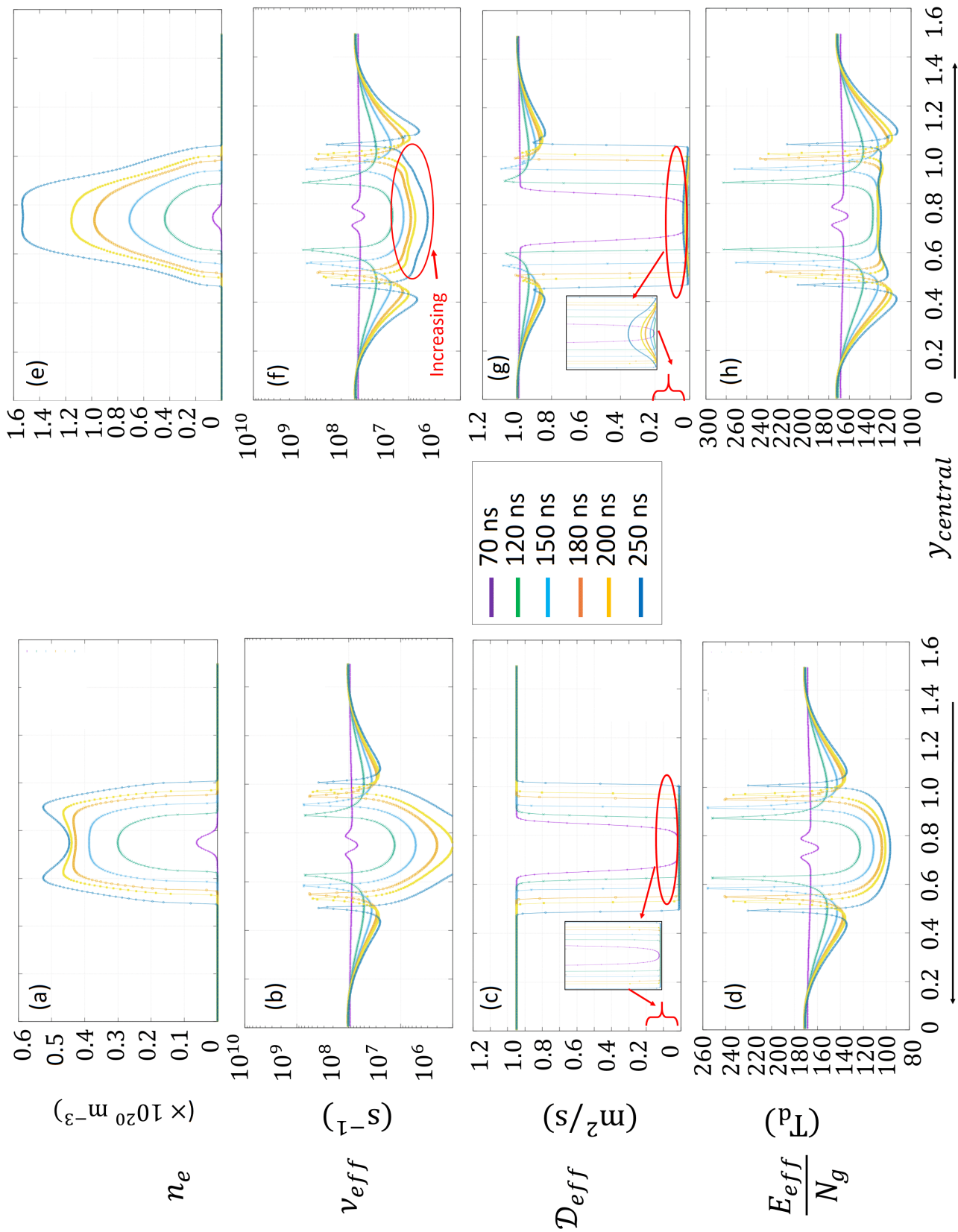


Figure 4.9: The 1D distribution of n_e , v_{eff} , D_{eff} and E_{eff}/N_g for (a-d) without and (e-h) with gas heating, respectively, for five different time instants along the vertical streamer axis, $y_{central}$ line.

the n_e in bulk is ~ 3 times less than n_e with gas heating for $t = 250$ ns. Figure 4.9 (a) shows the plasma density stretches towards tips as opposed to higher concentration in bulk; refer Fig. 4.9 (e). In Fig. 4.9 (b) without gas heating, distribution of ν_{eff} lowers in the plasma bulk region ($< 10^6 \text{ s}^{-1}$) due to higher N_g as compared to Fig. 4.9 (f) with gas heating. The higher N_g may lead to higher attachment losses (negative ions formation when electron attaches with gases such as oxygen in the air) [119]. As a result, the n_e saturates without gas heating, whereas it increases in bulk ($\sim 10^7$) with gas heating, refer Fig. 4.9 (a,e). Whereas, at the tip of the streamer, the ν_{eff} goes down for Fig. 4.9 (f) due to the broadening of streamer head and remains higher for Fig. 4.9 (b). Figure 4.9 (c) shows the D_{eff} flattens in the streamer bulk (inset) without gas heating, as D_{eff} follows inverse relation with N_g . Whereas, Fig. 4.9 (g) with gas heating the D_{eff} increases (inset) as N_g reduces. Therefore, the plasma diffuses from bulk along y_{central} . As a result, the streamer stretches. The higher ionization at the core sustains the bulk plasma density and widens the streamer head. In Fig. 4.9 (d) without gas heating the E_{eff}/N_g at streamer tips, rises (260 Td) at $t = 120$ ns and gradually modulates (lowers) with streamer elongation [45], same follows even in Fig. 4.9 (h) with gas heating. On comparing Fig. 4.9 (d) and 4.9 (h), the E_{eff}/N_g at $t = 120$ ns is higher (280 Td) under gas heating due to high polar fields at tips and higher streamer density. However, the E_{eff}/N_g value remains within (~ 130 Td) with gas heating, whereas without heating, it reaches a lower value (100 Td). The variation in E_{eff}/N_g suggests that the streamer growth depends more on bulk ionization than on polar E-fields at streamer tips when gas heating is present, according to the 1D analysis.

4.3.2 Effect of microwave-induced local gas heating on HPM switching and protection

We have observed that gas heating can control the HPM-induced plasma streamer generation process. Both HPM switching and protection require a faster generation of high-density breakdown-induced collisional plasma (where, $n_e = n_{\text{cutoff}}$, decides the switching and HPM limiter action) is required as shown in Fig. 4.5. The breakdown plasma can transmit, reflect, or absorb high-power microwaves depending on the incident microwave frequency due

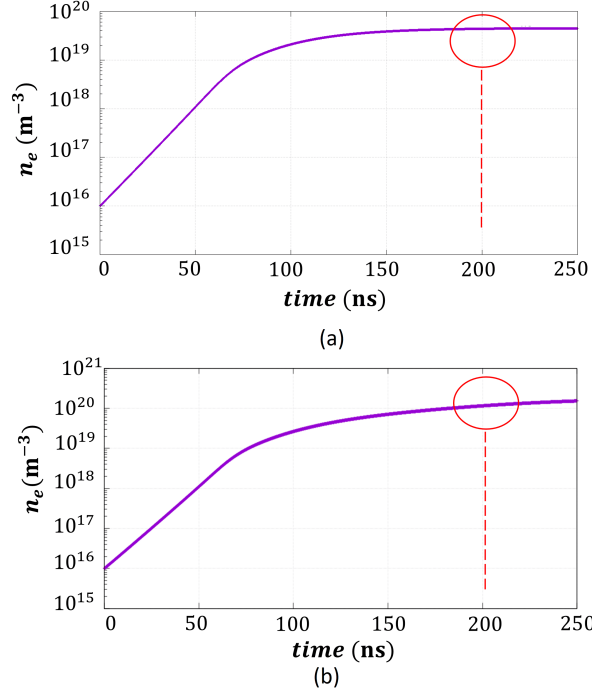


Figure 4.10: The effect of (a) without and (b) with gas heating, on the growth of the peak plasma density (1D) at the center of streamer core (at (x_c, y_c)).

to the dispersive nature of plasma. The dispersive nature controls tunable plasma dielectric properties that range from insulator to conductor, as shown in Fig. 4.6. Through numerical experiments, we studied the effect of with and without gas heating on the bulk plasma density distribution and its effect on the limiter action for different input microwave frequencies and finally on the t_{cutoff} , where the plasma shields the incoming microwave from penetrating the plasma profile.

Figure 4.10 (a) and 4.10 (b) shows at the streamer center (x_c, y_c) , the growth of peak plasma density with and without gas heating, respectively. The peak plasma density, for without gas heating saturates ($\sim 0.5 \times 10^{20} \text{ m}^{-3}$) at $t = 200$ ns whereas, with gas heating it reaches $\sim 1 \times 10^{20} \text{ m}^{-3}$ at $t = 200$ ns and saturates at higher density value at $t = 250$ ns. In Fig. 4.11, we observe the importance of higher bulk plasma density in HPM limiter action. Figure 4.11 (a) and 4.11 (b) shows the plasma density profile (along $x_{central}$ chosen corresponds to high peak density for without and with gas heating at $t = 200$ ns (refer Fig. 4.10 (a) and 4.10 (b)). From Fig. 4.11 (a) and 4.11 (b), the peak density of the chosen plasma profile has minimum skin depth for 1 GHz (the normalized rms E-field ratio ($\ll 1$)) and increases as frequency > 1 GHz. The skin depth is highest (wave transmits unhindered,

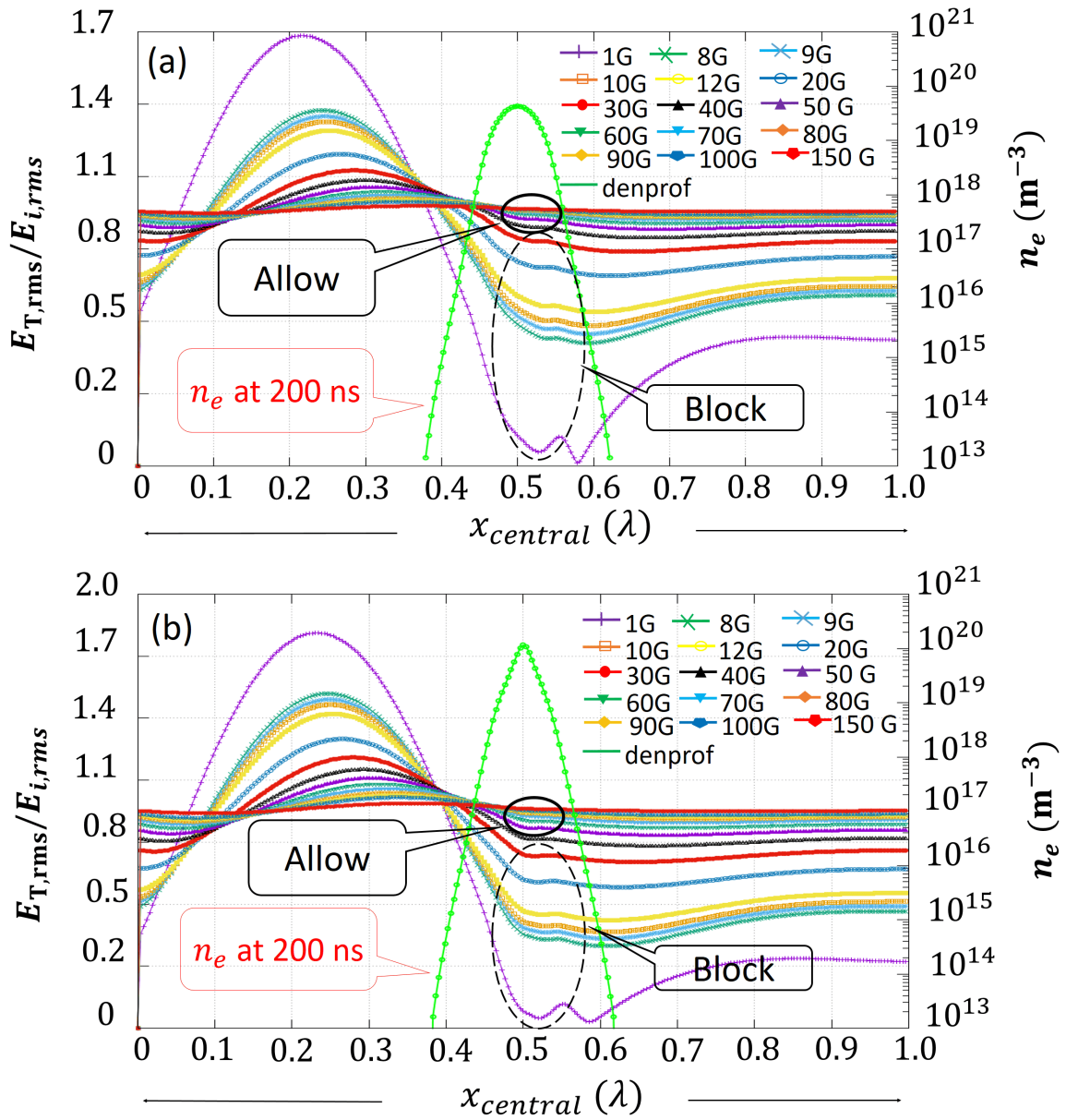


Figure 4.11: The effect of (a) without and (b) with gas heating, on the behavior of spatial plasma density profile along $x_{central}$ (passing through the center of streamer core, (x_c, y_c)). To block or allow certain microwave frequency based on the peak plasma density at the streamer core at 200 ns ($\sim 1 \times 10^{20} \text{ m}^{-3}$). For the simulation, discrete frequencies have been chosen from the 1 to 150 GHz range, and a normalized rms E-field ratio ($E_{T,rms}/E_{i,rms}$) is used to observe the blocking/transmitting nature of the profile. $E_{T,rms}$: Total E-field ($E_{T,rms} = E_{i,rms} + E_{scattered,rms}$), $E_{i,rms}$: rms incident E-field ($2E_0/\sqrt{2} = 3.84 \text{ kV/cm}$ or $3.84 \times 10^5 \text{ V/m}$).

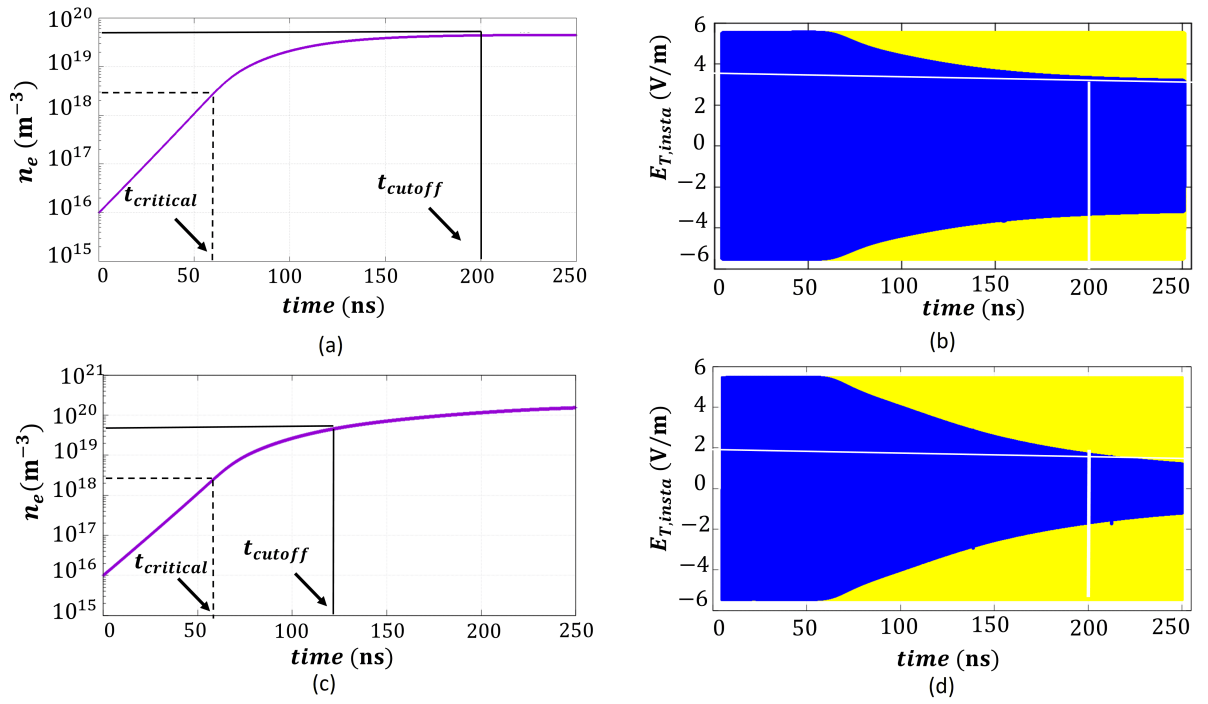


Figure 4.12: The effect of (a) without and (c) with gas heating on the cut-off time (t_{cutoff}) and ($t_{critical}$). The lower breakdown time is indicated by the (d) drop (2.7 times) (b) drop (1.7 times) in the signal transmission ($E_{T,insta}$) through the plasma at the corresponding t_{cutoff} , shifted from 200 ns (without gas heating) to 120 ns (with gas heating). $E_{T,insta}$: instantaneous Total E-field, $\max E_{T,insta} = 5.4 \times 10^5$ V/m (before breakdown)

$\omega \gg \omega_p$, $n_e < n_{critical} = 1.24 \times 10^{20} \text{ m}^{-3}$) for frequency ≥ 100 GHz. The microwave and plasma (electrons) and the plasma with the neutrals (for attenuation of MW E-field) cannot interact for those frequencies. For proper wave plasma interaction $n_e \sim n_{critical}$, for attenuation ($n_e \geq n_{cutoff}$). Gas heating results in lower N_g that results ν_m to drop, this has a significance in lowering $n_{cutoff} \propto ((\nu_m/\omega))^2$ for a given ω and $n_{critical}$. Thus, comparing $E_{T,rms}/E_{i,rms}$ ratio from Fig. 4.11 (b) with (a), it can be observed that the range of frequencies over which the limiter can work has increased (~ 1 to 40 GHz, corresponding n_{cutoff} , $4.33 \times 10^{19} - 6.32 \times 10^{19} \text{ m}^{-3}$). The gas heating has increased the peak plasma density from $\sim 4.4 \times 10^{19} \text{ m}^{-3}$ to $1 \times 10^{20} \text{ m}^{-3}$. Figure 4.12 (c,d) and 4.12 (a,b) show gas heating can lower cut-off time almost 1.66 times (200 to 120 ns). The decrease in cut-off time is indicated by a drop in the signal transmission ($E_{T,insta}$) through the plasma at the corresponding t_{cutoff} , almost 2.7 times as compared to 1.7 times without gas heating. The growth in bulk plasma density (n_e) proves beneficial in lowering the breakdown time.

4.4 Conclusions

In this chapter, we have conducted a computational investigation of two applications (HPM switching and protection) based on the physics of HPM breakdown. We identified the key parameters which play an important role in the optimal design of such applications. The key parameters are required plasma density and breakdown time, which are influenced by the E-field strength and the presence of seed electrons. The breakdown process leads to the creating of a plasma with the desired density. Furthermore, we investigate the electrical properties of the generated plasma and their correlation with plasma density, which govern the applications mentioned above. Additionally, we explored the effect of local gas heating on the accurate switching time calculation and achievable maximum plasma density required for HPM applications. The gas-heating phenomenon becomes prominent for a time greater than 100's nanoseconds. We have discussed how to integrate gas-heating with the existing fluid model. It is important to note that to simulate a higher time-scale gas-heating phenomenon, the lower time-scale physics (involving EM-plasma interaction) must be accelerated. DMR technique, as discussed in the previous chapter, has proved handy in such accelerated simulation.

The results reveal that gas heating influences plasma shape by inducing intense ionization in the plasma bulk and raising plasma density. In the absence of gas heating, high polar E-fields facilitate ionization at the plasma streamer's tip, controlling plasma shape differently. Higher plasma density in bulk can function as an HPM limiter, reducing the cut-off density for various incoming microwave frequencies and expanding the range of frequencies it can block. Gas heating lowers the breakdown threshold, enabling rapid growth in bulk plasma density and reduced cut-off time. In summary, our analysis highlights the necessity of incorporating gas heating effects into the HPM breakdown model for accurate calculations of switching time and achievable maximum plasma density. We find that most computational time is spent on the EM-plasma Maxwell solver to analyze multi-physics multi-scale applications involving EM-plasma interaction. Although the

overall numerical investigations could be effectively performed within a feasible time by utilizing the DMR technique, it is necessary to explore other alternative techniques to accelerate the computation.

CHAPTER 5

Machine learning based approach for 2-D simulation of microwave-plasma interaction

Our discussions from previous chapters indicate that the numerical investigation of microwave-plasma interaction is a computationally challenging problem to simulate within a feasible time. The study becomes challenging due to the inhomogeneous nature of plasma having complicated density profiles such as Gaussian plasma. More challenge lies in the HPM breakdown case due to the steep gradients in the scattered microwave E-field originating from the evolving plasma profile. The FDTD-based computational electromagnetics (CEM) technique has remained one of the most preferred methods to model and accurately simulate the microwave-plasma interactions [9, 43, 121, 122]. Most traditional CEM approaches, whether iterative or direct, are computationally challenging due to stringent numerical criteria that lead to high memory usage and longer simulation time as the problem size increases [108]. Different approaches are mostly employed to overcome such challenges inherent to traditional EM solvers. Those either use advanced parallelization or dynamic mesh refinement techniques to reduce long simulation time without loss in accuracy of results [8, 45]. The high computational cost associated with CEM techniques becomes prohibitive, where the real-time analysis of the EM-plasma interaction is of utmost importance. Therefore, exploring alternative approaches that can address the problem of high computational cost associated with traditional EM solvers is extremely valuable.

Two sets of data (plasma density profile and scattered EM wave pattern) are primarily associated with microwave-plasma interaction problems. The neural networks can be potentially used to learn the non-linear mappings between these two sets of data, and once the network is trained, it can give the outputs in roughly $O(1)$. In the last decade, there have been vast improvements in the development of large and powerful deep neural networks (DNNs), which have been applied to solve complex problems in computer vision and image processing. Physics-informed neural networks, a DNN framework, can also be used as a black box to approximate a physical system [51], and recent results have shown that DNNs with many layers perform a surprisingly good job in modeling partial differential equation-based complicated physics problems in terms of both speed and accuracy [52]. Of late, machine learning (ML)/ deep learning (DL) has also been used to successfully address different complex problems in plasma physics and computational electromagnetics. Deep reinforcement learning has been applied for tokamak magnetic controller design to produce new plasma configurations [53], the potential of AI/ML in predicting disruptive instabilities in controlled fusion plasmas has been established in several studies [54, 55], the feasibility of applying ML models for modeling, diagnostics, and control of non-equilibrium plasmas has been discussed in [56]. Deep learning has also been used for extracting electron scattering cross sections from plasma swarm Data [57].

This chapter discusses a data-driven approach and a novel DL architecture to study the 2-D EM-plasma interaction from modeling to prediction and validation of the predicted results. Results presented in Chapter 3 show the limitations of the traditional differential equation-based fluid approach and highlight that the achievable speedup is limited by the discretization techniques even after the application of DMR. Hence, the requirement to make the EM-plasma interaction studies feasible in real time has motivated us to adopt data-driven AI/ML-based techniques. As simulations can generate many data, which can be utilized to train the AI/ML-based model to predict the EM-plasma interaction.

Organization of this chapter

In section 5.1, the proposed deep learning methodology has been discussed. Section 5.2, discusses the data-set generation methodology. Section 5.3,

provides the DL model training details, including the criteria for parameter selection, the loss function calculation, and the optimization of the model for better prediction. In section 5.4, we discuss the various metrics to evaluate the performance of the proposed DL architecture. Subsequently, in section 5.5, we report the DL-based computational experiments and their simulated results, which are used to enhance the effectiveness of the proposed technique based on comparison with the existing results. Section 5.6 provides an ablation study to explore the effects of changing model parameters on the predicted result. Next, we provide the way DL-model learns important features using network visualization, as discussed in section 5.7. Finally, the conclusion is provided in section 5.8.

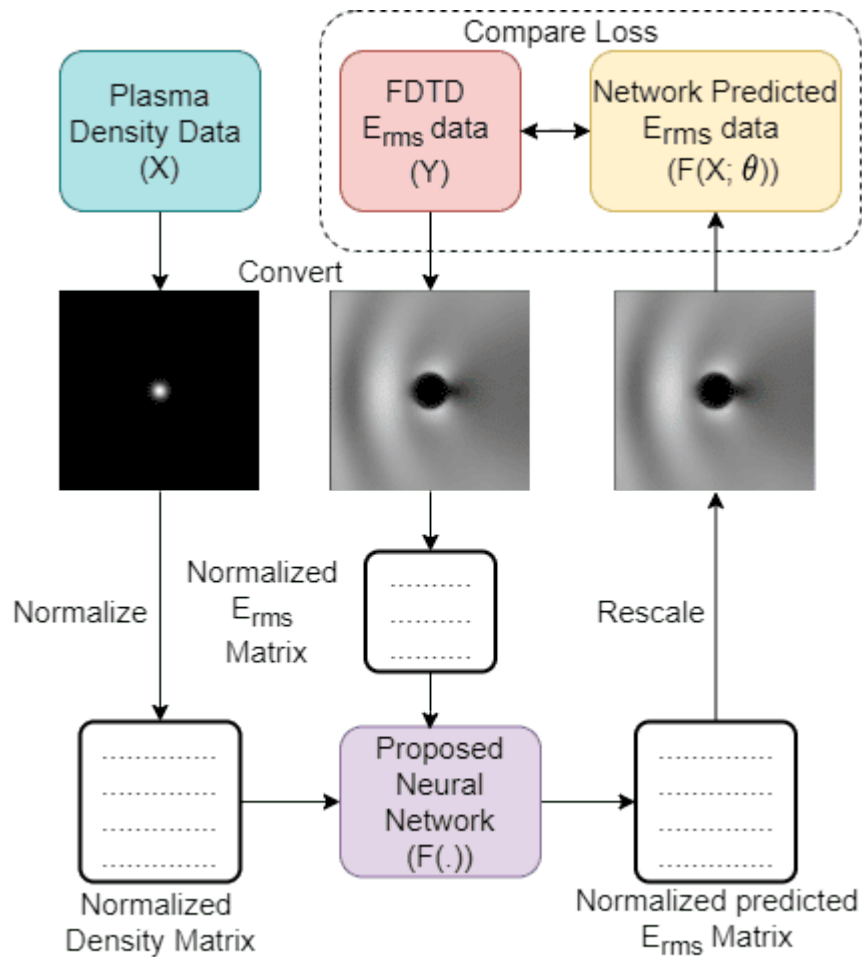


Figure 5.1: Flowchart for training the proposed data-driven ML model

5.1 Proposed deep-learning architecture

This section proposes a deep learning-based architecture for solving the microwave-plasma scattering problem given the plasma density and an EM

wave of fixed frequency. A general flowchart followed for carrying out the experiments in the next section is shown in Fig. 5.1, which is explained as follows: Deep learning models are trained on image data-sets, therefore the data obtained from the FDTD solver needs to be converted into images. To generate the data and to train the deep learning model, the plasma density and E_{rms} data from the 2D FDTD-based simulations is normalized between 0-1 using the maximum value of the plasma density and E_{rms} obtained from the complete data-set respectively. Both of these maximum values for plasma density (in m^{-3}) and E_{rms} (in V/m) are saved and used for scaling up the normalized output generated by the trained neural network. The normalized data-set is scaled in the range (0-255), and gray-scale images are generated to train the proposed deep learning network.

The generated pair of plasma density (X) and E_{rms} (Y) images are then used to train the proposed deep learning model. The model is then evaluated on the testing data. Plasma density image X is given as input to the trained network, which outputs the predicted E_{rms} image (denoted by $F(X; \theta)$, where F represents the deep learning model and θ is the trained model weight matrix. The predicted E_{rms} image is converted to the physical E_{rms} values (in V/m) by scaling the normalized output by the global maximum of the data-set as discussed earlier. The deep learning model's predicted E_{rms} values are then compared with the actual E_{rms} values from the 2D FDTD-based computational solver.

5.1.1 CNN-based UNet deep learning architecture

The proposed architecture is a CNN-based UNet [62] where the input to the network is the single-channeled, gray-scaled, normalized image of plasma density X and the output to the network is the corresponding single-channeled, gray-scaled, normalized image of the E_{rms} data. The architecture of the network is shown in Fig. 5.2. It can be seen that the gray-scale plasma density image is given as an input to the network. The model consists of an encoder and decoder-like structures. The encoder consists of a series of convolutional and max pooling layers, which learn the

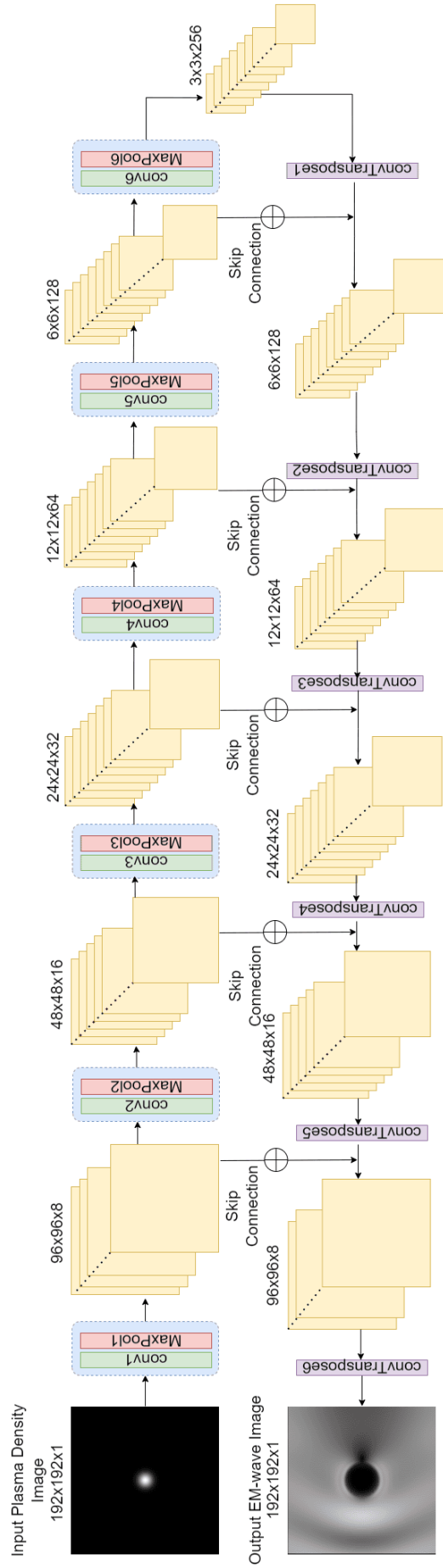


Figure 5.2: The proposed architecture having encoder, decoder, and skip connections for EM-wave scattered by plasma density prediction

features from the image and reduce the dimensions in each layer. The feature extraction allows the network to learn training weights, and the reduction in image dimension decreases the complexity of the model. There are six encoder units, each with a convolutional layer with n filters where n is twice the number of filters than the previous unit with 3×3 kernel size. The ReLU activation function follows the output of each layer.

Correspondingly, there are six decoder units, each with the transposed convolution operation layer with a kernel size of 2×2 followed by the ReLU activation function. The decoder layer will upsample the features to construct the output image of the network. The input to the decoder layer is connected directly to the encoder output. Each decoder layer is connected to the corresponding encoder unit's output using a skip connection, as shown in Fig. 5.2. The skip connections are implemented by concatenating the output of one layer to the other layer to which it is connected. The output of the final decoder unit is the predicted E_{rms} image from the proposed architecture.

5.1.2 Mathematical representation of encoder-decoder in CNN

We discuss the mathematical formulation to describe the symmetric configuration of the encoder-decoder (having the same number of layers, l) block in CNN architecture. We consider a similar analysis from [123], a simplified model where the signal (for a given problem, the signal is plasma density image) is given as input (X , where $x \in X \subset \mathbb{R}^{d_0}$) to the network shown in the Fig. 5.2. The encoder maps each x to a feature space, $g \in G \subset \mathbb{R}^{d_p}$. The feature map is used as input by the decoder to produce the output ($y \in Y \subset \mathbb{R}^{d_0}$). For any k^{th} layer, the input and output dimensions for the encoder layer E^k and the decoder layer D^k are symmetric, which can be expressed as,

$$E^k : \mathbb{R}^{d_{k-1}} \rightarrow \mathbb{R}^{d_k}, D^k : \mathbb{R}^{d_k} \rightarrow \mathbb{R}^{d_{k-1}} \quad (5.1)$$

Where $k \in [l]$. The dimension of input and output is the same, d_0 . For any k^{th} layer, the total dimension $d_k = c_k n_k$, where dimension of each channel is c_k and number of channels is n_k . The input signal to k^{th} layer of encoder arrives

from the n_{k-1} input channels of $k - 1^{th}$ layer can be expressed as,

$$E^{k-1} = \left[E_1^{k-1 T}, \dots, E_n^{k-1 T} \right]^T \quad (5.2)$$

The n_k channel output of k^{th} layer encoder can be expressed as,

$$E_j^k = r_e \left(\Phi^k T \sum_{i=1}^{n_{k-1}} E_i^{k-1} \otimes \Psi_{j,i}^k \right) \quad (5.3)$$

Where, $j \in [n_k]$, E_j^k is the j^{th} channel encoder output after convolutional filtering with $\Psi_{j,i}^k$ filters and max pooling operation with $\Phi^k T$. The non-linearity is introduced to the given encoder output by passing the convolution filter and max-pooling through the rectified linear unit (ReLU) r_e , used as an activation function. Similarly, the decoding is as followed, where k^{th} layer input signal for the decoder layer comes (encoding in reverse) from n_k channel inputs,

$$D^k = \left[D_1^k T, \dots, D_n^k T \right]^T \quad (5.4)$$

The decoder layer convolution output is given by,

$$D_j^{k-1} = r_e \left(\sum_{i=1}^{n_k} \Phi^k D_i^k \otimes \Psi_{j,i}^k \right) \quad (5.5)$$

In the case of the decoder, the reverse of the pooling operation with $\Phi^k T$ is performed before the convolution (the order is different in the encoder) to maintain the symmetry in the network. The nonlinearity is introduced to the given decoder output by passing through the rectified linear unit (ReLU) r_e , used as an activation function.

5.2 Data-set generation methodology

As discussed in Sec. 5.1, deep learning architectures require training data. Therefore, in this section, a discussion about how the data-set is generated is carried out. Figure 5.3 (a) provides a phenomenological picture of the 2D problem we are trying to simulate. Let us consider a linearly polarized plane EM wave propagating in air plasma in the X-direction. The simulation plane

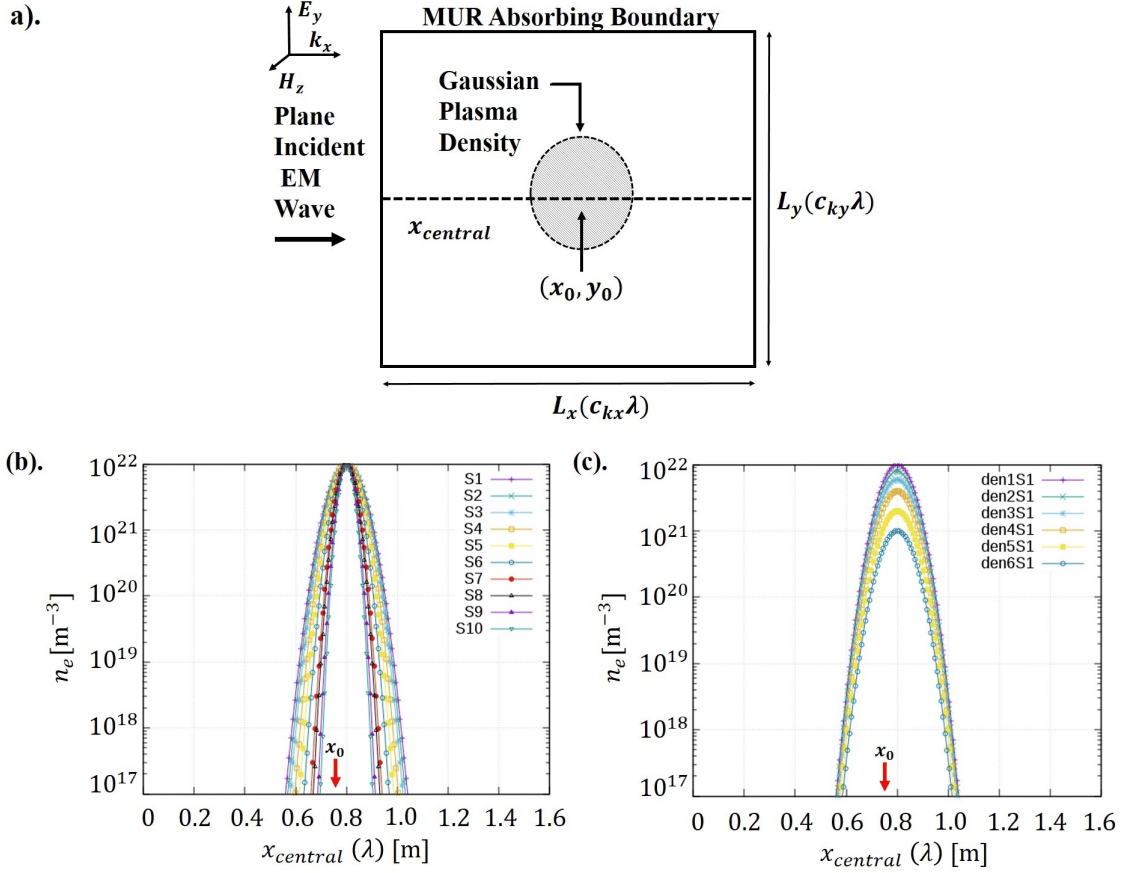


Figure 5.3: (a) The schematic representation of the square computational domain, $\{(c_{kx}, c_{ky}) \in \mathbb{Q}^+\}$; length of the domain L_x and L_y are taken in terms of the wavelength of the incident EM wave. The location x_0, y_0 is $0.5L_x$ and $0.5L_y$, respectively, and, $\{c_{kx}, c_{ky}\} = \{1.5, 1.5\}$, where λ corresponds to $\text{freq} = 1 \text{ GHz}$. The parameter space can be varied by changing two parameters of the 2D Gaussian profile - width and peak density. (b) plasma profile along the central x-axis ($x_{central}$) for different widths of Gaussian (S1: 0.05λ (highest) to S10: 0.02λ (lowest)) for a fixed peak plasma density, $n_0 = 10^{22} \text{ m}^{-3}$ (c) different peak plasma densities for a fixed width of Gaussian. The den1S1: $n_0 = 10^{22} \text{ m}^{-3}$ to den6S1: $n_0 = 10^{21} \text{ m}^{-3}$

XY contains an electric field E and the wave vector k parallel to the X-direction. The magnetic field H is in the YZ plane perpendicular to the X- direction. The simulation setup is equivalent to a Y-polarized (E-field), X-directed EM wave. A 2D Gaussian plasma density has been considered given by $n_e(x, y) = n_0 \exp(-(\{x - x_0\}^2/\sigma_x^2 + \{y - y_0\}^2/\sigma_y^2))$, where x_0 and y_0 are the center of the plasma peak density (n_0), and the spread of the plasma is controlled by the plasma width σ_x and σ_y , here $\sigma_x = \sigma_y = S$. Different Gaussian plasma profiles can be defined by tuning the two important parameters, the width of the Gaussian, S , and the peak plasma density, n_0 . Some representative plasma profiles for generating the data-set (pair of plasma density and E_{rms} field) to study the EM-plasma interaction are shown in Fig. 5.3 (b-c). The data-set to train the network is prepared by keeping the incident wave frequency fixed, and the shape of the 2D Gaussian plasma profile is varied. The size of the computational domain is $1.5\lambda \times 1.5\lambda$ as per the setup shown in Fig. 5.3. For each instance of the profile, the data file for the plasma density and the corresponding 2-D scattered EM wave data (E_{rms}) is generated via our in-house developed FDTD computational solver [108]. The generated data is a 2-D grid visualized in Fig. 5.4 for varying peak density. It can be observed that the EM wave transmits through in the case of lower peak densities while it gets reflected in the case of higher peak densities.

5.3 Training details

The proposed deep learning network is trained on the pair of the generated gray-scale images of the data-set. The plasma density image X is given as input to the network, and the network learns its parameters by minimizing the loss between the actual E_{rms} image denoted as Y and the output of the network which is the predicted E_{rms} image denoted as $F(X; \theta)$. The loss function for training the architecture is given as follows:

$$L(\theta) = \frac{1}{M} \sum_{i=1}^M \|F(X; \theta) - Y\|_2^2 + \lambda \sum_{j=1}^l \|W_j\|_1 \quad (5.6)$$

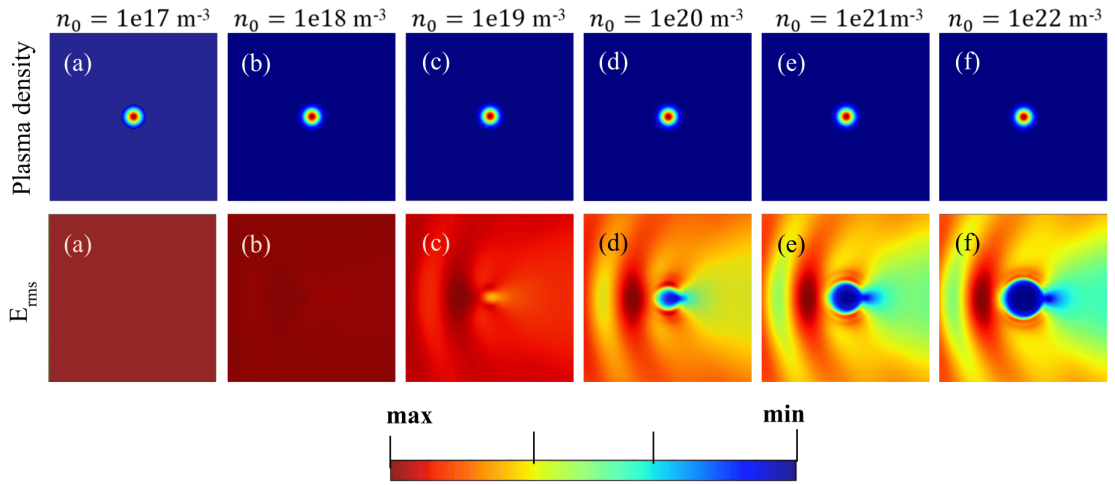


Figure 5.4: (a-f) Generated dataset of Plasma Density and corresponding scattered E_{rms} for varying peak density. The color-bar represents the maxima and minima corresponding to plasma density and the E_{rms} . The maxima for plasma density is indicated by n_0 and the minima is 0. For E_{rms} , maxima are 7.07, 7.15, 7.74, 9.37, 10.36, and 10.47 V/m, respectively, and minima is 0. The skin depth of microwave into plasma profile reduces as n_0 increases indicated by visibility of exact scatterer dimension (2D Gaussian profile) from E_{rms} plot (a) to (f).

where M is the total number of training images, θ is the network weight parameter matrix, l is the total number of kernels used and W_j is the weight of the j^{th} kernel. The loss is minimized using the Adam optimizer [124] with learning rate $\eta = 1e - 3$, $\beta_1 = 0.9$ (the exponential decay rate for first-order moment estimates), $\beta_2 = 0.999$ (the exponential decay rate for second-order moment estimates) and $\epsilon = 1e - 7$. The kernel weights matrix for the convolution and transposed convolution layers are initialized with Glorot-uniform, which draws samples from a uniform distribution. Here, L1 regularization is used to overcome the problem of overfitting with $\lambda = 1e - 7$. There are 611,833 trainable parameters in the proposed deep learning model with 6 convolutional encoders, 6 convolutional transposed decoders, and five skip connections. The network is trained on NVIDIA Tesla K40c GPU using Keras API with TensorFlow running in the backend. While training the model for 300 epochs, the loss is shown in Fig. 5.5. It can be observed that training and testing losses decrease with each epoch, indicating that our network is learning.

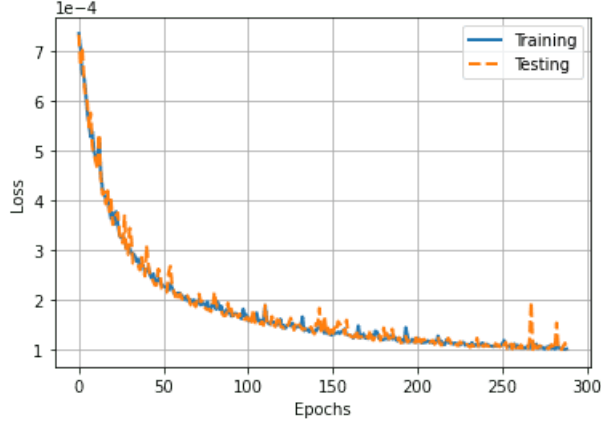


Figure 5.5: Mean squared error loss in training the model

5.4 Performance Comparison Metrics

To evaluate the performance of the proposed architecture in terms of predicting the image and the actual physical values of the E_{rms} data (in V/m), we have used existing metrics discussed in this section. In order to compare the quality of image reconstruction by the deep learning model with respect to the actual E_{rms} image, we use Structural Similarity Index Metric (SSIM) [125], where the image degradation is perceived change in structural information. For two images x and y of size $N \times N$, the similarity measure is given by:

$$SSIM = \frac{(2\mu_x\mu_y + (k_1L)^2)(2\sigma_{xy} + (k_2L)^2)}{(\mu_x^2 + \mu_y^2 + (k_1L)^2)(\sigma_x^2 + \sigma_y^2 + (k_2L)^2)} \quad (5.7)$$

where μ denotes the mean, σ^2 denotes the variance, L is the dynamic range of pixel values. As suggested by [126], in the work of [125], the two parameters (K_1 and K_2) are set to $K_1 = 0.01$ and $K_2 = 0.03$, to avoid the calculated SSIM to become unstable under the universal image quality index criteria as proposed in [127]. Values of the SSIM index are from 0 to 1. The closer the value of the SSIM metric to 1, the better the image reconstruction quality.

We use two metrics to evaluate the model's performance in predicting the E_{rms} values (in V/m) compared to the values obtained from the 2D FDTD-based solver. The first metric is the average of the percentage error over all the E_{rms} values on the 2D grid. Let A_{ij} and B_{ij} denote the E_{rms} values obtained from the 2D FDTD solver and DL-based approach at $(i, j)^{th}$ point on a $N \times N$ 2D grid

respectively. The average percentage error is given by

$$\text{Avg. percent error} = \frac{1}{N_{\text{images}}} \sum_{N_{\text{images}}} \left[\frac{1}{N^2} \sum_{i=1}^N \sum_{j=1}^N \left| \frac{B_{ij} - A_{ij}}{A_{ij}} \right| \right] \quad (5.8)$$

The second metric is the mean squared error (MSE), which is defined as

$$\text{MSE} = \frac{1}{N_{\text{images}}} \sum_{N_{\text{images}}} \left[\frac{1}{N^2} \sum_{i=1}^N \sum_{j=1}^N (B_{ij} - A_{ij})^2 \right] \quad (5.9)$$

5.5 Computational experiment Results and discussion

In the microwave-plasma interaction study, the 2D FDTD-based method discretizes the 2D computational domain of size $1.5\lambda \times 1.5\lambda$, where λ corresponds to free space wavelength, using Yee approximation [128]. The data provided to the proposed DL-based model is such that the number of grid points per wavelength (λ) of the EM wave is 128, resulting in 192×192 grid points in XY plane to accurately resolve the gradients in the E-field and the plasma density. In the simulation, the plane EM wave having the amplitude of 10 V/m is incident from the left-hand side of the domain as shown in Fig. 5.3. The frequency of the EM wave is 1 GHz.

Table 5.1: EM-Wave scattering predicted data comparison with the actual data

Dataset Range(in density m^{-3})	Avg. SSIM (image)	Avg. percent error (physical)	Avg. MSE (physical)
1e21 - 1e22	0.9894	1.8751%	0.00857
1e20 - 1e22	0.9932	1.1017%	0.00467
1e19 - 1e22	0.9935	1.3389%	0.00722
1e18 - 1e22	0.9946	1.0172%	0.00613
1e17 - 1e22	0.9955	0.9036%	0.00564

The data used in training the network is varied by changing the peak plasma density from $n_0 = 1e21 m^{-3} \rightarrow 1e22 m^{-3}$ to $n_0 = 1e17 m^{-3} \rightarrow 1e22 m^{-3}$ gradually. Table 5.1 shows the test cases' results with varying data-set sizes in training. It can be observed that the average SSIM index increases with the increase of the data-set range. The average percent error is observed to

be less than 2%. The FDTD-based solver and DL-based approach results for different plasma densities have been compared in Fig. 5.6. The first row in Fig. 5.6 represents density profiles changing from underdense (leftmost) plasma to overdense plasma (rightmost). The second row represents the scattered EM wave pattern obtained using the conventional FDTD-based solution. The third row shows the generated images from our proposed architecture, and it can be observed that the scattering patterns closely match that of the FDTD-based solver data shown in the second row. The fourth row shows the quantitative comparison of the scattered EM wave values shown in the second and third rows. It can be observed that the intensity values obtained by taking a 1-D profile across the central x-axis closely match each other (FDTD vs our proposed approach).

The aforementioned microwave-plasma interaction study in a $1.5\lambda \times 1.5\lambda$ computational domain using the FDTD-based technique with 128 cells per λ takes approximately 18 seconds on Intel Xeon CPU E5-2640 V3 @ 2.60 GHz with x86_64 architecture for a physical time duration of 15 wave periods. The stable scattering pattern is obtained after the EM wave has attained a steady state condition. It takes 0.0576 seconds on average per test case for the DL-based approach executed on the Intel(R) Xeon(R) CPU @ 2.20GHz with x86_64 architecture.

For the $1.5\lambda \times 1.5\lambda$ problem size, we observe a speedup of around 350 times using the DL-based approach compared to the FDTD-based technique. However, the computational time complexity of a 2-D FDTD-based solver is $O(n^3)$. If the problem size changes from $1.5\lambda \times 1.5\lambda$ to $3\lambda \times 3\lambda$ and finally to $6\lambda \times 6\lambda$, the execution time is around 93 and 744 seconds, respectively. However, in the case of DL based approach, it will be much smaller.

5.6 Ablation Study

In order to explore the effect of changing the model parameters on the predicted E_{rms} values given the plasma density, the ablation studies on the effects of skip connections, number of encoder-decoder units, and method of upsampling are discussed below. In these experiments, all the models

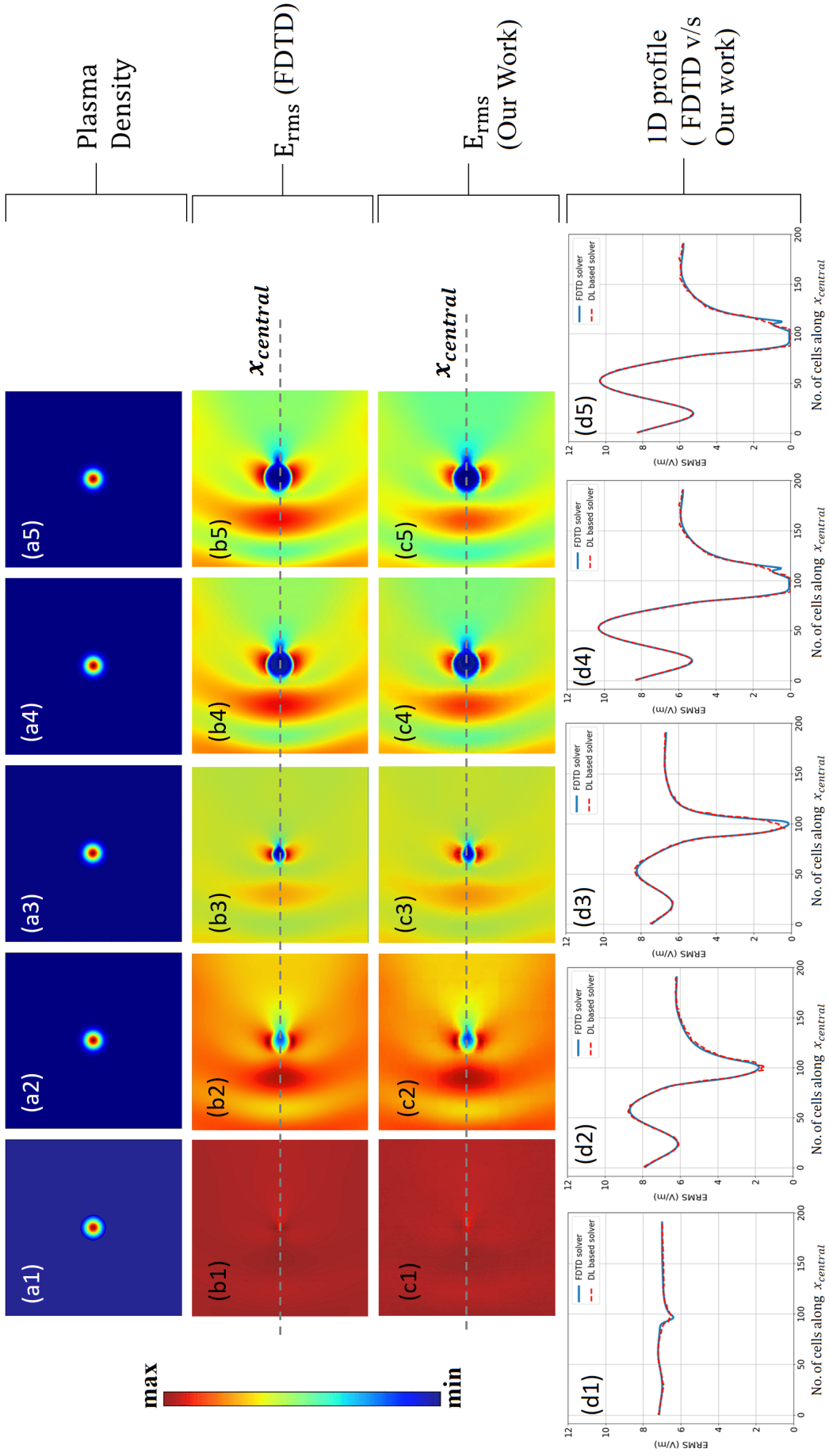


Figure 5.6: Comparative study and results of example cases; Row 1 (a1-a5): 2D profile of input plasma density (for increasing n_0 , $6e18, 6e19, 4e20, 6e21$ and $8e21 \text{ m}^{-3}$ from left to the right); Row 2 (b1-b5): 2D Scattering (E_{rms}) pattern obtained from FDTD solver; Row 3 (c1-c5): 2D Output E_{rms} image from the proposed deep learning based architecture; Row 4 (d1-d5): Comparison of 1D E_{rms} along the central x-axis ($x_{central}$) of the computational domain predicted from our work and FDTD based solver.

are trained (on the data-set having range $1e17 \text{ m}^{-3} - 1e22 \text{ m}^{-3}$) on the same training and testing images.

5.6.1 Effect of encoder-decoder units

In the proposed architecture, there are six encoder and decoder units. In this study, we perform additional experiments with four and five encoder-decoder units in the proposed architecture. The results are shown in Table 5.2 where it can be observed that adding more units will improve the results. For six unit pairs, we obtain an average SSIM value of more than 0.99 which is a good indicator for image reconstruction by the network. A similar observation is seen for average percentage and mean square error (MSE) metrics. Further, adding more encoder-decoder units will increase the computational cost.

Table 5.2: Impact of varying the number of encoder-decoder units

No. of encoder-decoder units	Avg. SSIM	Avg. Percent error	Avg. MSE
4 units	0.95881	4.919%	0.29512
5 units	0.97629	3.164%	0.09468
6 units	0.99574	0.897%	0.00628

5.6.2 Effect of skip connections

In the proposed model, five skip connections connect the output of the first five encoder and decoder units. For a second case, all the skip connections are removed. In the third case, two skip connections exist between the output of the second and fourth encoder and decoder units. We found the best results in the third case when there are two alternate skip connections, as shown in Table 5.3, although the difference is much less.

Table 5.3: Impact of varying the skip connections

No. of skip connections(SC)	Avg. SSIM	Avg. Percent error	Avg. MSE
All five SC	0.99574	0.897%	0.00628
Without SC	0.99533	0.955%	0.00805
With two alternate SC	0.99601	0.857%	0.00600

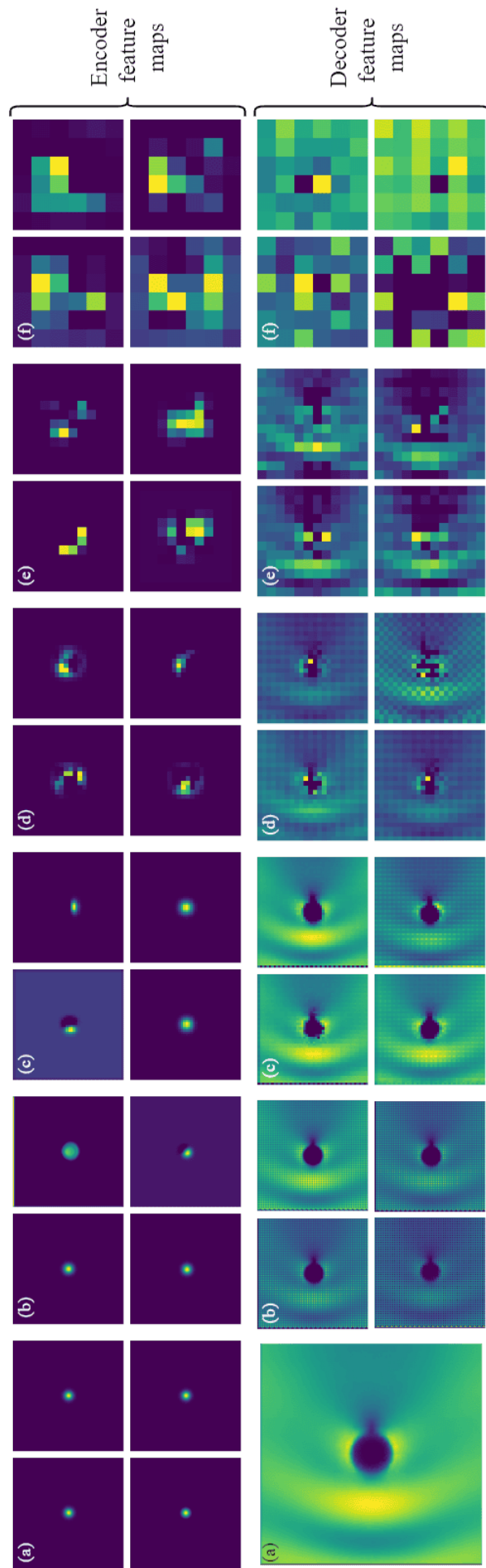


Figure 5.7: Row 1: Feature maps of the output of the six encoder units; Row 2: Feature maps of the output of the six decoder units. (a) is the final output E_{rms} image of the network; The corresponding (a)-(f) pairs of the encoder-decoder pairs give the feature output in the same spatial dimensions. Only four feature maps for a convolution unit are shown for representational purposes. The total number of feature maps for a unit is equal to the number of filters used in the convolution or transposed convolution layer.)

5.6.3 Effect of up-sampling method

The proposed architecture uses the transposed convolution operation in the decoder units. The transposed convolution operation can be replaced by a structure consisting of an up-sampling unit followed by a convolution unit. Unlike the transpose convolution, which is trainable, the up-sampling layers follow an interpolation scheme that increases the dimension of the input. Combining up-sampling with convolution is considered equivalent to the transposed convolution [129]. In this study, we use the bilinear and nearest neighbor and observe that using the up-sampling with nearest neighborhood interpolation followed by convolution layers gives the best results, as shown in Table 5.4.

Table 5.4: Impact of using various up-sampling methods

Up-sampling Methods	Avg. SSIM	Avg. Percent error	Avg. MSE
Transposed Convolution	0.99574	0.897%	0.00628
Bilinear interpolation	0.99568	0.960%	0.00749
Nearest neighbour interpolation	0.99637	0.857%	0.00579

5.7 Network visualization using feature maps

Figure 5.7 shows the feature maps (outputs of the convolution units) for an example case, which helps us visualize how the network learns the features. It can be observed that the encoder section of the network (shown in row 1 in Fig. 5.7) learns the high-level features initially, followed by learning low-level features (edges in the image) later. The decoder of the network (shown in row 2 in Fig. 5.7) learns the low-level features first, followed by the high-level features. The encoder down-samples the image from (a) to (f), while the decoder up-samples the image from (f) to (a). It can be observed that the decoder learns the scattering pattern, unlike the encoder, which learns the structural features and down-samples the image resolution to give the structural information of the plasma density profile.

5.8 Conclusions

This work presents a CNN-based deep learning model inspired by UNet with a series of encoder and decoder units with skip connections to simulate microwave plasma interaction. The scattering of a plane EM wave, with fixed frequency and amplitude, incident on a plasma medium with different Gaussian density profiles has been considered. The training data associated with microwave-plasma interaction have been generated using 2D-FDTD-based simulations. The trained deep learning model then reproduces the scattered EM wave from the plasma with an average percent error margin of less than 2%. The results obtained from the network have been evaluated using various metrics such as SSIM and MSE. Ablation studies and network visualization using feature maps have also been discussed. The deep learning technique proposed in this work is significantly faster than the existing FDTD-based computational techniques.

We observe when the DL model is trained using a data-set containing a wide range of plasma density ($1e17 - 1e22 \text{ m}^{-3}$) and the testing samples are taken from higher density regions ($1e21 - 1e22 \text{ m}^{-3}$) where scattering is significant, there is a minor mismatch between FDTD and DL based 1D results of E_{rms} along central x-axis (Fig. 5.6). The DL-based model can be improved further to address such issues by either modifying the loss function of our current DL model or by using a PINN [130] based additional loss function to consider the physics associated with microwave plasma interaction. This is the first effort toward exploring a DL-based approach to simulate complex microwave-plasma interaction. The DL technique proposed in this work is significantly faster when compared to the existing computational techniques and can be used as a new, prospective, and alternative computational approach for investigating microwave-plasma interaction-based applications in a real-time scenario.

CHAPTER 6

Deep learning assisted microwave-plasma interaction based technique for plasma density estimation

6.1 Introduction

The study of EM wave propagation through plasma is mathematically a well-posed problem with a unique solution. The problem can be solved computationally by numerical simulations through several techniques, such as FDTD-based iterative solutions of Maxwell-plasma fluid model [8, 43, 131–135]. This is referred to as a forward approach (or forward problem) using model-driven solutions (using numerical solutions to partial differential equations) as discussed in the chapter 2. On the other hand, the plasma characterization via wave interaction is mathematically an ill-posed problem, i.e., given a E_{rms} scattered pattern signature from a plasma density (n_e) profile, it is difficult to provide information regarding the plasma density profile that has resulted in such pattern. Thus, no unique solution is possible. Such an ill-posed problem to map the plasma density profile for a given electromagnetic field pattern is not directly possible. Figure 6.1 illustrates both types of problems through a schematic representation. The chapter proposes an efficient method for the estimation of plasma density (n_e) via microwave-plasma interaction-based technique by utilizing the collected scattered electric field pattern measured experimentally and fed to a deep learning-enabled model for the realization of the n_e profile. We utilize the similar DL-architecture framework as discussed in the previous chapter, which

has been used to determine the scattered E-field pattern from symmetric plasma profile for a forward problem [136], to investigate the DL-model prediction capability for the inverse problem.

Organization of this chapter

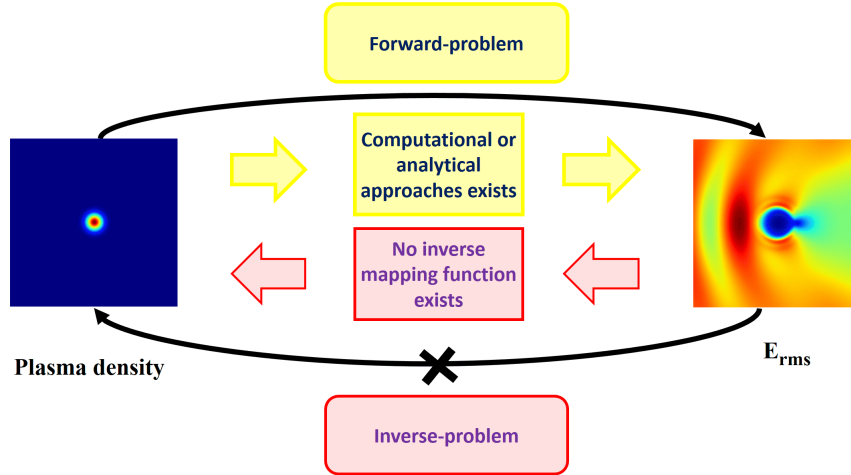


Figure 6.1: Schematic representation of the forward and inverse problem for EM-plasma interaction is shown. The 2-D representation of plasma density and corresponding E_{rms} obtained through the Maxwell-plasma fluid model (solution to forward problem) exists, but no direct inverse mapping exists.

A brief overview of microwave-plasma interaction based data-set generation via 2D electromagnetic fluid simulation is presented in section 6.2. The section also touches upon different aspects of synthetic data-set preparation for training the DL model. This is followed by a detailed account of the proposed machine learning (ML) assisted microwave-plasma interaction-based approach for estimation of plasma electron density as given in section 6.3. The section also discusses the employed deep learning architecture and machine learning aspects. The major finding of this work is presented in the results and discussion, section 6.4. A summary has been provided in section 6.5.

6.2 Data-set generation methodology

Sufficient and good quality data in the form of plasma density and the associated scattered electric field when an EM wave is incident on the plasma is required for robust application of the proposed deep learning-based technique. The required data has been generated using an in-house finite

difference time domain (FDTD) based fluid model, which can capture the EM plasma-interaction in the case of a weakly-ionized, collisional, unmagnetized plasma [8]. The interaction involves the EM wave transmission, reflection, and absorption through the plasma. A brief overview of the FDTD (a time-domain technique that numerically solves Maxwell's equation using Yee's algorithm [128]) based computational model to replicate a real microwave-plasma interaction experiment, which uses the following equations, is provided below.

$$\frac{\partial \vec{E}}{\partial t} = \frac{1}{\epsilon_0} (\nabla \times \vec{H}) - \frac{1}{\epsilon_0} (\vec{J}) \quad (6.1)$$

$$\frac{\partial \vec{H}}{\partial t} = -\frac{1}{\mu_0} (\nabla \times \vec{E}) \quad (6.2)$$

$$\frac{\partial \vec{v}_e}{\partial t} = -\frac{e \vec{E}}{m_e} - \nu_m \vec{v}_e \quad (6.3)$$

The model primarily comprises Maxwell's and momentum conservation equations to obtain the electron's velocity. Where, \vec{E} and \vec{H} , are electric and magnetic field respectively, μ_0 and ϵ_0 represents permeability and electrical permittivity of vacuum respectively, e is the electron charge, n_e is the electron density in (m^{-3}), \vec{v}_e is the electron velocity in (m/s), m_e is mass of electron in (kg), ν_m is the electron-neutral collision frequency in (s^{-1}). The electron current density term ($\vec{J} = n_e e \vec{v}_e$ in (A m^{-2})) couples the two sets of equations. The details of the model and its computational implementation are already provided in previous chapters.

Figure 6.2(b) provides a schematic representation of the 2-D simulation domain used for data generation, where a linearly polarized plane EM wave interacts with a plasma having a Gaussian density profile centered at (x_0, y_0) . The simulation plane (XY-plane) contains an electric field (E) and the wave vector k parallel to the X direction. The magnetic field (H) is Z-directed, perpendicular to the simulation domain. The simulation setup is equivalent to a Y-polarized, X-directed wave.

The inputs to the simulation model are the 2-D plasma density profile and the characteristics of the incident EM wave. The output is the 2-D scattered E_{rms} pattern. The plasma density profile is assumed to follow a 2D Gaussian profile given by $n_e(x, y) = n_0 \exp(-(\{x - x_0\}^2/\sigma_x^2 + \{y - y_0\}^2/\sigma_y^2))$, where x_0 and

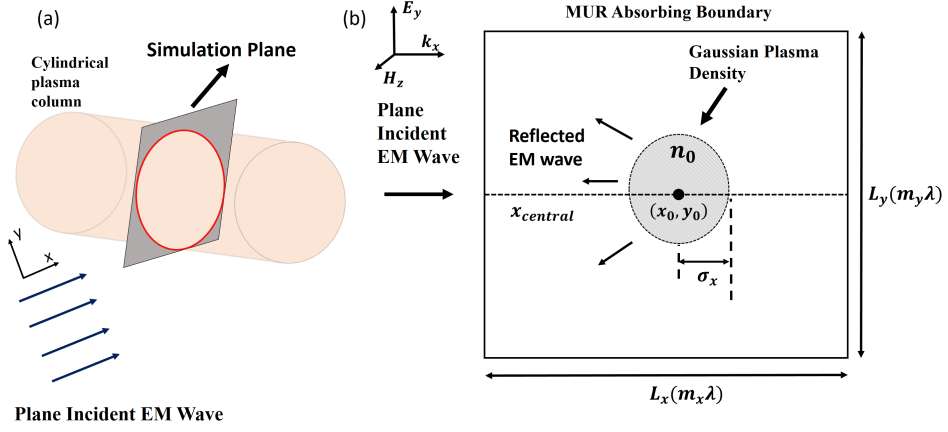


Figure 6.2: (a) A typical linear LTP device schematic. (b) The schematic representation of the square computational domain, $\{(m_x, m_y) \in \mathbb{Q}^+\}$; the length of the domain L_x and L_y is expressed in terms of the wavelength of the incident EM wave. The location coordinates x_0, y_0 is $0.5L_x$ and $0.5L_y$, respectively, and, the coefficients, $\{m_x, m_y\} = \{1.0, 1.0\}$, where λ corresponds to the freq = 500 MHz. The parameter space can be varied by changing two parameters of the 2D Gaussian profile - width ($\sigma_x = \sigma_y$) and peak density (n_0). $\sigma_x = \{0.01\lambda, 0.02\lambda, \dots, 0.05\lambda\}$ for a fixed peak plasma density, $n_0 = \{10^{16}, 10^{17}, \dots, 10^{19}\} \text{ m}^{-3}$

y_0 are the center of the plasma peak density (n_0). The spread of the plasma is controlled by the plasma width σ_x and σ_y , here $\sigma_x = \sigma_y$. Different Gaussian plasma profiles can be defined by tuning the two parameters, the width of the Gaussian (σ_x) and the peak plasma density, n_0 .

In the simulation, we have considered a plane EM wave with an amplitude of 10 V/m and frequency 500 MHz incident from the left-hand side of the domain as shown in Fig. 6.2. We have considered an air plasma at a pressure of 2 torr having a collision frequency of around 10 GHz (for air plasma considered here, $\nu_m = 5.3 \times 10^9 p$, where p is the ambient pressure in (torr)) [12]. Yee-approximation [128] has been used to discretize the computational domain of size $1\lambda \times 1\lambda$, where the λ corresponds to the EM-wave free-space wavelength. The number of grid points per wavelength of the EM wave is 256 to accurately resolve the gradients in the E-field and the plasma density [8]. The resulting total number of grid points in the XY plane is 256×256 , which is also the size of the data-set provided to the DL-based model for training/testing. The stable scattering pattern is obtained after the EM wave has attained a steady state condition.

The data-set to train the network is prepared by keeping the frequency of the incident wave fixed and the shape of the 2D Gaussian plasma profile is varied.

For each 2D plasma density profile, the corresponding 2-D scattered EM wave data, E_{rms} , is generated. The root mean square (RMS) of the E-field is the time-averaged E-field over one EM wave period, $E_{rms} = \left(\frac{1}{N} \sum_{i=1}^N E_{total}^2 \right)^{1/2}$, where i is the number of iteration going upto N , corresponds to 1 EM wave period. The generated 2D data is shown in Fig. 6.3 for different peak plasma densities. It can be observed that the EM wave transmits through plasma in the case of lower densities (cases a1 and a2), while there is a significant reflection in the case of higher densities, (a3-a5). The FDTD-based simulated results can be explained based on the physics of EM-plasma interaction. The plasma density profile controls the different electrical properties of the plasma, ranging from dielectric to a conductor. Depending on the relations $\omega > \omega_p$, $\omega \approx \omega_p$ or $\omega < \omega_p$, we can classify the different plasma density regimes as sub-critical, intermediate and over-critical, respectively. Each of those regimes corresponds to transmission, absorption, reflection, and minimum penetration into the plasma, also called skin depth (the distance over which the E-field of the wave decays $1/e$ of its initial strength). Thus, we can get the total information regarding the wave propagation in the medium by capturing the root mean square (RMS) value of the scattered microwave E-field.

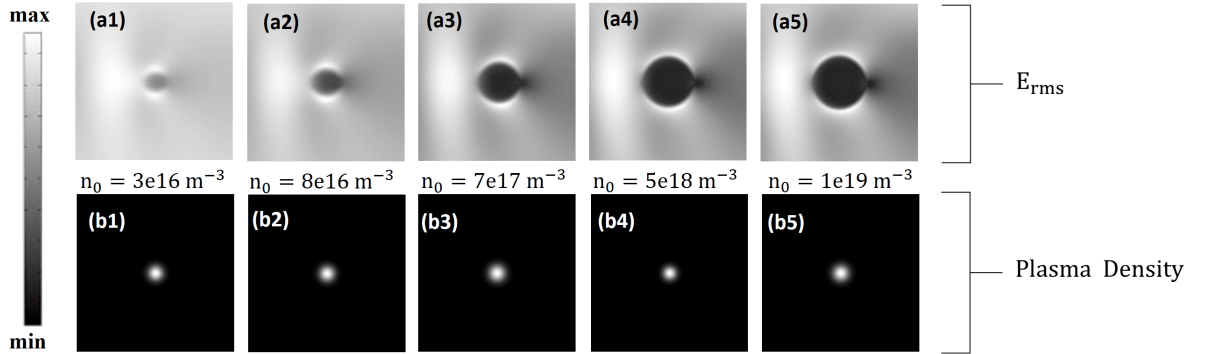


Figure 6.3: (a1-a5) Generated data-set of reflected E_{rms} from, (b1-b5) different plasma density profile having varying peak density (n_0). The maxima for plasma density is indicated by n_0 , and the minima is 0. For E_{rms} , maxima are 8.29, 9.34, 10.31, 10.36, and 10.37 V/m, respectively, and minima is 0. The skin depth of the microwave into the plasma profile reduces as n_0 increases.

6.2.1 Synthetic data-set preparation for training DL-model

Different real-life experimental considerations must be considered while preparing the training data-set for the feasible application of the DL-based

approach. We have considered the following three possibilities:

- The unavailability of the scattered electromagnetic field data within the chamber that confines the plasma.
- The collection of either dense or sparse E_{rms} data around the plasma by experimental techniques cite [137–139] based on scope of sensor deployment.
- The Presence of noise in the collected E_{rms} data is critical when some E-field is present due to plasma particle movement.

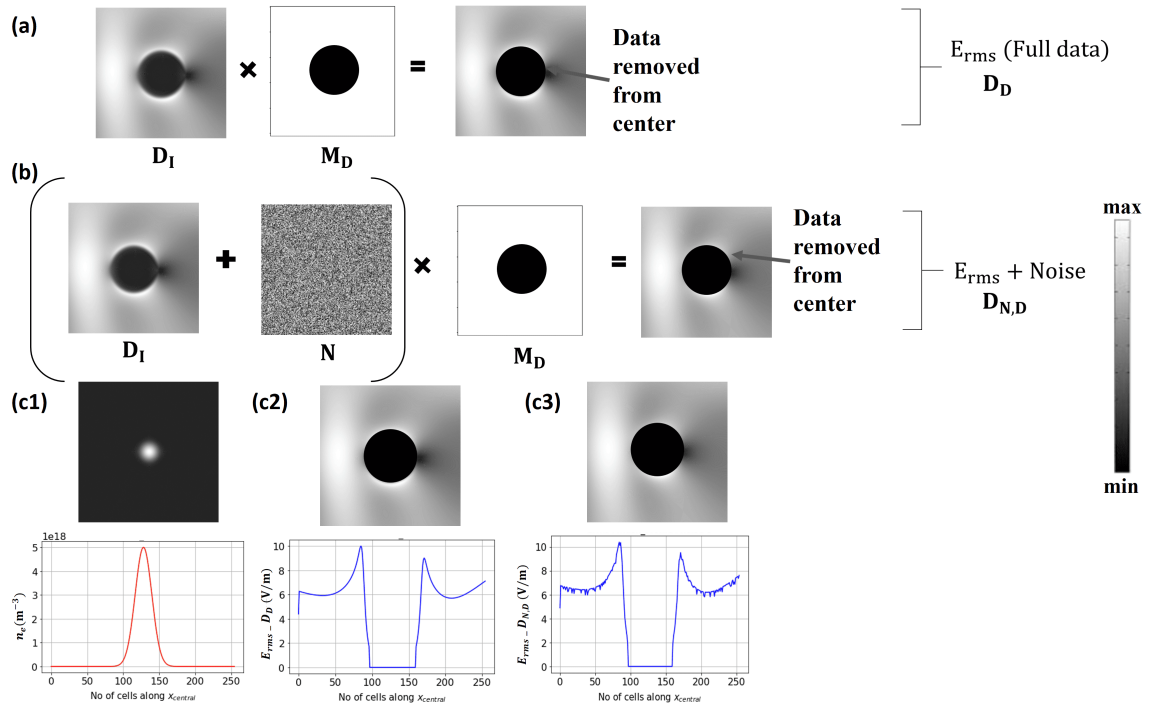


Figure 6.4: Dense E_{rms} data generation for ML training: (a) by removing the central part of the data and retaining the remaining, (b) addition of noise to the generated dense data, followed by removing the central part and retaining the remaining. (c1-c3) represents the 2-D as well as 1-D density profile, Furthermore, corresponding, dense E_{rms} data has been collected with and without noise (left to right). The color-bar maxima and minima correspond to E_{rms} . D_I : Initial data, M_D : Mask for dense data, N : Noise data

The unavailability of the data has been considered by masking the central region in the E_{rms} data where we wish to predict the plasma density. The dense or sparse data can be obtained by two different types of masks, as shown in Fig. 6.4 (a) and in Fig. 6.5 (a). The masking leads to either masked dense data, D_D , or masked sparse data, D_S . A mask is equivalent to a non-invasive diagnostic system that records the E_{rms} data outside the

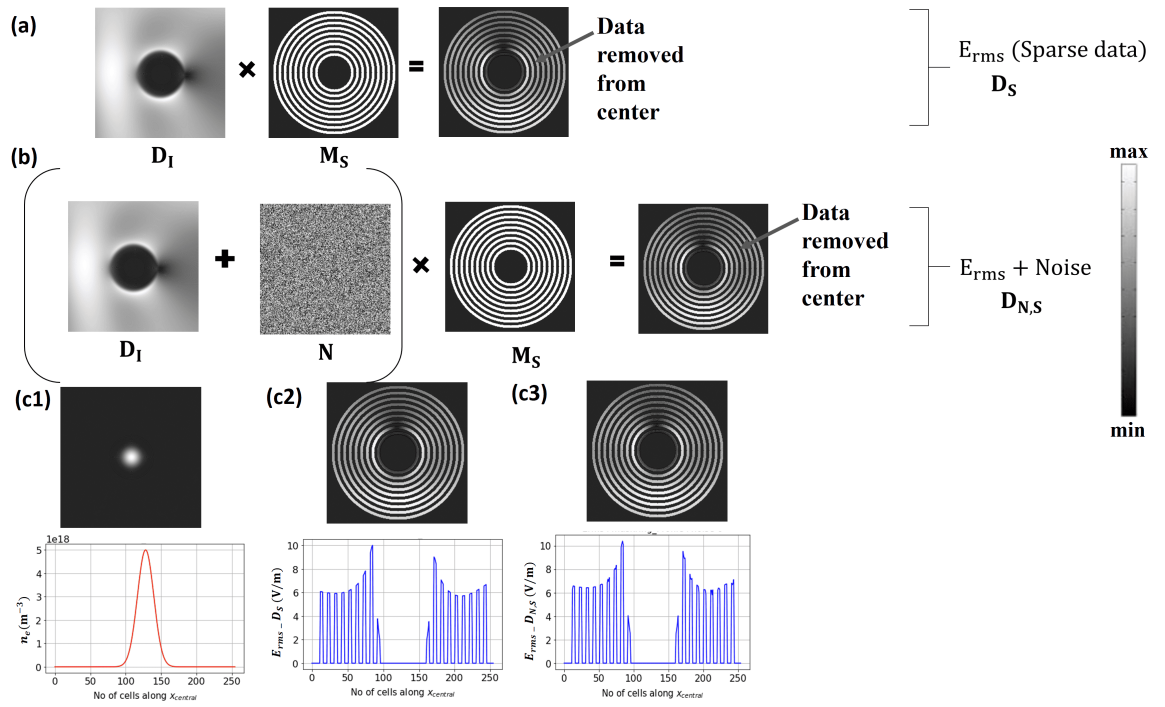


Figure 6.5: Sparse E_{rms} data generation for ML training: (a) by removing the central part of the data and retaining the sparse data using a concentric ring-based mask, (b) addition of noise to the generated dense data, followed by removing the central part and retaining the remaining. (c1-c3) represents the 2-D as well as 1-D density profile, and corresponding, dense E_{rms} data collected for both with and without noise (left to right). The color-bar maxima and minima correspond to E_{rms} . D_I : Initial data, M_S : Mask for sparse data, N : Noise data

plasma confinement. Here, we have considered the white Gaussian noise model [140] to mimic various random processes that add from the natural environment to the experimentally collected data, which is E_{rms} data. The noise model uses a random function to generate numbers between 0 and 1, which follow a Gaussian distribution. For each of the E_{rms} data samples, the noise magnitude has been restricted to 1 – 10% of that sample’s highest E_{rms} amplitude. Thus, it ensures the E_{rms} data and the added noise lie within 20% of actual E_{rms} magnitude for each data sample. Subsequently, a mask is applied to the noisy E_{rms} data to generate either dense or sparse noisy data. Thus, we have obtained four different kinds of E_{rms} data measurements corresponding to a particular density profile, considering the different possibilities in a real experimental setup. This will lead to the following four different data-sets where information in the central part is absent due to masking:

- D_D : dense E_{rms} data-set without noise for different plasma density profiles. Refer to Fig. 6.4 (a).
- $D_{N,D}$: dense E_{rms} data-set with noise for different plasma density profiles. Refer Fig. 6.4 (b).
- D_S : sparse E_{rms} data-set without noise for different plasma density profiles. Refer Fig. 6.5 (a).
- $D_{N,S}$: sparse E_{rms} data-set with noise for different plasma density profiles. Refer Fig. 6.5 (b).

6.3 Deep learning based methodology

The important steps involved in this study (using the proposed data-driven deep-learning (DL) methodology) for the prediction of plasma density from scattered field data obtained outside a plasma chamber are shown in Fig. 6.6. The first step involves the generation of a 2-D scattered E_{rms} field from different plasma profiles when exposed to an EM wave having a fixed frequency. The scattered E_{rms} is achieved using the FDTD-based solver (shown in Fig. 6.6 - block A). Next, the data processing step is followed (Fig. 6.6 - block B), which will lead to one of the masked E_{rms} data pattern ($D_D, D_S, D_{N,D}$,

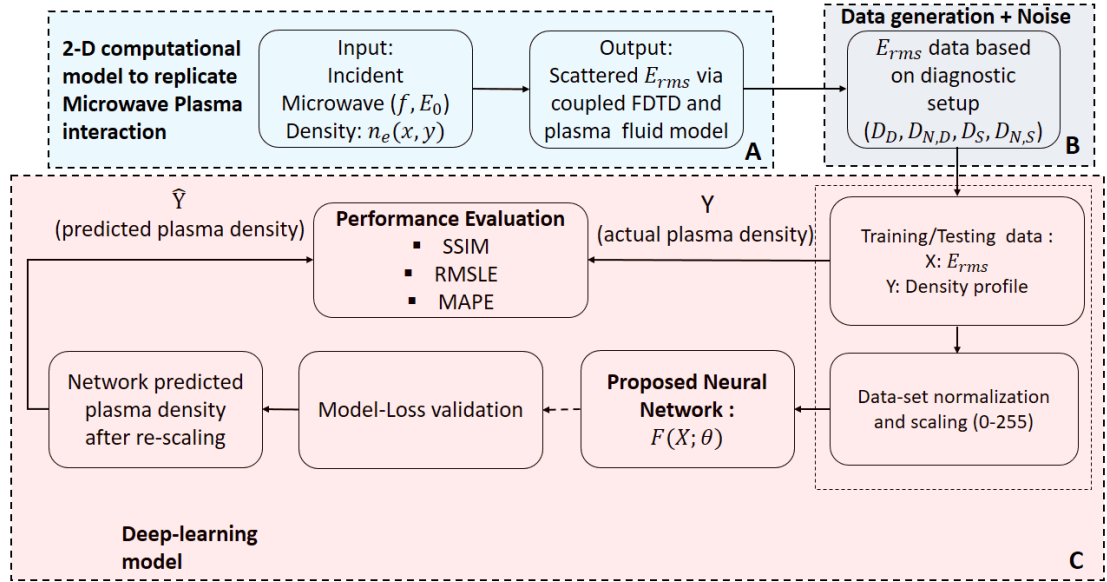


Figure 6.6: Complete workflow used in this study for prediction of plasma density via DL

$D_{N,S}$). The computational steps involved in blocks A and B are explained in the previous section, and we assume that they can also be replicated in a real-experimental diagnostics setup. Training/ testing data consists of a pair of plasma density profiles (Y) and the corresponding masked scattered E_{rms} (X). Figure 6.6 - block C shows the suitable DL model (CNN-based UNet described in the next section) followed by training and evaluation. The DL model requires to be trained on an image data-set. Therefore, first, the generated data pair, the masked E_{rms} (Y), and its corresponding plasma density (X) are normalized between 0 and 1 using the already obtained maximum value from the entire training/testing data-set. Both the maximum plasma density (in m^{-3}) and E_{rms} (in V/m) values are saved to reconstruct the actual magnitude of the quantity, which the trained neural network will generate, through the re-scaling process. For training the proposed DL network, the normalized data-set is scaled in the range of (0-255), and gray-scale images are generated, which are stored as 4-D image arrays with each of the indices representing the number of images, their dimension, and channel (gray-scale) information. The proposed DL model is trained using the generated pair of image-array data-set of masked E_{rms} (X) and plasma density (Y). Since the gray-scale images are generated by scaling the pixel intensity corresponding to the actual normalized value of the data-set pair, proper care must be taken to avoid losing the value due to rounding-off errors. Hence, the image array is fed to

the model to avoid errors instead of directly providing the gray-scale image. The model is then tested using the remaining data sample (testing) from the train/test data-set. The trained network receives masked E_{rms} image X as input and generates the predicted plasma density image (denoted by $F(X; \theta)$, where F represents the DL model and θ is the trained model weight matrix). As previously discussed, the predicted plasma density image is converted to physical density values (in m^{-3}) by re-scaling the predicted normalized output using the saved global maximum obtained from the entire data-set. The DL model's predicted plasma density values are then compared to the 2-D computational solver's actual plasma density values for evaluation.

6.3.1 Deep learning architecture

The DL- architecture uses a CNN-based UNet [62] as depicted in Fig. 6.7.

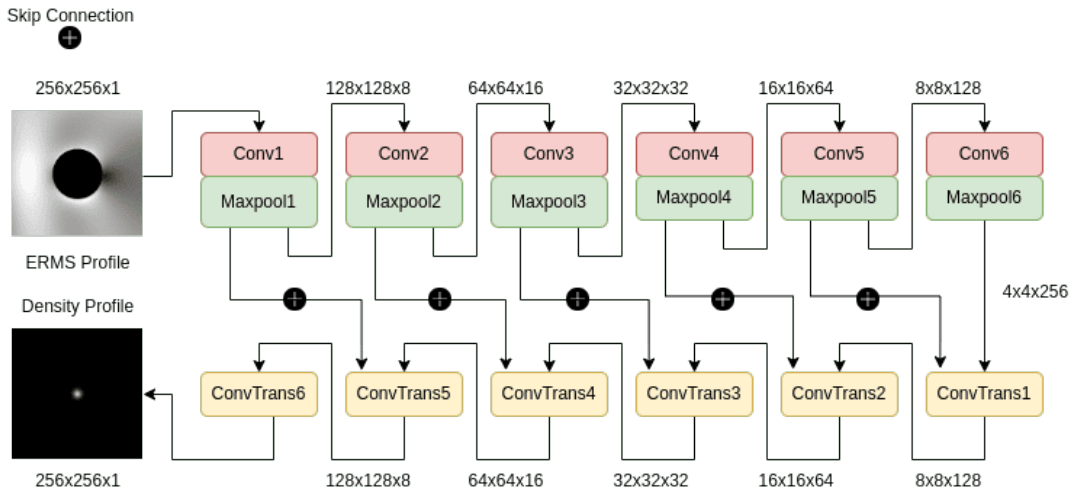


Figure 6.7: The model architecture uses encoder, decoder, and skip connections to predict the plasma density profile from masked EM-wave scattered pattern data-sets

The network consists of two parts: encoders and decoders. The encoder has six convolution layers and six max pool layers. Each convolutional and max pooling layer decreases the input dimension in the encoder to extract finer information at each level. Each of the six encoder units has a convolutional layer with a different number of filters, where the number of filters doubles from the 3×3 kernel size of the preceding unit. The ReLU activation function follows the output of each layer. There are six decoder units, each with a

transposed convolution operation layer with a 2×2 kernel size and a ReLU activation function. The decoder layer will upsample the features to create the network output. The output of the encoder is directly coupled to the input of the decoder. The proposed architecture also implements skip connections by connecting the output of each encoder layer to its matching decoder layer, as shown in Fig. 6.7. It helps to solve the vanishing gradient problem by instantly passing the information through the network and propagating it from the shallower layers to the deeper ones. The final decoder unit produces the predicted density profile data based on the masked E_{RMS} data provided as an input.

6.3.2 Performance metrics

Performance evaluation of the DL-based approach has been carried out in two steps. Firstly, the images (actual and predicted) of the plasma density (n_e) are compared using the Structural Similarity Index Metric (SSIM). The SSIM [125] is an important metric used to compare the quality of the reconstructed images, where the image degradation is recognized as a change in the structural information. For two images x and y of size $N \times N$ pixels, the similarity measure is given by:

$$SSIM = \frac{(2\mu_x\mu_y + (k_1L)^2)(2\sigma_{xy} + (k_2L)^2)}{(\mu_x^2 + \mu_y^2 + (k_1L)^2)(\sigma_x^2 + \sigma_y^2 + (k_2L)^2)} \quad (6.4)$$

where μ denotes the mean, σ^2 denotes the variance, L is the dynamic range of pixel values and $k_1 = 0.01$ and $k_2 = 0.03$. The values of the SSIM index lie between 0 and 1. SSIM metric close to 1 suggests good quality of image reconstruction.

To evaluate the performance of the model in predicting the values of n_e (in m^{-3}) compared to the actual values considered for 2-D FDTD-based fluid-solver, we use two metrics - the MAPE and RMSLE errors metric. The first metric is the average of the absolute percentage error over all the n_e values on the 2-D grid. Let A_{ij} and B_{ij} denote the n_e values used in the FDTD-based computational solver and n_e obtained from DL based approach at $(i, j)^{th}$ point on a $N \times N$ 2D grid, respectively. For the given problem, we have

considered only those grid points within a circular cross-section of the plasma confinement (which corresponds to the central region). The mean absolute percentage error (MAPE) is given by

$$\text{MAPE} = \frac{1}{N_{\text{images}}} \sum_{N_{\text{images}}} \left[\frac{1}{N^2} \sum_{i=1}^N \sum_{j=1}^N \left| \frac{B_{ij} - A_{ij}}{A_{ij}} \right| \right] \quad (6.5)$$

The second metric is the root mean squared logarithmic error (RMSLE) [141]. The RMSLE is defined as

$$\text{RMSLE} = \sqrt{\frac{1}{N_{\text{images}}} \sum_{N_{\text{images}}} \left[\frac{1}{N^2} \sum_{i=1}^N \sum_{j=1}^N (\ln(B_{ij} + 1) - \ln(A_{ij} + 1))^2 \right]} \quad (6.6)$$

The quantity RMSLE is a better performance metric than the root-mean-square error (RMSE) for the studied problem for two reasons. Firstly, high magnitude density data, in both the actual and predicted values, results in a very large RMSE. Secondly, RMSE cannot handle exploding error terms due to outliers that RMSLE can easily scale down and nullify the effects of the prediction error.

6.4 Results and discussion

The study and performance evaluation of the proposed model has been carried out in two phases. First, using the dense data (D_D , $D_{N,D}$) and then using the sparse data (D_S , $D_{N,S}$). In the following subsections, we first discuss the training details and explain the computational experiments and results for each of the two phases.

6.4.1 Training details

The deep learning network is separately trained on different data-sets (D_D , D_S , $D_{N,D}$ and $D_{N,S}$). The network takes a pair of normalized data matrices, the masked E_{rms} , which is given as input to the network (or X) and the corresponding plasma density (Y). The network learns its parameters by minimizing the loss between the actual plasma density (Y) and the output of

Table 6.1: RMSLE and MAPE-based comparison of predicted plasma density with the actual density data for different types of dense data samples

Types of Data sample	Peak plasma density (n_0) (m^{-3})						SSIM 1e16-1e19 (m^{-3})
	1e16-1e17		1e17-1e18		1e18-1e19		
	sub-critical $\omega > \omega_p$		intermediate $\omega \approx \omega_p$		over-critical $\omega < \omega_p$		
	RMSLE	MAPE	RMSLE	MAPE	RMSLE	MAPE	
D_D	0.142	0.12	0.031	0.024	0.025	0.016	0.9998
$D_{N,D}$	0.166	0.153	0.057	0.048	0.043	0.038	0.9995

the network, the predicted plasma density denoted by $F(X; \theta)$ in Fig. 6.6. The loss function for the training of the architecture is given as follows:

$$L(\theta) = \frac{1}{M} \sum_{i=1}^M \|F(X; \theta) - Y\|_2^2 + \lambda \sum_{j=1}^l \|W_j\|_1 \quad (6.7)$$

where M is the total number of training samples, θ represents the network weight parameter matrix, l is the total number of kernels used and W_j is the weight of the j^{th} kernel. The optimizer used for the training is Adam optimizer [124] with a learning rate of $\alpha = 0.001$ and $\epsilon = 10^{-7}$ for numerical stability. The exponential decay for the first moment has been taken as $\beta_1 = 0.9$, and the exponential decay for the second moment is $\beta_2 = 0.999$. L1 regularization is used to counter the problem of overfitting with $\lambda = 10^{-6}$. Uniform Xavier initialization [142] is used as the kernel initializer. The normalized initialization of the Weights of each layer can be heuristically expressed as,

$$W \sim U \left[-\frac{\sqrt{6}}{\sqrt{n_j + n_{j+1}}}, \frac{\sqrt{6}}{\sqrt{n_j + n_{j+1}}} \right] \quad (6.8)$$

where, U is the uniform distribution and n_j is the number of nodes in j^{th} layer. The proposed deep learning model, consisting of six convolutional layers, six Transpose convolution layers, and five skip connections, has 611,833 trainable parameters. The network is trained on NVIDIA Tesla K40c GPU using Keras API with TensorFlow running in the backend.

Table 6.2: Performance evaluation for computational experiments performed with dense data samples (D_D) in the limited range having $n_0 : 1e18 - 1e19 \text{ m}^{-3}$

Number of Data samples	$n_0 : 1e18 - 1e19 \text{ (m}^{-3}\text{)}$		
	RMSLE	MAPE	SSIM
200	0.042	0.032	0.9978
500	0.041	0.030	0.9987
750	0.034	0.029	0.9992
1000	0.021	0.025	0.9994
1500	0.0156	0.021	0.9996

6.4.2 Experiments with dense data (D_D and $D_{N,D}$)

We generated the dense dataset without noise (D_D) by changing the Gaussian plasma density profiles with n_0 ranging from $1e16$ to $1e19 \text{ m}^{-3}$. The data-set comprised 8000 sample pairs (density profile and masked scattered E_{rms}). Subsequently, a dense-dataset with noise ($D_{N,D}$) is prepared as described in section 6.2.1. DL model has been trained separately with D_D and $D_{N,D}$. Both the data-sets were divided in the ratio of 80 to 20 data-samples for training and testing, and the test data-set is further divided with a similar ratio for cross-validation. The MAPE and RMSLE metrics have been separately reported (in Table 6.1) for different ranges of n_0 to understand the prediction capability of the proposed approach in different density ranges. The SSIM metric is reported for the overall range of plasma densities ($1e16 - 1e19 \text{ m}^{-3}$), and we observe that the overall SSIM is very high (0.999). RMSLE and MAPE is < 0.1 for $n_0 > 1e17 \text{ m}^{-3}$ for both D_D as well as $D_{N,D}$, but > 0.1 for density range $1e16 - 1e17 \text{ m}^{-3}$. The better prediction for higher density values can be attributed to the high reflection component in the scattered E_{rms} pattern, which gets more appropriately captured as features by the DL model. We observe improvement in both MAPE and RMSLE (Table 6.2) when the model is trained with samples in the overcritical density range ($1e18 - 1e19 \text{ m}^{-3}$). We also observe that an acceptable prediction can be obtained even using a surprisingly small Data-set size (less than 1000 measurements).

MAPE, RMSLE, and SSIM provide a single number summary about the predictive capability of the proposed approach; however, to obtain a complete qualitative as well as a quantitative understanding of the predicted values of plasma density, we have performed a 2D data analysis as shown in Fig. 6.8

Table 6.3: RMSLE and MAPE-based comparison of predicted plasma density with the actual density data for different sparse data sets

Types of Data sample	n_0 (m^{-3})						SSIM 1e18-1e19 (m^{-3})
	1e16-1e17		1e17-1e18		1e18-1e19		
	RMSLE	MAPE	RMSLE	MAPE	RMSLE	MAPE	
D_S	0.054	0.038	0.031	0.023	0.012	0.010	0.9999
$D_{N,S}$	0.188	0.11	0.051	0.041	0.035	0.027	0.9996

(for D_D) and Fig. 6.9 (for $D_{N,D}$). The first row (a1-a5) in both the figures (Fig. 6.8 and Fig. 6.9), indicates the masked scattered E_{rms} pattern, the input to the model. The second row (b1-b5) shows the corresponding actual density profile based on which the FDTD-based computational solver has generated the scattered E_{rms} pattern. From both the figures (refer Fig. 6.8 and Fig. 6.9), we observe plasma density varies from low to high values (b1-b5). Based on the plasma density profile, the E_{rms} pattern varies, indicating transmission, reflection, and absorption of the propagating microwave. The predicted 2-D profile of plasma density (n_e) from the DL network is shown in row 3 (c1-c5). We observe a good qualitative match with the actual density profile in row 2 (b1-b5). In row 4 (Fig. 6.8 and Fig. 6.9), 1-D comparison between the actual and the predicted n_e profile along the central X-axis ($x_{central}$) shows a good quantitative match between the two. We observe better predictions for dense plasma with peak density (n_0), $> 1e17 \text{ m}^{-3}$. Thus, it validates the observed trend of low MAPE and RMSLE in Table 6.1 and Table 6.2. We have conducted another set of experiments with samples in the density range $1e18 - 1e19 \text{ m}^{-3}$ to understand whether training the model with a narrow range of density values leads to better predictive ability. The experiment also aims to determine the minimum number of measurements required for DL-based prediction with desirable accuracy.

6.4.3 Experiments with sparse data (D_S and $D_{N,S}$)

A similar study is repeated with the sparse E_{rms} data-set, for both without (D_S) and with noise ($D_{N,S}$). The data-sets comprised 7000 samples each for without and with noise, with plasma peak density (n_0) varying in the range $1e16 - 1e19 \text{ m}^{-3}$. Based on training with the masked sparse $E_{rms} - n_e$ data pairs, the trained DL-model has been used to predict the unknown n_e for a masked sparse E_{rms}

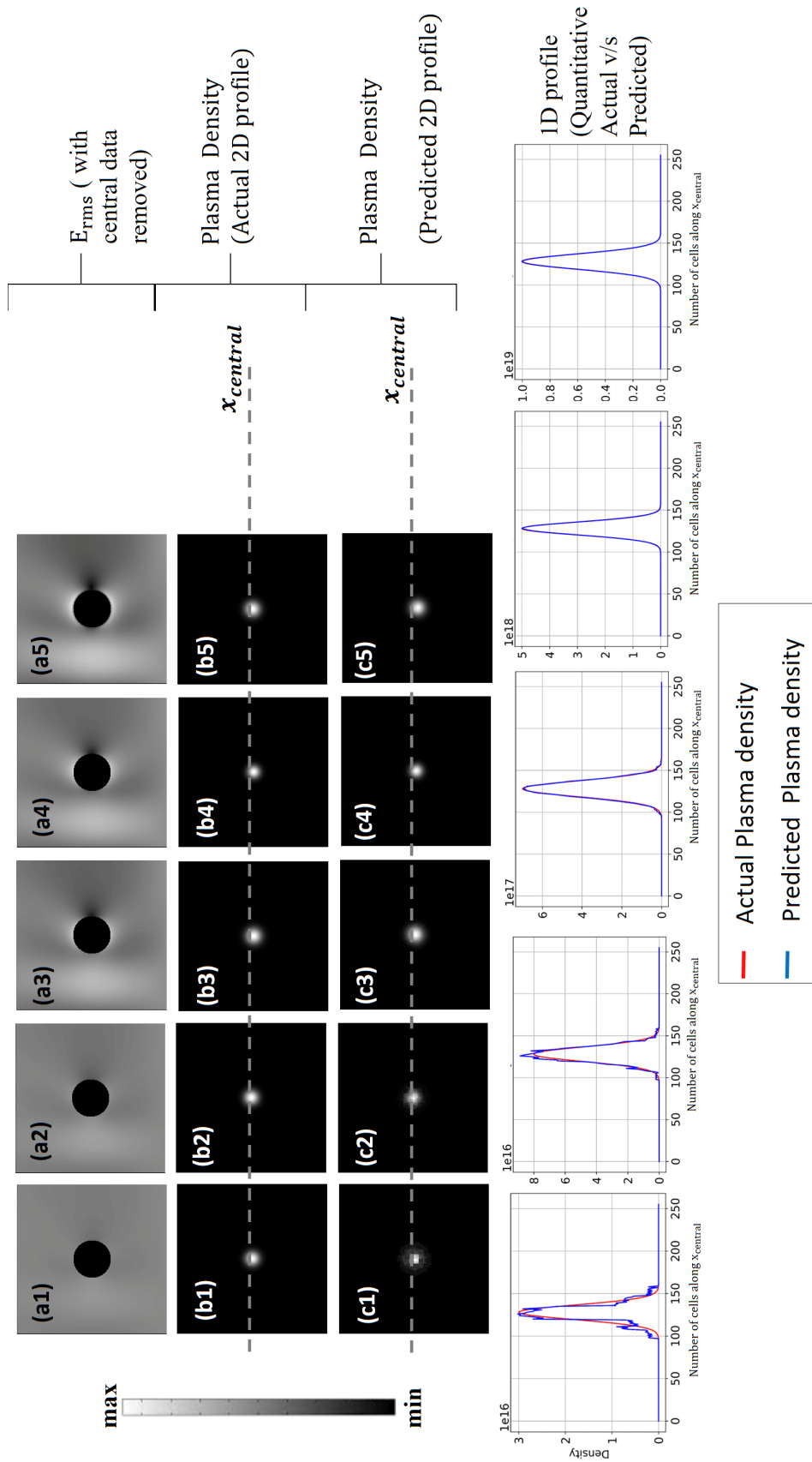


Figure 6.8: Comparative study and results for dense data-set (D_D); Row 1 (a1-a5) masked 2-D E_{rms} dense data obtained from simulations for given input density profile; Row 2 (b1-b5) The actual input plasma 2-D density profile; Row 3 (c1-c5) The predicted 2-D profile of plasma density from the proposed deep learning based architecture; Row 4, Comparison of the accuracy between the magnitude of the actual and predicted 1-D plasma density along the central X-axis ($x_{central}$) of the computational domain.

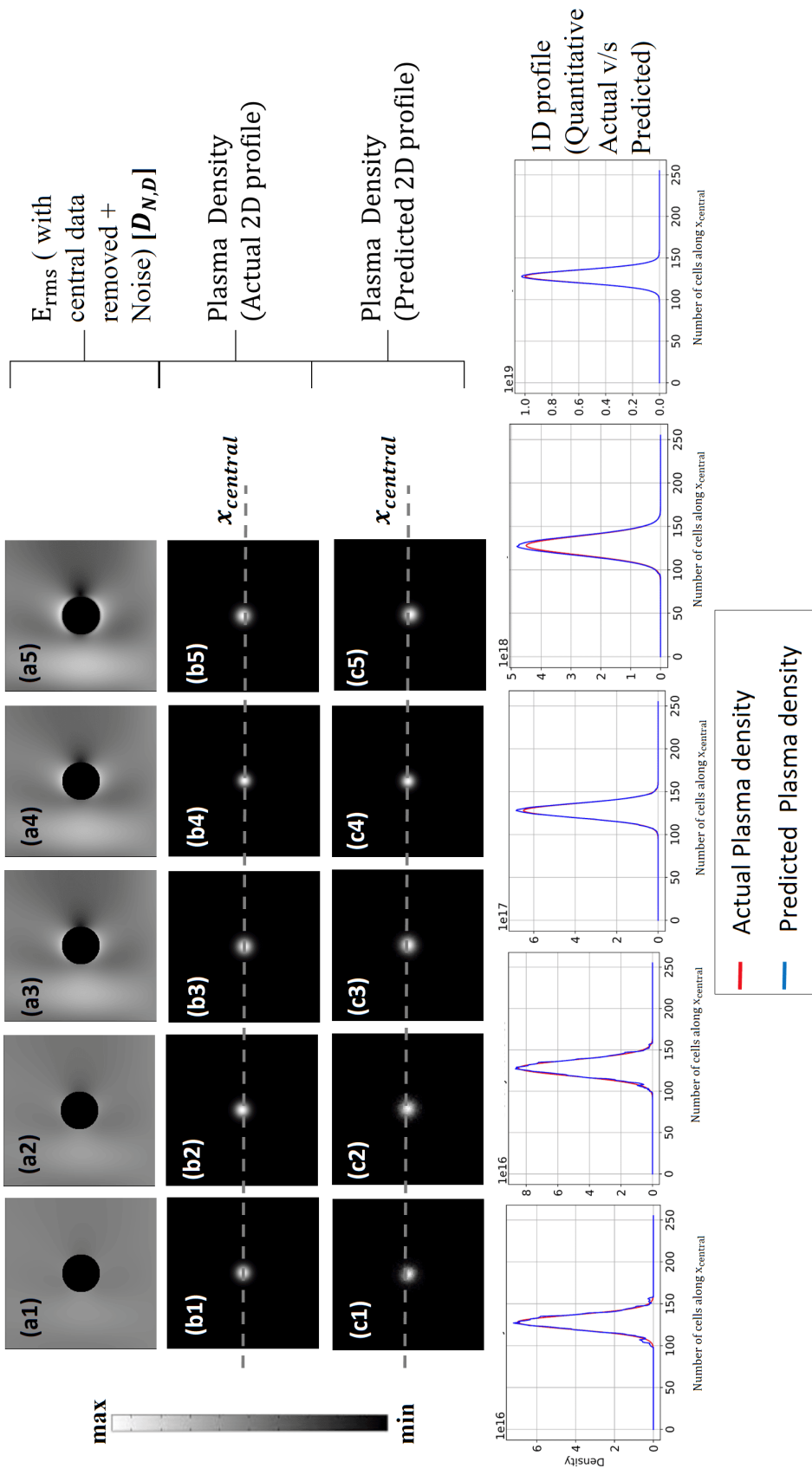


Figure 6.9: Comparative study and results for dense data-set with noise ($D_{N,D}$); Row 1 (a1-a5) 2-D E_{rms} (the increasing maxima in V/m from left to right) dense data with Gaussian noise obtained from plasma density profile using FDTD; Row 2 (b1-b5) The actual plasma 2-D density profile; Row 3 (c1-c5) The predicted 2-D profile of plasma density from the proposed deep learning based architecture; Row 4, Comparison of the accuracy between the magnitude of the actual and predicted 1-D plasma density along the central X-axis ($x_{central}$) of the computational domain in the presence of noise.

test sample. The error metrics RMSLE and MAPE has been separately reported for different range of n_0 in Table 6.3. In addition, the SSIM metric is reported for the overall n_0 range, which is very high (0.999). Even with sparse data where a significant amount of scattered E-field information is absent, based on the metrics' results in Table 6.3, we can infer that the proposed approach can determine the plasma density within an acceptable range.

A comparison between the actual and the predicted 2D plasma profiles for five test samples with different peak density values (under-dense (leftmost) to over-dense plasma (rightmost)) have been shown in Fig. 6.10 (for D_S) and Fig. 6.11 (for $D_{N,S}$). We observe a good qualitative match in both cases with better results for a higher range of density values (for the intermediate and overcritical plasma density regime). 1-D comparison between the actual and the predicted n_e profile along the central X-axis (row 4 in Fig. 6.10 and Fig. 6.11) shows a good quantitative match. Our study shows that the proposed methodology can also be employed with good confidence with sparse measurements of scattered E-field signals outside the plasma with a non-invasive approach.

6.5 Conclusions

A novel deep learning-based plasma diagnostics approach is presented for the first time. The combination of microwave-plasma interaction physics, existing plasma diagnostics techniques, and deep learning to train neural networks for plasma density prediction with high accuracy and minimal effort are proposed. The approach is based on computational experiments involving the scattering of microwaves by considering an unmagnetized, collisional, partially ionized low temperature plasma. Experimentally, the E_{rms} generated from the scattering of the microwave are processed for the estimation of n_e . The approach is applied to different experimental conditions, a range of noises, symmetric density profiles, and sparseness of the E_{rms} collection and their combinations. Every condition has experimental significance, addressing the experimental limitations. The SSIM for a different combination of the experimental conditions for the density estimation remains near ≈ 0.99 , which suggests convincing evidence of accurate n_e estimations. The DL model

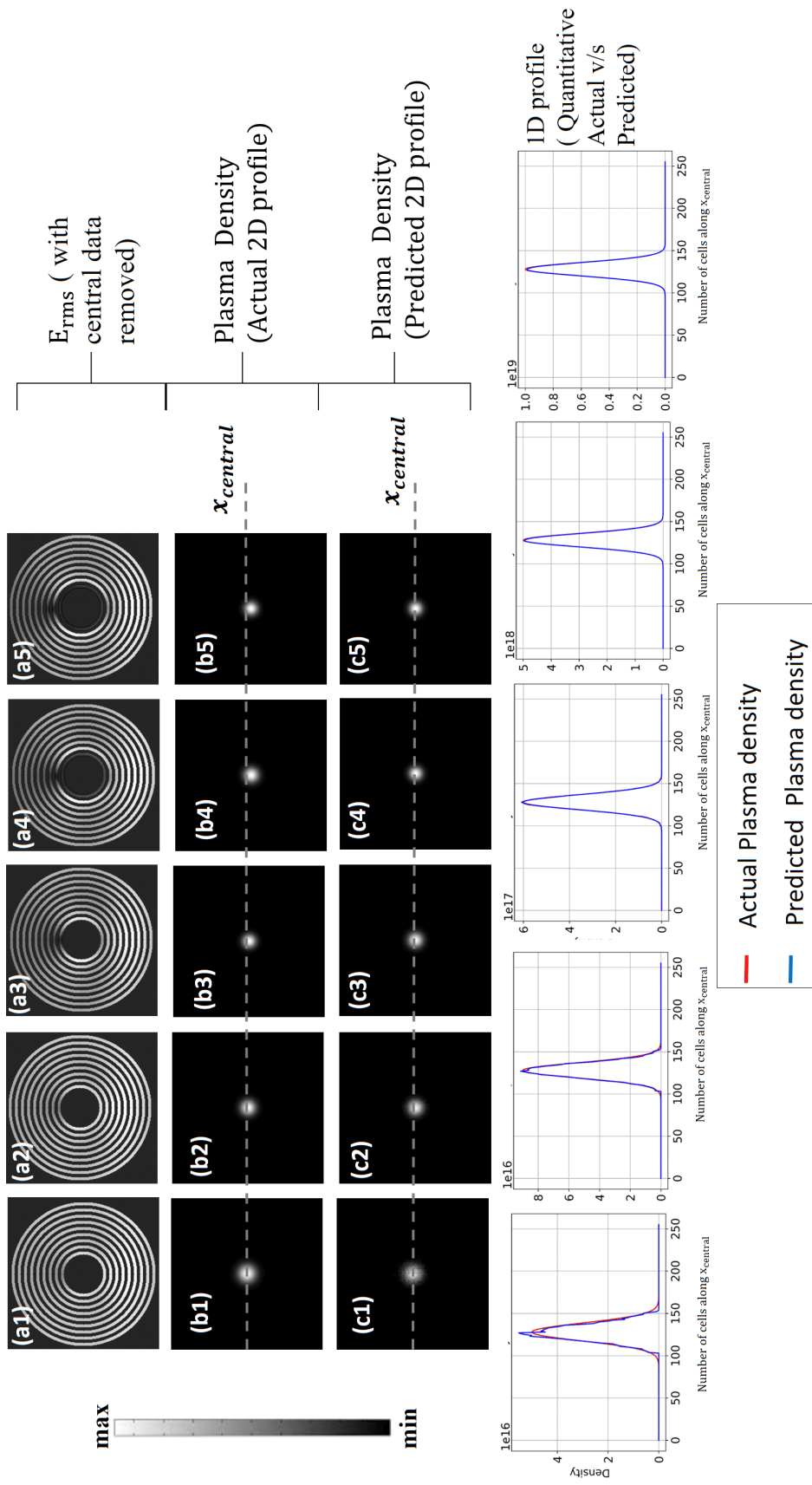


Figure 6.10: Comparative study and results for sparse data-set (D_S); Row 1 (a1-a5) 2-D E_{rms} (the increasing maxima in V/m from left to right) sparse data obtained from plasma density profile using FDTD; Row 2 (b1-b5) The actual plasma 2-D density profile; Row 3 (c1-c5) The predicted 2-D profile of plasma density from the proposed deep learning based architecture; Row 4, Comparison of the accuracy between the magnitude of the actual and predicted 1-D plasma density along the central X-axis ($x_{central}$) of the computational domain.

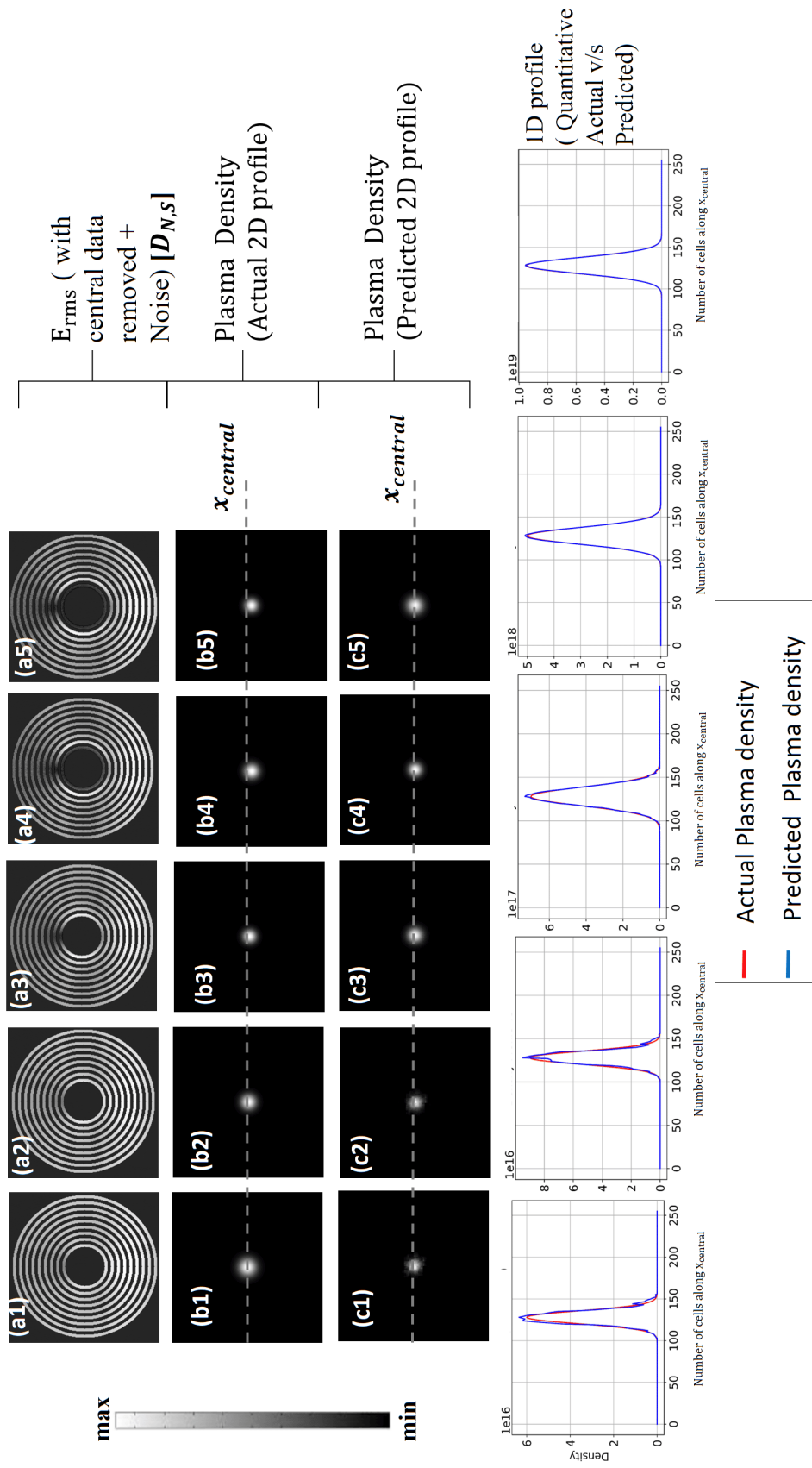


Figure 6.11: Comparative study and results for sparse data-set with noise ($D_{N,S}$); Row 1 (a1-a5) 2-D E_{rms} (the increasing maxima in V/m from left to right) sparse data with Gaussian noise obtained from plasma density profile using FDTD; Row 2 (b1-b5) The actual plasma 2-D density profile; Row 3 (c1-c5) The predicted 2-D profile of plasma density from the proposed deep learning based architecture; Row 4, Comparison of the accuracy between the magnitude of the actual and predicted 1-D plasma density along the central X-axis ($x_{central}$) of the computational domain in the presence of noise.

performed well in reproducing the plasma density profile under the different possible experimental conditions. The predicted results are within acceptable ranges. The percentage error (MAPE and RMSLE) in predictions lies within 1 to 10%. The network performs well even for noisy E_{rms} data. The percentage error lies within the similar range of 1 to 10%. Our study also demonstrates that it is possible to obtain desirable results in the proposed approach even with very few measurements compared to the general belief of large input data requirements for DL training. These results are significant as they are addressed to the real experimental considerations. However, an important real-life issue related to the plasma density profile remains to be addressed: whether this approach will work efficiently in the presence of asymmetry in plasma density profile.

CHAPTER 7

Data-driven approaches for investigation of microwave interaction with asymmetric plasma profiles

7.1 Introduction

In previous chapters 5 and 6, we discussed two classes of problems to study the microwave-plasma interaction, forward and inverse problems. The 2-D scattered E_{rms} pattern is predicted from a given plasma density profile in the forward problem. Whereas for an inverse problem, using the 2-D scattered E_{rms} pattern, the plasma density profile is predicted, leading to such a pattern. However, for both classes of problems, the numerical experiments are limited to the symmetric Gaussian profiles, which are idealistic compared to any real plasmas. The complexity arises in natural and laboratory-generated plasma profiles due to asymmetric and non-homogeneous plasma density distributions, as asymmetry profiles are inherent in any real or laboratory-generated plasma. As discussed earlier, free-space plasma discharges generated during HPM breakdown results in asymmetric plasma profiles [1,2,8,35].

As most of the real plasmas possess asymmetries such as multiple plasma density peaks, random location of the peaks, or width of the profile, these features must be considered while evaluating the proposed DL-based methodology, as discussed in the previous chapter. Such plasma density profiles have sharp gradients, which may result in complex microwave E-field patterns compared to symmetric plasma (Gaussian). The challenge lies in

obtaining sufficient and good quality asymmetric data, which is a prerequisite for any data-driven deep-learning approach.

In this chapter, we present our work in two parts, which are carried out in two phases. Phase-1 is associated with a forward-problem, using DL-model to reconstruct the scattered microwave E-field from the asymmetric plasma profile, and, in Phase-2, an inverse-problem, the model reconstructs the asymmetric profile from a given scattered E-field pattern. The key contributions lie in consideration of a wide range of 2-D asymmetric plasma density profiles inspired by real experiments as a rich set of data for training/testing the deep learning model.

Organization of this chapter

We provide the synthetic data-set generation methodology in section 7.2. Section 7.3 provides an overview of the data-driven deep learning approach, including a flow diagram, data generation, and model architecture for both experiments, Phase-1 and Phase-2. Section 7.4 discusses results, model validation and evaluation, and feature-map-based insights. The conclusion is provided in Section 7.5.

7.2 Synthetic data-set generation methodology

The synthetic data generation for Phase-1 and Phase-2 experiments requires a 2-D scattered E_{rms} field obtained from asymmetric plasma profiles using an FDTD-based simulation of microwave-plasma interaction. The plasma density profile can be generated using either of the two methods: mathematical functions to represent the asymmetric plasma density profile or fluid-based numerical simulations. Phase-1 experiments have been performed using data (fully asymmetric plasma density profiles) generated by mathematical functions and numerical simulations. In contrast, Phase-2 experiments have been performed on mathematical functions based on partial and fully asymmetric (non-Gaussian) profiles. This section discusses the techniques for generating data for Phase-1 and Phase-2 experiments.

7.2.1 Phase-1 plasma-profile generation technique

Phase-1 experiments consist of fully asymmetric data such as non-Gaussian and filamentary types. The two approaches for asymmetric profile generation have been discussed below.

7.2.1.1 Mathematical function based density profiles

The most commonly used 2-D plasma profile for numerical simulation of low-temperature plasmas is a single Gaussian plasma density profile or a combination of multiple such Gaussians [9, 35, 36], which allows accurate replication of experimental results. The density profiles can also be Non-Gaussian, as shown in Fig. 7.1. A representative mathematical formula describing such diverse profiles is provided below,

$$n_e(x, y) = \sum_{i=1}^{P_N} n_{0,i} \exp\left(-\left[\frac{(x - x_{location,i})^2}{2\sigma_{x,i}^2} + \frac{(y - y_{location,i})^2}{2\sigma_{y,i}^2}\right]\right) \quad (7.1)$$

where, the number of plasmoids varies as i goes from 1 to P_N number of plasma peaks, $x_{location,i}$ and $y_{location,i}$ are the center of the i^{th} plasma peak density ($n_{0,i}$) and the spread of the i^{th} plasmoid is controlled by the plasma width $\sigma_{x,i}$ and $\sigma_{y,i}$. Based on the different combination of the parameters, $n_{0,i}$, $x_{location,i}$ or $y_{location,i}$ and, σ_x or σ_y , the non-Gaussian plasma density profiles can be obtained. For Phase-1, we mainly consider the fully asymmetric plasma represented by the Non-Gaussian profile,

- Multiple Non-Gaussian plasmoid profiles, have been generated by varying $n_{0,i}$, $i \in [1, \dots, P_N = 5]$, from density range $\{1e18 - 1e19\}$, as well as vary the location of the peaks which satisfy, $\left\{(x, y) \mid r \in [0, W/4], r = \sqrt{(x - x_{location,i})^2 + (y - y_{location,i})^2}\right\}$, corresponding to different i associated with different number of plasmoids. The $x_{location,i} = x_0 + r_l \cos \theta_i$ and $y_{location,i} = y_0 + r_l \sin \theta_i$, $r_l \in (0, W/16]$ and $\theta_i \in [0, 2\pi]$. The spread of the plasma $\sigma_{x,i} = \sigma_{y,i}$ remains fixed for each i .

- To obtain a Non-Gaussian profile such as Ellipsoid shaped, we keep number of peaks ($P_N = 1$), such that $\{n_{0,i} = n_{0,1} = n_0\}$ and location of a single peak ($x_{location,i} = x_0$ and $y_{location,i} = y_0$) fixed, only vary $\sigma_{x,i} \neq \sigma_{y,i}$, either $\sigma_{x,i} > \sigma_{y,i}$ or $\sigma_{x,i} < \sigma_{y,i}$.

Where x_0 and y_0 define the center of the computational domain, shown in Fig. 7.2, W is the width of the confinement (assumed the plasma exists within the confinement) in terms of EM wavelength (λ), r is the radial distance from the domain center to $W/2$. Where the constraint lies on the spread of the plasma $\sigma_{x,i} = \sigma_{y,i}$, such that $\{\sigma_{x,i} = \sigma_{y,i}\} \in (W/16, W/8)$ to avoid sharp gradients in plasma profile. The profiles are primarily over-dense and correspond to the cutoff condition (high reflection and minimum penetration) for the incoming non-ionizing microwave, which results in a high-quality scattering E_{rms} pattern for DL-model training, as shown in Fig. 7.3 (c1-c3). For Phase-1, the data-set consists of 1200 pairs of fully asymmetric or Non-Gaussian (multiple plasmoids as well as Ellipsoid shaped) plasma density profiles (refer Fig. 7.1 (a2-a3) and Fig. 7.1 (b2-b3)) and corresponding E_{rms} .

7.2.1.2 Fluid simulation based plasma density profiles

The asymmetric plasma profiles can also be generated through numerical simulation of dynamic evolving plasma, such as streamers or filaments, when plasma profiles are exposed to high-power microwaves, resulting in breakdown-induced plasma [8]. The plasma profiles may possess different asymmetry in shape (Gaussian, Ellipsoid, fish-bone, diffused, or streamer), size, occurrence of multiple peaks, and filaments. As discussed in section 2.2, we use the solution of coupled Maxwell's and electron momentum conservation equation (2.1-2.3) along with the fluid continuity equation (2.4) that governs the spatio-temporal evolution of the plasma density averaged over one period of the EM wave during the gas breakdown. The scattered E_{rms} captured from different numbers of filaments can be observed in Fig. 7.4 (c1-c3), with typical peak plasma density in the range $1e18 - 1e22 \text{ m}^{-3}$. We have generated almost 8000 data-set pairs consisting of filamentary patterns, a few shown in Fig. 7.1 (c1-c3) and Fig. 7.1 (d1-d3), and corresponding E_{rms} for

training/testing the DL model.

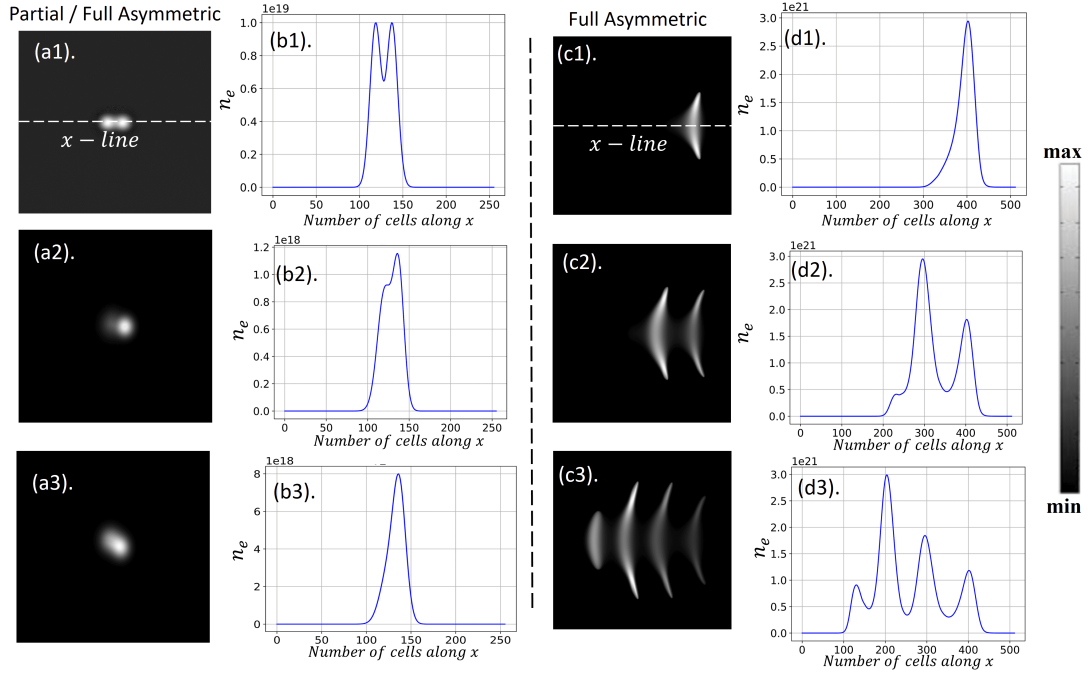


Figure 7.1: Mathematical function-based partial/ fully asymmetric plasma density, (a1-a3) 2-D distribution and (b1-b3) 1-D distribution along x-line. Fluid simulation based fully asymmetric plasma density, (c1-c3) 2-D distribution, and (d1-d3) 1-D distribution along x-line.

7.2.2 Phase-2 plasma profile generation technique

For Phase-2 we consider both partial asymmetric and fully asymmetric plasma profiles, which can be obtained using mathematical function-based density profiles. We have already described fully asymmetric profiles in subsection 7.2.1. The partial asymmetry can be obtained by Gaussian profiles that are not centered at the simulation domain's midpoint but instead distributed randomly (e.g., left, right, top, or bottom relative to x_0 and y_0), as well as profiles composed of Gaussian plasma profiles with more than one peak.

- We have generated multiple Gaussian plasmoids, keeping peak density, $n_{0,i} = n_0$, fixed for $\mathbf{i} \in [1, P_N = 2]$, restricted four plasmoids within W . Vary the location of Gaussian peaks such that $x_{location,i} = x_0 + (-1)^i W/8$ or $W/4$ and $y_{location,i} = y_0 + (-1)^i W/8$. The spread of the plasma $\sigma_{x,i} = \sigma_{y,i}$ remains fixed for each \mathbf{i} .
- To obtain double Gaussian, we keep $n_{0,i} = n_0$ for $\mathbf{i} \in [1, P_N = 2]$ as well as $\sigma_{x,i} = \sigma_{y,i}$ fixed, vary the location of Gaussian peak, $x_{location,i} =$

$$x_0 + (-1)^i W/8 \text{ or } W/4 \text{ and } y_{location} = y_0.$$

where the constraint lies on the spread of the plasma $\sigma_{x,i} = \sigma_{y,i}$, such that $\{\sigma_{x,i} = \sigma_{y,i}\} \in (W/16, W/8)$ to avoid sharp gradients in plasma profile.

Next, we discuss the data preparation associated with Phase-2 to obtain the masked E_{rms} data required for density estimation.

7.2.2.1 Data-set preparation

The data processing step is important for the Phase-2 experiment, which mimics the real experimental conditions while obtaining scattered E_{rms} data required for the plasma density estimations. The outcome of data pre-processing leads to one of the masked E_{rms} data patterns ($D_D, D_S, D_{N,D}, D_{N,S}$) as discussed in section 6.2.1. The difference lies in the plasma density profile, which is asymmetric here. Additionally, we have considered highly sparse data (for D_S and $D_{N,S}$) equivalent to sparse sensor deployment, as well as higher noise in the input data for both dense and sparse ($D_{N,D}$ as well as $D_{N,S}$).

For Phase-2, the data-set consists of 9000 pairs from partial asymmetry profile (double and multiple Gaussian (with random peak density locations)) as well as 1200 pairs of fully asymmetric or Non-Gaussian (multiple plasmoids as well as Ellipsoid shapes), and corresponding E_{rms} . The plasma profiles are shown in Fig. 7.1 (a1-a3) and Fig. 7.1 (b1-b3).

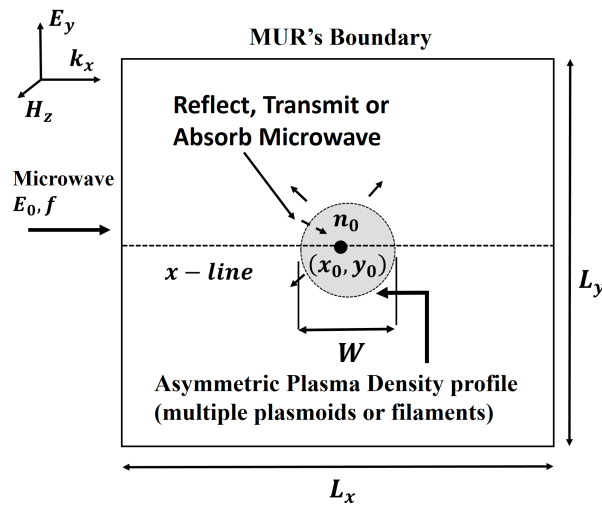


Figure 7.2: Schematic representation of the computational domain to simulate the microwave interaction with various asymmetric plasma profiles. Domain length along x and y , L_x and L_y , is expressed in terms of EM wavelength (λ).

7.2.3 FDTD-based synthetic training data-set generation

In subsection 7.2.1 and 7.2.2, we discussed the generation of plasma density profiles corresponding to Phase-1 and Phase-2 investigations. The profiles include fully and partially asymmetric types such as Non-Gaussian Ellipsoids, multiple (Gaussian and Non-Gaussian) plasmoids, and plasma filaments. For training, we need the corresponding scattered E_{rms} when an EM wave is incident on this asymmetric profile. For this purpose, we performed FDTD simulations using a discretized 2-D computational domain as depicted in Fig. 7.2, with dimensions of $1\lambda \times 1\lambda$. Here, λ represents the free space wavelength. The grid resolution uses 256 grid points per wavelength (λ) for the multiple plasmoids and 512 grid points for filaments, for better accuracy [8]. In Phase-1 experiments, the plasma profiles are exposed to EM waves with

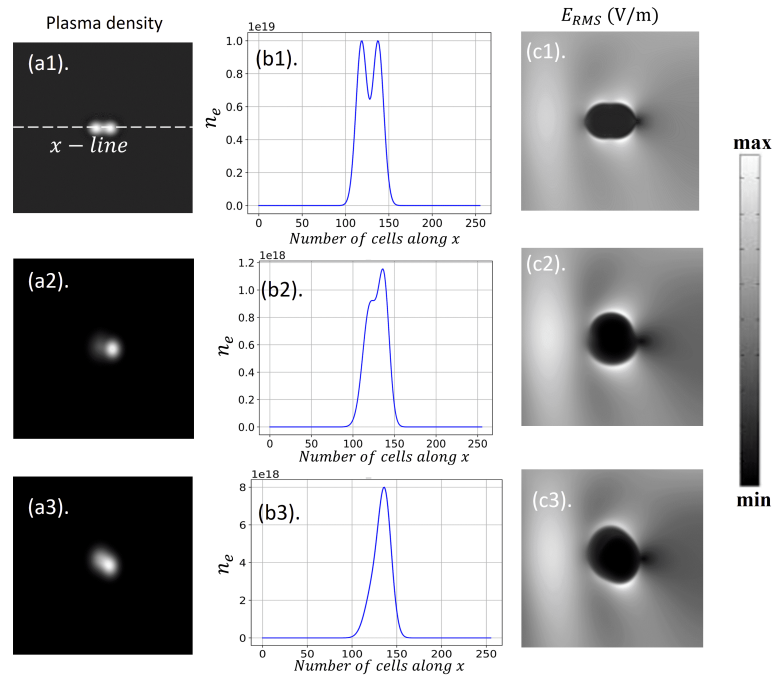


Figure 7.3: Mathematical formulation of Partial/Full asymmetric profile (Gaussian multiple plasmoids, Non-Gaussian (multiple plasmoids and Ellipsoid)) data-set, plasma density (a1-a3) 2-D distribution, and (b1-b3) 1-D distribution along x-line. (c1-c3) The corresponding scattered E_{rms} 2-D pattern.

different amplitudes and frequencies. For Non-Gaussian (multiple plasmoids and Ellipsoids), the microwave E-field amplitude of 10 V/m and a frequency of 1 GHz. In the case of plasma filaments, E-field amplitude of 5 MV/m and a frequency of 110 GHz. For Phase-2 experiments, partial and full asymmetry plasmoids are exposed to a plane EM wave with an amplitude of 10 V/m and a

frequency of 500 MHz. These waves are incident from the left-hand side of the computational domain, as illustrated in Fig. 7.2. For the Phase-1, air plasma is considered at 2 and 760 torr pressures. For the air plasma in this study, the collision frequency ν_m is calculated using $\nu_m = 5.3 \times 10^9 p$, where p represents the ambient pressure in torr. In contrast, Phase-2 experiments only utilize air plasma at 2 torr. The FDTD simulated scattered E_{rms} pattern originating from Non-Gaussian (Fig. 7.3 (a1-a3)) and filamentary (Fig. 7.4 (a1-a2)) profiles are shown in Fig. 7.3 (c1-c3) and Fig. 7.4 (c1-c3), respectively.

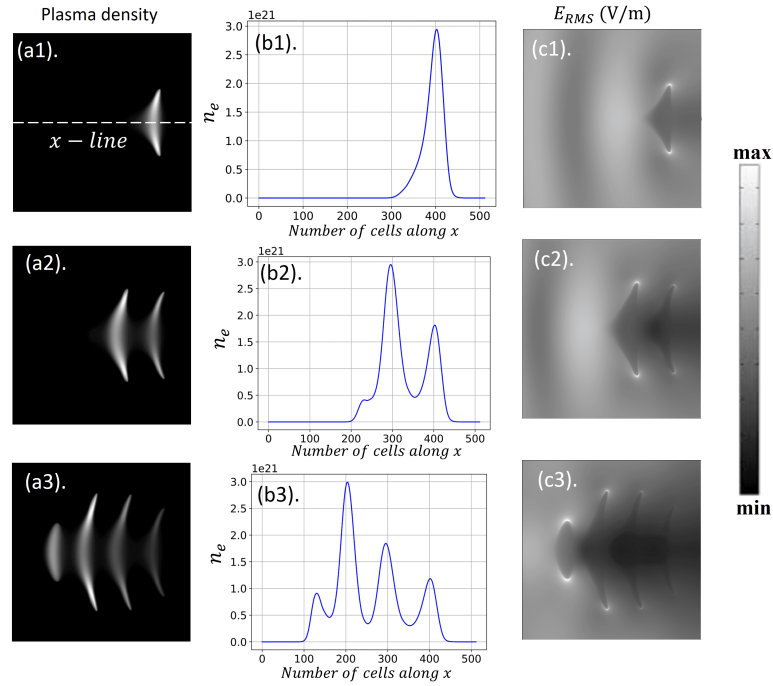


Figure 7.4: Fluid simulation based filamentary profile data-set, plasma density (a1-a3) 2-D distribution and (b1-b3) 1-D distribution along x-line. (c1-c3) The corresponding scattered E_{rms} 2-D pattern.

7.3 Data-driven deep learning based approach

We provide a brief overview of the data-driven deep-learning based approach to study the interaction of microwaves with asymmetric plasma density profile for both Phase-1 and Phase-2 experiments.

7.3.1 Deep-learning methodology

The proposed DL methodology for the two experiments resembles the earlier methods. Specifically, for Phase-1, we refer to the methodology outlined in

section 5.1, while for Phase-2, the methodology is detailed in section 6.3. The DL model training and testing data-sets for Phase-1 comprise pairs of scattered E_{rms} (Y) corresponding to plasma density profiles (X), generated in subsection 7.2.1. For Phase-2, the data-set consists of pairs of plasma density profiles (Y), generated in subsection 7.2.2, and the corresponding masked scattered E_{rms} data (X, from the set $(D_D, D_S, D_{N,D}, D_{N,S})$). All the data (the plasma density profile and corresponding FDTD simulated E_{rms} pattern obtained from the discretized computational domain) are converted into gray-scale images obtained by normalization (using the global maximum of the data-set) and scaling to the 0-255 range. The remaining steps are similar as in section 5.1 and 6.3, for Phase-1 and Phase-2, respectively.

7.3.2 Deep-learning architecture

The proposed architecture for training/testing the Deep learning model uses the similar CNN-based UNet architecture discussed in chapters 5 and 6. All the architecture details remain the same, except the input-output data-pairs must be interchanged as per the requirement of both experiment phases.

7.3.3 Training details

During training, the DL-network adapts its parameters to minimize the discrepancy between the predicted image data, labeled as $F(X;\theta)$, and the actual image, denoted as Y . Here Y is E_{rms} for Phase-1 and plasma density profile for Phase-2. This optimization is achieved by using a loss function ($\mathcal{L}(\theta)$), as discussed in previous chapters. The training details remain the same as discussed in Chapters 5 and 6. Training takes place on an NVIDIA Tesla K40c GPU, utilizing Keras with the TensorFlow backend, spanning 300 epochs. The loss values observed during training serve as an indicator of effective learning of the DL model. As an example, we show in Figure 7.5 (a) and (b), the trends in the training and testing loss values over 300 epochs corresponding to Non-Gaussian and filament plasma profiles. The lower loss magnitude for the Non-Gaussian profile compared to filaments is likely attributed to the former having a less asymmetric density distribution, resulting in smoother variations in the E_{rms} data.

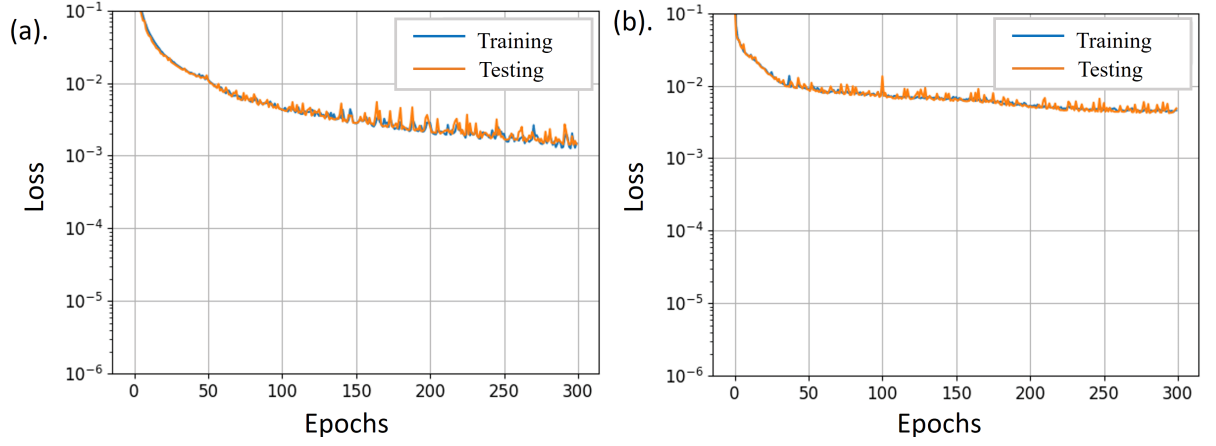


Figure 7.5: Mean squared error loss in training (learning sample)/testing (unseen data-sample) the model for (a) Non-Gaussian and (b) filament plasma profile.

7.4 Results and discussion

In this section, we provide separate discussion for each, Phase-1 and Phase-2, which comprises different computational experiments for DL model training-testing, followed by data-driven DL-model performance evaluation on the corresponding generated data-set, using 2-D/1-D based comparative results and discussion, and, finally, DL-network's feature-map based learning for each data-set.

7.4.1 Phase-1: Experiments with Non-Gaussian profile and filaments for forward-problem

7.4.1.1 DL-model training/testing simulated results

While training the network, we used separate data-sets containing Non-Gaussian (multiple plasmoids and Ellipsoids) profiles and filaments (single, double, three, and more). For training the DL-model with both types of data-set, we gradually changed the peak plasma density from $n_0 = 1e18 \text{ m}^{-3} \rightarrow 1e22 \text{ m}^{-3}$. The FDTD-based solver and DL-based approach results for two different plasma density profiles have been compared in Fig. 7.6. The first row in Fig. 7.6 represents the 2-D and 1-D comparison between the ground truth (FDTD generated) and predicted E_{rms} pattern resulting from Non-Gaussian profile, which is overdense ($n_0=1e18 - 1e19 \text{ m}^{-3}$). The second row represents the 2-D and 1-D scattered EM wave pattern obtained using the

conventional FDTD-based solution and predicted E_{rms} pattern resulting from filamentary profiles which are overdense ($n_0 - 1e18 - 1e22 \text{ m}^{-3}$). We can observe that both the scattering patterns closely match when observed as the near zero residual plot in 2-D and as a quantitative (magnitude-wise) 1-D plot obtained by taking a 1-D profile across the x -line.

For the $1\lambda \times 1\lambda$ problem size, we observe a speedup of around 300-500 times using the DL-based approach compared to the traditional technique, such as FDTD, for simulations performed on an Intel(R) Xeon(R) CPU @ 2.20GHz with x86_64 architecture.

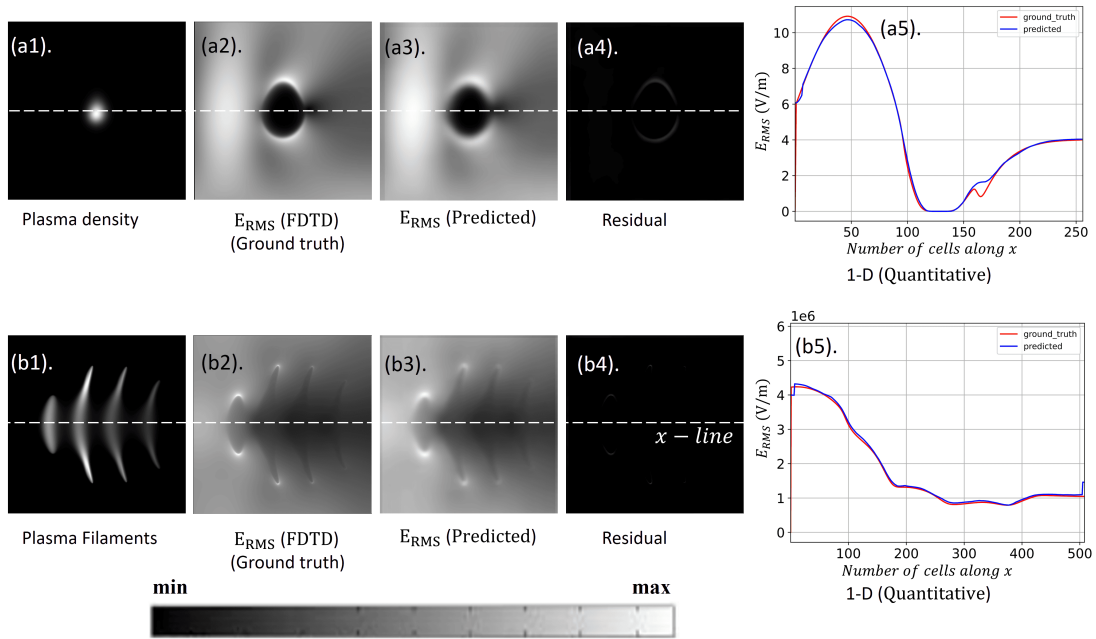


Figure 7.6: The 2-D, 1-D qualitative and quantitative comparison of actual and predicted scattered E_{rms} from Non-Gaussian (a1-a5) and (b1-b5) filamentary plasma profile, respectively.

7.4.1.2 Model performance evaluation using different metrics

We assessed the performance of the DL-model using different performance metrics, such as SSIM and RMSLE or RMSE, as discussed in previous chapters. We compared the real (ground-truth) and predicted images of scattered E_{rms} pattern obtained from the asymmetric plasma profile (such as Non-Gaussian plasmoids and filaments (denoted as n_e)) using the Structural Similarity Index Metric (SSIM). The SSIM produced a score between 0 and 1. A score nearing 1 indicates high-quality image reconstruction. Additionally, we use RMSLE or RMSE to determine accuracy between the model predicted E_{rms}

Table 7.1: Performance metrics evaluation for scattered E_{rms} obtained from different computational experiments on asymmetric dense plasma density profile data. The peak plasma density is n_0 .

Data-set	$n_0 : 1e18 - 1e22 \text{ (m}^{-3}\text{)}$	
	RMSLE/RMSE	SSIM
Non-Gaussian	0.44 (RMSE)	0.982
Filaments	0.66 (RMSLE)	0.987

values (expressed in V/m) against the ground truth E_{rms} data obtained from simulating a 2-D FDTD-based fluid-solver. The results on the test cases for varying data-set profiles and density range in training are shown in Table 7.1. We can observe that the average SSIM index is similar for both the profiles ≈ 0.98 , a score nearing 1. The mean squared error (RMSLE/RMSE) is observed to be within one order. Both indicate the high fidelity of the DL technique in terms of reconstruction and accuracy of the E_{rms} pattern.

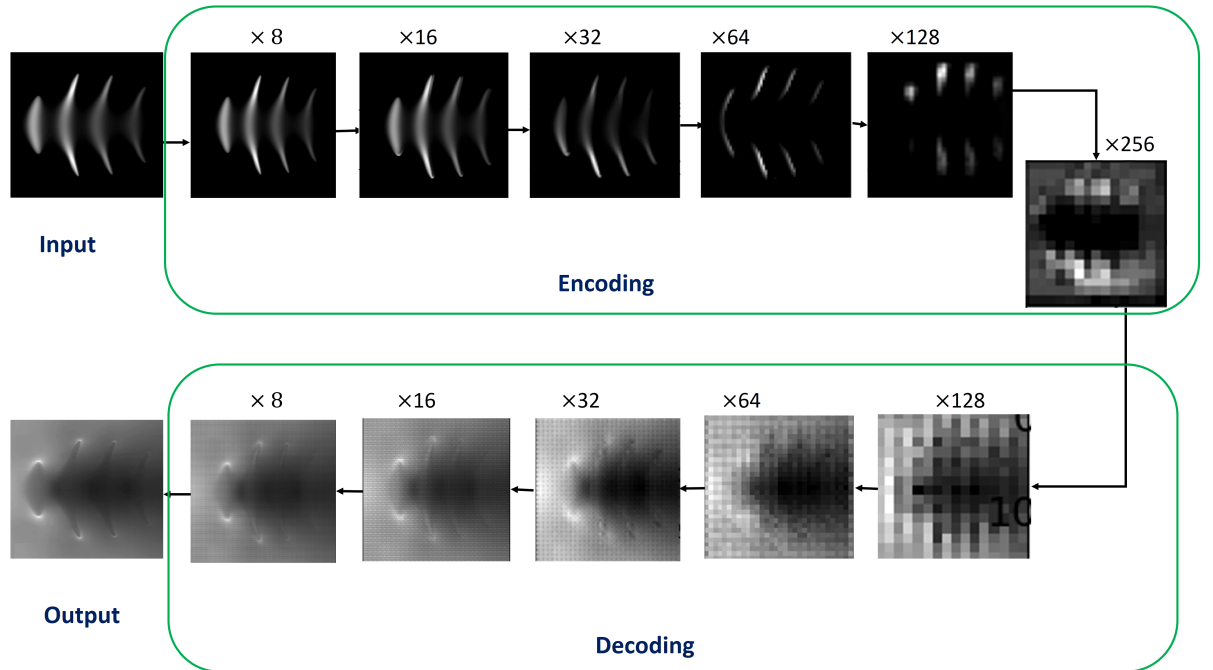


Figure 7.7: Feature maps correspond to the output of each of the encoder and decoder units of the DL model. A single feature map from each convolutional unit is shown for representation. The model input and the final output of the DL-network are the plasma density profile and its corresponding E_{rms} image.

7.4.1.3 Model feature-map based learning from asymmetric filamentary plasma

We discuss here the CNN-Unet feature-map based learning methodology. Figure 7.7, shows the encoding and the decoding unit. The encoding and decoding unit uses the convolution and the transposed convolution layers, whose outputs are the important features, as shown in the figure. The features conserve the spatial locality in the image and allow better reconstruction of the output. The numbers over each image denote the total number of filters in the convolution/transpose-convolution unit. The process involves down-sampling the actual image into more refined features, and encoders learn to detect the edges or boundaries (finest features), followed by up-sampling that allows the decoder to learn a mapping between the finest features with the required prediction. Here, we can observe that the model extracts the important features from the original filamentary plasma density data. Mostly, the patches of pixels that have useful plasma density variation (as intensity in gray-scale images) to predict the scattering E_{rms} pattern information as reconstructed image data.

7.4.2 Phase-2 : Experiments with asymmetric plasma profiles for inverse-problem

Phase-2 experiments with asymmetric profiles have been performed in the density range ($1e18 - 1e19 \text{ m}^{-3}$). We have considered various real-life situations during the plasma density estimation in designing our numerical experiments. Those include the sensor (capturing scattered E_{rms} pattern) deployment strategy, which may result in highly sparse data and additional background noise to the sensor data. For the asymmetry profiles, we have considered Gaussian profiles with centers located at random locations (top, bottom, left, or right relative to x_0, y_0), two Gaussian profiles, and Non-Gaussian profiles with multiple peaks. The Gaussian data-sets have been referred to as partially asymmetric, while the Non-Gaussian data-set as a fully asymmetric data-set. Both dense (D_D) and sparse (D_S) data-sets have

been considered similar as in chapter 6. The simulated results are presented based on the training and testing of the DL-model performed on the different data-sets (dense (D_D) and highly sparse data (D_S)) as well as the effect of noisy input (masked E_{rms} dense data(D_D)) are presented here.

7.4.2.1 1D/2D comparison of DL-model simulated results and performance evaluation

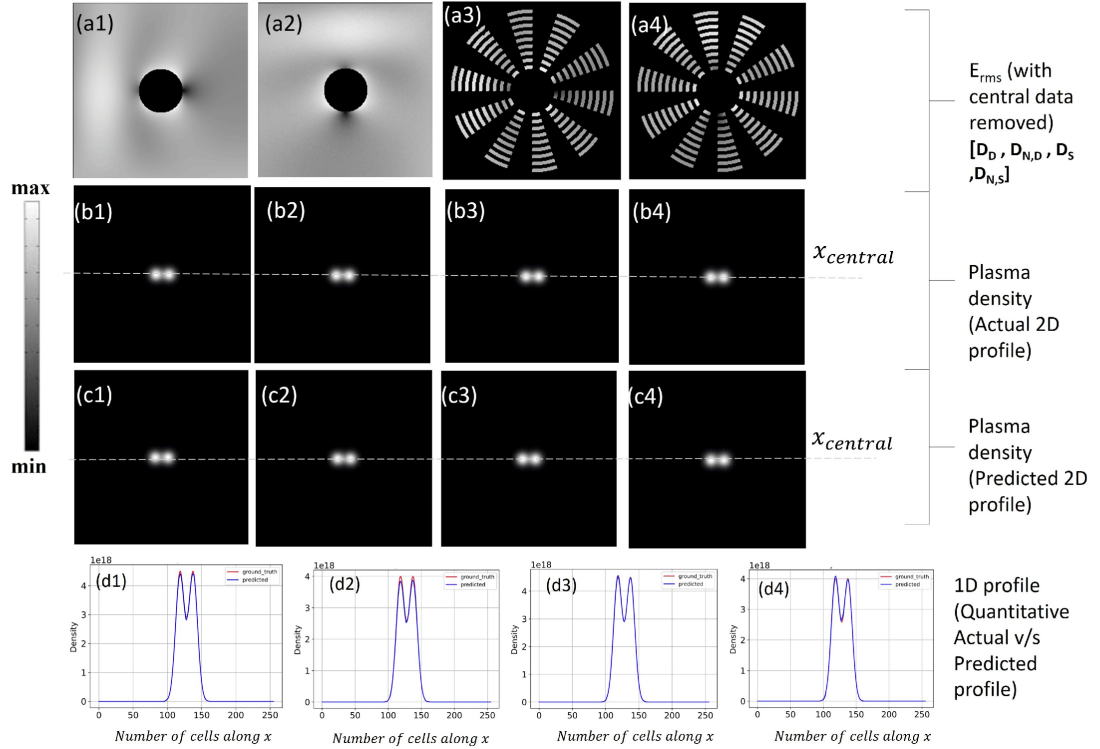


Figure 7.8: Comparison of results for dense (D_D) and sparse (D_S) data samples without and with noise (for partially asymmetric), having two Gaussian plasma profiles with peaks not located at the center of the simulation domain (x_0, y_0).

Comparison between the actual and the predicted 2-D plasma profiles for four test samples (two each for dense and very sparse masked E_{rms} data) for different locations of the peak density values in the case of partial asymmetric data-set has been shown in Fig. 7.8. We observe a good qualitative match for both dense and very sparse data. 1-D comparison between the actual and the predicted n_e profile along the X-axis (row 4 in Fig. 7.8) shows a good quantitative match.

We use 2-D plots of the actual and model-predicted plasma profile along with the residual to evaluate the results for fully asymmetric data (Non-Gaussian shapes with multiple peaks) as shown in Fig. 7.9 and 7.10 (for input E_{rms} , data

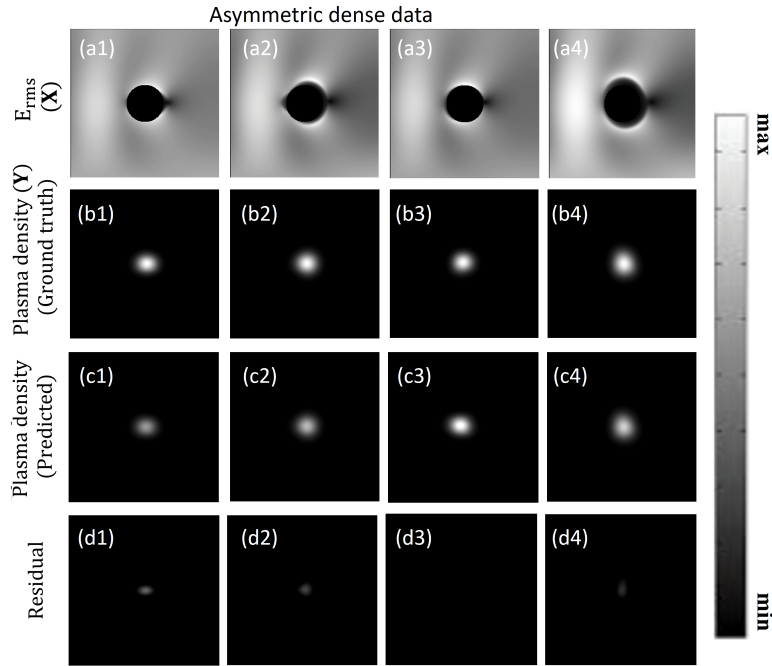


Figure 7.9: Comparison of results for completely asymmetric density profile for dense E_{rms} data, D_D . (a1-a4) the masked E_{rms} , (b1-b4) the ground truth, (c1-c4) the predicted plasma density profile for D_D , and (d1-d4) the residual (difference between actual and predicted) to indicate the degree of mismatch.

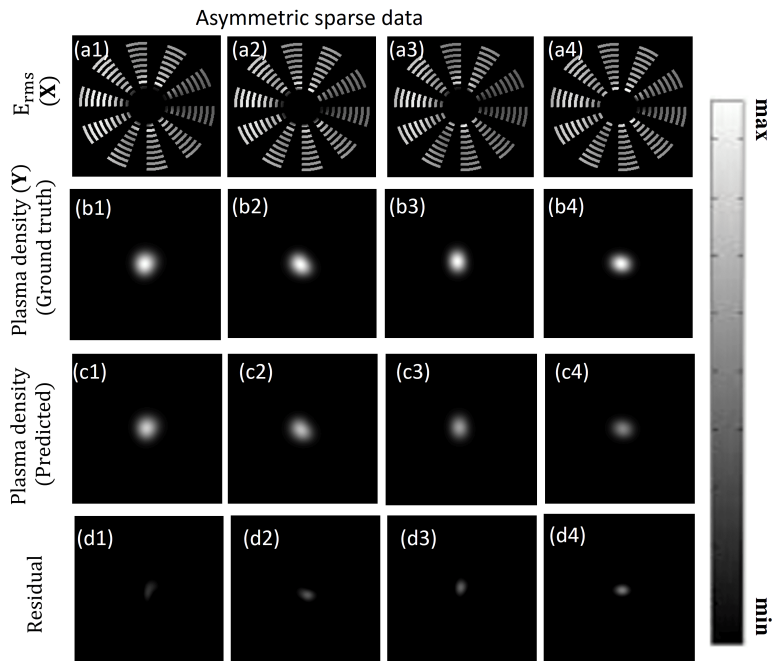


Figure 7.10: Comparison of results for completely asymmetric density profile for sparse E_{rms} data, D_S . (a1-a4) the masked E_{rms} , (b1-b4) the ground truth, (c1-c4) the predicted plasma density profile for D_S and (d1-d4) the residual to indicate the degree of mismatch between actual and predicted asymmetric profiles.

Table 7.2: Performance evaluation for computational experiments performed with E_{rms} data both (dense and sparse) corresponds to plasma density profile having partial and full asymmetry. The peak density range having $n_0 : 1e18 - 1e19 \text{ m}^{-3}$

Types of density profiles and Data samples	$n_0 : 1e18 - 1e19 \text{ (m}^{-3}\text{)}$			
	RMSLE	MAPE	SSIM	
Partial asymmetry	D_D	0.03	0.024	0.9998
	D_S	0.0425	0.035	0.9998
Fully asymmetry	D_D	0.3	0.28	0.9963
	D_S	0.24	0.18	0.9964

D_D and highly sparse D_S , respectively). We can observe that the DL model can capture asymmetry (either multiple peaks with different peak densities that are merged together, locations of the different peaks, or the shape of the profile, such as Ellipsoid, and more) in the plasma profile within acceptable accuracy. It is interesting to observe that the model-predicted plasma density profile has a good spatial resolution that matches the actual plasma profile, and we obtain an average SSIM of more than .99 for different samples refer to Table 7.2. Also, we can observe that the DL model can preserve the order of the plasma peak densities within a desirable accuracy. The decrease in accuracy compared to predictions of symmetric Gaussian profiles (in chapter 6) can be attributed to multiple factors, particularly high-density gradients, and asymmetry, leading to complex scattering patterns. The results (shown in Fig. 7.9, Fig. 7.10 and Table 7.2) indicate that the DL-based approach can predict the profile shape, the location of plasma peaks, and the peak plasma density with desirable accuracy, the primary diagnostic requirement for any real laboratory experiment.

7.4.2.2 Effect of noisy input data on the DL-model performance

We performed noise effects (by changing the amplitude/relative amplitude of noises to the measured E_{rms} signal, i.e., SNR analysis) on the DL-model prediction performance. Based on [143], we found choosing relative noise amplitudes, 10% to 25% results in an SNR reduction from 10 to 4 dB, which makes noise levels nearly indistinguishable from the desired E_{rms} signal. Our

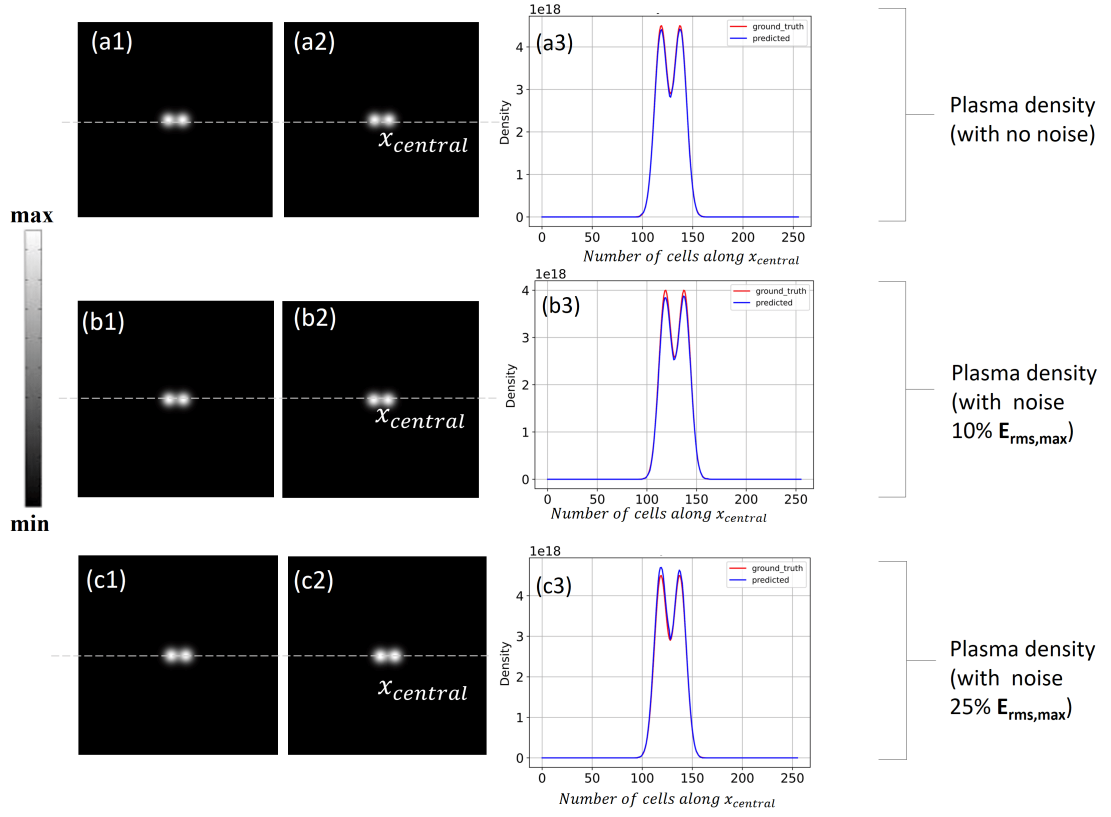


Figure 7.11: Comparative study and results for dense data (D_D), considering two Gaussian plasma profiles not symmetric about the computation domain center, with different relative noise amplitudes.

Table 7.3: Performance evaluation for computational experiments performed with dense E_{rms} data corresponds to plasma density profile having asymmetry. The peak density range having $n_0 : 1e18 - 1e19 \text{ m}^{-3}$

Density profile	Test data-sample	$n_0 : 1e18 - 1e19 \text{ (m}^{-3}\text{)}$		
		RMSLE	MAPE	SSIM
Partial asymmetry	D_D	0.03	0.024	0.9998
	$D_{N,D}$ (10%)	0.056	0.046	0.9997
	$D_{N,D}$ (25%)	0.055	0.042	0.9996

numerical experiment tried to predict the plasma profile, with two Gaussian peaks whose center does not coincide with the domain center (a spatial asymmetry), from the E_{rms} dense data-set. We varied the added noise level (10 to 25%), the results can be observed in Fig. 7.11.

From Table 7.3, we can observe that different relative amplitudes of added noise to the signal can vary the predicted plasma density peak value (increase in MAPE and RMSLE values compared to a no-noise case). However, shape-wise (spatial distribution) remains unchanged (similar SSIM). Further increase of noise amplitude (10-25%) has a negligible effect on the overall model performance.

7.4.2.3 Feature-map based learning for inverse-problem

For the Phase-2 experiments similar to Phase-1, we present the DL-model feature-map based learning strategy. Figure 7.12, shows outputs of the

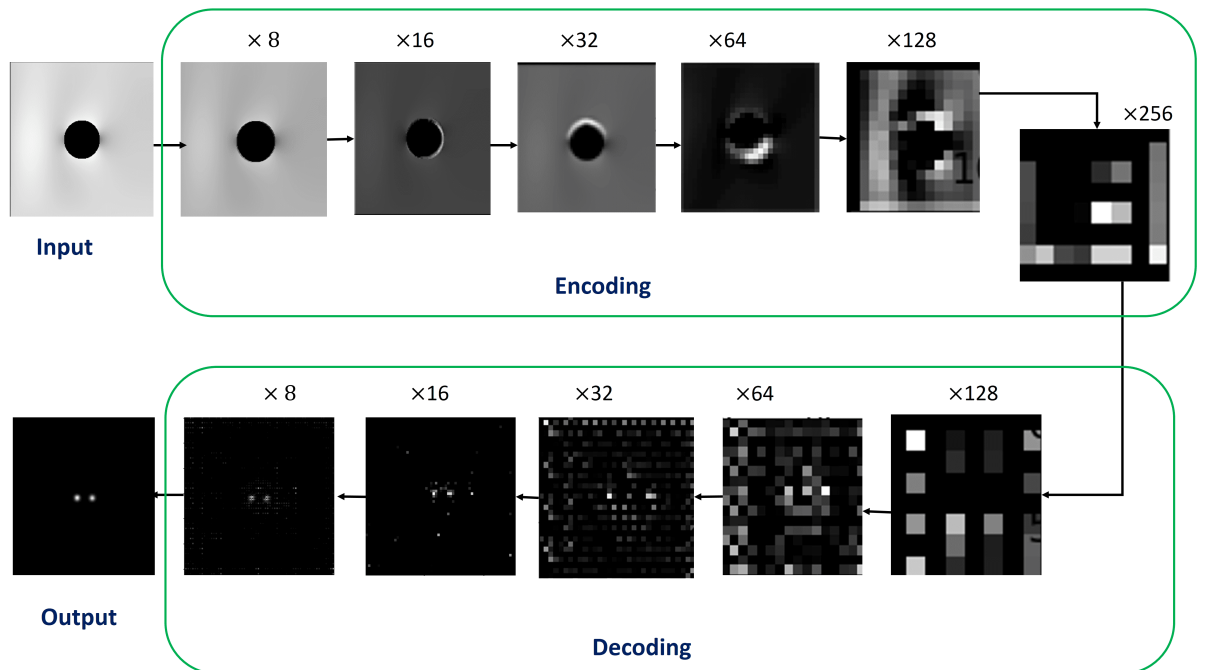


Figure 7.12: Feature maps correspond to the output of each of the encoder and decoder units of the DL model. The model input and output are the E_{rms} image and the image of the plasma density profile.

the encoding and the decoding unit, representing the important features. The features conserve the spatial locality in the image and allow better reconstruction of the output. The down-sampling of the actual image into refined features helps the encoder to detect the edges or boundaries (finest features), followed by up-sampling, which allows the decoder to learn a

mapping between the finest features with the required prediction. We can observe that from the original masked E_{rms} pattern, the model extracts the important features, mainly the patches of pixels that have useful scattering information (as variation in gray-scale intensity), and uses them to reconstruct the plasma profile.

7.5 Conclusion

This chapter discusses a data-driven deep learning-assisted microwave-plasma interaction-based study on asymmetric plasma density profiles categorized under Phase-1 and Phase-2, both motivated by realistic experiments. The deep-learning model designed on CNN-Unet architecture has been trained and evaluated on image data-sets obtained from diverse data. Those data pairs include multiple non-homogeneous plasmoids (Gaussian as well as Non-Gaussian) and highly asymmetric bands of plasma known as filaments) and their corresponding scattered E_{rms} pattern. Different metrics, such as SSIM, RMSLE, and RMSE, have been used to evaluate the results obtained from the model. For both experiments, the SSIM score for the predicted quantities is ≈ 0.98 , which nearly equals 1. The high SSIM convinces high similarity of reconstructed, E_{rms} pattern (for Phase-1) or plasma density profile (for Phase-2) with the ground truth data. We observe that the magnitude of error (RMSE or RMSLE) in reproducing two different outputs (E_{rms} or plasma profile) corresponding to Phase-1 and Phase-2 is well within an acceptable range. The increase in error may be attributed to sharp gradients in the fully asymmetric filaments compared to partial asymmetric profiles. The network performs well even for noisy (10-25% increase in noise amplitude) E_{rms} data and can predict partially asymmetric plasma profiles both in the presence and absence of noise. The percentage error lies within the similar range of 1 to 10%. Using a larger training data-set or proper noise filtering techniques may allow smoothing out the predicted profile, lowering the percentage error for asymmetric profile prediction. Further, the network's learning of important features has been highlighted using feature-map-based visualization.

CHAPTER 8

Conclusion and future scope

8.1 Introduction

The thesis presents two efficient computational techniques (dynamic mesh refinement and data-driven deep learning-based model) for accelerating the computational investigations of microwave plasma interaction-based diverse applications. Most of the applications are multi-scale and multi-physics in nature, where microwave-plasma interaction physics is associated with the smallest time-scale and controls the overall computational time. Our results reveal that these techniques can play a crucial role in accelerating the simulation of the microwave plasma interaction, which controls the discharge physics and plays a significant role in the overall breakdown-induced plasma generation process. The proposed techniques can also be applied to investigate longer time-scale phenomena, such as gas-heating effects, and efficiently understand the formation of different plasma structures observed in experiments. Additionally, the applicability of the two techniques has been shown and evaluated by studying important applications related to HPM breakdown-assisted plasma dynamics, plasma switching and protection, and plasma diagnostics.

DL-based approach provides a significantly faster alternative to existing FDTD-based computational techniques. It can accurately predict the scattered EM wave from a plasma medium with different plasma density profiles (Gaussian and Non-Gaussian types). A novel deep learning-based plasma diagnostics approach is presented, combining microwave-plasma interaction physics, existing plasma diagnostics techniques, and deep learning to train

neural networks for plasma density prediction with high accuracy and minimal effort.

8.2 Summary of main results and accomplishments of the thesis

- C-language based implementation and validation of a 2-D Maxwell-Plasma fluid model to simulate HPM breakdown. Analysis of associated computational challenges to address such multi-physics and multi-scale nature of the problem. Through a novel spatio-temporal investigation, we have explained the evolution of plasma filamentary structures during HPM breakdown experiments using different physical parameters.
- Development and implementation of the DMR (Dynamic Mesh Refinement) technique for accelerating the Maxwell-Plasma fluid model-based 2-D simulations on Cartesian grids. The technique is validated and analyzed for performance against published results to ensure reliability and accuracy. The DMR technique generates a self-aware fine mesh that evolves with time depending on plasma and electric field topology. Applying the DMR technique leads to accurately reproducing complex plasma dynamics and structures at significantly lower computational costs.
- EM-plasma interaction has also been investigated using dispersion relation to properly understand the EM wave reflection, transmission, and absorption in this work's parameter space of interest. Additionally, the complex dielectric and refractive index are computationally analyzed from the application point of view. The parametric study helped identify the different parameters that control the plasma formation time, required plasma profiles for manipulating the wave propagation, and how different applications can be developed based on the physics of microwave-plasma interaction.
- A simple gas heating model for air has been developed and coupled

with a Maxwell-plasma fluid solver, considering proper chemistry corresponding to the pressure and effective field used in the study. It has been used to perform 2-D simulations to understand the effect of gas heating on the growth and shape of plasma. Application related to switching and HPM limiter action for a wide frequency range has been investigated.

- For the first time, we propose a data-driven deep learning-based approach to investigate microwave-plasma interaction. An end-to-end UNet architecture accelerates the solution of Maxwell's equations with plasma current density. Training data has been generated using FDTD-based simulations with symmetric Gaussian plasma profiles and asymmetric plasma profiles such as non-Gaussian and filamentary. Extensive experiments are conducted to demonstrate the effectiveness and accuracy of the approach while comparing the results with conventional FDTD-based solutions. The results obtained from the DL network have been evaluated using various metrics such as MSE and MAPE. The reconstructed results are found to lie within an error margin of less than 1%. The proposed technique achieves a speedup of around 100-350 times compared to the existing FDTD-based computational techniques.
- A novel Deep learning-assisted microwave-plasma interaction-based technique for plasma density estimation has been proposed. The technique is based on microwave-plasma interaction physics. It uses a data-driven approach to realize the plasma density (n_e) profile from measured scattered electric field patterns when such plasma is exposed to a microwave. The proof of concept has been established on synthetically generated data considering several important experimental scenarios, such as noise in the experimentally measured scattered signals and the amount of experimentally measured data (dense vs sparse). The DL-based technique can determine the electron density profile within the plasma. The performance of the proposed deep learning-based approach has been evaluated using the structural similarity index (SSIM). The obtained results show promising performance in estimating the 2D radial

profile of the density for the given linear plasma device and affirm the potential of the proposed ML-based approach in plasma diagnostics.

- Using a data-driven approach, we numerically investigated microwave-plasma interactions under realistic experimental conditions by considering diverse synthetically generated training data-sets. Several plasma profiles have been considered, such as symmetric Gaussian profiles, asymmetric density profiles with multiple Gaussians and non-Gaussians, ellipsoids, filamentary plasma profiles, and more. Different peak densities have been considered for each of these profiles to capture different aspects of microwave-plasma interaction. The enriched data-set proved beneficial to train the DL model like real experimental data. Our results on this diverse data-set prove the feasibility of the proposed data-driven approach for deployment and use in real-practical scenarios.

8.3 Future scope

- **Extension to a 3-D DMR and its parallelization:** The 2-D fluid model for HPM breakdown cannot completely capture EM-plasma interactions in detail, particularly the 3D effects, as observed in real HPM breakdown experiments. A 3-D DMR-based model will be valuable to capture these intricacies, and parallelization of the DMR technique on emerging computing architectures will be a prerequisite for such investigations.
- **More accurate Gas-heating model:** The HPM breakdown model discussed in the thesis applies to overcritical breakdown conditions (applied electric field greater than breakdown field) with approximate air chemistry. A more accurate gas heating model is needed to investigate branching processes and replicate experimental observations for intermediate to sub-critical pressures and metallic initiator-based breakdown conditions. This model should have accurate plasma chemistry and consider evolving electron energy distribution functions.
- **A PINN based model:** The DL model in the thesis uses standard loss functions instead of physics-based loss-function calculation, resulting in

a slight mismatch between the FDTD and predicted results for E_{rms} . A customized loss function can be used to improve the DL model further and address this issue, or a PINN [130] based approach with the physics of microwave plasma interaction can be explored.

- **A DL-based hybrid model:** A DL-based hybrid HPM model can be a better alternative than the time-consuming iterative solvers. In the hybrid approach, the data-driven AI/ML models can accelerate the Maxwell solver. In contrast, a traditional differential equation-based approach can be used for the spatio-temporal evolution of the plasma using a continuity equation.

List of Publications

Journal:

1. Pratik Ghosh, Bhaskar Chaudhury, Shishir Purohit, Vishv Joshi, Ashray Kothari, Devdeep Shetranjiwala, *Deep Learning assisted microwave-plasma interaction based technique for plasma density estimation*, **Journal of Physics D: Applied Physics**, Sep 2023.
2. Pratik Ghosh and Bhaskar Chaudhury, *Efficient Dynamic Mesh Refinement Technique for Simulation of HPM Breakdown-Induced Plasma Pattern Formation*, **IEEE Transactions on Plasma Science**, vol. 51, page no- 66-76, Jan 2023.
3. Mihir Desai, Pratik Ghosh, Ahlad Kumar and Bhaskar Chaudhury, *Deep-Learning Architecture-Based Approach for 2-D-Simulation of Microwave Plasma Interaction*, **IEEE Transactions on Microwave Theory and Techniques**, vol. 70, page no- 5359-5368, Dec 2022.

Full length conference papers:

1. Pratik Ghosh and Bhaskar Chaudhury *Investigation of Microwave Induced Local Gas Heating in HPM Switching and Protection Using Two-dimensional Computations*, **2022 IEEE Microwaves, Antennas, and Propagation Conference (MAPCON)**, Bangalore, India, page no-404-409, 12-15 Dec., 2022.
2. Pratik Ghosh and Bhaskar Chaudhury, *Computational Investigation of Microwave Breakdown in HPM Switching and Protection*, **2021 IEEE MTT-S International Microwave and RF Conference (IMARC)**, IIT Kanpur, India, page no-1-4,17-19 Dec, 2021.
3. Pratik Ghosh and Bhaskar Chaudhury, *Mesh Refinement Based Simulation of Complex Plasma Dynamics during High Power Millimeter Wave Breakdown*, **2020 IEEE MTT-S International Conference on Numerical Electromagnetic and Multiphysics Modeling and Optimization (NEMO)**, Hangzhou, China, page no-1-4, 07-09 Dec, 2020.

Abstracts:

1. Pratik Ghosh and Bhaskar Chaudhury, *A Novel Self-Aware Dynamic Mesh Refinement Technique for Plasma Fluid Simulations of Microwave Breakdown*, in **2022 IEEE International Conference on Plasma Science (ICOPS)**, Seattle, WA, USA, 22-26 May 2022.
2. Pratik Ghosh and Bhaskar Chaudhury, *Fast simulation of gas heating effects during high power mmWave breakdown*, in **74th Annual Gaseous Electronics Conference (GEC-2021)**, Virtual: GEC Platform, USA, October 4–8, 2021.
3. Pratik Ghosh and Bhaskar Chaudhury, *Modelling and Simulation of Gas Heating Mechanism During High Power Millimeter Wave Breakdown in Air*, **2020 IEEE International Conference on Plasma Science (ICOPS)**, Singapore, Singapore, 06-10 Dec, 2020.
4. Pratik Ghosh, Vishrut Jetly, Bhargav Jhetwa and Bhaskar Chaudhury, *Mesh refinement based fluid simulations of plasma dynamics during high power microwave breakdown*, **34th National Symposium on Plasma Science & Technology (PLASMA 2019)**, VIT Chennai, India, 03-06 Dec, 2019.
5. Pratik Ghosh and Bhaskar Chaudhury, *Computational modeling of gas heating mechanism during high power microwave breakdown in air*, **12th International Conference on Plasma Science and Applications (ICPSA-2019)**, Lucknow, India, 11-14 Nov, 2019.

References

- [1] Y. Hidaka, E. M. Choi, I. Mastovsky, M. A. Shapiro, J. R. Sirigiri, R. J. Temkin, G. F. Edmiston, A. A. Neuber, and Y. Oda. Plasma structures observed in gas breakdown using a 1.5 MW, 110 GHz pulsed gyrotron. *Phys. Plasmas*, 16(5):055702, 2009.
- [2] Y. Hidaka, E. M. Choi, I. Mastovsky, M. A. Shapiro, J. R. Sirigiri, and R. J. Temkin. Observation of Large Arrays of Plasma Filaments in Air Breakdown by 1.5-MW 110-GHz Gyrotron Pulses. *Phys. Rev. Lett.*, 100:035003, Jan. 2008.
- [3] V. S. Barashenkov, L. P. Grachev, I. I. Esakov, B. F. Kostenko, K. V. Khodataev, and M. Z. Yur'ev. Threshold for a cumulative resonant microwave streamer discharge in a high-pressure gas. *Technical Physics*, 45(11):1406–1410, Nov 2000.
- [4] A. Cook, M. Shapiro, and R. Temkin. Pressure dependence of plasma structure in microwave gas breakdown at 110 GHz. *App. Phys. Lett.*, 97(1):011504, 2010.
- [5] K. V. Khodataev. Microwave Discharges and Possible Applications in Aerospace Technologies. *J. Propuls. Power*, 24(5):962–972, 2008.
- [6] Y. Oda, M. Takahashi, N. Ohnishi, K. Komurasaki, K. Sakamoto, and T. Imai. A study on the macroscopic self-organized structure of high-power millimeter-wave breakdown plasma. *Plasma Sources Sci. Technol.*, 29(7):075010, jul 2020.
- [7] A. M. Cook, J. S. Hummelt, M. A. Shapiro, and R. J. Temkin. Measurements of electron avalanche formation time in W-band microwave air breakdown. *Phys. Plasmas*, 18(8):080707, 2011.

- [8] P. Ghosh and B. Chaudhury. Efficient Dynamic Mesh Refinement Technique for Simulation of HPM Breakdown-Induced Plasma Pattern Formation. *IEEE Trans. Plasma Sci.*, pages 1–11, Dec. 2022.
- [9] B. Chaudhury and J. -P. Boeuf. Computational Studies of Filamentary Pattern Formation in a High Power Microwave Breakdown Generated Air Plasma. *IEEE Trans. on Plasma Sci.*, 38:2281 – 2288, 10 2010.
- [10] A. D. Macdonald. *"Microwave breakdown in gases"*. Wiley, New York, 1966.
- [11] D. Anderson, M. Lisak, and T. Lewin. Generalized criteria for microwave breakdown in air-filled waveguides. *J. Appl. Phys.*, 65(8):2935–2945, 1989.
- [12] M. Yang, P. Dong, K. Xie, X. Li, L. Quan and J. Li. Broadband microwave reflectometry plasma diagnostic based on invariant point of reflection data. *Phys. Plasmas*, 28(10):102105, 2021.
- [13] G. Q. Zhu. *Modeling of plasma dynamics and pattern formation during high power microwave breakdown in air*. PhD thesis, Université Paul Sabatier - Toulouse III, 2012.
- [14] I. Alexeff, T. Anderson, S. Parameswaran, E. Pradeep, J. Hulloli and P. Hulloli. Experimental and theoretical results with plasma antennas. *IEEE Trans. Plasma Sci.*, 34:166 – 172, Apr. 2006.
- [15] R. Vidmar. On the Use of Atmospheric Pressure Plasmas as Electromagnetic Reflectors and Absorbers. *IEEE Trans. Plasma Sci.*, 18:733 – 741, Sep. 1990.
- [16] B. Chaudhury and S. Chaturvedi. Study and Optimization of Plasma-Based Radar Cross Section Reduction Using Three-Dimensional Computations. *IEEE Trans. Plasma Sci.*, 37(11):2116–2127, Nov. 2009.
- [17] D. M. Sheen, D. L. McMakin, and T. E. Hall. Chapter 9 - detection of explosives by millimeter-wave imaging. In Jehuda Yinon, editor, *Counterterrorist Detection Techniques of Explosives*, pages 237–277. Elsevier Science B.V., Amsterdam, 2007.

- [18] M. Thumm. Novel applications of millimeter and submillimeter wave gyro-devices. *International Journal of Infrared and Millimeter Waves*, 22(3):377–386, Mar 2001.
- [19] O. Sakai and K. Tachibana. Plasmas as metamaterials: a review. *Plasma Sources Sci. Technol.*, 21(1):013001, Jan. 2012.
- [20] M. N. Shneider and R. B. Miles. Microwave diagnostics of small plasma objects. *J. Appl. Phys.*, 98:033301 – 033301, Sep. 2005.
- [21] S. Gold and G. Nusinovich. Review of high-power microwave source research. *Rev. Sci. Instrum.*, 68:3945–3974, 11 1997.
- [22] A. I. Saifutdinov, E.V.Kustova, A. G. Karpenko, and A. V. Lashkov. Dynamics of Focused Pulsed Microwave Discharge in Air. *Plasma Phys. Rep.*, 45(6):602–609, Jun 2019.
- [23] M. Fukunari, T. Yamaguchi, Y. Nakamura, K. Komurasaki, Y. Oda, K. Kajiwara, K. Takahashi, and K. Sakamoto. Thrust generation experiments on microwave rocket with a beam concentrator for long distance wireless power feeding. *Acta Astronaut.*, 145:263–267, April 2018.
- [24] J. Benford. Space Applications of High-Power Microwaves. *IEEE Trans Plasma Sci*, 36:569 – 581, 07 2008.
- [25] E. M. Walling. High Power Microwaves: Strategic and Operational Implications for Warfare. Technical report, Air University Press Maxwell AFB, AL 36112-6615, 02 2000.
- [26] T. Tang, C. Liao, P. Zhao, Q. Gao and Y. Wu. Breakdown characteristics of ultra-wideband high-power microwave transmission through the lower atmosphere. In *2010 Int. Conf. Microw. Millim. Wave Technol.*, pages 805–808, 2010.
- [27] J. P. Boeuf, B. Chaudhury, and G. Q. Zhu. Theory and Modeling of Self-Organization and Propagation of Filamentary Plasma Arrays in Microwave Breakdown at Atmospheric Pressure. *Phys. Rev. Lett.*, 104:015002, Jan 2010.

- [28] B. Chaudhury, J-P Boeuf, G. Q. Zhu, and O. Pascal. Physics and modelling of microwave streamers at atmospheric pressure. *J. Appl. Phys.*, 110(11):113306, Dec. 2011.
- [29] K. Frigui, D. Baillargeat, S. Verdeyme, S. Bila, A. Catherinot, J. Puech and D. Pacaud. Microwave Breakdown in Waveguide Filters Theoretical and Experimental Investigations. *IEEE Trans. Microw. Theory Tech.*, 56:3072 – 3078, Jan. 2009.
- [30] A. Semnani, S. O. Macheret, and D. Peroulis. A High-Power Widely Tunable Limiter Utilizing an Evanescent-Mode Cavity Resonator Loaded With a Gas Discharge Tube. *IEEE Trans. Plasma Sci.*, 44(12):3271–3280, Dec. 2016.
- [31] S. C. Schaub, J. S. Hummelt, W. C. Guss, M. A. Shapiro and R. J. Temkin. Electron density and gas density measurements in a millimeter-wave discharge. *Phys. Plasmas*, 23(8):083512, 2016.
- [32] M. Fukunari, S. Tanaka, R. Shinbayashi, Y. Yamaguchi, Y. Tatematsu, and T. Saito. Observation of a comb-shaped filamentary plasma array under subcritical condition in 303-GHz millimetre-wave air discharge. *Sci. Rep.*, 9(1):17972, Nov 2019.
- [33] K. V. Aleksandrov, L. P. Grachev, I. I. Esakov, V. V. Fedorov, and K. V. Khodataev. Domains of existence of various types of microwave discharge in quasi-optical electromagnetic beams. *Tech. Phys.*, 51(11):1448–1456, Nov 2006.
- [34] P. Bulat, I. Esakov, L. Grachev and K. Volkov and I. Volobuev. Experimental Study of Air Breakdown Induced by Subcritical Streamer Microwave Discharge. *IEEE Trans. Plasma Sci.*, 49(3):1041–1049, 2021.
- [35] B. Chaudhury, J. P. Boeuf, and G. Q. Zhu. Pattern formation and propagation during microwave breakdown. *Phys. Plasmas*, 17(12):123505, Dec. 2010.
- [36] K. Kurtzanidis, F. Rogier, and J. P. Boeuf. Gas heating effects on the formation and propagation of a microwave streamer in air. *J. Appl. Phys.*, 118:103301, 09 2015.

- [37] J. A. Bittencourt. *Fundamentals of Plasma Physics*. Springer-Verlag New York, springer edition, 2004.
- [38] F. F. Chen. *Introduction to plasma physics and controlled fusion*. A Division of Plenum Publishing Corporation, 1984.
- [39] Y. N. Taranenkov, U. S. Inan, and T. F. Bell. Interaction with the lower ionosphere of electromagnetic pulses from lightning: Heating, attachment, and ionization. *Geophysical Research Letters*, 20(15):1539–1542, 1993.
- [40] C. K. Birdsall and A. B. Langdon. *Plasma Physics via Computer Simulation*. CRC press, 2004.
- [41] T. Tajima. *Computational plasma physics: with applications to fusion and astrophysics*. CRC press, 2018.
- [42] K. G. Budden. *The propagation of radio waves: the theory of radio waves of low power in the ionosphere and magnetosphere*. Cambridge University Press, 1988.
- [43] B. Chaudhury and S. Chaturvedi. Comparison of wave propagation studies in plasmas using three-dimensional finite-difference time-domain and ray-tracing methods. *Phys. Plasmas*, 13(12):123302, Dec. 2006.
- [44] P. Ghosh and B. Chaudhury. Computational Investigation of Microwave Breakdown in HPM Switching and Protection. In *2021 IEEE MTT-S Int. Microw. RF Conf. (IMaRC)*, pages 1–4, Feb. 2021.
- [45] B. Chaudhury, A. Gupta, H. Shah, and S. Bhadani. Accelerated simulation of microwave breakdown in gases on Xeon Phi based cluster-application to self-organized plasma pattern formation. *Comput. Phys. Commun.*, 229:20 – 35, Apr. 2018.
- [46] S. Yan, A. D. Greenwood, and J. Jin. Modeling of Plasma Formation During High-Power Microwave Breakdown in Air Using the Discontinuous Galerkin Time-Domain Method. *IEEE J. Multiscale and Multiphys. Comput. Techn.*, 1:2–13, 2016.

- [47] S. Yan, J. Qian, and J. M. Jin. An advanced em-plasma simulator based on the dgtd algorithm with dynamic adaptation and multirate time integration techniques. *IEEE J. Multiscale Multiphys Comput. Techn.*, 4:76–87, 2019.
- [48] J. Wang, L. Cai, X. Zhu, Y. Wang, and C. Xuan. Numerical simulations of high power microwave dielectric interface breakdown involving outgassing. *Phys. Plasmas*, 17(6), Jun 2010. 063503.
- [49] L. Cai, J. Wang, X. Zhu, Y. Wang, and D. Zhang. Two-dimensional simulation research of secondary electron emission avalanche discharge on vacuum insulator surface. *Phys. Plasmas*, 22(1), Jan 2015. 013502.
- [50] J. Wang, D. Zhang, C. Liu, Y. Li, Y. Wang, H. Wang, H. Qiao, and X. Li. UNIPIC code for simulations of high power microwave devices. *Phys. Plasmas*, 16(3), Mar 2009. 033108.
- [51] M. Raissi, P. Perdikaris, G.E. Karniadakis. Physics-informed neural networks: A deep learning framework for solving forward and inverse problems involving nonlinear partial differential equations. *J. Comput. Phys.*, 378:686–707, Nov. 2018.
- [52] J. Han and A. Jentzen and W. Ee. Solving high-dimensional partial differential equations using deep learning. *Proc. Natl. Acad. Sci.*, 115, Jul. 2017.
- [53] J. Degraeve, F. Felici, J. Buchli et al. Magnetic control of tokamak plasmas through deep reinforcement learning. *Nature*, 602:414–419, Feb. 2022.
- [54] J. Kates-Harbeck, A. Svyatkovskiy and W. Tang. Predicting disruptive instabilities in controlled fusion plasmas through deep learning. *Nature*, 568, Apr. 2019.
- [55] N. Dalsania, Z. Patel, S. Purohit and B. Chaudhury. An Application of Machine Learning for Plasma Current Quench Studies via Synthetic Data Generation. *Fusion Eng. Des.*, 171:112578, Oct. 2021.
- [56] A. Mesbah and D. Graves. Machine learning for modeling, diagnostics, and control of non-equilibrium plasmas. *J. Phys. D: Appl. Phys.*, 52, May 2019.

- [57] V. Jetly and B. Chaudhury. Extracting Electron Scattering Cross Sections from Swarm Data using Deep Neural Networks. *Mach. learn.: sci. technol.*, 2, Mar. 2021.
- [58] Z. Wei and X. Chen. Physics-Inspired Convolutional Neural Network for Solving Full-Wave Inverse Scattering Problems. *IEEE Trans. Antennas Propag.*, 67(9):6138–6148, Sep. 2019.
- [59] M. Raissi, A. Yazdani and G. Em Karniadakis. Hidden fluid mechanics: Learning velocity and pressure fields from flow visualizations. *Science.*, 367(6481):1026–1030, Jan. 2020.
- [60] A. Massa, D. Marcantonio, X. Chen, M. Li, and M. Salucci. DNNs as Applied to Electromagnetics, Antennas, and Propagation - A Review. *IEEE Antennas Wirel. Propag. Lett.*, 18(11):2225–2229, May 2019.
- [61] S. Qi, Y. Wang, Y. Li, X. Wu, Q. Ren, and Y. Ren. Two-Dimensional Electromagnetic Solver Based on Deep Learning Technique. *IEEE J. Multiscale Multiphys Comput. Techn.*, 5:83–88, May 2020.
- [62] O. Ronneberger, P. Fischer and T. Brox. U-Net: Convolutional Networks for Biomedical Image Segmentation. In N. Navab, J. Hornegger, W. M. Wells and A. F. Frangi, editor, *Med. Image Comput. Comput. Assist Interv. – MICCAI 2015. Lecture Notes in Computer Science*, pages 234–241, Cham, 2015. Springer International Publishing.
- [63] P. Zhang, Y. Hu, Y. Jin, S. Deng, X. Wu and J. Chen. A Maxwell’s Equations Based Deep Learning Method for Time Domain Electromagnetic Simulations. *IEEE J. Multiscale Multiphysics Comput. Tech.*, 6(6481):35–40, Feb. 2021.
- [64] D. R. Ferreira, P. Carvalho and H. Fernandes. Deep Learning for Plasma Tomography and Disruption Prediction From Bolometer Data. *IEEE Trans. Plasma Sci.*, 48(1):36–45, Jan. 2020.
- [65] L. Cheng, E. A. Illarramendi, G. Bogopolsky, M. Bauerheim and B. Cuenot. Using neural networks to solve the 2d poisson equation for electric field computation in plasma fluid simulations. *CoRR*, abs/2109.13076, 2021.

- [66] N. S. Punn and S. Agarwal. Modality specific U-Net variants for biomedical image segmentation: a survey. *Artif. Intell. Rev.*, 55(7):5845–5889, Oct. 2022.
- [67] J. Long, E. Shelhamer and T. Darrell. Fully convolutional networks for semantic segmentation. In *2015 IEEE Comput Soc Conf Comput Vis Pattern Recognit (CVPR)*, pages 3431–3440, 2015.
- [68] V. Badrinarayanan, A. Kendall and R. Cipolla. SegNet: A Deep Convolutional Encoder-Decoder Architecture for Image Segmentation. *IEEE Trans. Pattern Anal. Mach. Intell.*, 39(12):2481–2495, Dec. 2017.
- [69] A. Hamiaz, X. Ferrieres, and O. Pascal. Efficient numerical algorithm to simulate a 3D coupled Maxwell-plasma problem. *Math. Comput. Simul.*, 174:19–31, 2020.
- [70] M. Löfgren, D. Anderson, H. Bonder, H. Hamnén, and M. Lisak. Breakdown phenomena in microwave transmit-receive switches. *J. Appl. Phys.*, 69(4):1981–1992, 1991.
- [71] M. Bäckström, U. Jordan, D. Andersson, A. Kim, M. Lisak, and O. Lundén. Can intentional electrical discharges be used for HPM protection? *IEEE Int. Symp. Electromagn. Compat.*, Aug. 2011.
- [72] Z. V. Missen, S. Macheret, A. Semnani, and D. Peroulis. Plasma Switch-Based Technology for High-Speed and High-Power Impedance Tuning. In *2021 IEEE 21st Annual Wirel. Microw. Technol. Conf. (WAMICON)*, pages 1–4, 2021.
- [73] N. Sadeghi and U. Czarnetzki. Preface: The 8th workshop on frontiers in low temperature plasma diagnostics the 8th workshop on frontiers in low temperature plasma diagnostics. *Journal of Physics D-applied Physics - J PHYS-D-APPL PHYS*, 43, 03 2010.
- [74] M. Moisan and J. Pelletier. *Physics of Collisional Plasmas: Introduction to high-frequency discharges*. 01 2012.
- [75] F. Chen. Industrial applications of low-temperature plasma physics. *Physics of Plasmas - PHYS PLASMAS*, 2:2164–2175, 06 1995.

- [76] A. Keudell and V. Gathen. Foundations of low-temperature plasma physics - an introduction. *Plasma Sources Science and Technology*, 26, 09 2017.
- [77] S. Samukawa, M. Hori, S. Rauf, K. Tachibana, P. Bruggeman, G. Kroesen, J. Whitehead, A. Murphy, A. Gutsol, S. Starikovskaia, U. Kortshagen, J. P. Boeuf, T. Sommerer, M. Kushner, U. Czarnetzki, and N. Mason. The 2012 plasma roadmap. *Journal of Physics D: Applied Physics*, 45:253001, 06 2012.
- [78] I. Adamovich, S. Baalrud, A. Bogaerts, P. Bruggeman, M. Cappelli, V Colombo, U. Czarnetzki, U. Ebert, J Eden, P Favia, D Graves, S. Hamaguchi, G. Hieftje, M Hori, I. Kaganovich, U Kortshagen, M Kushner, N. Mason, S. Mazouffre, and A. Vardelle. The 2017 plasma roadmap: Low temperature plasma science and technology. *Journal of Physics D: Applied Physics*, 50:323001, 08 2017.
- [79] I. Adamovich, S Agarwal, E. Ahedo, L.L. Alves, S. Baalrud, N Babaeva, A Bogaerts, A. Bourdon, P. Bruggeman, C Canal, E Choi, S Coulombe, Z. Donkó, D Graves, S. Hamaguchi, D. Hegemann, M Hori, H.-H Kim, G.M.W. Kroesen, and T Woedtke. The 2022 plasma roadmap: low temperature plasma science and technology. *Journal of Physics D: Applied Physics*, 55:373001, 09 2022.
- [80] A. Mesbah and D. Graves. Machine learning for modeling, diagnostics, and control of non-equilibrium plasmas. *Journal of Physics D: Applied Physics*, 52, 05 2019.
- [81] X. Lu, P. Bruggeman, S. Reuter, G. Naidis, A. Bogaerts, M. Laroussi, M. Keidar, E. Robert, J-M. Pouvesle, D. Liu, and K. Ostrikov. Grand challenges in low temperature plasmas. *Frontiers in Physics*, 10, 10 2022.
- [82] S. N-Kuok. *Theory of Low-Temperature Plasma Physics*, volume 95. 2017.
- [83] R. J Goldston and P. H Rutherford. *Introduction to Plasma Physics*. 1995.
- [84] V. Jetly and B. Chaudhury. Extracting electron scattering cross sections from swarm data using deep neural networks. *Machine Learning: Science and Technology*, 2, 03 2021.

- [85] S. Jardin. *Computational methods in plasma physics*. 2010.
- [86] M. Laroussi, X. Lu, and M. Keidar. Perspective: The physics, diagnostics, and applications of atmospheric pressure low temperature plasma sources used in plasma medicine. *Journal of Applied Physics*, 122, 2017.
- [87] W.L. Wiese. Spectroscopic diagnostics of low temperature plasmas: techniques and required data. *Spectrochimica Acta Part B: Atomic Spectroscopy*, 46(6):831–841, 1991.
- [88] B. Engeln, R. and Klarenaar and O. Guaitella. Foundations of optical diagnostics in low-temperature plasmas. *Plasma Sources Science and Technology*, 29, 01 2020.
- [89] F. Leipold, R. H. Stark, A. El-Habachi, and K. H. Schoenbach. Electron density measurements in an atmospheric pressure air plasma by means of infrared heterodyne interferometry. *Journal of Physics D: Applied Physics*, 33, 2000.
- [90] J. Y. Choi, N. Takano, K. Urabe, and K. Tachibana. Measurement of electron density in atmospheric pressure small-scale plasmas using co2-laser heterodyne interferometry. *Plasma Sources Science and Technology*, 18, 2009.
- [91] E. Mazzucato. Microwave reflectometry for magnetically confined plasmas. *Rev. Sci. Instrum.*, 69(6):2201–2217, 1998.
- [92] M. Takahashi, Y. Kageyama, and N. Ohnishi. Joule-heating-supported plasma filamentation and branching during subcritical microwave irradiation. *AIP Adv.*, 7(5):055206, 2017.
- [93] M. Takahashi and N. Ohnishi. Gas propellant dependency of plasma structure and thrust performance of microwave rocket. *J. Appl. Phys.*, 125(16):163303, 2019.
- [94] L. Wang , D. Ding, R. Chen, W. Cui, and R. Wang. Transient Analysis of High-Power Microwave Air Breakdown under External DC Magnetic Field. *IEEE Trans. Antennas Propag.*, 68(6):4894–4903, June 2020.

- [95] P. Zhao , C. Liao, W. Lin, L. Chang, and H. Fu. Numerical studies of the high power microwave breakdown in gas using the fluid model with a modified electron energy distribution function. *Phys. Plasmas*, 18(10):102111, 2011.
- [96] J. Wang, Y. Chen , R. Fan, H. Yu, and D. Ge. Numerical studies on nonlinear coupling of high-power microwave pulses into a cylindrical cavity. *IEEE Trans. Plasma Sci.*, 24(1):193–197, Feb 1996.
- [97] S. K. Nam and J. P. Verboncoeur. Theory of Filamentary Plasma Array Formation in Microwave Breakdown at Near-Atmospheric Pressure. *Phys. Rev. Lett.*, 103:055004, Jul 2009.
- [98] Y. Nakamura, K. Komurasaki, M. Fukunari and H. Koizumi. Numerical analysis of plasma structure observed in atmospheric millimeter-wave discharge at under-critical intensity. *J. Appl. Phys.*, 124(3):033303, 2018.
- [99] A. I. Saifutdinov and E. V. Kustova. Dynamics of plasma formation and gas heating in a focused-microwave discharge in nitrogen. *J. Appl. Phys.*, 129(2):023301, 2021.
- [100] K. Kourtzanidis, J. P. Boeuf and F. Rogier. Three dimensional simulations of pattern formation during high-pressure, freely localized microwave breakdown in air. *Phys. Plasmas*, 21(12):123513, 2014.
- [101] V. G. Brovkin and P. V. Vedenin. Study of the microwave streamer evolution using a new semi-analytical model. *J. Appl. Phys.*, 128(11):113301, 2020.
- [102] K. Kourtzanidis and L. L. Raja. Analysis and characterization of microwave plasma generated with rectangular all-dielectric resonators. *Plasma Sources Sci. Technol.*, 26(4):045007, 2017.
- [103] G. J. M. Hagelar. *Modelling Methods for Low-Temperature Plasmas*. PhD thesis, Plasmas. Université Toulouse III Paul Sabatier (UT3 Paul Sabatier), 2008.
- [104] K. Kourtzanidis and L. L. Raja. Limitations of the effective field approximation for fluid modeling of high frequency discharges in

- atmospheric pressure air: Application in resonant structures. *Phys. Plasmas*, 24(11):112105, 2017.
- [105] K.S. Kunz and R.J. Luebbers. *The Finite Difference Time Domain Method for Electromagnetics*. Taylor & Francis, 1993.
- [106] A. Taflove and S. C. Hagness. *Computational electrodynamics: the finite-difference time-domain method*. Artech House, Norwood, 3rd edition, 2005.
- [107] G. Mur. Absorbing Boundary Conditions for the Finite-Difference Approximation of the Time-Domain Electromagnetic-Field Equations. *IEEE Trans. Electromagn. Compat.*, EMC-23(4):377–382, Nov 1981.
- [108] P. Ghosh and B. Chaudhury. Mesh Refinement Based Simulation of Complex Plasma Dynamics during High Power Millimeter Wave Breakdown. In *2020 IEEE MTT-S Int. Conf. Numer. Electromagn. Multiphys. Modeling and Optimization (NEMO)*, pages 1–4, Feb. 2020.
- [109] Q. Zhou and Z. Dong. Modeling study on pressure dependence of plasma structure and formation in 110 GHz microwave air breakdown. *Appl. Phys. Lett.*, 98(16):161504, 2011.
- [110] M. Takahashi and K. Komurasaki. Discharge from a high-intensity millimeter wave beam and its application to propulsion. *Adv. Phys.- X*, 3(1):1417744, 2018.
- [111] D. Knight, Y. F. Kolesnichenko, V. Brovkin, D. Khmara, V. Lashkov and I. Mashek. Interaction of Microwave-Generated Plasma with a Hemisphere Cylinder at Mach 2.1. *AIAA Journal*, 47(12):2996–3010, 2009.
- [112] J. B. Michael, A. Dogariu, M. N. Shneider, and R. B. Miles. Subcritical microwave coupling to femtosecond and picosecond laser ionization for localized, multipoint ignition of methane/air mixtures. *J. Appl. Phys.*, 108(9):093308, 2010.
- [113] S. S. Zivanovic, K. S. Yee, and K. K. Mei. A subgridding method for the time-domain finite-difference method to solve Maxwell's equations. *IEEE Trans. Micro. Theory Tech.*, 39(3):471–479, 1991.

- [114] K.Xiao, D. J. Pommerenke, and J. L. Drewniak. A Three-Dimensional FDTD Subgridding Algorithm With Separated Temporal and Spatial Interfaces and Related Stability Analysis. *IEEE Trans. Antennas Propaga.*, 55(7):1981–1990, 2007.
- [115] C. D. Sarris. *"Adaptive Mesh Refinement for Time-Domain Numerical Electromagnetics"*. Morgan & Claypool, 2007.
- [116] Y. Kolesnichenko, D. Knight, V. Brovkin, and D. Khmara. High Speed Flow Control Using Microwave Energy Deposition. In *46th AIAA Aerosp. Sci. Meet. and Exhibit*. 2008.
- [117] H. Fayazi, A. B. Lashak, and M. R. A Pehlavani. Numerical and Experimental Investigation of the Effects of Dimensional Parameters on Carbon-Nanotube-Coated Copper Plasma Limiter. *IEEE Trans. Plasma Sci.*, 50(5):1246–1254, 2022.
- [118] A. Semnani, S. O. Macheret., and D. Peroulis. A High-Power Widely Tunable Limiter Utilizing an Evanescent-Mode Cavity Resonator Loaded With a Gas Discharge Tube. *IEEE Trans. on Plasma Sci.*, 44(12):3271–3280, 2016.
- [119] J. Rasch. *Microwave Gas and Multipactor Breakdown in Inhomogeneous Fields*. PhD thesis, Chalmers University of Technology, 2012.
- [120] P. Ghosh and B. Chaudhury. Investigation of microwave induced local gas heating in hpm switching and protection using two-dimensional computations. In *2022 IEEE Microwaves, Antennas, and Propagation Conference (MAPCON)*, pages 404–409, 2022.
- [121] K. Kourtzanidis, F. Rogier and J-P Boeuf. ADI-FDTD modeling of microwave plasma discharges in air towards fully three-dimensional simulations. *Comput. Phys. Commun.*, 195:49–60, May 2015.
- [122] G. Wang, L. Zhang, H. Feng and J. Ouyang. Numerical Study on Microwave Scattering by Various Plasma Objects. *Plasma Sci. Technol.*, 18:791–797, Aug. 2016.
- [123] J. C. Ye and W. K. Sung. Understanding geometry of encoder-decoder cnns, 2019.

- [124] D. P. Kingma and J. Ba. Adam: A method for stochastic optimization, 2014.
- [125] Z. Wang, E. P. Simoncelli, and A. C. Bovik. Multiscale structural similarity for image quality assessment. In *The Thirty-Seventh Asilomar Conf. Signals Syst. Comput. 2003*, volume 2, pages 1398–1402 Vol.2, May 2003.
- [126] Z. Wang, A.C. Bovik, H.R. Sheikh, and E.P. Simoncelli. Image quality assessment: from error visibility to structural similarity. *IEEE Transactions on Image Processing*, 13(4):600–612, 2004.
- [127] Z. Wang and A.C. Bovik. A universal image quality index. *IEEE Signal Processing Letters*, 9(3):81–84, 2002.
- [128] K. S. Yee. Numerical solution of initial boundary value problems involving maxwell’s equations in isotropic media. *IEEE Trans. Antennas Propag.*, 14(3):302–307, May 1966.
- [129] V. Dumolin and F. Visin. A guide to convolution arithmetic for deep learning, 2016.
- [130] Y. Chen, Lu Lu, G. Em Karniadakis and L. D. Negro. Physics-informed neural networks for inverse problems in nano-optics and metamaterials. *Opt. Express*, 28(8):11618–11633, Apr. 2020.
- [131] R. J. Vidmar. On the use of atmospheric pressure plasmas as electromagnetic reflectors and absorbers. *IEEE Trans. Plasma Sci.*, 18(4):733–741, 1990.
- [132] A. Ghayekhloo, A. Abdolali. Use of Collisional Plasma as an Optimum Lossy Dielectric for Wave Absorption in Planar Layers, Analysis, and Application. *IEEE Trans. Plasma Sci.*, 42(8):1999–2006, 2014.
- [133] E. Noori. Investigation of near cut-off properties of electromagnetic wave propagation in homogeneous, collisional plasma slab. *Contrib. to Plasma Phys.*, 62(8):e202200016, 2022.
- [134] S. Zhang, X. Hu, Z. Jiang, M. Liu and Y. He. Propagation of an electromagnetic wave in an atmospheric pressure plasma: Numerical

solutions, journal = Phys. Plasmas. 13(1):013502, 2006.

- [135] G. Cheng, L. Liu. Direct Finite-Difference Analysis of the Electromagnetic-Wave Propagation in Inhomogeneous Plasma. *IEEE Trans. Plasma Sci.*, 38(11):3109–3115, 2010.
- [136] M. Desai, P. Ghosh, A. Kumar and B. Chaudhury. Deep-Learning Architecture-Based Approach for 2-D-Simulation of Microwave Plasma Interaction. *IEEE Trans. Microw. Theory Tech.*, 70(12):5359–5368, 2022.
- [137] M. Nishiura, Z. Yoshida, T. Mushiake, Y. Kawazura, R. Osawa, K. Fujinami, Y. Yano, H. Saitoh, M. Yamasaki, A. Kashyap, N. Takahashi, M. Nakatsuka, and A. Fukuyama. Electro-optic probe measurements of electric fields in plasmas. *Review of Scientific Instruments*, 88(2):023501, 2017.
- [138] M. A. Razzak, S. Takamura, T. Tsujikawa, H. Shibata, and Y. Hatakeyama. Measurement of electric field distribution along the plasma column in microwave jet discharges at atmospheric pressure. *Plasma and Fusion Research*, 4:047–047, 2009.
- [139] K. Orr, Y. Tang, M. Simeni Simeni, D. van den Bekerom, and I. V Adamovich. Measurements of electric field in an atmospheric pressure helium plasma jet by the E-FISH method. *Plasma Sources Science and Technology*, 29(3):035019, mar 2020.
- [140] D. Ye, W. Wang, C. Yin, Z. Xu, H. Zhou, H. Fang, Y. Li, and J. Huang. Pulsed terahertz spectroscopy combined with hybrid machine learning approaches for structural health monitoring of multilayer thermal barrier coatings. *Opt. Express*, 28(23):34875–34893, Nov 2020.
- [141] A. A. Mir, F. V. Çelebi, H. Alsolai, S. A. Qureshi, M. Rafique, J. S. Alzahrani, H. Mahgoub, and M. A. Hamza. Anomalies Prediction in Radon Time Series for Earthquake Likelihood Using Machine Learning-Based Ensemble Model. *IEEE Access*, 10:37984–37999, 2022.
- [142] X. Glorot and Y. Bengio. Understanding the difficulty of training deep feedforward neural networks. In *Proceedings of the Thirteenth International Conference on Artificial Intelligence and Statistics*, volume 9 of *Proceedings of*

Machine Learning Research, pages 249–256, Chia Laguna Resort, Sardinia, Italy, 13–15 May 2010. PMLR.

- [143] Cadence PCB solutions. What is Signal to Noise Ratio and How to calculate it?, 2023.